Examination of the Ion Beam Response of III-V Semiconductor Substrates

by

Kevin A. Grossklaus

A dissertation submitted in partial fulfillment
of the requirements for the degree of
Doctor of Philosophy
(Materials Science and Engineering)
in The University of Michigan
2012

Doctoral Committee:

Professor Joanna M. Millunchick, Chair
Professor Roy Clarke
Professor Xiaoqing Pan
Assistant Professor Akram Boukai

Acknowledgements

With the utmost gratitude I would like to thank all of the people who have guided me through my graduate career and helped me reach this point. First and foremost I must thank my advisor, Professor Joanna Mirecki Millunchick, for all of her guidance and help. In the later parts of my graduate career I've found myself on numerous occasions advising younger grad students to choose their research group based not on the research project or the group's equipment, but by its advisor, and I'm happy that 5 years ago I followed that advice myself. I don't think I could have asked for a better supervisor, mentor, or teacher to help me through my graduate career. Professor Millunchick has been a constant source of intellectual and professional support to me. She has been understanding when equipment breaks, experiments fail, or when the events of life just throw a wrench into the workings of science. She has provided me with many opportunities to advance my career and myself, and she has helped me to learn a great many things I never even knew I wanted to learn. I am immensely grateful to her, and wish her nothing but the best in every part of her life.

There are too many other professors and staff at the University of Michigan to whom I owe thanks to name them all, but I am grateful for all their advice and assistance over the years. Specifically I would like to thank the other members of my graduate committee, Professors Roy Clark, Xiaoqing Pan, and Akram Boukai, for helping to see me through these final steps on the road to a doctorate. I would also like to specifically thank the staff of EMAL, Dr. John Mansfield, Dr. Kai Sun, and Dr. Haiping Sun, for all of their help. Much of the business of my research has been the process of looking at very small things with very large, expensive microscopes, and they have helped me to carry out that work and advised me constantly.

I must also thank my many co-workers at the University of Michigan and my friends there and abroad. Thank you for all the advice, all the insightful conversations,

all the absurd conversations, and for all the times you helped me step back from work and enjoy being in graduate school. I've had a great time in graduate school, and you have been much of the reason for it. I must of course specially thank all the members of my research group past and present who have helped me to succeed on so many occasions. Thank you Jennifer Lee-Feldman, Lee Sears, Jessica Bickel, John Thomas, Andy Di Deng, Denis Nothern, Adam Duzik, Andrew Martin, and Matthew DeJarld for all the training you've given me, experiments you've helped me to run, and all the broken equipment you've helped me to fix. May your futures be bright and full of mostly working equipment.

I would like to thank my parents and sister as well. My family has always made time for me, regardless of what events in their own lives might be keeping them busy or what troubles of their own they might be facing. They have supported me at every step of my life and education, and I love them for it. Without their help throughout my life I would not be the person I am today.

Finally, but most importantly, I would like to acknowledge my wife Heather. When I came to the University of Michigan to start work on my doctorate she was my girlfriend, in the midst of my research and time in Ann Arbor she agreed to become my fiancé, and now as my time at Michigan comes to an end I have been blessed to call her my wife for over two years. She has supported me throughout the trials of graduate school, she has helped me through the stress of having too much to do in too little time, she has helped me to relax and open up, and most importantly every day she has reminded me that I am loved. Heather, I love you and thank you for helping me make it through all of this. Graduate school has been a good part of my life.

Table of Contents

List of Figures

List of Tables

Abstract

This work examines the response of the III-V materials to ion beam irradiation in a series of four experimental studies and describes the observed results in terms of the fundamental materials processes and properties that control ion-induced change in those compounds. Two studies investigate the use of Ga^+ focused ion beam (FIB) irradiation of III-V substrate materials to create nanostructures. In the first, the creation of FIB induced group III nanodots on GaAs, InP, InAs, and AlAs is studied. The analysis of those results in terms of basic material properties and a simple nanodot growth model represents the first unified investigation of the fundamental processes that drive the nanodot forming behavior of the III-V compounds. The second nanostructure formation study reports the discovery and characterization of unique spike-like InAs nanostructures, termed "nanospikes," which may be useful for nanoscale electronic or thermoelectric applications. A novel method for controlling nanospike formation using InAs/InP heterostructures and film pre-patterning is developed, and the electrical properties of these ion erosion created nanostructures are characterized by in-situ TEM nanoprobe testing in a first-of-its-kind examination. The two remaining studies examine methods for using ion beam modification of III-V substrates to accommodate lattice-mismatched film growth with improved film properties. The first examines the effects of film growth on a wide range of different FIB created 3-D substrate patterns, and finds that 3-D surface features and patterns significantly alter film morphology and that growth on or near FIB irradiated regions does not improve film threading defect density. The second substrate modification study examines broad beam ion pre-implantation of GaAs wafers before InGaAs film growth, and is the first reported study of III-V substrate pre-implantation. Ar^+ pre-implantation was found to enhance the formation of threading defects in InGaAs films and so improve their roughness and degree of relaxation. This effect, combined with a threading dislocation filtering structure, is anticipated to produce high quality buffers for lattice-mismatched film growth.

Chapter 1

Introduction and Background

Ion implantation has long seen extensive use in the semiconductor industry as a method for altering the electronic and structural properties of semiconductor films and substrates. Its first application was to provide a means for controlled introduction of dopant atoms over a broad area at a desired concentration and depth beneath a semiconductor surface. Ion implantation technology has since been further developed, and its common uses in the semiconductor industry now include the production and removal of implantation damage, enhancing diffusion and electrical activation of implanted dopants during subsequent annealing, formation of insulating or conducting layers by direct implantation, and controlled introduction of irradiation-induced defects to tailor specific electrical and optical properties [1]. As a processing method for the III-V compound semiconductors, ion implantation has seen broad use as a way to introduce nearly any desired dopant species in precise manner, to create insulating layers by inducing heavy ion damage in the semiconducting material, and to intentionally disorder the composition of III-V heterostructure film stacks [2].

Beyond current industrial applications, the effect of ion implantation on semiconductors has in the past and continues to be in the present an area of scientific interest, and broad area implantation of the III-V semiconductors has been studied extensively in the literature. Implantation of the III-V semiconductors has been used to examine the fundamental processes and factors that control the production of ion damage, creation of associated defect structures, and materials amorphization [1,3-9]. Lower energy broad area ion irradiation has also been examined as a method for sputtering away or otherwise modifying III-V semiconductors surfaces. As two examples, ion irradiation of InP has been used to induce cone formation [10] and produce ordered surface mounding [11]. Ion implantation of III-V heterostructures has also been examined previously as a method for altering the strain state and defect density of thin film structures [12,13]. Within these areas and others new scientific work is being carried out and new applications for ion beam irradiation are being discovered.

The development of focused ion beam (FIB) technology has also allowed new ion implantation and damage related phenomena to be explored using the III-V semiconductors. In particular, the relatively high rate at which the III-V materials preferentially sputter under FIB irradiation has resulted in the discovery of several unique methods for creating nanostructures. For example, metallic droplets (also called nanodots) can be produced by FIB irradiation of GaAs [14], InAs [15], and InP [16], while irradiation of GaSb leads to the creation of a porous structure and eventually nanowires [17]. Additionally, many different FIB based techniques have been developed for characterization and surface modification of semiconductors and other materials. These take advantage of a FIB system's unique ability to quickly remove material on the nanoscale by ion milling in nearly any geometry or pattern desired by the user. These existing FIB techniques are opening up new avenues of study in the areas of ion beam materials modification and nanostructure generation. Broad beam and focused ion beam irradiation continue to be active areas of research with much space left for novel experimentation, especially in the area of ion beam modification of semiconducting materials.

The broad theme of this dissertation is the examination of the response of the III-V semiconductors to ion irradiation. To that end, this work contains four studies which each examine a method by which ion irradiation, in the form of either FIB or broad area implantation, of the III-V compound semiconductor substrate materials may be used to either create unique nanostructures or to modify a substrate for subsequent film growth. The III-V semiconductor materials were chosen for study because of their technological importance and because they respond to ion irradiation in a number of unique ways. The methods and motivations of each study are different, but the overarching common goals of all four studies were to thoroughly characterize the effects of ion irradiation on the III-V materials, to characterize any ion-created structures, and to try to understand the observed results in terms of the fundamental materials processes and properties which control ion-induced changes in those materials. Each portion of this work either presents the discovery of new ways in which a III-V material responds to ion irradiation or presents new characterization and unique analysis aimed at providing an enhanced understanding of ion-induced phenomena in the III-V materials. The results of the work presented here may have application in the creation of nanostructure based electronic, optoelectronic, and thermoelectric devices and in the area of high quality, low-defect density lattice-mismatched heterostructure film growth.

1.1 Objectives and Organization

This research is composed of four studies, all of which are focused on examining the response of common III-V substrate materials to ion beam irradiation. Two studies are examinations of different methods for using FIB irradiation of common III-V binary materials to created nanostructures that may be useful for novel nanoscale device applications. The other two studies examine possible ways in which ion irradiation may be used to modify a III-V substrate in order to improve the quality of a lattice mismatched thin films subsequently grown on it. Though the experimental methods and implications of each study are different, all four are connected by the common need to characterize the effect of ion irradiation on III-V semiconducting material. Because of that commonality, conducting each of these four studies required many of the same experimental techniques and types of analysis.

This dissertation has been organized in the following way: The remainder of this first chapter will provide a general overview of the III-V material set, broad beam ion implantation, focused ion beam instrumentation and techniques, and an overview of the experimental instruments and techniques common to each study. Chapters 2 and 3 cover the studies examining FIB nanostructure creation, and chapters 4 and 5 cover the studies that examine ion beam modification of substrates before film growth. Each individual chapter will cover the background and introductory materials specific to it. Chapter 6 summarizes results and offer conclusions regarding the implications of all four studies. A brief summary of each chapter follows:

Chapter 2: Describes research examining the phenomena of FIB induced metallic nanodot formation on several common III-V materials. While FIB metallic nanodot or droplet formation has previously been reported in the literature for multiple III-V materials, no previous published work has attempted to compare this phenomenon across materials or examine nanodot formation in light of the general materials properties and physical processes common to the compound semiconductors. Based on original experimental work this study includes description of a model for FIB nanodot formation and uses it to provide insight into the processes that control the phenomenon.

Chapter 3: Describes research examining the creation and properties of unique FIB created InAs nanowire-like spike structures, deemed “nanospikes.” The optimum FIB irradiation conditions for creating nanospikes and a novel method for templating nanospikes into arrays using heterostructure pre-patterning are demonstrated. Nanospikes were created using both homoepitaxial InAs films and InAs/InP film heterostructures, and the results from those two different cases are compared. The structures of the nanospikes were characterized, and individual nanospikes were electrically tested. The electrical testing of individual ion erosion created nanostructures as reported here is a first-of-its-kind study. The electrical testing results are analyzed relative to nanospike physical properties and compared to the electrical responses reported in the literature for more standardly grown nanowires.

Chapter 4: Describes research examining the use of FIB to pre-pattern III-V substrates for subsequent lattice mismatched film growth in the hopes of improving film quality. 3-D patterns were created by FIB on both InP and GaAs substrates and then InAs and InGaAs films respectively were grown on them. The patterned regions before and after film growth were characterized, and the effect of FIB-pre-patterning is reported. It was found that 3-D surface features can be used to alter film morphology. It was also found that substrate pre-patterning using FIB milling is detrimental to film quality, and the possible reasons for this are discussed.

Chapter 5: Describes research examining the use of broad beam pre-implantation of GaAs substrates for lattice mismatched film growth with the goal of improving film quality. This study is the first to examine substrate pre-implantation in the III-V system. GaAs substrates were blanket implanted with both In^+ and Ar^+ ions at varying energies, and then InGaAs films were grown on them. The effects of implantation on the GaAs substrate and InGaAs films were characterized. In^+ implantation was found to in no way improve film quality, and the possible reasons for this will be discussed. Ar^+ implantation was found to lower film roughness and increase relaxation, but to also increase the density of threading defects. Ar^+ pre-implantation was combined with growth of an InAlAs/InGaAs superlattice dislocation filtering structure in an attempt to create a high quality substrate for further active layer growth. The resulting heterostructures are characterized and discussed with respect to the goal of improving film quality.

Chapter 6: Summarizes the primary results and conclusions of each project and suggests future work.

1.2 Overview of the III-V Compound Semiconductors

From a technological standpoint semiconductors are an incredibly important class of materials. This is primarily because their electronic structure contains a band of forbidden electronic energy states between their electronic carrier containing valence band and normally empty or nearly empty conduction band. This bandgap structure makes many of our modern technologies possible, including solid-state transistors, light-emitting diodes (LEDs), solid-state lasers for communications, many types of light detectors, solar cells, and modern microelectronics in general. The most commonly used semiconductors materials are silicon and Si/Ge heterostructures. Silicon is widely used because it is cheap to produce, relatively easy to process and fabricate devices out of, and is a well-understood and technologically very mature material. However, Si and Ge are both group IV semiconductors and have indirect band gaps. The result of this indirect bandgap is that both Si and Ge are very poor light emitters and have low light absorption coefficients [18], making them unsuitable for many optoelectronic applications. Si also has a relatively low electron mobility [19], making it unsuitable for certain high-speed electronic applications.

The compound semiconductors offer many of the properties that the group IV semiconductors lack, and the III-V semiconductors in particular have historically been the most widely used compound semiconductors [18] and have seen the broadest use in optoelectronic and high mobility electronic applications. The III-V semiconductors are binary compounds of elements from periodic table group III (including Al, Ga, and In) and group V (including N, P, As, Sb, and Bi). Many of the III-V compounds and III-V alloys have direct bandgaps. Most of the III-V compounds in their equilibrium state and as they are technologically applied have a zinc blende crystal structure (space group $F\bar{4}3m$, number 216), with the exception of the N containing compounds, which form a wurtzite structure as commonly grown for device applications. This commonality of structure is one of the reasons that the III-V compounds have been so technologically valuable, as they may be grown as single crystalline films epitaxially upon one another and readily alloyed together. This opens up a wide range of electronic and device structures that may be achieved through heteroepitaxial growth and alloying. Alloying of the III-V compounds also allows their electronic bandgap to be continuously varied, and with it the optical and electronic properties of an alloy [18]. This dissertation contains experimental work only with the arsenic containing III-V compounds, their alloys, and InP. Figure 1.1 shows the wide range of bandgaps that may be achieved using those materials [20]. Figure 1.1 also shows how III-V lattice constant varies between compounds and with alloying over a wide range. This variation in lattice parameter is often what limits the types of III-V heterostructures that may be grown and thus limits the III-V combinations that may be used to create devices. Epitaxial growth of materials with dissimilar lattice parameters, or lattice-mismatched growth, produces strain in the system that can lead to the creation of structures and defects that are deleterious to electronic and optoelectronic device performance. Mismatch strain and the ways in which its affects may be mitigated are of concern to this work and will be more thoroughly discussed in the later chapters of this dissertation. Despite the fabrication challenges created by mismatch strain, the very wide range of bandgaps and corresponding optical properties accessible to the III-V materials has resulted in their widespread use in technology and in the large amount of previous and ongoing research into their use.

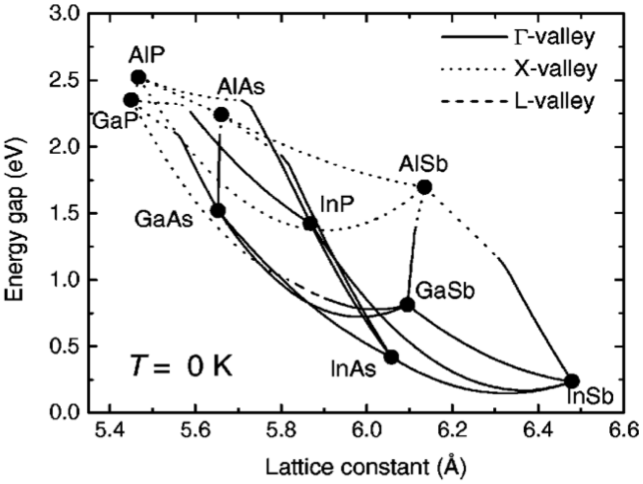

Figure 1.1 : Bandgap vs. lattice constant diagram for some III-V compounds, with direct bandgaps shown as solid lines. Taken from [20].

1.3 Introduction to Ion Implantation and Ion Damage

As mentioned at the start of this chapter, ion irradiation and implantation may be used to modify semiconductors in a number of useful and scientifically interesting ways. At their simplest, both ion implantation and ion irradiation refer to the process of accelerating charged ions of a single selected elemental species at a target material, which the ions then penetrate and are implanted into. As the ions are driven through the material they undergo a series of processes that cause them to lose energy until they eventually stop, and those processes give rise to the variety of effect that fall under the general category of ion damage. Within the context of this paper, the terms ion implantation and ion irradiation will be used interchangeable as both the effects of ion-sample interactions and the stopping location of those ions are of interest. There are a number of ways to direct ions at a target, but the two methods examined in this dissertation are focused ion beam (FIB) and broad beam ion implantation. As it is used here, the term broad beam ion implantation refers to the use of a broad beam of ions to evenly blanket irradiate a large sample area at once and at a continuous rate. This is in contrast to FIB irradiation, which uses a focused probe of ions that are rastered across the area to be exposed. FIB will be discussed more thoroughly in the next section. Broad beam implantation is the technique used widely within the semiconductor industry for tasks such as doping and other forms of electronic structure modification as referenced in the initial introduction of this chapter. Any basic implantation system will contain and an ion source, a potential difference across which the ions are accelerated to energies in the range of keV to MeV, additional components such as a mass selector or ion decelerators, and components to control the shape of the beam and direct it onto the target, such as ion optics and apertures. The exact arrangement and nature of these components varies from one implanter to another, so only a very general schematic of an ion accelerator/implanter is give in Figure 1.2. For more on the general make-up and operation of an implantation system, see reference [21].

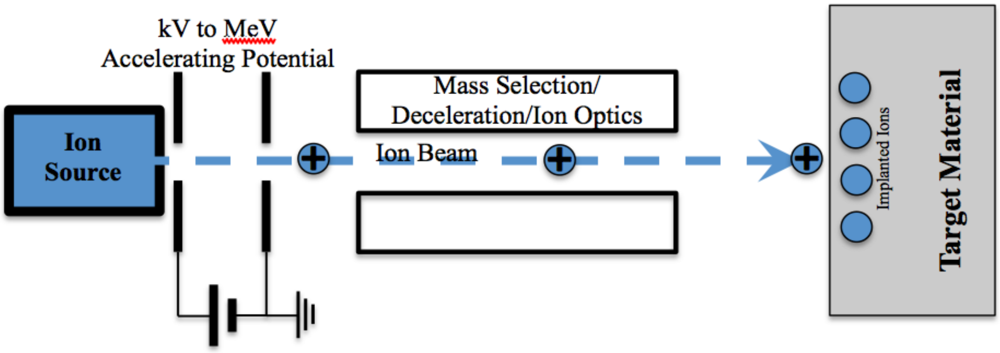

Figure 1.2: A general schematic showing the most basic components of an ion implantation system.

Regardless of how the ions are directed at the target surface, the types of interactions and damage they induce in the target are common to all implantation processes. As the ions penetrate into a target material they will interact with both the nuclei and electrons of that material and lose energy to a number of different processes as they are slowed. Ion-target interactions may include elastic scattering of the ion, local heating of the target material, generation of secondary electrons, direct displacement of target atoms from their original location, generation of material defects due to the displacement of target atoms, generation of defects due to insertion of the implanted species into the host lattice, ion-induced mixing in multicomponent materials due to target atom displacement, sputtering of the target material, and the generation of free neutral particles and secondary ions due to the action of sputtering. As the ions pass into the target material the damage they cause locally disorders it, and high ion doses may cause longer range effects such as amorphization or recrystallization. The type, number, and depth at which different ion-target interactions occur are strongly a function of ion species, ion energy, and target composition. Those same factors also determine the distribution of depths at which implanted ions come to rest in the target (also referred to as ion range). For more on the specifics of how implanted ions interact with a target material and the types of resulting ion damage, please see reference [21]. For more information specifically about ion implantation and damage in the III-V semiconductors, see references [2] and [1].

1.4 Introduction to Focused Ion Beam Techniques and Sputtering

Focused ion beam (FIB) technology has been under development since the 1970's and continues to be an active area in both instrument development and scientific study. Unlike the broad beam implantation techniques discussed in the previous section, the purpose of a FIB instrument is to direct a focused beam of ions with a small probe diameter onto a target. This small focused ion probe can then be rastered across the target to deliver a blanket ion dose to a chosen area or scanned in user specified patterns to locally expose those regions to the ion beam and resulting damage. The total area that may be easily irradiated using a FIB setup is much less than that of a broad beam implantation system, being on the order of nanometers to at most millimeters, but a FIB can be used to locally control ion dose on the nanometer scale and deliver a large controlled ion dose to a small area quickly. Correspondingly, FIB systems are used for different applications than broad beam implantation. In particular, FIB is often used specifically to sputter material from a target surface and thus provide a method for milling 3-D features on the nanometer scale. As a result FIB systems are operated at beam energies and currents designed to optimize the rate of sputtering from the target. Common FIB beam energies lie in the range of 1 to 10s of keV [22]. As a target is exposed to a FIB, it undergoes the same types of ion damage processes listed earlier for broad beam implantation, with the difference that sputtering of surface atoms is a dominant process. Sputtering of a surface atom occurs as an incoming ion knocks target atoms off of their sites with enough energy to allow them to knock additional atoms from their sites, starting a collision cascade. The movement of atoms within this cascade may then cause surface atoms to be ejected from the target. For a more in depth look at the theory of sputtering, see references [21] and [23]

A FIB column will consist of a few basic components: an ion source, electrodes for extracting and accelerating ions from the source, typically two electrostatic lenses to form and focus the ion beam, a set of apertures to define the beam shape and help determine probe current, a set of deflector plates to blank the ion beam, and additional plates or cylindrical octupole lens to deflect the ion beam, correct stigmation, and allow for further beam alignment [22]. A schematic showing the components of a FIB ion column like those used in this work is given in Figure 1.3. The most common type of ion source is a gallium liquid metal ion source (LMIS), which consists of Ga reservoir, a tungsten needle, and a heating coil. An LMIS is capable of creating a very small sized and high current density ion source. An LMIS is operated by heating the reservoir so that a small amount of metal flows over the tungsten needle. A strong electric field is then applied to the needle tip, which shapes the molten Ga into a sharp cone. Once the Ga metal cone is sufficiently sharp the high electric field concentration at the tip will pull Ga atoms from it and field ionize them. Ga LMIS sources are so commonly used because Ga has a low melting point (29.8 ˚C), flows evenly over a tungsten tip, will remain molten for long time periods at room temperature, has a low vapor pressure which promotes long source life, and the heavy Ga ions are useful for generating high sputtering rates [22]. Once extracted the Ga ions are accelerated to keV energies. All the FIB work reported in this study was carried out using a Ga^+ ions from an LMIS source and an accelerating voltage of 30 kV.

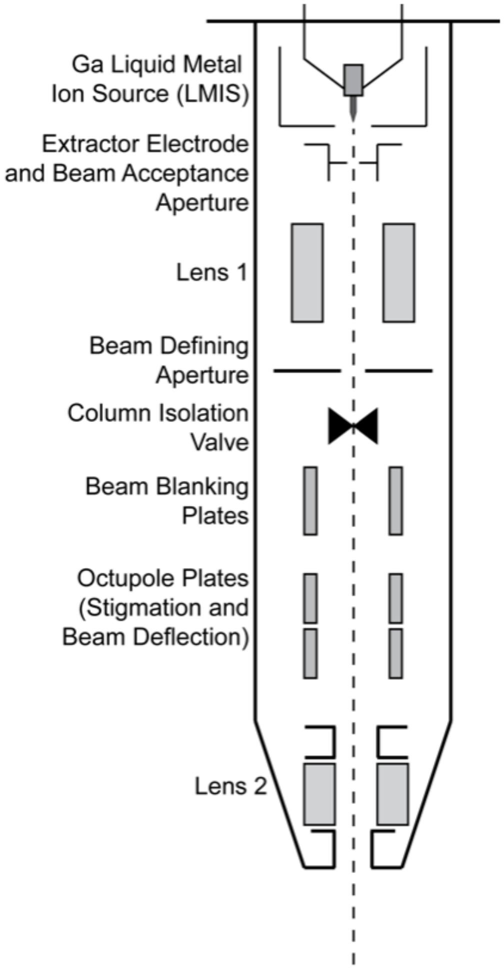

Figure 1.3: Schematic showing the primary components of a FIB column.

Many different applications have been developed which rely on FIB irradiation, only some of which will be mentioned here. By rastering the ion beam over an area and collecting the secondary electrons (SE) or secondary ions (SI) created at each point the FIB may be used to image in a manner analogous to how a scanning electron microscope (SEM) operates. By either increasing the number of times the ion beam is passed over an area or by increasing the time the beam dwells at each point, the target material may be locally milled to an arbitrary depth in a chosen pattern or blanket irradiated to a chosen ion dose. In general, imaging and milling resolution decrease and beam current and sputtering rate increase with increasing FIB probe size. FIB milling may be used for a number of tasks. Milling may be used to locally cross-section a sample for further imaging and analysis or used to thin a sample to electron transparency for transmission electron microscopy (TEM) analysis. Milling may be used to substractively fabricate microstructures or pattern a sample surface. With the inclusion of a gas injection system (GIS) into a FIB vacuum chamber, the FIB may be used to decompose a gas and deposit material to build structures additively. This approach is commonly used to inject a metal-organic gas for depositing a metal to build conductive structures or protect specific underlying features from additional ion damage. By combining its additive, substractive, and imaging capabilities a FIB may be used for complex tasks such as lithographic mask repair and microelectronic circuit edit and analysis. For a more complete overview of how a FIB may be used to alter material and specific applications of FIB, see reference [22]. In this work, FIB was used to blanket irradiate, create nanostructures, pattern surfaces, and aid in SEM and TEM sample preparation.

1.5 Overview of Experimental Methods

As each of the four different experimental studies that make up this dissertation all examine in some aspect the effects and uses of ion beam irradiation on the III-V semiconductors, it is unsurprising that many of the same experimental techniques and materials characterization methods were used to conduct each study. This section will provide brief overviews of those techniques most commonly used throughout this work, while more study specific experimental details will be given in the relevant succeeding chapters.

1.5.1 Molecular Beam Epitaxy (MBE)

The only technique used for epitaxial III-V semiconductor thin film growth in this work was Molecular Beam Epitaxy (MBE). At its simplest MBE might be viewed as an ultra-high vacuum (UHV) evaporation deposition method. In practice MBE is a complex process that requires precise instrumentation and provides significant advantages as a growth method. MBE growth can be used to reproducibly growth very pure and high quality compound semiconductor thin films, provide extremely precise control over thin film composition and doping, and produce very sharp hetero-interfaces. However, the trade-off for these benefits is that MBE is a relatively slow growth method and requires relatively complex instrumentation and precise control.

MBE is carried out in an ultra-high vacuum chamber using effusion cells that heat source material to generate a flux of evaporated atoms or molecules, which are directed towards a target substrate by the opening the cell. As such MBE is a line-of-sight growth process, with the constituents allowed to impinge on the substrate controlled by shutters that may be opened or closed to block a particle effusion cell. The type of compound grown at any one time may be precisely controlling by opening and closing the relevant shutters, allowing the creation of specific alloys or film heterostructures. Film growth is carried out epitaxially on whole or pieces of single crystalline wafers with specific crystallographic orientation. The wafers are mounted on a heated substrate manipulator. The kinetics of growth are controlled by the substrate temperature and the magnitude of the impinging source fluxes. Source fluxes are controlled by effusion cell temperature, which determines evaporation rate, or by a combination of cell temperature and a valve, which may be adjusted to allow more or less material through. For more information on the general details of MBE growth, see reference [24].

In this work all growth was carried out in an EPI 930 MBE system which contained Ga, In, Al, and Bi effusion cells, As and Sb valved-cracker cells, and Si and Be dopant effusion cells. Arsenic species is determined by cracker temperature, with the cracker kept at 600 ˚C to select a flux of primarily As_4. Film growth was carried out on pieces of singly crystalline wafer material attached by In bonding to a Mo sample puck. The In wets the back of the wafer and the Mo puck to hold the wafer in place. In this work growth was carried out on pieces of [001] oriented, front-side polished, epi-ready n+ doped GaAs, InAs, or InP wafers. Samples are initially loaded into an intro vacuum chamber where they are baked to ~150 ˚C to aid desorption of contaminants. From there they are transferred into a buffer chamber and then the growth vacuum chamber, where they are mounted on a rotating heated substrate manipulator. Before or after film growth samples could also be transferred while under vacuum to an attached FIB chamber, which contained a FEI UHV Magnum FIB column, or to an attached scanning tunneling microscope (STM) chamber, which was not used in the work reported here. Vacuum quality in the growth chamber was maintained by an ion pump, a helium cryopump maintained at 10 K, and a liquid nitrogen filled cryo-shroud. Sample temperature was monitored using an optical pyrometer pointed at the center of the sample area and calibrated relative to the III-V oxide desorption temperatures and GaAs β2(2x4) to c(4x4) surface reconstruction transition temperature. Film growth and surface condition were monitored during growth using a Staib reflection high-energy electron diffraction (RHEED) gun and phosphor view screen. Growth rates and fluxes were determined by taking RHEED intensity oscillations using sacrificial calibration samples and by using a beam-flux monitor (BFM) ion gauge that could lowered directly in front of the sample. The principles of RHEED operation and method for determining growth rate by RHEED oscillation will be discussed in the next section.

A general growth process starts with heating the sample on the substrate manipulator. During heating and growth the samples were kept under a continuous As_4 overpressure to prevent sample degradation. Sample wafers are heated to above their oxide desorption temperature to remove their protective oxide layer, and then cooled to the chosen growth temperature. The series of source material shutters necessary to grow the selected thin film type or film stack were then opened and subsequently closed once the required film thickness had been achieved. Following growth samples were either immediately quenched to below ~300 ˚C or briefly annealed and then quenched. All growth in this work was carried out using an excess group V overpressure, with group V to group III flux ratios in the range of 2 to 10. Thus film growth rates were always controlled by the group III flux. Specific growth parameters varied from experiment to experiment, and will be given at the relevant points later in this dissertation. The general growth procedure for each study was varied as little as possible to eliminate as many unknowns as possible.

1.5.2 Reflection High Energy Electron Diffraction (RHEED)

Reflection high-energy electron diffraction (RHEED) is a glancing angle electron diffraction technique that can be used to provide information about a semiconductor film surface during the process of MBE growth. RHEED can be used to determine data about atomic surface structure, film smoothness, growth mode, and growth rate during deposition. A high energy and collimated beam of electrons is directed towards the sample at a glancing angle in the range of <1-3˚. The electron beam interacts with the sample and a phosphorus screen collects the resulting diffracted and specular beams on the opposite side of the growth chamber and fluoresces in response to electrons striking it. In this work RHEED analysis was conducted using a Staib Instruments electron gun operated at a beam energy of 15 keV. The very small angle of electron beam incidence means that the probability of inelastic scatter is very high, such that only those electrons elastically scattered from the top few atomic layers of the sample surface are able to escape without being rescattered and losing energy [25]. This makes RHEED a surface sensitive technique, and the diffraction patterns that result from electron scatter are the product of the atomic structure of the sample surface. Because of this diffraction geometry, a RHEED diffraction pattern has extended lines or streaks instead of sharp diffraction spots. The pattern of streaks indicates both the periodicity of the sample surface and near-surface bulk in the in-plane direction normal to the direction of beam incidence. Thus by rotating the sample to different crystallographic directions the periodicity of the sample surface and the corresponding way in which the surface atoms have reconstructed can be probed. Figure 1.4 shows an example RHEED pattern displaying the x2 periodicity of the GaAs β2(2x4) surface reconstruction. Measurement of the intensity of features in RHEED patterns and changes in their periodicity and spacing with time may be used to accurately detect changes in surface structure and to quantitatively measure effects such as changes in the periodicity of atomic surface structures and relaxation during film growth.

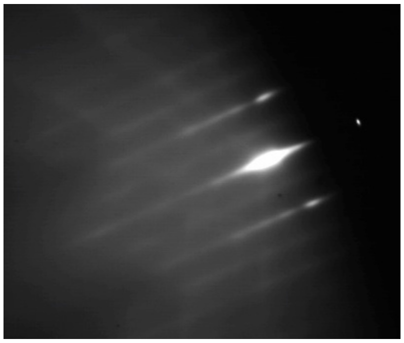

Figure 1.4: RHEED pattern of a GaAs buffer surface showing x2 periodicity.

The work reported in this dissertation did not use RHEED to determine surface structure, but rather to monitor the condition of film surfaces during and after growth and to determine growth rates. The intensity of a RHEED pattern is affected by surface roughness, with a bright pattern of streaks corresponding to a smooth surface and a dimming of the pattern corresponding to surface roughening. If a RHEED pattern transitions from streaks to spotty pattern, it indicates that the surface has become very rough and formed structures such as islands, mounds, or large quantum dots. For a layer-by-layer film growth mode, the brightening and dimming of the RHEED pattern with roughness can be used to determine growth in terms of the monolayers of material being incorporated into the film per second (ML/s). As each monolayer of material is deposited the roughness of the film oscillates as the incoming material flux starts to form a new layer, completes that layer and smooths, and then starts another layer. This roughness oscillation is matched by an oscillation in the intensity of the RHEED specular spot. Thus the time it takes for the RHEED intensity to go through one oscillation can be correlated to the time it takes for one monolayer of material to be incorporated. In this work the incorporation rates for Ga, In, Al, and As in ML/s were determined using RHEED oscillations.

1.5.3 Scanning Electron Microscopy (SEM)

Scanning electron microscopy (SEM, also refers to the instrument) as a technique employs a beam of electrons focused to sharp probe and scanned over a sample surface in a raster pattern to create an image. As the electron probe scans over each point in the area to be imaged, it interacts with the sample and causes the emission of either secondary electrons (SE) from the sample or backscattered electrons (BSE) from the beam. A detector collects these electrons, and the brightness of each pixel in the image corresponds to the number of electrons emitted at that point. Focusing the beam is accomplished with a series of electrostatic or magnetic lenses and the beam is shaped and deflected using scan coils or plates. Decreasing the area over which the beam is scanned increases magnification. SEM is employed as a surface imaging technique, however the information output from each scan point is actually the product of a finite volume of material reacting as the electon beam penetrates into and excites it. Decreasing the diameter of the electron probe and decreasing the electron beam energy can decrease the size of that interaction volume. The SEM instruments used in this study were capable of beam energies ranging from 2 to 30 kV, with 5 kV being used for all high-resolution imaging. For more on the principles of SEM operation and instrument construction see reference [26].

As the electron beam interacts with and energetically excites the sample it may also cause x-ray emission. Many of these x-rays will be characteristic of specific electron energy level transitions in the atoms that emitted them, and so may be used to identify the atomic species in the beam excitation volume. The process of doing so is called energy dispersive spectrometry (EDS), and by collecting EDS data from each point in a SEM scan area elemental maps may be created. EDS was used in this work both for semi-quantitative composition analysis and elemental mapping.

An SEM column may also be paired with a FIB column in the same vacuum chamber to create a dual-beam FIB/SEM instrument. This combination allows for simultaneous ion and electron imaging of a sample and a wide range of other characterization processes. As examples, the FIB may be used to locally cross-section a sample for immediate SEM analysis or the FIB may be used to blanket irradiate a region while the SEM is used to observe the result. When combined with a GIS system to allow for deposition of material with the ion or electron beam and a nanomanipulator, a dual-beam system may be used to cut, thin, and lift-out a chosen section of sample for TEM analysis. A schematic showing the layout of a dual-beam system resembling those used in this work is shown in Figure 1.5. All of the SEM analysis conducted in this work was carried out in dual-beam FIB system, as well as many of the FIB irradiation experiments detailed in the following chapters. An FEI Nova Nanolab 200 equipped with a field-emission SEM column, FEI Magnum ion column, EDS detector, and GIS for Pt metal deposition was used for high-resolution SEM imaging, FIB irradiation experiments, EDS analysis, and FIB cross-section preparation. An FEI Quanta 200 Workstation equipped with a tungsten filament SEM column, FEI Magnum ion column, GIS for Pt deposition, EDS detector, and a tungsten nanoprobe/manipulator was used for TEM sample preparation and lift-out and basic FIB patterning operations.

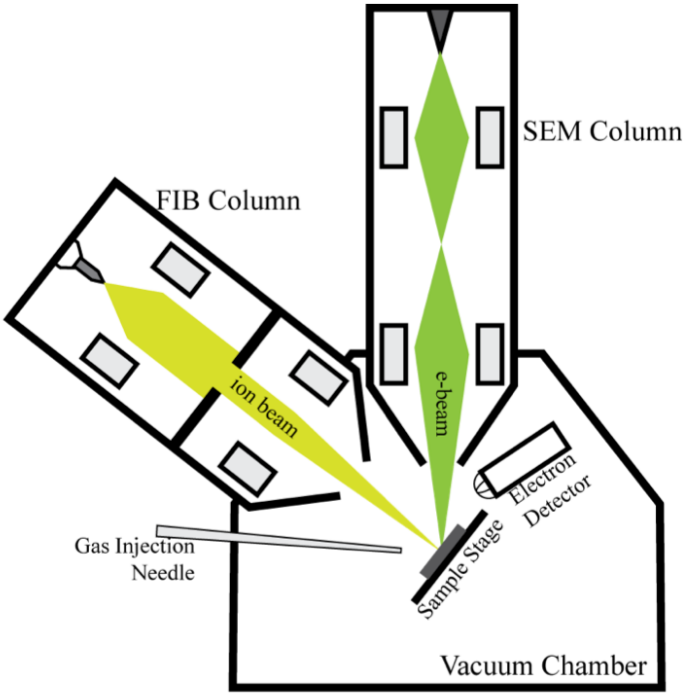

Figure 1.5: Schematic of a general dual-beam FIB/SEM instrument.

1.5.4 Transmission Electron Microscopy (TEM)

Transmission electron microscopy (TEM, also refers to the instrument) as a technique encompasses many different imaging and analysis methods and overall is a fairly complex characterization method. For this reason only the few techniques used in this work will be discussed here. In general the TEM instrument directs a beam of high-energy electrons in the range of 80-300 keV at a sample thin enough that most of the electons can pass through it. Some of the electrons interact with the sample as they pass through, and the transmitted and scattered electrons are collected to form an image or for analysis. For more on the set-up of a TEM and the specifics of many different TEM techniques, please see reference [27].

Five basic TEM techniques were employed in this study: bright-field (BF) imaging, dark-field (BF) imaging, phase-contrast high resolution TEM (HRTEM) imaging, selected area electron diffraction (SAD), and scanning transmission electron microscopy (STEM) high-angle annular dark-field (HAADF) imaging. BF and DF imaging both use plane-parallel coherent illumination of the sample and rely on diffraction contrast from the sample in order to produce an image. As the electron beam passes through a crystalline sample it elastically scatters of off the atoms in its structure.

When the sample is oriented so that a crystalline plane or zone axis of planes is aligned to the electron beam such that the Laue condition is satisfied and the structure factor is non-zero the scattered electrons will interfere constructively to form diffracted beams in addition to the beam of electrons transmitted directly through the sample [27]. BF imaging uses an aperture to select only the central transmitted beam to form an image, while DF imaging uses that same aperture to select one or more diffracted beam and excludes the transmitted beam to form an image. Thus contrast in BF and DF images comes areas that did or did not strongly diffract the electron beam. These imaging modes can be used to directly image strain and extended crystalline defects such as twin boundaries, stacking faults, and dislocations. By focusing the back focal plane of the TEM objective lens onto the imaging screen, the diffracted beams can also be used to create an electron diffraction pattern. SAD involves the use of an aperture to select a smaller area of the illuminated sample region to collect diffraction data from. Electron diffraction was used in this study to both determine the crystalline orientation of a sample and to allow the sample to be accurately tilted to a zone axis or specific diffraction condition for BF, DF, and HRTEM imaging. HRTEM imaging was generally carried out while tilted to a zone axis, and HRTEM contrast is the result of shifts in electron phase as they pass through the sample and are elastically scattered coherently to small angles. At very high magnification this phase contrast is manifested as a series of periodic light and dark fringes that directly correlate to the crystalline atomic plane spacings of the sample. Thus these lattice fringes can be used to directly image the periodicity and crystalline structure of the sample. HRTEM imaging was used in this study to examine defect structures, heterointerfaces, and sample structure at the atomic scale. STEM makes use of a converged electron probe focused on the sample rather than a diverged parallel beam. This beam is then scanned over the area of the sample to be imaged in a manner analogous to the operation of a SEM, and the electons scattered at each point are collected to form an image. Also similar to the SEM, STEM can be combined with EDS collection at each point to assemble elemental maps of the area scanned by the electron beam. The STEM method used in this work, HAADF imaging, uses an annular detector that allows electrons transmitted and elastically scattered to low angles to pass through it while collecting those that are incoherently scattered to higher angles. This scattering is much more sensitive to atomic weight than BF and DF imaging, and so HAADF images provides excellent z-contrast, with brighter areas in the image corresponding to areas with higher weight atoms or a higher density. HAADF STEM imaging was used in this work to allow clear imaging of heterostructure interfaces and compositional inhomogeneity in nanostructures.

Two TEM instruments were used in this work. A JEOL 3011 High Resolution Electron Microscope operated at a beam energy of 300 keV was used for complimentary BF and DF imaging, SAD, and was the primary instrument used for HRTEM. A JEOL 2010F Analytical Electron Microscope was used for BF imaging, SAD, secondarily for HRTEM, STEM HAADF imaging, and STEM/EDS elemental mapping.

1.5.5 Atomic Force Microscopy (AFM)

Atomic force microscopy (AFM, also refers to the instrument) is a surface characterization tool that allows surfacing mapping of small sample areas. Generally, AFM is carried out by rastering a sharp tip at the end of a cantilever back and forth over the sample surface and monitoring the response of that tip to the surface at each point. There are many different imaging modes and types of property information that can be extracted by using the AFM in different ways and with different tips and attachments. However, in this study AFM was only used to record topographic maps of sample surfaces. Topographic maps could be taken over areas ranging from >100nm to ~50 µm on a side. Maps of sample height were recorded using tapping mode AFM. This involves oscillating a sharp Si probe on the end of a stiff Si cantilever at one of its resonance frequencies, and then scanning the oscillating tip across the sample surface. The movement of the tip and cantilever are monitored by a laser reflected off of the top of the cantilever and onto a four-quadrant photodiode. As the tip is scanned it “taps” the surface as it oscillates. The tip is scanned in the x and y directions using piezoelectric actuators, and its height in the z-direction is adjusted by another piezoelectric element. As the oscillating tip encounters changes in the sample height its oscillation frequency and amplitude are altered. The z-height of the cantilever is then adjusted to re-achieve the original level of oscillation, and this height adjustment is used to map sample height as a function of tip position. Change in tip oscillation frequency can be mapped to create a “phase” image. Using tapping mode AFM, changes in sample height as small as one single atomic step edge could be detected. Tapping mode AFM height maps were used in this study to examine the roughness of III-V surfaces, to examine the height of FIB created features, and to determine the size and shape of FIB-created nanostructures. The two instruments used in this work were a Digital Instruments (Veeco) Nanoscope IIIa AFM and a Veeco Dimension Icon AFM.

1.5.6 High Resolution X-ray Diffraction (HRXRD)

At its most basic x-ray diffraction (XRD) as a technique involves the illumination of a crystalline sample with a beam of x-rays and then the detection of x-rays that were elastically scattered by the sample. When the x-ray beam and detector are aligned at specific angles relative to the sample the x-rays scattering off of correctly aligned crystalline planes in the sample will interfere constructively and cause a spike in signal at the detector. The angular location of these diffraction peaks can be used to determine information about the atomic periodicity and orientation of the sample, and in many cases other additional information such as crystallite size, dislocation density, and sample texturing can be determined from relative peak heights and widths.

The specific XRD technique employed in this work was the recording of high-resolution XRD (HRXRD) spectra from single crystalline thin film specimens. These were recorded using a Bede D1 triple-axis diffractometer and copper $K\alpha_1$ radiation. The angular and chromatic spread of the beam were reduced using two Si channel-cut crystals at the x-ray source before the sample and a series of slits in the beam path both before and after sample, giving the instrument an angular resolution on the order of a one to a few arcseconds (arcsec, 1 arcsec=1/3600 degree). The x-ray beam was first aligned to the sample and detector at a specific sample substrate peak, and spectra were then collected either by rocking the sample relative to the source and detector (Ω-axis rocking curve) or by locking the angle between the detector and sample and then tilting the detector (2θ axis) and sample (Ω-axis) together to generate an Ω-2θ curve. Ω-2θ curves were taken about the substrate 004 and 224 diffraction peaks, and when the instrument was properly aligned the GaAs 004 substrate peak regularly had a full-width at half-maximum (FWHM) of approximately 30 arcsec. Examining the area near the substrate peak could reveal the presence of amorphous material in the sample, which manifested as a low, broad peak or hump near the substrate peak. When a thin film structure was examined, spectra containing both diffraction peaks corresponding to the substrate and film(s) were recorded. The angular separation of the film peaks relative to the substrate could then be used to determine the difference in the lattice plane-spacing of the film relative to the known substrate. By taking both the 004 and 224 glancing exit (GE) geometry Ω-2θ curves, both the in-plane and out-of-plane lattice parameters of the film could be measured. Using these values, assuming Vegard's law (simple rule of mixing) is valid for calculating film composition, and with known elastic constants and their variation with composition for the alloy system, the composition of an alloy film and the degree to which it is strained in plane to match the substrate (or oppositely the amount it has relaxed back towards its equilibrium lattice parameter) can be quantitatively determined. These calculations fail to produce correct results when variations in lattice parameter or the elastic properties of the alloy system as a function of composition are incorrectly modeled. Calculations to find film composition and relaxation were carried out using a library of material properties and semi-automated routine in the XRD instrument's software. The number of counts in the 224 GE peaks of thin films was often very low, introducing some error into calculations using them. HRXRD was used in this manner to determine the composition and strain/relaxation state of epitaxially grown III-V alloy films. For more information on HRXRD instrumentation and thin-film analysis, please see reference [28].

1.6 References

[1] Williams, J. S. *Materials Science and Engineering A* **253**, 8-15 (1998).

[2] Wesch, W. *Nuclear Instruments and Methods in Physics Research Section B: Beam Interactions with Materials and Atoms* **68**, 342-354 (1992).

[3] Bryant, F. J. & Cox, A. F. J. *Journal of Physics C: Solid State Physics* **1**, 1734 (1968).

[4] Narayan, J. & Holland, O. W. *Journal of the Electrochemical Society* **131**, 2651 (1984).

[5] Pearton, S. J. et al. *Nuclear Instruments and Methods in Physics Research Section B: Beam Interactions with Materials and Atoms* **19**, 369-380 (1987).

[6] Pearton, S. J. et al. *Journal of Applied Physics* **64**, 629-636 (1988).

[7] Wesch, W., Wendler, E., Götz, G. & Kekelidse, N. P. *Journal of Applied Physics* **65**, 519 (1989).

[8] Bench, M. W., ROBERTSON, I. M. & Kirk, M. A. *Nuclear Instruments and Methods in Physics Research Section B: Beam Interactions with Materials and Atoms* **59**, 372-376 (1991).

[9] Jones, K. S. & Santana, C. J. *J. Mater. Res* **6**, (1991).

[10] Chini, T., Kato, J. & Tanemura, M. *Nuclear Instruments and ...* (1995).

[11] Frost, F., Schindler, A. & Bigl, F. *Physical Review Letters* **85**, 4116-4119 (2000).

[12] Myers, D. R. et al. *Superlattices and Microstructures* **4**, 585-589 (1988).

[13] Pathak, A. P., Dhamodaran, S., Sathish, N. & Rao, N. S. *Radiation Effects and Defects in Solids* **162**, 131-150 (2007).

[14] Lugstein, A., Basnar, B. & Bertagnolli, E. *Journal of Vacuum Science & Technology B: Microelectronics and Nanometer Structures* **20**, 2238 (2002).

[15] Lugstein, A., Basnar, B., Smoliner, J., Bertagnolli, E. & Weil, M. *Journal of Vacuum Science & Technology B: Microelectronics and Nanometer Structures* **22**, 2995 (2004).

[16] Callegari, V. & Nellen, P. M. *physica status solidi (a)* **204**, 1665-1671 (2007).

[17] Lugstein, A., Bernardi, J., Tomastik, C. & Bertagnolli, E. *Applied Physics Letters* **88**, 163114 (2006).

[18] Bhattacharya, P. *Semiconductor optoelectronic devices, 2nd Edition* (Prentice Hall, Upper Saddle River, NJ, 1997).

[19] Sze, S. M. & Ng, K. K. *Physics of Semiconductor Devices, 3rd Edition* (John Wiley & Sons, Inc., Hoboken, NJ, 2007).

[20] Vurgaftman, I., Meyer, J. R. & Ram-Mohan, L. R. *Journal of Applied Physics* **89**, 5815 (2001).

[21] Nastasi, M., Mayer, J. W. & Hirvonen, J. K. *Ion-Solid Interactions: Fundamentals and applications,* (Cambridge University Press, Cambridge, Great Britain, 1996).

[22] Giannuzzi, L. A. & Stevie, F. A. (eds) *Introduction to Focused Ion Beams: Instrumentation, Theory, Techniques and Practice,* (Springer Science+Business Media, Inc., Boston, MA, 2005).

[23] Sigmund, P. in *Sputtering by Particle Bombardment I: Physical Sputtering of Single-Element Solids,* (ed Behrisch, R.) 9-67 (Springer-Verlag, Berlin Heidelberg, Germany, 1981).

[24] Farrow, R. F. C. (ed) *Molecular Beam Epitaxy: Applications to Key Materials,* (Noyes Publications, Park Ridge, NJ, 1995).

[25] Holloway, P. H. & McGuire, G. E. (eds) *Handbook of Compound Semiconductors: Growth, Processing, Characterization, and Devices,* (Noyes Publications, Park Ridge, NJ,

[26] Goodhew, P. J., Humphreys, J. & Beanland, R. *Electron microscopy and analysis, 3rd Edition* (Taylor &Francis, London, UK, 2001).

[27] Fultz, B. & Howe, J. M. *Transmission Electron Microscopy and Diffractometry of Materials, 3rd Edition* (Springer-Verlag, Berlin Heidelberg, Germany, 2008).

[28] Bowen, D. K. & Tanner, B. K. *High Resolution X-Ray Diffractometry and Topography,* (Taylor & Francis, London, UK, 1998).

Chapter 2

The Mechanisms of Nanodot Formation on III-V Semiconductors Under Focused Ion Beam Irradiation

2.1 Introduction and Background

The self-assembly of nanoscale group III metallic nanodots and other nanostructures on III-V semiconductor surfaces has in the recent past become an area of much interest, both from a scientific standpoint and for the proposed device applications for those structures. For instance, group III metallic nanodots and clusters show interesting optical qualities [1,2] that make them promising for use in negative index of refraction materials. They may also be used in the creation of quantum dots by a droplet epitaxy process [3-5] and in the growth of nanowires [6], where they could serve as a catalyst particle for vapor-liquid-solid (VLS) type growth. While it is possible to create group III dots by direct deposition of metal atoms on a surface [3-5], it is also possible to induce their formation in compound semiconductors using both broad area ion irradiation [7-9] and FIB irradiation [10-13]. Both direct metal deposition and broad area ion irradiation provide a simple synthesis route for the creation of nanostructures over large areas, but a drawback is that those nanostructures may be at random locations and in a distribution of sizes. Focused ion beam (FIB) irradiation of III-V compound semiconductors has shown promise as a viable approach for producing nanoscale group III metallic nanodots at random locations [10-13], in self assembled arrays [14], and at selected locations via patterning [14-16]. As such, FIB irradiation serves as both a bottom-up and top-down method for the creation of nanostructures on semiconductor surfaces. However, if FIB created metallic nanostructures are to be used reliably in device applications, the physical mechanisms and processing parameters that govern their creation need to be understood and the response of the III-V compounds to FIB irradiaton needs to be thoroughly characterized.

The metallic nanostructures that develop on a semiconductor surface depend strongly on the material being irradiated, and a series of previous studies have individually shown that each III-V compound responds differently to FIB irradiation. The Ga+ FIB responses of GaAs [10,13,14,17,18], InP [16], InAs [11], and GaSb [19,20] substrates have all been examined. FIB irradiation of InP, GaAs, and InAs in those studies has been shown to produce group III nanodots of varying sizes and morphologies, a phenomenon which has been attributed to preferential sputtering of the group V element followed by assembly of the excess group III atoms [10-12,14,15]. Preferential sputtering occurs in compound materials when the sputtering yields (atoms sputtered per ion) are uneven for the different atomic species in the target. This unevenness in the sputtering yield causes the ion-effected area to become enriched with the more slowly removed atomic species. Preferential sputtering of the III-V materials by broad beam irradiation has been thoroughly studied and reviewed previously [21,22]. FIB-created metallic nanodots on GaAs and InAs have been identified as nearly pure Ga [14,17,18] and In [11] respectively. Previous FIB studies of InP do not identify the composition of the nanodots in that system [16], however other studies examining low energy inert gas ion irradiation of InP have identified the nanodots as In-enriched [23-25]. Nanostructure creation on irradiated GaSb has been shown to produce cellular voids, a network of stoichiometric nanoscale GaSb wires, and Ga precipitates on those wires depending on ion dose [19,20], all of which are presumed to form due to the movement and coalescence of ion-damage created point-defects [26,27].

Regardless of intended application and nanostructure placement requirements, if a FIB method is to be used to create reproducible and useful nanostructures, the FIB responses of the III-V semiconductors as a material system need to be carefully measured and theoretically understood. Previous studies of the FIB response of III-V binary compounds have focused on the response of each III-V compound individually and except for the case of GaAs [14,17], have not carefully tracked the development of nanostructure sizes on each compound as a function of increasing ion dose. A coherent physical picture of how ion induced nanodot formation proceeds that spans material systems is still lacking. If strategies for FIB induced creation of nanostructures for a variety of applications are to be developed, then a comparison of FIB response across multiple materials is needed that relates their response to fundamental mechanisms driving nanostructure creation.

This study examines the 30 keV Ga^+ FIB response of GaAs, InAs, InP, and AlAs and the distribution of metallic nanodots formed on each material as a function of increasing 30 keV Ga^+ FIB dose in order to compare the different responses of those materials based on a few basic physical properties. Careful tracking of nanodot development as a function of ion dose has not been reported for InAs, InP, or AlAs, and a comparison across this set of materials has not been previously conducted. The FIB response of each material is characterized by ion-induced secondary electron (ISE) microscopy or by SEM, EDS, and AFM. Based on these experimental observations, a simple model that incorporates basic physical drivers for nanodot creation is employed in order to provide a description of how they affect the FIB response of each compound semiconductor. No similar study comparing and attempting to explain the different nanodot forming behaviors of multiple III-V materials in terms of the material properties and physical processes common to all has previously been reported the literature. The nanoscale wire forming FIB response of GaSb, while remarkable, does not lend itself to direct comparison with the metallic nanodot forming response of the other materials as it is driven by a fundamentally different mechanism. Thus the theory developed in this work does not attempt to incorporate the response of GaSb. The results of this work were used to inform experimental design of the FIB-induced nanostructure formation and FIB III-V substrate modification studies reported in chapters 3 and 4 respectively.

2.2 Experimental Methods

The FIB responses of GaAs, InP, and InAs (001) substrates were determined by irradiating each with a Ga^+ focused ion beam and characterizing the results. GaSb (001) substrate material was irradiated and then imaged, but no attempt at further analysis was made. All wafers used in this study were commercially obtained epi-ready substrates intended for use in epitaxial film growth. Analysis of the response of GaAs, InP, and InAs to ion irradiation was conducted using the FEI Nova Nanolab dual-beam FIB system equipped with a field-emission SEM and a FEI Magnum FIB column capable of producing a 5-30 keV Ga^+ beam (see section 1.5.3). An ion beam energy of 30 keV was used for all experiments, while beam current and applied dose were varied.

The FIB response of AlAs films grown on GaAs (001) wafers was also examined. In order to avoid oxidation of the AlAs between the time of growth and FIB exposure, a FEI UHV Magnum FIB column connected *in vacuo* to an MBE growth system was used for these studies (see section 1.5.1 for information on that MBE system). Approximately 50 nm thick AlAs films were grown on GaAs buffer layers at a temperature of 620 ˚C and at an AlAs growth rate of approximately 0.5 ML/s in the MBE system and then transferred in vacuum to the vacuum chamber containing the ion column. As in the case of the other materials examined, the energy of the ion beam used to examine the AlAs films was maintained at 30 keV while beam current and dose were varied. Thicker AlAs films were not examined due to difficulty in growing smooth AlAs films and then preventing their degradation. All thicker AlAs films that were grown were too rough to be useful for quantitative FIB response characterization or degraded too quickly after removal from vacuum for further analysis.

In order to examine the FIB response of GaAs, InP, InAs, and AlAs, square regions ranging in size from 1 to 100 μm^2 were irradiated. The ion beam was repeatedly scanned in a serpentine pattern over each sample area in order to achieve the desired ion dose. A beam spot overlap of 50% and a dwell time of 1 μs at each spot were used in all cases. Beam dwell time was maintained at 1 μs, as changing dwell time was observed to have an effect on the final distribution of nanodots in some cases. During all irradiation experiments, the ion beam was kept at normal incidence to the substrate. FIB irradiation was carried out using beam currents ranging from 5 to 290 pA and ion doses ranging from 10^{15} to 10^{18} ions/cm^2. By irradiating different areas with varying doses it was possible to examine the tendency of each material to form metallic nanodots, determine the ion dose at which nanodots first appear, examine the development and size distribution of those structures with increasing ion dose, and establish the FIB milling rate of each material. Figure 2.1 shows an example series of 2x2 μm square regions milled into GaAs using different ion doses and an approximately 5.5 pA ion beam. Figure 2.1(a) shows a SEM image of the milled areas which was used to examine the ion dose range over which nanodots on GaAs first appear, and Figure 2.1(b) shows an AFM scan of that same area that was used to measure milling depth as a function of ion dose.

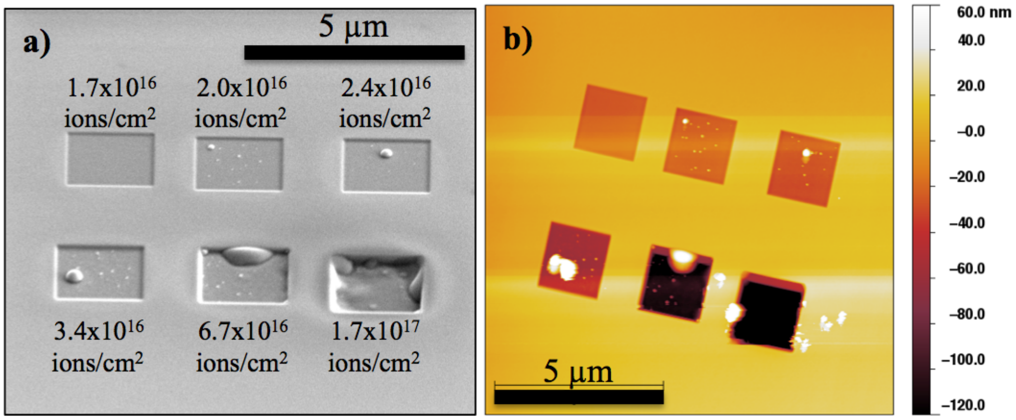

Figure 2.1: (a) shows a SEM image of a series of 2x2 µm squares milled into GaAs, with the dose used to mill each area listed by it. (b) shows an AFM scan of that same area used to determine milling depth as a function of ion dose. Scan and tip artifacts are visible in (b).

Following irradiation, characterization of each material was carried out using several techniques. GaAs, InP, and InAs samples were examined *in-situ* in the Nova dual-beam FIB/SEM system by SEM immediately before and following ion irradiation without removal from vacuum. In the cases where nanodots formed their size and distribution were characterized immediately following formation by SEM and their composition was probed using an attached the EDS system. EDS was used to qualitatively verify that the primary constituent of the nanodots was the group III element corresponding to the III-V compound they were produced on. SEM examination of areas irradiated with different ion doses was also used identify the threshold dose for group III nanodot formation. Average nanodot sizes and distributions at each dose were found through image analysis of SEM micrographs using a threshold method and then plotted to allow examination of trends in nanodot size as a function of ion dose. For consistency's sake and to allow examination of metallic nanodots away from any effect of the pattern edge, images for nanodot size analysis were taken only from large 10x10 µm square regions irradiated using a 0.3 nA FIB aperture, with actual measured beam currents ranging from 0.28 to 0.29 nA. Immediately following removal from the dual-beam FIB system, samples were examined using the Nanoscope IIIa AFM to corroborate nanodot sizes, measure ion milling depths in the irradiated regions of GaAs, InP, and InAs samples, and verify the threshold dose for nanodot formation determined by SEM. Milling depth measurements did not take into account the effect of ion-induced swelling in the irradiated region. The AlAs films grown on GaAs were examined *in-situ* by ISE, with a resolution limit of approximately 20 nm due to vibration of the vacuum system. Beyond limited ISE imaging it was not possible to characterize the AlAs films without first removing those films from vacuum. Upon removal from vacuum they were taken and characterized as quickly as possible by AFM in a manner similar to the other III-V materials. However, upon exposure to atmosphere the AlAs films began to visibly oxidize within a few minutes. Following AFM evaluation AlAs films were also placed into the dual-beam FIB system and characterized by SEM and EDS.

2.3 FIB Response and Nanodot Formation Results

In agreement with work of previous authors [10,11,13,14,16-18], metallic nanodots were observed to form on GaAs, InP, and InAs wafer substrates following 30 keV Ga^+ FIB irradiation. No resolvable nanodots were observed by ISE examination *in vacuo* or by later *ex situ* AFM examination of the AlAs films following irradiation, even up to the maximum applied dose of > 6.24×10^{16} ions/cm^2, past which the AlAs ~50 nm films were completely milled through. The different responses of GaAs, InP, InAs, and AlAs are demonstrated in Figure 2.2, which shows an area of each material following exposure to similar ion doses of approximately 4×10^{16} to 5×10^{16} ions/cm^2. Figure 2.3 shows an image of GaSb following a dose of ~2.7×10^{16} ions/cm^2 in which can be seen that material's unusual nanostructure forming response to FIB irradiation. As visible in the Figure 2.2 SEM images, GaAs, InP, and InAs form nanodots with different average sizes and size distributions at comparable ion dose. Table 2.1 reports several quantities for each material that characterize their response to FIB irradiation: r, the experimentally determined milling rate, $D_{\max}$, the maximum dose before the initial appearance of nanodots, and $h_{\max}$, the maximum depth that can be milled to before the appearance of nanodots, calculated using the values of r and $D_{\max}$. Milling rates were determined by using AFM to measure the depths relative to the undisturbed wafer surface milled to by different ion doses. The maximum dose before initial nanodot formation was determined by milling 5x5 and 2x2 μm squares at increasing doses and noting the point at which nanodots were first observed by SEM and AFM. This approach is then inherently limited by the minimum nanodot size capable of being resolved by the SEM and AFM instruments used, and it is possible that metallic nanodots smaller than the clearly resolvable size formed at lower doses. The resolutions of the SEM and AFM systems used to image all four materials were limited to ~5 nm, while the ISE imaging system used to initially examine the AlAs films *in vacuo* was limited to ~20 nm. Comparing the r and $D_{\max}$ values given in Table 2.1, it can be seen that InP and InAs both mill quickly and produce droplets at relatively low doses. AlAs has a significantly lower FIB milling rate than any of the other three materials studied and does not produce droplets. The lower milling rate of AlAs is not unexpected, as AlAs has been previously shown to be more resistant to ion damage than the other III-V compounds [28,29]. The size distribution of nanodots created on GaAs, InP, and InAs was found to depend on the dose, beam current, and size of the irradiated area. Figure 2.4(a) shows a series of areas FIB milled areas in GaAs used to examine the effects on nanodot size of changing dose, irradiated area size, and beam current. Figure 2.4(b) shows a 10x10 μm areas milled with a 0.28 nA beam and ion dose of 9.6×10^{16} ions/cm^2. Figure 2.4(c) shows a 2x2 μm area milled using the same beam current and ion dose as (b). Figure 2.4(d) shows a 2x2 μm area milled using a 5.2 pA beam and ion dose of 5.3×10^{16} ions/cm^2. By comparing the droplet size distribution in (b), (c), and (d) it can be seen that changing both irradiation area and beam current changed the distribution of nanodot sizes. This is why the experiments reported below tracking nanodot size as a function of ion dose for each material were all conducted using the same beam current (0.28 nA), the same spot dwell time (1 μs), and the same irradiation area (10x10 μm).

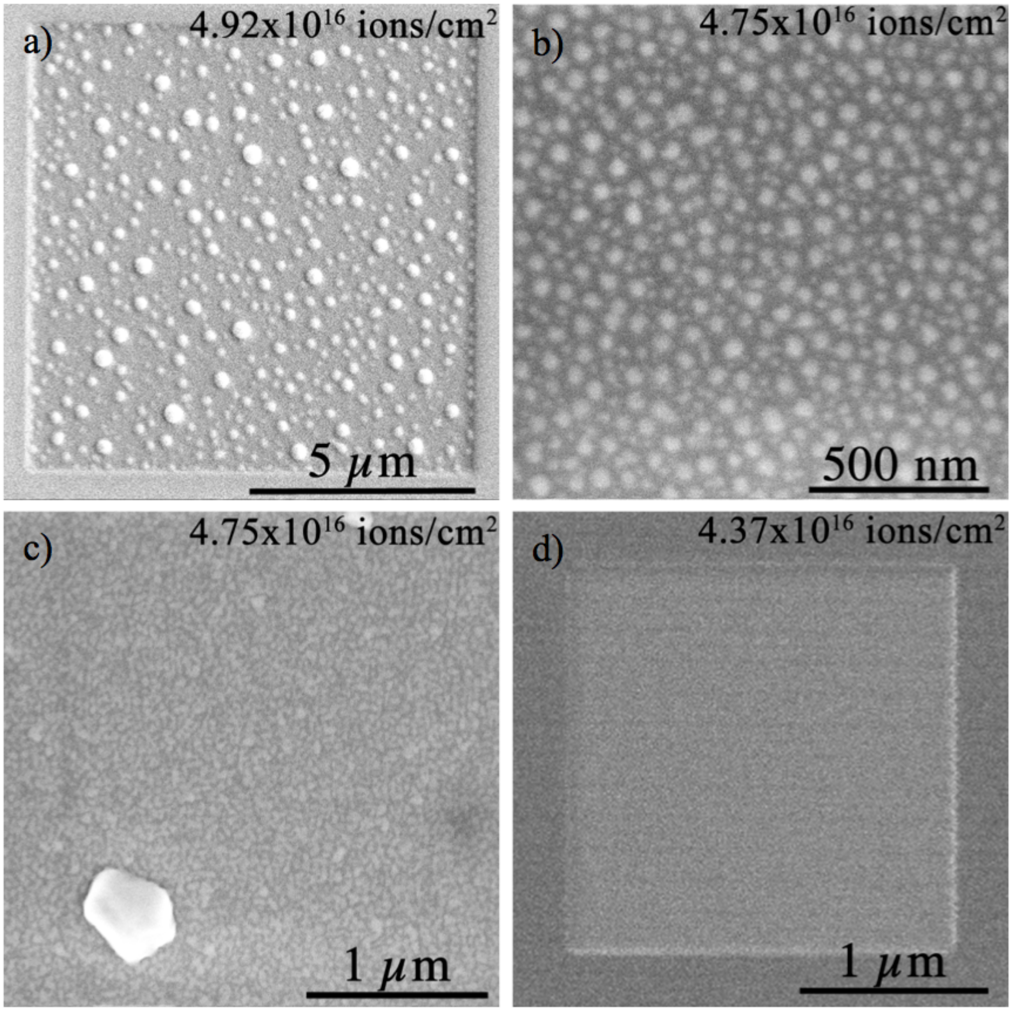

Figure 2.2: Three SEM micrographs comparing areas of a) GaAs, b) InP, and c) InAs following FIB irradiation with similar ion doses, as indicated in the upper right hand corner of each image. d) shows an ISE micrograph of an area of FIB irradiated AlAs.

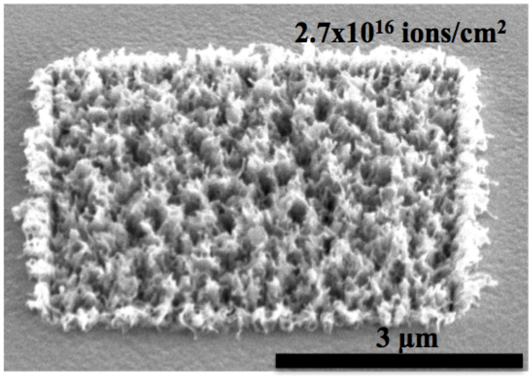

Figure 2.3: SEM micrograph showing nanostrucure formation in a FIB irradiated region of GaSb. Ion dose is given in the upper right hand corner.

Table 2.1: Comparison of the experimentally found milling rate, r, the maximum FIB dose before nanodot appearance, D_{max}, and the maximum depth that can be milled to before the appearance of nanodots, h_{max}, for each of the III-V materials studied. ± values represents 1 standard deviation from the mean plus AFM measurement error.

	r (μm³/nC)	**D_{max} (ions/cm²)**	**h_{max} (nm)**
GaAs	0.77 ±0.12	1.7×10^{16}	21
InP	1.07 ±0.11	1.7×10^{15}	3
InAs	1.25 ±0.15	6.4×10^{15}	13
AlAs	0.36 ±0.06	N/A	N/A

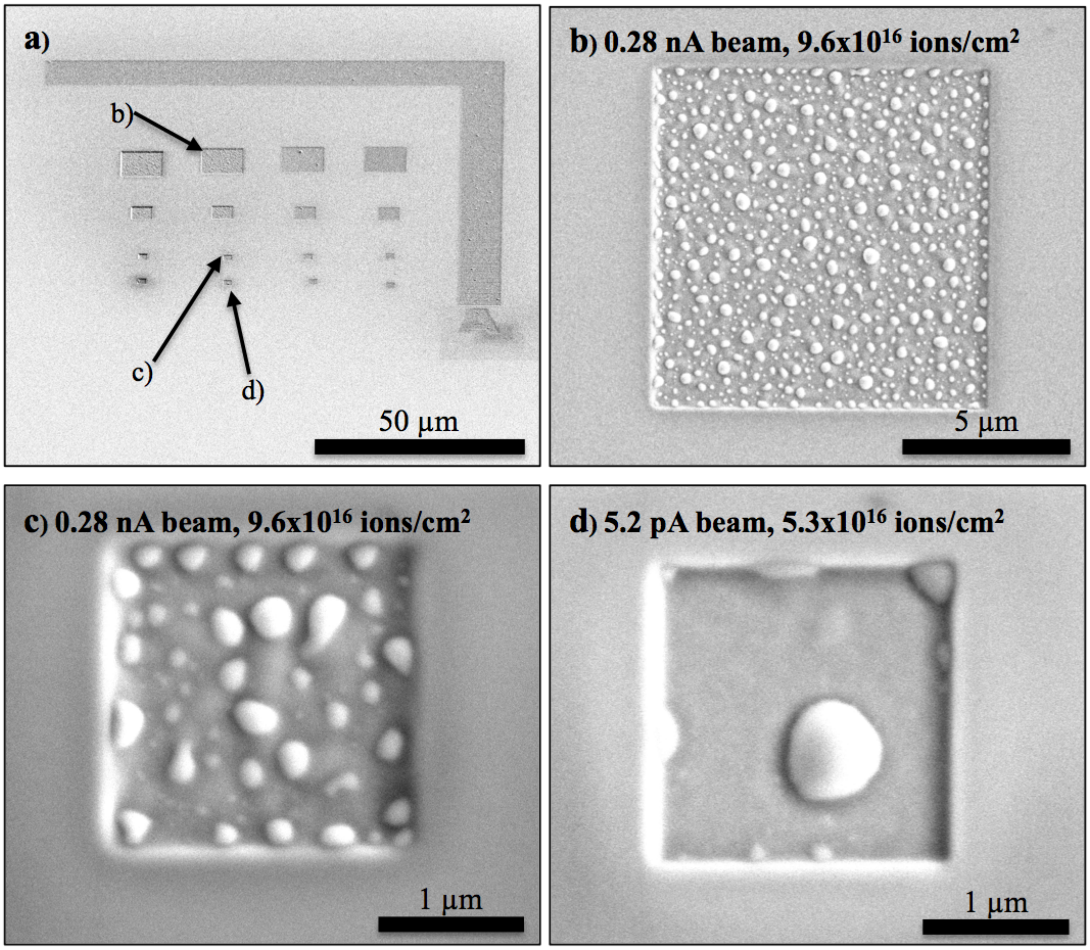

Figure 2.4: (a) shows a SEM image of a series of square areas milled into GaAs to examine the effects of changing ion dose, FIB current, and irradiated area on nanodot size. (b) shows a 10x10 μm area from that series milled with a 0.28 nA beam, (c) shows a 2x2 μm area milled with a 0.28 nA beam, and (d) shows a 2x2 μm area milled with a 5.2 pA beam.

In addition to the milling rate and dose at which group III metallic nanodots first appear, the manner with which the distributions of nanodots in the FIB irradiated regions develop also differs for GaAs, InP, and InAs. Following their initial appearance, Ga nanodots on GaAs grow to a stable average size over a dose range of $1\text{x}10^{16}$ to $1\text{x}10^{17}$ ions/cm^2. Figure 2.5(a) shows the evolution of nanodot size as a function of ion dose, while Figures 2.5(b)-(d) show SEM images taken of the GaAs nanodot distribution at increasing ion doses that are indicated by the corresponding letters on Figure 2.5(a). Nanodots on GaAs reach a stable average nanodot size of approximately 150 ±10 nm with a broad distribution of sizes (see Figure 2.5(d)).

Nanodots on InP grow over a shorter dose interval of approximately $1\text{x}10^{15}$ to $2\text{x}10^{16}$ ions/cm^2 to a smaller stable average diameter of approximately 33 ±3 nm and into a stable distribution of sizes. Figure 2.6(a) shows the evolution of nanodot size on InP as a function of ion dose, and Figures 2.6(b)-(d) show SEM images taken of the InP nanodot distribution at increasing doses as indicated by the corresponding letters on Figure 2.6(a). Barring the differences in doses and sizes, the nanodot versus dose trends exhibited by InP and GaAs are similar, with both materials reaching a stable average nanodot size and distribution after a short initial growth period.

Figure 2.7(a) shows the evolution of nanodots on InAs as a function of ion dose, and Figures 2.7(b)-(d) show SEM images taken of the InAs nanodot distribution at increasing doses as indicated by the corresponding letters on Figure 2.7(a). InAs shows an initial period of nanodot growth above its nanodot threshold dose and begins to approach a stable distribution in a manner similar to InP and GaAs. However, rather than reaching a stable average size and distribution, the nanodot size distribution of InAs abruptly and becomes bimodal at a dose of approximately $1.9\text{x}10^{16}$ ions/cm^2. The dose at which this change occurs was verified several times using different samples. This sudden change is shown in Figure 2.7(a) by a splitting of the nanodot size data into larger and smaller nanodot distributions above a dose of $1.9\text{x}10^{16}$ ions/cm^2 and by the rapid increase in the size of In nanodots/particles visible in the larger particle data set. This change can also be seen by noting the significant change in nanodot size distribution between the images shown in Figures 2.7(c) and 2.7(d). The large In particles reach sizes greater than 600 nm and exhibit clear faceting. This transition and faceting of large nanodots on InAs is evident in the experiments of Lugstein et al. as well [11], though it is not noted as a sharp, repeatable transition by those authors. No nanodot faceting was observed in the case of the GaAs or InP. By comparing the drastic differences in group III metallic nanodot size, shape, and distribution for GaAs, InP, and InAs visible in Figures 2.5, 2.6, and 2.7 respectively, the very different FIB responses of these materials are made readily apparent.

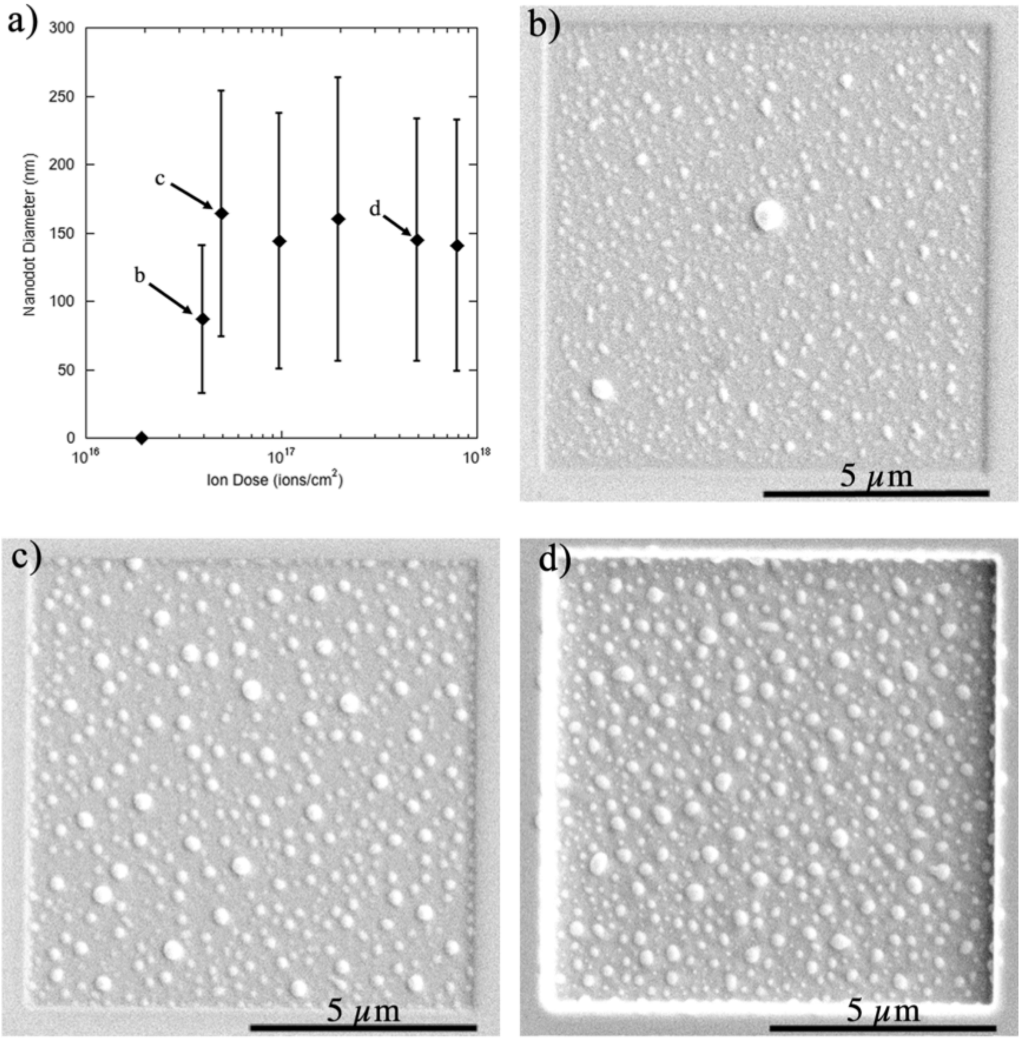

Figure 2.5: A plot and SEM micrographs showing change in Ga nanodot size as a function of ion dose on different regions of irradiated GaAs. The plot in a) shows average nanodot diameter plotted as a function of dose, with the error bars indicating nanodot diameter one standard deviation above and below the mean for each dose. b), c), and d) show images at the doses corresponding to the correspondingly labeled points in a).

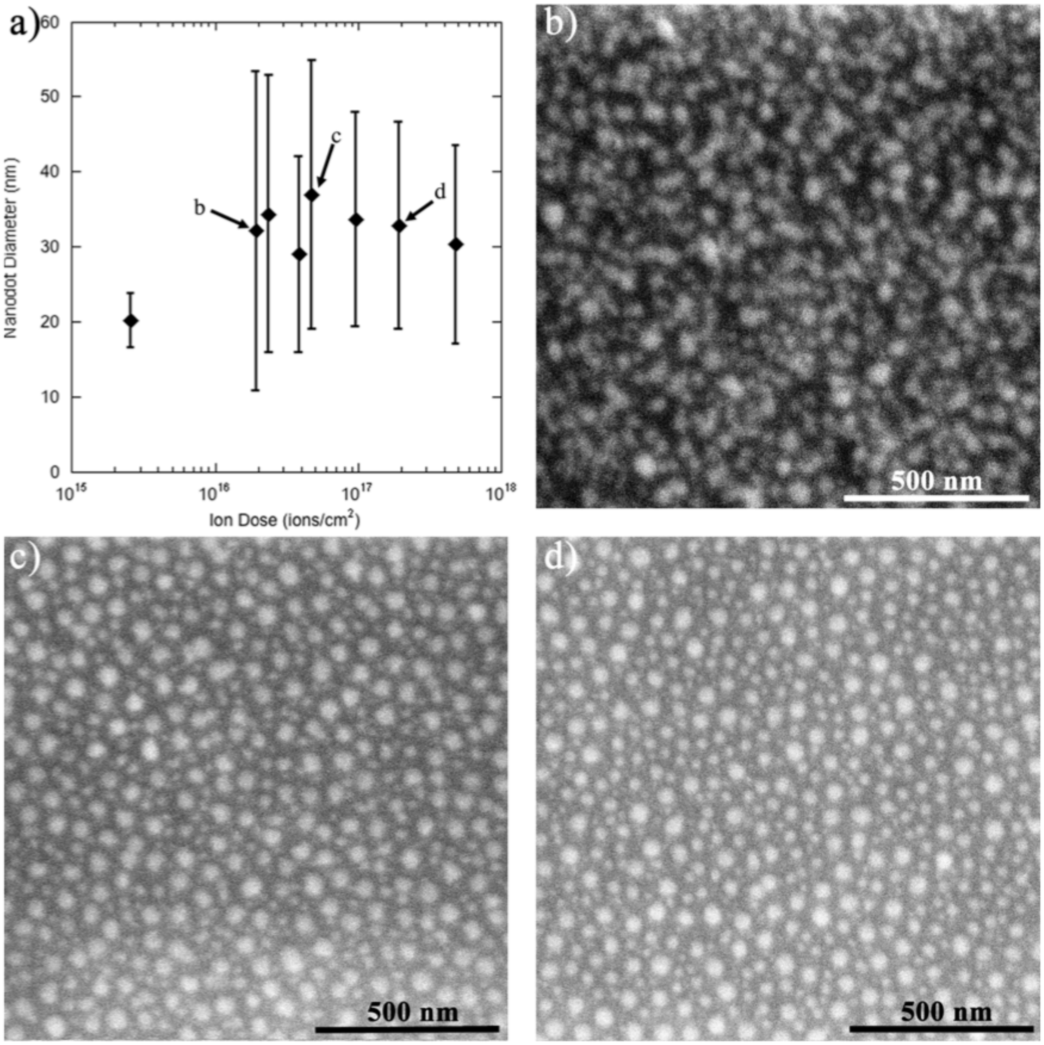

Figure 2.6: A plot and SEM micrographs showing change in nanodot size as a function of ion dose on different regions of irradiated InP. The plot in a) shows average nanodot diameter plotted as a function of dose, with the error bars indicating nanodot diameter one standard deviation above and below the mean for each dose. b), c), and d) show images at the doses corresponding to the correspondingly labeled points in a).

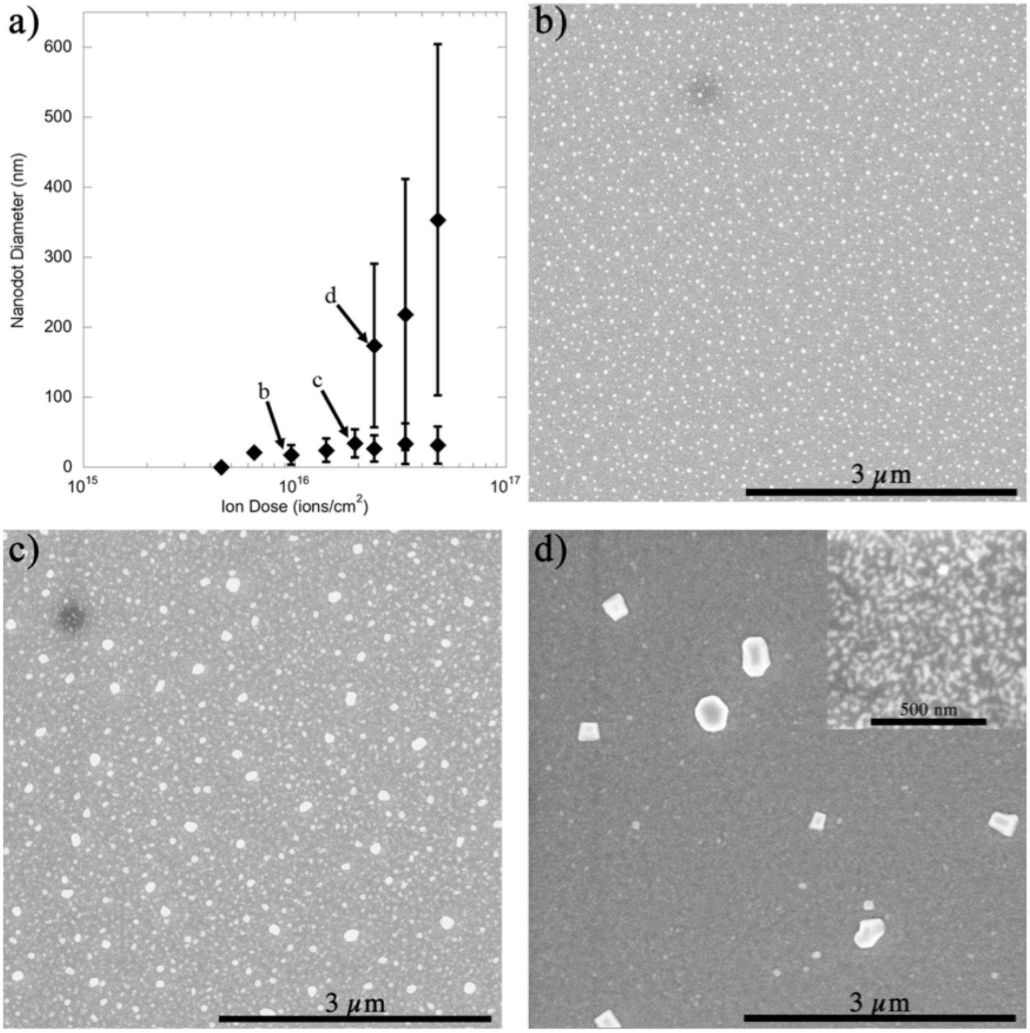

Figure 2.7: A plot and SEM micrographs showing change in In nanodot size as a function of ion dose on different regions of irradiated InAs. The plot in a) shows average nanodot diameter plotted as a function of dose, with the error bars indicating nanodot diameter one standard deviation above and below the mean for each dose. b), c), and d) show images at the doses corresponding to the correspondingly labeled points in a).

2.4 Nanodot Formation Model Development and Discussion of Results

The results presented in the previous section highlight that the FIB response and nanodot forming behavior of each III-V material is different despite the commonalities in the crystalline structures of GaAs, InP, InAs, and AlAs. If FIB directed creation of nanostructures is to be used for demanding electronic and optoelectronic applications, then a broader and more complete understanding of what controls the FIB response of these materials is needed. The formation of metallic nanodots on specific III-V semiconductors under ion irradiation has been attributed to the preferential sputtering of the group V element [12,24,30], which produces an excess of group III atoms that diffuse together to allow for nucleation, growth and ripening of group III nanodots [18]. It is reasonable then to assume that the material properties that determine the FIB response and nanodot forming behavior of the III-V materials studied here are those that have a strong effect on their multicomponent sputtering behavior and the ability of free group III atoms to diffuse on the surface, nucleate into metallic nanodots, and grow into a distribution of nanodot sizes.

Following the theoretical work of Sigmund concerning preferential sputtering in a multicomponent system [31], the properties that affect the relative partial sputtering yields of the group III and group V atoms, Y_{III} and Y_{V} respectively, are elemental surface binding energy and atomic mass. Here the sputtering yield is defined as the number of atoms sputtered per incident ion. The ratio of Y_{III} to Y_{V} in the linear cascade regime is approximated by:

$$\frac{Y_{\mathrm{III}}}{Y_{\mathrm{V}}} = \frac{c_{\mathrm{III}}}{c_{\mathrm{V}}}\left(\frac{M_{\mathrm{V}}}{M_{\mathrm{III}}}\right)^{2m}\left(\frac{U_{\mathrm{V}}}{U_{\mathrm{III}}}\right)^{1-2m} \tag{2.1}$$

Where c_{III} and c_{V} are atomic concentrations at the material surface, U_{III} and U_{V} are the surface binding energies of each element, and M_{III} and M_{V} are the atomic masses of the group III and group V species respectively. m is the sputtering exponential factor, which is dependent on the reduced energy, ε, for each atom-ion pair and E, the energy of each incident ion. In developing Equation (2.1), Sigmund makes the assumption that the compound being sputtered is amorphous and homogeneous. Previous work with Si^+ implantation of GaAs, InP, and InAs has shown that at ion doses of ~1×10^{15} ions/cm^2 the near surface region of these materials is amorphized by ion damage [28,29], indicating that the assumption of an amorphous medium in this study is reasonable. Those same studies demonstrated that AlAs is much more resistant to amorphization and remains crystalline to much higher doses. An m value may be defined for each atomic species, but component specific m values are not readily available in the literature. Therefore, a single m value is used in this work, a condition most valid when $M_{\mathrm{V}} \approx M_{\mathrm{III}}$ [31]. For sputtering applications, m takes a value between $0 \leq m \leq 0.2$ [32]. Malherbe et al. found a value of *m*=0.165 to be consistent with their results for Ar^+ ion sputtering of (100) InP surfaces [7] and this is the value used for this analysis.

Atomic surface binding energies are often approximated as the elemental heat of sublimation or heat of formation from gaseous atoms, which when used in Equation (2.1) produces reasonable results for metallic alloys [31,32]. The strong non-metallic bonding in the III-V compounds will have a large impact on their surface binding energies, making the use of elemental heats of sublimation less accurate in predicting their behavior. However, experimental values for the surface binding energies of the III-V atomic constituents are not readily available, so we use the elemental heats of sublimation/formation (Table 2.2 [33,34]) out of necessity. It may be possible to attain reasonable surface binding energies through simulation-based methods. Based solely on the elemental heats of sublimation/formation, it would be expected that upon sputtering the surfaces of GaAs, InAs, and AlAs would become group III enriched, as in their cases $U_{\mathrm{III}}>U_{\mathrm{V}}$. This is in agreement with experimental observations for GaAs and InAs. Based on the magnitude of the Al and As binding energies the surface of AlAs is expected to become group III enriched upon irradiation, but metallic nanodots were not observed here. The AlAs surface may be in fact becoming Al enriched, but insufficiently so to form nanodots before the thin AlAs films used here were milled through. For InP $U_{\mathrm{III}}<U_{\mathrm{V}}$, indicating that based on heat of sublimation alone its surface would be expected to become group V enriched. This is not the case, as group III nanodots have been experimentally observed on InP in this study and previous inert gas sputtering studies have identified nanodots on InP as comprised of In [23-25]. The cases of InP and AlAs demonstrate that resorting to any one material property, such as the surface binding energy, alone is insufficient to predict the sputtering response of these compound materials and that more complex relationships must be used to understand their observed behavior.

Table 2.2: Approximate group III and V surface binding energies, U_{III} and U_V respectively, used for sputter yield ratio calculations, the group III surface enrichment predicted by Equation (2.2), c_{III}^s/c_V^s, and the partial sputter yield ratio calculated using Equation (2.1), Y_{III}/Y_V. The surface binding energies given for Ga, In, Al, and As are elemental heats of sublimation taken from reference [33]. The value given for P is its elemental heat of formation from a gas taken from reference [34].

	U_{III} (eV/atom)	U_V (eV/atom)	c_{III}^s/c_V^s	Y_{III}/Y_V
GaAs	2.82	1.26	1.68	0.60
InP	2.49	3.28	1.28	0.78
InAs	2.49	1.26	1.82	0.55
AlAs	3.38	1.26	1.39	0.72

Another term in Equation (2.1) that needs consideration is the ratio of the elemental surface concentration during sputtering, c_{III}/c_V, but its determination is non-trivial. For a III-V binary compound at the start of sputtering c_{III}/c_V has a value of 1, the ratio of the elemental concentrations in the bulk. As ion irradiation is underway the action of preferential sputtering will enrich the surface with the more slowly sputtering element, and in response the partial sputtering yield of that element will increase. In the absence of other competing effects a steady-state will be achieved when the partial sputtering yield of the enriching element has increased to the point where it equals the sputtering yield of the other element. At this point the partial sputtering yield ratio, Y_{III}/Y_V, will reach a constant value of 1 and the elemental surface concentration ratio will have reached a constant maximum steady-state value. Using the form of the partial sputtering yields given in Equation (2.1), the enrichment of the surface at steady-state, c_{III}^s/c_V^s, may be predicted by [31]

$$\frac{c_{III}^{\,s}}{c_V^{\,s}} = \frac{c_{III}^{\,b}}{c_V^{\,b}}\left(\left(\frac{M_V}{M_{III}}\right)^{2m}\left(\frac{U_V}{U_{III}}\right)^{1-2m}\right)^{-1} \qquad (2.2)$$

where c_{III}^b and c_V^b are the concentrations in the bulk of the group III and group V elements respectively. Values for c_{III}^s/c_V^s predicted using Equation (2.2), m=0.165, and the elemental heats of fusion range in value from 1.2 to 1.9 (Table 2.2). This approach does not take the nucleation of nanodots into account, which would deplete the surface of group III atoms. Thus, growth of nanodots will decrease the final level of group III surface enrichment and may also prevent the steady-state case of $Y_{III}/Y_V= c_{III}^b/c_V^b$ from ever being achieved. With this in mind the result of Equation (2.2) may be thought of as a theoretical upper limit for group III surface enrichment, such that from the start of sputtering the surface concentration ratio will vary within the bounds of $(c_{\mathrm{III}}^{\mathrm{b}}/c_{\mathrm{V}}^{\mathrm{b}}) \leq (c_{\mathrm{III}}/c_{\mathrm{V}}) < (c_{\mathrm{III}}^{\mathrm{s}}/c_{\mathrm{V}}^{\mathrm{s}})$. There will also be a significant Ga concentration in the near surface region due to implantation from the FIB, which for the case of GaAs will affect the relevant group III surface concentration. The fraction of Ga ions that remain on the surface at steady state, ζ, can be predicted by the method given in reference [31] along with the values of $Y_{\mathrm{III}}/Y_{\mathrm{V}}$ and $c_{\mathrm{III}}^{\mathrm{s}}/c_{\mathrm{V}}^{\mathrm{s}}$. This value has been taken here as $\zeta=0.1$ [14,35]. However, as the Ga ions from the FIB are a different group III species than that present in InP, InAs, and AlAs, for this analysis the contribution of Ga to the surface composition will be neglected except for in the case of GaAs.

Predictions of $Y_{\mathrm{III}}/Y_{\mathrm{V}}$ found using Equation (2.1) with the elemental heats of sublimation, $m=0.165$, and $c_{\mathrm{III}}/c_{\mathrm{V}}=c_{\mathrm{III}}^{\mathrm{b}}/c_{\mathrm{V}}^{\mathrm{b}}=1$ are tabulated in Table 2.2. Examining the zero fluence case, where $c_{\mathrm{III}}/c_{\mathrm{V}}=1$, will provide $Y_{\mathrm{III}}/Y_{\mathrm{V}}$ values that are representative of each III-V compound and can be used to compare their behavior. From Table 2.2 it can be seen that Equation (2.1) predicts a $Y_{\mathrm{III}}/Y_{\mathrm{V}}$ value of less than 1 for all four III-V compounds studied, indicating preferential sputtering of the group V element will occur and result in an excess of the group III element for each. An approximate yield of excess group III atoms produced per incident ion can then be calculated using the total sputter yield for each compound. The total ion sputter yields, $Y_{\mathrm{total}}=Y_{\mathrm{III}}+Y_{\mathrm{V}}$, have been approximated by multiplying the experimental milling rate values listed in Table 2.1 by the bulk atomic volume of each compound. Those Y_{total} values are listed in Table 2.3. The number of excess group III atoms generated per ion, Y_{E}, may be estimated using the experimental Y_{total} value, the zero fluence $Y_{\mathrm{III}}/Y_{\mathrm{V}}$ ratio predicted by Equation (2.1), and the readily derived relationship:

$$Y_{\mathrm{E}} = Y_{\mathrm{total}}\left[\frac{1}{\left(Y_{\mathrm{III}}/Y_{\mathrm{V}}+1\right)} - \frac{1}{\left(Y_{\mathrm{V}}/Y_{\mathrm{III}}+1\right)}\right] \tag{2.3}$$

The calculated values of Y_{E} for each compound are given in Table 2.3. It should be noted that several simplifications and assumptions have been made in calculating those values, and therefore they should be treated with caution. The values of Y_{E} may be used to compare the behaviors of each compound relative to one another and provide some insight into the nature of their FIB responses. However, they should not be used in a quantitative capacity. It should also be noted that for the case of GaAs, the number of excess Ga atoms will be increased by ζ=0.1, the fraction of Ga^+ ions supplied directly from the FIB beam that remain on the surface at steady state. In order to take this into account, the GaAs Y_E value given in Table 2.3 was found by taking the sum of ζ and the Y_E value predicted by Equation (2.3).

Table 2.3: The partial sputter yield ratios calculated using Equation (2.1), Y_{III}/Y_V, the approximate total III-V sputter yield, Y_{total}, calculated using the experimental r values listed in Table 2.1, and the estimated excess group III adatom yields, Y_E, calculated using Y_{total} and the results of applying Equations (2.1) and (2.3).

	Y_{III}/Y_V	Y_{total} (atoms/ion)	Y_E (excess group III atoms/ion)
GaAs	0.60	5.5	1.48
InP	0.78	6.8	0.83
InAs	0.55	7.2	2.09
AlAs	0.72	2.5	0.41

Comparing the Y_{III}/Y_V and Y_E values given in Table 2.3, it can be seen that preferential sputtering of the group V element and production of excess group III atoms on the material surface is expected for all four of the III-V compounds studied as part of this analysis. Materials with high Y_{III}/Y_V ratios and low Y_{total} values such as InP and AlAs have a lower predicted Y_E. This may serve as a partial explanation for why InP is only able to form small nanodots (relative to GaAs and InAs) and why nanodot formation on AlAs is suppressed. However, a low Y_E value only indicates that enrichment of the surface with group III atoms before nanodot nucleation and nanodot growth after nucleation will be slow, and does not preclude nanodot formation or nanodot growth to larger sizes. The differences in the Y_{III}/Y_V, Y_{total}, and resulting Y_E values for each material are insufficient to explain all of the different experimentally observed behaviors of each material. In particular those values alone fail to provide any explanation for how the nanodot of GaAs and InP are able to develop in to stable size distributions.

To develop a satisfactory explanation for the different FIB responses of GaAs, InP, InAs, and AlAs a model must be employed that describes the transport of group III atoms across their respective irradiated III-V surfaces and how transport and excess group III production compete with sputtering losses to determine metallic nanodot growth and size distribution. A suitable model has been developed previously by Wei, et al [14,35] in order to describe their results for off-normal FIB bombardment of GaAs. Their approach was to modify the classic model for Ostwald ripening in a diffusion-limited system [36] to accommodate the effects of sputtering from and implantation into Ga nanodots by a FIB and continuous generation of excess group III atoms on the III-V surface. They arrive at the their final model through the solution of the diffusion equation in polar coordinates, with an additional source term to account for the generation of excess Ga adatoms from preferential sputtering and with each nanodot assumed to be a hemispherical cap surrounded by a denuded adatom capture zone. We adopt Wei et al's general approach with some slight modifications to generalize it for other compounds and to incorporate the form of Y_{E} developed above, again assuming diffusion rather than interface attachment limited behavior. The detailed development of the model as adapted for this study is given in the appendix located at the end of this chapter, and follows closely the derivation of Wei et al [35]. However, the full equation derivation is not necessary to understand its results and the trends that those results imply. The final derivation result only is presented here. The evolution of the nanodot radius of curvature, R, and correspondingly nanodot size, as a function of time is given by

$$\frac{\mathrm{d}R}{\mathrm{d}t} = A\left(1 - \frac{R^*}{R} + BR^2\right) \tag{2.4}$$

where

$$\begin{aligned}
A(R) &= \frac{D_{\mathrm{III}}\left(C_\lambda - C_0\right)\Omega_{\mathrm{III}}}{R^2 \ln\left(\lambda / R\right)} \\
R^* &= \frac{2\Omega_{\mathrm{III}}\gamma C_0}{kT(C_\lambda - C_0)} \\
B(R) &= \left(\frac{Y_{\mathrm{E}} I \ln\left(\lambda / R\right)}{2D_{\mathrm{III}}\left(C_\lambda - C_0\right)}\right)\left[\frac{\left(\lambda / R\right)^2 - 1}{\ln\left(\lambda / R\right)^2} - 1 - 2\left(\frac{Y_{\mathrm{III}}^*\Omega_{\mathrm{III}} - 0.5\Omega_{\mathrm{Ga}}}{Y_{\mathrm{E}}\Omega_{\mathrm{III}}}\right)\right]
\end{aligned} \tag{2.5}$$

D_{III} is the coefficient of ion enhanced diffusion for group III atoms on an irradiated III-V surface, Ω_{III} is the atomic volume of the group III element, λ is the nanodot denuded zone radius past which the adatom density recovers its average value,

C_λ is the adatom concentration at λ, C_0 is the flat-surface equilibrium group III adatom concentration, γ is the metallic nanodot-vapor surface tension, k is the Boltzmann constant, T is the absolute temperature, I is the flux of incoming ions, Y_{III}^* is the sputtering yield of the pure group III element taken to approximate the sputtering yield from a nanodot, and Ω_{Ga} is the atomic volume of gallium. As defined in Equation (2.4), R^* is the critical nanodot size and B is the sputtering dependent parameter. A is a positive term and represents the contribution of Ostwald ripening, such that when B=0 Equation (2.4) reduces to the standard equation for diffusion limited Ostwald ripening in a conservative system [37]. Thus all the direct contributions of FIB irradiation are contained in the B term. For the case of sputtering from the nanodot, B will have a value less than zero.

As a result of $B<0$, Equation (2.4) predicts that once the average nanodot size reaches a critical value the competing effects of atoms being sputtering from the nanodot (B term), ions being implanted into it (B term), and adatoms diffusing to it (A term) will balance each other and produce a stable average nanodot size. Wei et al. used this result to explain the creation of a stable array of uniform and stationary Ga nanodots with off-normal FIB bombardment of GaAs [14]. Because in this study the FIB was at normal incidence, new nanodot nucleation, growth, and dot coalescence with other dots was continual, preventing the creation of a single uniform nanodot size. Despite this, the experimental results presented above show that a stable distribution of nanodot sizes will develop for normal incidence FIB irradiation of GaAs and InP in agreement with the prediction of Equation (2.4), and InAs begins to develop a stable distribution before it is prevented from doing so by its transition to a bimodal nanodot size distribution.

The property dependencies and general trends described by Equations (2.4) and (2.5) can be used to further describe the FIB response behavior of the III-V materials examined. Because many of the property values required by Equation (2.5) are not readily available or only available by approximation, Equations (2.4) and (2.5) are not suitable for quantitatively predicting average nanodot sizes and distributions and do not accurately predict the experimental distributions reported in this study. The trends of Equations (2.4) and (2.5) indicate that higher values of D_{III} and Y_{E} will respectively result in a higher rate of growth by Ostwald ripening, indicated by the coefficient A, and a less negative value of B. Both effects will cause the rate of nanodot material lost to sputtering to take longer before balancing the rate of nanodot growth. This will allow a larger average nanodot size to become stable. Conversely, higher values of Y_{III}^* and γ will make B more negative and lower R^*, resulting in a smaller final nanodot size. A high γ value is also indicative of a high barrier for nanodot nucleation and so will affect the point at which nanodots are initially able to form. No nucleation analysis was done as part of this work. Nanodot size is influenced by all four of the above quantities, and they will be used as a basis for explaining the relative differences in the experimentally found nanodots size distributions for each material.

In order to facilitate a comparison across the materials studied, some of the physical quantities specified in Equation (2.5) for the group III metals are listed in Table 2.4. γ values were taken from reference [38] and are the surface tension of the solid group III metal species for each III-V compound. Y_{III}^* values were calculated using 10000 ion SRIM-2008 (version 2008.05, [39]) simulations of 30 kV Ga^+ implantation into an amorphous solid of each respective group III atom [40]. SRIM is a computational package that uses a Monte Carlo method and quantum-mechanical treatment of ion-atom interactions to simulate ion implantation processes into amorphous targets. Ω_{III} values were approximated by converting to the appropriate units from the room temperature density and molar mass of each solid metallic element. The homologous melting temperature at 300 K, $T_{\mathrm{H}}=300/T_{\mathrm{M}}$, of each group III metal is listed in place of a D_{III} value, with melting temperatures, T_{M}, taken from reference [33]. T_{H} is assumed to be an indicator of the relative magnitude of D_{III}, with higher values of T_{H} indicating that the group III element is nearer to its bulk melting temperature and can be expected to diffuse more rapidly across the III-V surface. This approximation is made necessary because D_{III} values are not available for ion-enhanced diffusion of the group III species studied here.

Table 2.4: A list of group III metal properties which influence the nanodot forming behavior of the III-V compounds. Tabulated are the metal-vapor surface tension, γ, homologous melting temperature at 300 K, T_H*, SRIM-2008 predicted elemental sputter yield,* Y_{III}^**, and atomic volume,* Ω_{III}*, of each group III metal examined in this work.*

	γ (J/m^2)	**T_H at 300 K**	**SRIM-2008 Y_{III}^* (atoms/ion)**
Ga	0.767	0.990	6.1
In	0.633	0.698	11.2
Al	1.14	0.321	3.9

Through the use of Equations (2.4) and (2.5) and the properties given in Tables 2.3 and 2.4, a number of trends may be predicted that reflect the experimental observations noted in the previous section. Equation (2.4) predicts that a balance will develop between loss of nanodot volume to sputtering and nanodot growth by diffusion of adatoms and implantation of Ga ions. The development of stable average nanodot sizes and distributions after prolonged irradiation of GaAs (Figure 2.5) and InP (Figure 2.6) may be explained on the basis of this prediction. However, the balance predicted by Equation (2.4) will only develop in the absence of other effects that influence nanodot size. As shown in Figure 2.7(a), InAs undergos an initial period of nucleation and growth that begins to saturate with increasing ion dose in a manner similar to GaAs and InP. However, nanodots on InAs are prevented from ever reaching a stable size and distribution by the onset of a shape transition. The transition from pseudospherical nanodots with small sizes to faceted nanodots of larger size is indicative of a surface energy driven transition [41]. Past some critical point the InAs system may able to lower the overall energy of the nanodot distribution by eliminating a number of small In nanodots in order to form a few larger and faceted crystallites, which will decrease the surface energy contribution to the total system energy. The In nanodots formed on InP might be expected to undergo a similar transition if they were able to grow large enough to reach a similar critical size. However, nanodots on InP reach a stable average size of ~33 nm and cease to increase in size beyond that point. Based on the analysis above and the property values reported in Table 2.4, InAs and InP are expected to have comparable In adatom surface diffusion rates and rates of sputtering losses from existing nanodots (as indicated by Y_{III}^*). However, the predicted InAs rate of excess group III adatom production (Y_E) is twice that of InP. The lower InP Y_E will result in slower nanodot growth in that system and following from Equations (2.4) and (2.5) will result in nanodots on InP being stabilized at a relatively smaller size. Correspondingly, the higher Y_E of InAs allows nanodots on InAs to grow to larger sizes, such that the system can reach the point where the bimodal transition occurs before nanodot size is stabilized by sputtering losses.

The balance of sputtering losses and nanodot growth predicted by Equation (2.4) is insufficient to account for why AlAs does not form nanodots, but the property trends of Equation (2.5) provide some insight. AlAs has small Y_E and D_III (as reflected by T_H) values, which indicate respectively that relatively few adatoms will be generated from sputtering in the AlAs system and nanodot growth by diffusive processes will be slow relative to the other materials. Al also has a large γ value, indicating that Al nanodots will have a large energy barrier to overcome before nucleation of Al nanodots is possible. The combination of a high barrier to nanodot nucleation and expected low rate of growth by adatom attachment will act to prevent Al nanodots from forming on AlAs after receiving ion doses in the same ranges as necessary to form nanodots on the other materials, or at least keep nanodots from growing to a size above the detection limit of the instruments used in this work. This prediction is in agreement with the experimental observation that AlAs does not develop nanodots at room temperature even at ion doses high enough to completely mill through the thin films examined. AlAs may be able to form nanodots after receiving much higher ion doses than those used in this work. However, verifying this would require much thicker AlAs films than were available for this study.

The large final average nanodot size in the GaAs case relative to InP and InAs may be explained by examining the terms of Equation (2.5). GaAs has large relative Y_E and T_H values, indicating it will have a large adatom production rate and initially high rate of diffusion driven nanodot growth. Ga also possesses a small Y_III^*, meaning that its rate of nanodot volume loss to sputtering will be relatively low. These effects collectively indicate that nanodots on GaAs will be able to grow to a larger average size before nanodot material loss to sputtering balances adatom addition and stabilizes the nanodot distribution. In contrast, InP has smaller Y_E and T_H values relative to GaAs and a large Y_{III}^* value. This indicates that nanodot growth by adatom diffusion will be slow in that system and that losses to sputtering will rapidly reach the point where they match the rate of nanodot growth. The smaller initial nanodots sizes of InAs may be similarly explained. InAs has a larger Y_E value than GaAs, but a smaller T_H value and larger Y_{III}^* value. Thus slower adatom diffusion and higher nanodot sputtering losses may still be keeping nanodot sizes in the InAs system (before its bimodal transition point) smaller than those of GaAs. The relative sizes of the nanodots in the GaAs, InP, and InAs systems predicted by the trend of Equation (2.5) agree with the experimental results reported in the previous section.

The qualitative trends laid out in the above analysis reveal the basic physical phenomena controlling nanodot formation. FIB response in the materials examined here is controlled both by those properties that determine the multicomponent sputtering behavior, and those that control the ability of group III adatoms to diffuse and collect into nanodots on the irradiated III-V surface. Both the multicomponent sputtering and adatom diffusion behavior of each compound can be related back to the relative strength of the atomic bonds holding atoms into the III-V structure or onto the III-V surface. Those materials with very high bond strength, like AlAs, are more resistant to sputtering and have more tightly bound surface atoms that diffuse slowly. As a result of this higher bond strength AlAs shows a lower rate of group III adatom production, a lower predicted adatom diffusion rate, and difficulty in forming nanodots. In contrast, the lower atomic bond strength of InAs results in a high sputtering rate and excess group III adatom yield. The less tightly bound In surface atoms diffuse more quickly, resulting in a compound that forms nanodots readily under FIB irradiation. There is a direct relationship between atomic bond strength and the physical parameters present in the model developed here to describe FIB response. By consideration of the role of atomic bond strength and the resulting basic properties, the approach developed here may be used to better understand the FIB response of other multicomponent materials. The qualitative nature of the conclusions drawn above is necessitated by a lack of accurate values for many of the physical properties called for by the model of Equations (2.4) and (2.5), but the qualitative trends identified do correctly reflect the physical observations from experiment.

2.5 Conclusions and Future Work

GaAs, InP, InAs, and AlAs all have been shown to have different responses to focused Ga^+ ion irradiation, despite all belonging to the III-V class of compounds and having the same crystalline structure. GaAs, InP, and InAs all form metallic group III nanodots following irradiation, but do so at different ion doses and their nanodots develop into different size distributions. At doses above ~1.9×10^{16} ions/cm^2 nanodots on InAs were observed to undergo a transition to a bimodal size distribution. No droplets were observed to form on the thin AlAs films examined. In order to better understand these experimentally observed results, a model was used that combines sputtering theory and diffusive growth driven by Ostwald ripening. The model predicts that for a system of growing nanodots, the competing effects of nanodot growth and material loss due to sputtering will balance and result in a stable average nanodot size after an initial period of growth. Trends regarding the final stable nanodot size and the ease with which nanodots will nucleate and grow on a particular material were predicted using the physical quantities that make up the final form of the model. The experimentally observed Ga^+ FIB responses of each material examined agree qualitatively with the model predictions. Materials which have a higher rate of group III adatom diffusion across the irradiated semiconductor surface and a higher rate of excess group III atom production due to preferential sputtering will correspondingly have nanodots that are able to grow to larger sizes before growth is stopped by sputtering losses. In contrast, materials that exhibit a high pure group III sputtering yield and a high group III surface tension will have nanodots that are stabilized at smaller relative sizes. In keeping with classical nucleation theory, a high surface tension is also indicative of a high barrier to initial nanodot nucleation. All of these properties are in some capacity related to the relative atomic bonding strength of the III-V material or pure group III element. Those III-V compounds with higher bond strengths will sputter more slowly and have more tightly bound and slowly diffusing surface adatoms, resulting in smaller nanodots. Those that have weaker bond strengths will sputter more rapidly and produce more excess group III atoms. Stronger bonding in the group III nanodots will result in a lower sputtering rate from them and so stabilize larger nanodot sizes.

This study is the first reported attempt to compare the group III nanodot forming behaviors of different III-V compounds to each other as a material set and to explain those behaviors in terms of basic properties and processes common to all those materials. The results of this work have implications for the design of ion beam processes aimed at creating nanostructure for device applications. The FIB response parameters reported serve as useful basic guidelines for how quickly the materials examined mill and begin forming nanodots. However, for device purposes the size, location, and density of group III metallic nanodots will need to be controlled. The trends predicted in this study reveal the material properties that control and may be used to predict group nanodot formation. Those same properties are what may be influenced by process design to better control the point at which nanodots form and their size distribution as desired for a specific purpose. The characteristics of III-V FIB response reported in this work also provide insight into the general ion beam response of that material system and the material factors and FIB irradiation parameters that control that response.

In order to provide more insight into the FIB response of the III-V materials and the phenomena of group III metallic nanodot formation, there are several different ways in which this work could be built upon. This study of FIB response could easily be extended to other III-V materials, such as the Nitrides, which are also candidates for FIB-induced nanostructure based devices. The FIB response of thicker AlAs films should also be studied. The AlAs films irradiated in this work were too thin to conclusively determine if AlAs is capable of forming stable Al nanodots. The FIB response, nanodot forming behavior, and nanodot composition of the III-V ternary alloys could also be determined using the same experimental methods as those employed here. Nanodot formation on alloys may be technologically relevant, as many devices where nanodots for droplet epitaxy or plasmonic applications would be employed may make use of III-V alloying to control optical and electrical properties. Alloying may also serve as another process parameter which may be used to control nanodot size and distribution, and studying alloys of the binary compounds already characterized here may give greater insight into which of the nanodot controlling factors identified in this work have the greatest impact on nanodot formation. From the standpoint of the model employed here, further development and additions to that model may allow it to be used in a more quantitative manner as a predictive tool for design of experiments or processes. A theoretical treatment of nanodot nucleation and inclusion of some type of nucleation barrier effect into the model used here or a different one may help to give a better understanding of the factors which control the initial appearance of nanodots and their early stages of growth. Many of the material properties called for by the model used in this work were not available and had to be approximated roughly here. Experiments to better characterize basic III-V compound properties under ion irradiation to provide those values will bring the model closer to serving as a useful quantitative tool.

2.6 Appendix: Derivation of Nanodot Growth Model

Following the general approach of Wei, et al [14,35], a description for the growth of nanodots formed by ion irradiation of a compound material may be developed from the classic model for Ostwald ripening in a diffusion limited system [36] by adding an additional source term to account for adatom production by preferential sputtering. As a starting assumption, each metallic nanodot is assumed to be a spherical cap resting on an amorphous or otherwise ion disrupted III-V compound surface. The flux of excess group III adatoms diffusing to the nanodot may be found by solving the diffusion equation in polar coordinates for a radial area around each nanodot. Each spherical cap has a radius of curvature R and is surrounded by a denuded zone of radius λ, past which point the concentration of group III adatoms returns to the equilibrium concentration of a flat surface, C_0. The areal concentration of adatoms, $C(r,t)$, where r is the radial distance from the nanodot center and t is time, may be determined by solving

$$\frac{\partial C}{\partial t} = \frac{1}{r}\frac{\partial}{\partial r}\left[r D_{\mathrm{III}} \frac{\partial C}{\partial r} \right] + Y_{\mathrm{E}} I \qquad (2.6)$$

where D_{III} is the ion-enhanced diffusion coefficient of the excess group III atoms on the material surface. The second right-hand term takes into account the creation of excess group III atoms, and depends on the product of Y_{E}, the yield of excess group III atoms per ion, and I, the flux of incoming ions given in ions/cm^2/s. If steady state is reached such that diffusion of group III atoms to the nanodot is balanced by the addition of adatoms into the capture volume enclosed by $R\sin(\theta) \leq r \leq \lambda$, where θ is the contact angle between the nanodot and III-V surface, then Equation (2.6) will have a solution of the form

$$C(r) = K_1 \ln(r) + K_2 - \frac{Y_{\mathrm{E}} I r^2}{4D_{\mathrm{III}}} \tag{2.7}$$

where K_1 and K_2 are constants to be determined shortly. Let us assume for the sake of simplicity that each nanodot is a hemispherical cap, such that $R\sin(\theta)=R$. This is a reasonable assumption, as Wei et al. found the wetting angle of FIB produced Ga droplets on GaAs to be near θ=90° [35]. Experimental values of θ for the other compounds were not readily obtainable in this study due to the very small size of the In nanodots seen on InP and InAs and the absence of nanodots in the case of AlAs. The assumption that θ=90° allows the use of the boundary conditions:

$$\begin{aligned} C(r) &= C_{\mathrm{R}} \text{ at } r = R \\ C(r) &= C_{\lambda} \text{ at } r = \lambda \end{aligned} \tag{2.8}$$

Application of those conditions to Equation (2.7) results in:

$$K_1 = \frac{\left(C_{\lambda} - C_{\mathrm{R}}\right)}{\ln\left(\lambda / R\right)} + \frac{Y_{\mathrm{E}} I}{4D_{\mathrm{III}}} \frac{\left(\lambda^2 - R^2\right)}{\ln\left(\lambda / R\right)} \tag{2.9}$$

The number of group III atoms attaching per second to the periphery of the nanodot through surface diffusion is given by

$$J = 2\pi R \left[D \frac{\partial C}{\partial r} \right]_{r=R} \tag{2.10}$$

Substituting Equations (2.7) and (2.9) into Equation (2.10) produces

$$J = \frac{2\pi D_{\mathrm{III}}\left(C_{\lambda} - C_{\mathrm{R}}\right)}{\ln\left(\lambda / R\right)} + \pi Y_{\mathrm{E}} I R^2 \left[\frac{\left(\lambda / R\right)^2 - 1}{\ln\left(\lambda / R\right)^2} - 1 \right] \tag{2.11}$$

The rate equation for change in hemispherical nanodot volume with time is

$$\frac{\partial}{\partial t}\left[\frac{2\pi R^3}{3}\right] = \left(J - 2\pi R^2 Y_{\mathrm{III}}^{*} I\right)\Omega_{\mathrm{III}} + \pi R^2 I \Omega_{\mathrm{Ga}} \tag{2.12}$$

where Y_{III}^{*} is the sputtering yield of the pure group III element and Ω_{III} is the atomic volume of the group III atoms in a metallic nanodot, assumed to be approximately that of the bulk group III metal here. Ω_{Ga} is the atomic volume of Ga. The second term on the right side of Equation (2.12) accounts for the loss of adatoms to

FIB sputtering and the third term accounts for the addition of Ga atoms due to implantation in the nanodot by the FIB beam. Using the Gibbs-Thomson relationship, the equilibrium concentration, C_{R}, can be found by

$$C_{\mathrm{R}} = C_0 + C_0\left(\frac{2\Omega_{\mathrm{III}}\gamma}{kT}\right)\frac{1}{R} \tag{2.13}$$

where γ is the metallic nanodot-vapor surface tension, k is the Boltzmann constant, and T is the absolute temperature. Substituting Equations (2.11) and (2.13) into Equation (2.12) and rearranging produces the result discussed in the above sections of this chapter:

$$\frac{\mathrm{d}R}{\mathrm{d}t} = A\left(1 - \frac{R^*}{R} + BR^2\right) \tag{2.4}$$

where

$$A(R) = \frac{D_{\mathrm{III}}\left(C_\lambda - C_0\right)\Omega_{\mathrm{III}}}{R^2\ln\left(\lambda / R\right)}$$

$$R^* = \frac{2\Omega_{\mathrm{III}}\gamma C_0}{kT(C_\lambda - C_0)} \tag{2.5}$$

$$B(R) = \left(\frac{Y_{\mathrm{E}} I \ln\left(\lambda / R\right)}{2D_{\mathrm{III}}\left(C_\lambda - C_0\right)}\right)\left[\frac{\left(\lambda / R\right)^2 - 1}{\ln\left(\lambda / R\right)^2} - 1 - 2\left(\frac{Y_{\mathrm{III}}^*\Omega_{\mathrm{III}} - 0.5\Omega_{\mathrm{Ga}}}{Y_{\mathrm{E}}\Omega_{\mathrm{III}}}\right)\right]$$

This is the result arrived at by Wei et al. [14,35], slightly altered here to accommodate Y_E as defined in this work and to generalize the model for the case of III-V compounds beyond GaAs.

2.7 References

[1] Nisoli, M. et al. *Physical Review Letters* **78**, 3575-3578 (1997).

[2] Wu, P. C. et al. *Applied Physics Letters* **90**, 103119 (2007).

[3] Koguchi, N. & Ishige, K. *Jpn, J. Appi. Phys. Vol* **32**, 2052-2058 (1993).

[4] Watanabe, K., Koguchi, N. & Gotoh, Y. *JAPANESE JOURNAL OF APPLIED PHYSICS PART 2 LETTERS* **39**, 79-81 (2000).

[5] Kim, J. S. & Koguchi, N. *Applied Physics Letters* **85**, 5893 (2004).

[6] Hong, L., Liu, Z., Zhang, X. T. & Hark, S. K. *Applied Physics Letters* **89**, 193105 (2006).

[7] Malherbe, J. B. & Barnard, W. O. *Surface Science* **255**, 309-320 (1991).

[8] Malherbe, J. B., Barnard, W. O., Strydom, I. L. R. & Louw, C. W. *Surface and Interface Analysis* **18**, 491-495 (1992).

[9] Datta, D., Bhattacharyya, S. R., Chini, T. K. & Sanyal, M. K. *Nuclear Instruments and Methods in Physics Research B* **193**, 596-602 (2002).

[10] Lugstein, A., Basnar, B. & Bertagnolli, E. *Journal of Vacuum Science & Technology B: Microelectronics and Nanometer Structures* **20**, 2238 (2002).

[11] Lugstein, A., Weil, M., Basnar, B., Tomastik, C. & Bertagnolli, E. *Nuclear Instruments and Methods in Physics Research Section B: Beam Interactions with Materials and Atoms* **222**, 91-95 (2004).

[12] Lugstein, A., Basnar, B., Smoliner, J., Bertagnolli, E. & Weil, M. *Journal of Vacuum Science & Technology B: Microelectronics and Nanometer Structures* **22**, 2995 (2004).

[13] Rose, F., Fujita, H. & Kawakatsu, H. *Nanotechnology* **19**, 035301 (2008).

[14] Wei, Q., Lian, J., Lu, W. & Wang, L. *Physical Review Letters* **100**, 076103 (2008).

[15] Lugstein, A., Basnar, B. & Bertagnolli, E. *Journal of Vacuum Science & Technology B: Microelectronics and Nanometer Structures* **22**, 888 (2004).

[16] Callegari, V. & Nellen, P. M. *physica status solidi (a)* **204**, 1665-1671 (2007).

[17] Lugstein, A., Basnar, B. & Bertagnolli, E. *Nuclear Instruments and Methods in Physics Research Section B: Beam Interactions with Materials and Atoms* **217**, 402-408 (2004).

[18] Wu, J. H. et al. *Applied Physics Letters* **95**, 153107 (2009).

[19] Lugstein, A., Bernardi, J., Tomastik, C. & Bertagnolli, E. *Applied Physics Letters* **88**, 163114 (2006).

[20] Lugstein, A. et al. *Nuclear Instruments and Methods in Physics Research Section B: Beam Interactions with Materials and Atoms* **255**, 309-313 (2007).

[21] Malherbe, J. B. *Critical Reviews in Solid State and Materials Sciences* **19**, 55-127 (1994).

[22] Malherbe, J. B. *Critical Reviews in Solid State and Materials Sciences* **19**, 129-195 (1994).

[23] Chew, N. G. & Cullis, A. G. *Applied Physics Letters* **44**, 142-144 (1984).

[24] Nozu, M., Tanemura, M. & Okuyama, F. *Surface Science* **304**, L468-L474 (1994).

[25] Tan, S. K. & Wee, A. T. S. *Journal of Vacuum Science & Technology B: Microelectronics and Nanometer Structures* **24**, 1444 (2006).

[26] Nitta, N. et al. *Journal of the Japan Institute of Metals* **64**, 1141-1147 (2000).

[27] Perez-Bergquist, A. et al. *Small* **4**, 1119-1124 (2008).

[28] Jones, K. S. & Santana, C. J. *J. Mater. Res* **6**, (1991).

[29] Williams, J. S. *Materials Science and Engineering A* **253**, 8-15 (1998).

[30] Singer, I. L., Murday, J. S. & Cooper, L. R. *Surface Science* **108**, 7-24 (1981).

[31] Sigmund, P. in *Sputtering by Particle Bombardment I: Physical Sputtering of Single-Element Solids,* (ed Behrisch, R.) 9-67 (Springer-Verlag, Berlin Heidelberg, Germany, 1981).

[32] Betz, G. & Wehner, G. K. in *Sputtering by Particle Bombardment II,* (ed Behrisch, R.) 11-90 (Springer-Verlag, Berlin, 1983).

[33] Moses, A. J. *The Practicing Scientists Handbook,* (Van Nostrand, New York, 1978).

[34] Lide, D. R. (ed) *CRC Handbook of Chemistry and Physics, 89th* (CRC, Boca Raton, 2008).

[35] Wei, Q., *Self-organized Nanoscale Patterning under Ion Beam Irradiation,* PhD Thesis, University of Michigan, Ann Arbor, 2009.

[36] Chakraverty, B. K. *Journal of Physics and Chemistry of Solids* **28**, 2413-2421 (1967).

[37] Chakraverty, B. K. *Journal of Physics and Chemistry of Solids* **28**, 2401-2412 (1967).

[38] Kumikov, V. K. & Khokonov, K. B. *Journal of Applied Physics* **54**, 1346 (1983).

[39] http://www.srim.org/

[40] Ziegler, J. F., Biersack, J. P. & Littmark, U. *The Stopping and Range of Ions in Solids,* (Pergamon, New York, 1985).

[41] Searcy, A. W. *Journal of Solid State Chemistry* **48**, 93-99 (1983).

Chapter 3

Nanospike Formation, Characterization, and Electrical Transport

3.1 Introduction and Background

The creation of III-V semiconductor nanostructures is of interest to the semiconductor community because of their possible use in a variety of different nanoscale devices. The small size and unique transport properties offered by nanostructures may provide significant advantages for specific electronic, optoelectronic, and thermoelectric applications. Semiconductor quantum dot based devices have already been demonstrated, and quantum dots continue to be intensely studied because of their possible uses in next generation high efficiency light emission and solar cell applications [1]. The previous chapter of this dissertation discussed the FIB creation of group III droplets, which may be used with a droplet epitaxy process to create semiconductor quantum dots. However, the size and "0-D" geometry of quantum dots limits the types of device architectures and corresponding applications in which they may be used. Higher aspect ratio nanostructures, such as nanowires, have also seen intense study and are being used in new nanoscale applications. These long, "1-D" structures are still physically constrained in 2 dimensions while being extended in the third. This allows them to be incorporated into 2-D and 3-D device architectures, and nanowires have been identified as promising for use in a variety of electronic, optoelectronic, and photonic applications [2-4]. Certain nanostructure may also provide improvements over bulk materials in thermoelectric applications either through quantum confinement effects due to their small size or because their structures may be designed to effectively scatter phonons and so lower thermal conductivity [5,6]. Specifically, high aspect ratio semiconductor nanowires have already been shown to conduct electricity effectively but also inherently possess poor thermal conductivity down their length due to their structure [7-9].

Long, 1-D nanostructures have most often been created using bottom-up growth methods such as metal particle catalyzed vapor-liquid-solid (VLS) growth and selected-area epitaxial growth using templates or masks [10]. However, ion beam methods may also be a viable route for the production of high aspect ratio III-V nanostructures. Broad beam ion irradiation of III-V semiconductor surfaces has previously been demonstrated as a method for creating high aspect ratio cone and pillar nanostructures in a variety of compound semiconductors, including GaAs [11], InP [12-14], and GaSb [15,16]. Ion irradiation may be a promising fabrication route for nanowire-like nanostructures because the irradiation process inherently damages and disrupts the semiconductor material. When used in a controlled manner, ion damage may be used to create nanostructures with locally disordered regions that may lower the thermal conductivity of the structure. As a synthesis route, ion irradiation also offers greater simplicity relative to nanowire growth methods that require catalyst deposition or masking. However, the ion beam based approaches reported previously in the literature allow for the creation of nanostructures over a wide area but do not allow for careful control of their placement. The structures reported in the literature also were made using homogenous starting material, and no heterostructure or doped device structures produced using an ion beam method have been reported. Both the creation of heterostructures and accurate nanostructure placement will be needed in order for ion beam created structures to be useful for many device applications. Additionally, unlike the case of traditionally grown nanowires, the transport properties of ion beam created high aspect ratio nanostructures have not previously been examined. For any nanostructure to be included in a functioning device its transport properties and the physical features that determine them need to be established. For a nanostructure intended for thermoelectric applications, this means that the electrical and thermal conductivity of the structures need to be characterized.

This work examines the creation, templating, and characterization of nanoscale semiconductor spike structures created by normal incidence Ga^+ FIB irradiation of undoped InAs/n+ InAs and undoped InAs/n+ InP film heterostructures. Similar structures have been produced using broad beam irradiation of GaAs [11], InP [12-14], and GaSb [15,16]. However, the creation of high aspect ratio nanostructures using FIB irradiation has not been previously reported for InAs or InP, and the only other case of similar structures created by a FIB method reported in the literature is GaAs cones produced by 70° off-normal FIB irradiation of GaAs [17]. Thus the nanoscale InAs spikes created in this work, deemed "nanospikes," are unique FIB created nanostructures. They were first accidently created and then discovered around regions of irradiated InAs films grown on InP being prepared for TEM examination by a FIB-liftout method in a dual-beam FIB/SEM system. As part of this work the optimum FIB irradiation conditions that result in nanospike creation were determined and a mechanism for their formation is proposed. It was also discovered that the locations where nanospikes form may be controlled by controlling film morphology, and a novel a two-step InAs/InP heterostructure pre-patterning and irradiation process was developed to allow nanospikes to be templated into arrays. That nanospike formation mechanism and templating method will be discussed with regards to the factors that control nanospike height, location, and density. The mechanism of nanospike formation and templating may be understood in terms of the different FIB responses and interplay between the different materials present. Structural characterization of nanospikes formed using both InAs alone and InAs/InP heterostructures was carried out by TEM, and the nanospikes were found to have an inhomogeneous structure with ion damaged regions. Electronic characterization of the nanospikes was carried out using an *in-situ* TEM nanoprobe technique, made necessary by the unique structures of the nanospikes. The results of that testing are analyzed with respect to spike geometry and discussed with regards to simple proposed nanospike electronic structures and work in the literature examining conduction in nanowires. This study is a first-of-kind, as no electrical testing of similar ion beam created nanostructures has been reported in the literature. All discussion is carried out in the context of understanding nanospike formation, structure, and transport properties so that their possible use for device applications may be considered. The ability to create nanowire-like structures using an ion beam method, controlling the locations at which they form, and the unique partially ion disrupted structure and corresponding transport properties of the nanospikes make the results of this work novel and of scientific and practical interest.

3.2 Experimental Methods

Nanospikes were produced by first growing undoped InAs films on <001> oriented n+ InAs and n+ InP substrates using molecular beam epitaxy (MBE) and then exposing the films to FIB irradiation. The n+ InAs wafers were purchased from Wafer Technology Ltd. with a manufacturer determined carrier concentration of $2.0\text{x}10^{18}$ cm^{-3} and resistivity of $3.8\text{x}10^{-4}$ Ω*cm. The n+ InP wafers were purchased from Crystacomm Inc. with a manufacturer specified carrier concentration of $4.8\text{x}10^{18}$ cm^{-3} and resistivity of 0.001 Ω*cm. 500 nm thick homoepitaxial InAs films and 200 nm and 500 nm thick InAs films on InP were grown at temperatures between $460<T< 470$ ˚C at a rate of 0.2-0.35 monolayers per second under an As_4 overpressure to give a V:III ratio of approximately 10. For more information on the MBE growth system used to produce InAs films for this study, please see section 1.5.1 of this dissertation. For the InAs/InP case, the growth temperature was varied in order to control film roughness, with samples grown at 460 ˚C being significantly rougher than those grown at 470 ˚C. Following growth, the samples were placed in the FEI Nova Nanolab dual-beam FIB/SEM system and irradiated using a normal incidence, 30 keV Ga^+ ion beam. FIB exposure was carried out using beam currents varying from 7 pA to 7 nA and spot dwell times varying from 100 ns to 10 µs. The FIB was scanned in a serpentine pattern over 5x5 µm areas repeatedly using a 50% spot overlap to provide even blanket irradiation of the entire exposed area. FIB current (and correspondingly beam spot size) and spot dwell times were varied in order to determine the optimum conditions for nanospike creation. For experiments using pre-patterned templates to control nanospike location, arrays of raised square mesas were first created by inputting the mesa array as a bitmap into the FIB control software and then scanning a 30 kV, 0.1 nA FIB to match the image. Spot dwell times were varied from 10 to 50 µm and the number of beam passes was varied to mill array patterns of different depths. Nanospikes were then created by irradiating the mesa arrays using the methods described above. Arrays of mesas with different dimensions were examined, and the details of specific experiments will be given in the description of the nanospike templating results.

SEM characterization of the nanospikes was carried out during and after their creation. The nanospike formation process was examined by blanking the FIB at regular intervals to allow SEM images to be taken, after which irradiation was resumed. This interval method allowed each stage of nanospike formation to be examined and also allowed the irradiation process to be monitored and stopped once the desired nanostructures had been created. Nanospikes created using both homoepitaxial InAs and InAs/InP heterostructures were examined by TEM. Nanospike cross-sectional samples for TEM analysis were created using a modified H-bar method [18]. This involved mechanically thinning a cleaved film cross-section to <100 μm thickness and then epoxying that thinned section to a flat Mo TEM hole grid. The cross-sectional sample was then placed into a dual-beam FIB/SEM system and a section of the sample was further thinned using 30 kV FIB cleaning cross-section patterns to a thickness of <5 μm. All sample thinning was carried out before nanospike creation in order to limit redeposition of sputtered material in the regions containing nanospikes. Nanospikes were then created by irradiating regions of the thinned area in the same manner as described above. Care was taken to align the thinned cross-section for normal incidence FIB irradiation. Templated nanospikes for TEM were created by pre-patterning a single row of square mesas in the thinned region and then irradiating to create nanospikes. Nanospikes created in this manner projected above the thicker region, allowing them to be viewed in transmission without the need for any additional FIB thinning following their production. Two SEM images showing a nanospike TEM sample prepared in the manner described above can be seen in Figure 3.1. On each TEM sample prepared in this way an area of the thinned region was further FIB thinned. This was done to provide an electron transparent bulk region to aid alignment of the sample to the desired zone-axis using electron diffraction. BF diffraction contrast imaging and HRTEM imaging of the nanospikes were carried out using both a JEOL 3011 TEM and a JEOL 2010F TEM. HAADF STEM imaging and STEM EDS composition analysis of the InAs/InP nanospikes were conducted using the JEOL 2010F system. TEM structural characterization of the nanospikes was generally carried out with the sample tilted to a [110]-type zone-axis.

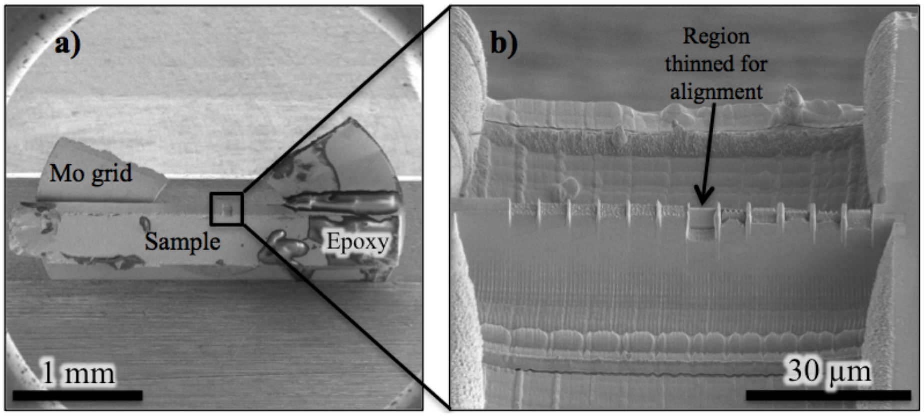

Figure 3.1: SEM images showing tilted views of a nanospike TEM sample. (a) shows a low magnification view of the entire sample and Mo TEM grid clamped into a SEM sample holder. (b) shows a higher magnification view of the region thinned for nanospike creation and TEM imaging.

Electronic characterization of the nanospikes was carried out in the JEOL 2010F TEM system using an *in-situ* TEM nanoprobe technique that allowed for simultaneous BF imaging and electronic testing of the nanospikes. Cross-sectional TEM samples for electrical testing were prepared in the same manner as described above, with some differences. Film cross-sections were mounted on Mo grids with a portion of the ring cut out to allow easier access to the sample area by the electrical probe (see Figure 3.1(a)). After nanospike creation on the FIB thinned region of the TEM specimens, a small amount of conductive colloidal carbon paint was placed on the portions of the sample epoxied to the Mo grid to ensure good electrical contact to the grid, as the epoxy electrically isolated the sample. In the case of InAs/InP heterostructure nanospike TEM samples, two additional FIB cuts through the InAs film were made before nanospike creation on either side of the region to be FIB thinned. These cuts through the InAs film into the underlying InP were made to ensure that the electrical path from the nanospikes to the carbon paint and Mo grid would go through the InP substrate and not through the InAs film to the Mo grid. Following creation, nanospike TEM samples were placed in a Nanofactory STM-TEM Electrical Probing double-tilt holder. That holder contained piezo-electric actuators designed to allow a conductive probe to be directed with nanoscale accuracy into contact with a TEM sample. For the testing conducted here, Tungsten needle probes produced by electrochemically etching polycrystalline Tungsten wire in 5 molar NaOH with a DC power supply were used. During testing the sharp probe was directed into the tip of a nanospike, completing a conduction path from the probe, through the sample, to the TEM holder. The voltage of the probe relative to the holder could then be ramped to positive or negative values up to ±10 V. The current through the probe to the holder was recorded externally during the voltage ramp, with the number of data points, collection time at each point, voltage ramp rate, and upper current limit set by the user for each test. The total time for each voltage ramp, regardless of the voltage range, was set to 10 seconds. The current limit for each test was kept to as low a range as possible because it was found that the level of system noise increased with current limit. For data recorded for the purpose of quantitatively analyzing nanospike electrical response a maximum current limit of 10 μA was used, corresponding to a fluctuating system noise level of ~10 nA at zero bias. Higher current limits with correspondingly higher noise levels were used for tests examining nanospike structural response to higher voltages and currents, resulting in an offset of the data to the noise level. Using this nanoprobe method the current-voltage (IV) response of individual nanospikes could be recorded while the nanospike was imaged. TEM imaging also allowed the point of contact between the W probe and nanospike to be unambiguously determined. Multiple sweeps through negative and positive voltages were conducted for each nanospike, with initial sweeps run over the same voltage range to ensure the repeatability of the IV response, and then later sweeps run at increasing voltages. This would eventually cause the nanospike to degrade or be destroyed. Due to the limitations of the nanoprobe holder, imaging could not always be carried out with the sample aligned to the [110] zone-axis. In those cases the sample was tilted as close to the zone-axis as possible and then tilted into a 2-beam condition near the zone-axis orientation. To provide a standard against which to compare the nanospike IV results, the nanoprobe was also directed into contact with FIB created In droplets on the InAs film surface and into bare regions of InAs and IV data was taken. All TEM nanoprobe testing was carried out with the direct assistance of Jacob Jokisaari of Professor Xiaoqing Pan's group at the University of Michigan- Ann Arbor.

3.3 Nanospike Creation Results and Formation Mechanism

Nanospikes were found to form as homoepitaxial InAs films and the underlying wafer were eroded by successive passes of the ion beam, with the formation and placement of the nanospikes depending strongly on the irradiation parameters and the morphology of the ion-eroded InAs. Attempts were made to create nanospikes using a variety of different FIB irradiation parameters, and low beam currents and short spot dwell times were found to aid nanospike creation. Figure 3.2 shows regions of homoepitaxial InAs irradiated using several different FIB parameters and similar ion doses, with only Figure 3.2(d) actually showing nanospike production. No nanospikes were ever produced using beam currents greater than ~50 pA or dwell times longer than 1 μs. The tallest and greatest number of nanospikes was produced using an approximately 7 pA beam and 100 ns dwell time. Using these optimum beam parameters and 12000 passes of the ion beam (corresponding to an ion dose of ~1.5×10^{17} ions/cm^2), nanospikes with a density of 2.84 ±0.8 spikes/μm^2 could be produced using homoepitaxial InAs. Final nanospike height depended on how early in the erosion process nanospikes began to form and the total number of ion beam passes. Using 12000 beam passes, InAs nanospikes were produced in a wide range of heights with an average of 400 ±200 nm and an average diameter measured at half maximum height of 120 ±25 nm. The tallest nanospike created using homoepitaxial InAs and 12000 beam passes was ~975 nm. Increasing the number of beam passes causes more nanospikes to form and causes existing nanospikes to increase in height up to a maximum of ~1 μm.

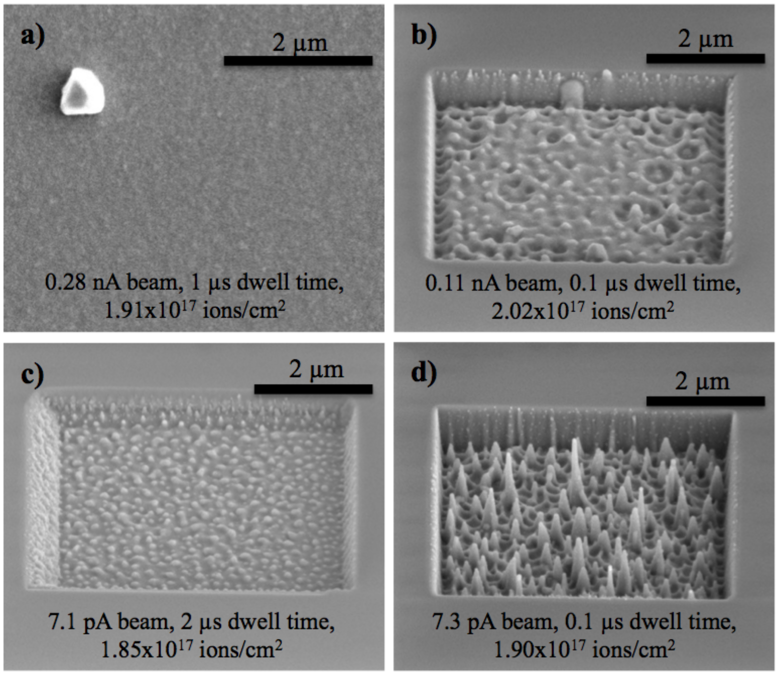

Figure 3.2: SEM images of InAs regions 30 kV FIB irradiated using different beam currents and dwell times. The beam current, dwell time, and ion dose are given on each image. Images (b)-(d) were taken with the sample tilted 52° off the electron beam normal.

Figure 3.3 shows a region of homoepitaxial InAs film irradiated with the optimum beam conditions identified above at various steps through the nanospike creation process. Shortly after the start of FIB irradiation, In droplets form on the InAs film due to preferential sputtering of As [19,20] (Figure 3.3(a)) and then migrate randomly across its surface. With continued FIB erosion and increasing amounts of excess In present the film forms ripples that result in a raised, web-like pattern of In globules and recessed areas (Figure 3.3(b)). That rippling transition may be caused by changes in sputter yield due to variation in local curvature [21] and due to local shadowing from the presence of excess surface In, and often started at a large In droplet or the edge of the irradiated region. Some of the Indium droplets traveling across the uneven eroded surface eventually come to apexes in the ripple pattern, where they become stationary. As a result the stationary droplets mask the underlying material, causing nanospikes to form and continue to grow at those locations as the surrounding material is milled away (Figure 3.3(c)). As erosion proceeds the rippled morphology persists and additional nanospikes form as In droplets come to other apexes at later times (Figure 3.3(d)). This process of continuous nanospike formation with ion erosion results in a random distribution of InAs nanospikes with a broad range of heights (Figure 3.3(e)). A higher magnification image of some of the nanospikes created can be seen in Figure 3.3(f).

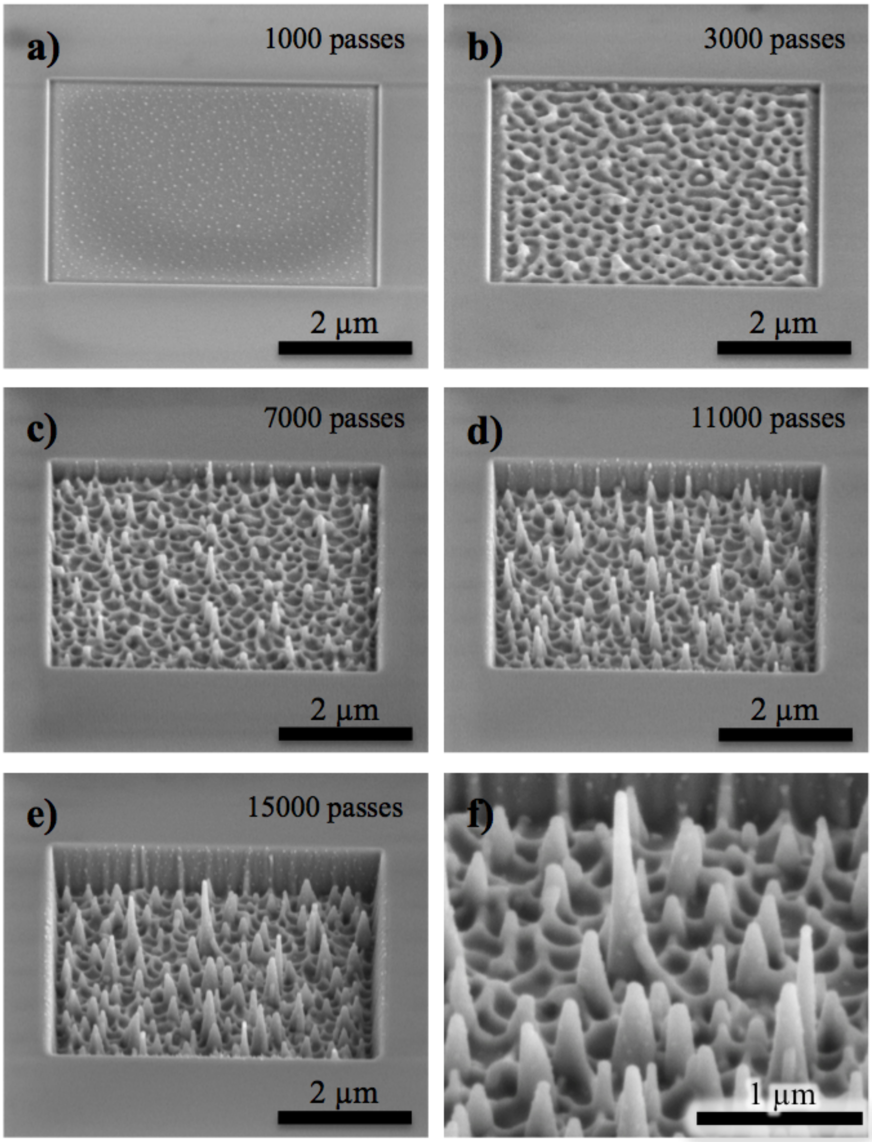

Figure 3.3: SEM images showing a region of homoepitaxial InAs at various points during the nanospike creation process. The number of FIB passes that the area had received prior to that image being taken is given in the upper right-hand corner of the image. Image (f) shows a higher magnification view of the nanospikes in (e). The nanospikes were created using a 30 kV 7.3 pA FIB and 100 ns spot dwell time.

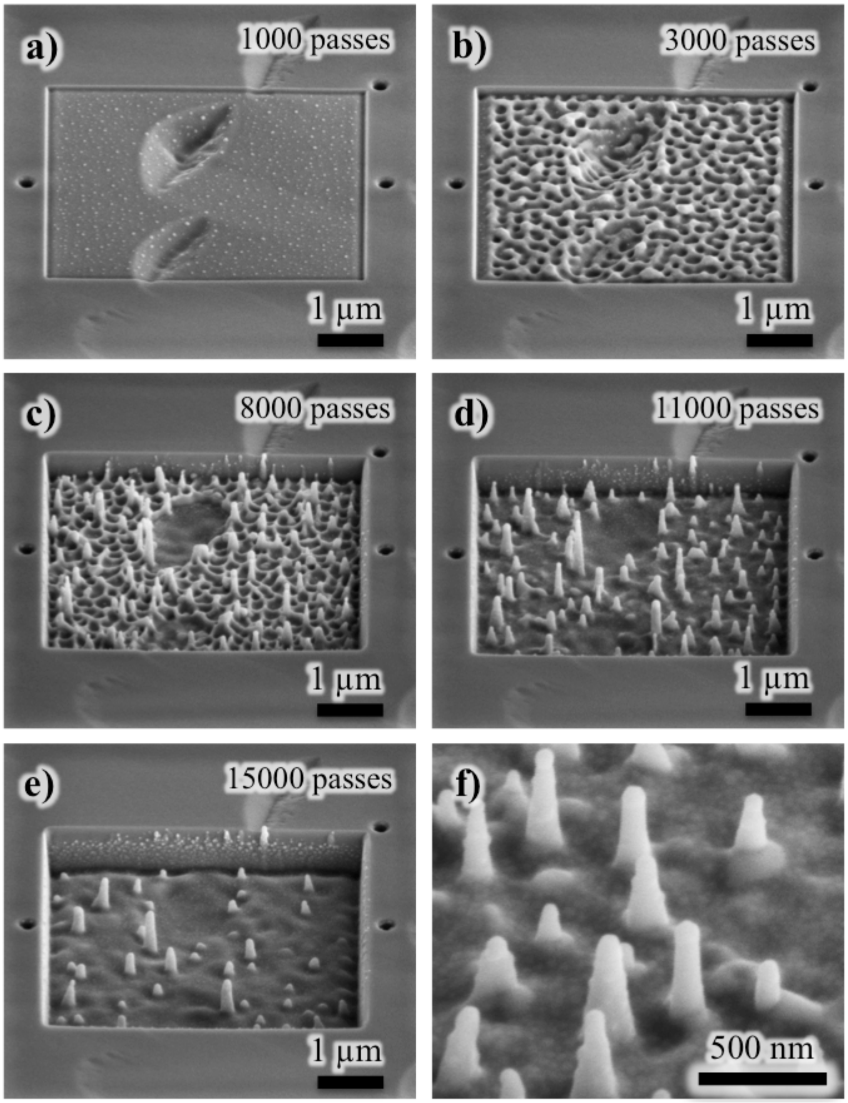

Figure 3.4: SEM images of nanospikes formed by irradiating a rough InAs film grown on InP. (a)-(e) show a region of InAs/InP at various points during the nanospike creation process, with the number of beam passes delivered before imaging indicated in the upper right hand corner of each image. The three circular holes outside the irradiated region in those images were milled before irradiation for image alignment purposes. These nanospikes were created using a 30 kV 7.3 pA FIB and 100 ns spot dwell time. (f) shows a higher magnification image of nanospikes representative of those produced in this study using an InAs/InP heterostructure.

Nanospikes that are formed by FIB irradiation of an InAs/InP heterostructure are produced in a manner similar to the homoepitaxial InAs case, but with some important differences. Figure 3.4(a) shows a rough, faceted, 500 nm thick InAs film on InP shortly after the start of irradiation. As in the homoepitaxial InAs case, In droplets form on the

InAs film due to preferential sputtering and with continued FIB exposure the InAs film forms a raised, web-like pattern (Figure 3.4(b)). As the underlying InP becomes partially exposed, nanospikes form and increase in height at locations where large In droplets become stationary on the web-like pattern (Figure 3.4(c)). New nanospike formation stops at the point where all of the InAs has been milled away (Figure 3.4(d)). Once the InAs film has been completely milled away nanospike height increase slows and eventually width and height begin to decrease as the spikes are eroded by the ion beam (Figure 3.4(e)). No large In droplets or nanospikes were ever observed to form on regions of exposed InP. As with the homoepitaxial film, lower beam currents and dwell times resulted in taller and more densely packed nanospikes. The tallest and greatest number of nanospikes were created using an approximately 7 pA beam and 100 ns dwell time, requiring in excess of 10000 beam passes to fully erode a 500 nm InAs film. Using these optimum beam parameters, an average density of 1.98 ±0.5 spikes/μm^2 was produced. On average final nanospike height increased with InAs film thickness. Using a 500 nm InAs starting film, nanospikes were created in a wide range of heights with an average of 300 ±100 nm and an average diameter measured at half maximum height of 110 ±30 nm. The maximum observed nanospike height was approximately 875 nm, greater than the initial 500 nm thickness of the InAs film, demonstrating that in some cases nanospikes continue to become taller after erosion of the InAs film is complete. This occurs because the nanospike's In droplet mask still requires a finite amount of time once the surrounding InAs has been removed to be sputtered away, and so will still continue to protect the nanospike for a short period.

The physical mechanism of nanospike formation is nearly the same for nanospikes produced using both homoepitaxial InAs and InAs/InP heterostructures. In both cases nanospike density and placement are determined by surface energy effects and differences in material sputtering behavior, and these properties are determined locally by InAs film morphology and the quantity of excess In present. The formation of nanospikes on an InAs/InP heterostructure deviates from the InAs case in that the different sputtering rates of InAs and InP and the location of the InAs/InP interface also affect nanospike creation. Figure 3.5(a)-(c) illustrates the mechanism of nanospike formation as it pertains to both the InAs and InAs/InP cases, while Figure 3.5(d) illustrates the role of the InAs/InP interface for the heterostructure case. With the start of FIB exposure, As preferentially sputters away and leaves an excess of In which eventually forms In droplets on the InAs surface (Figure 3.5(a)), and those droplets become mobile due to ion beam induced migration. As InAs film erosion continues, a web-like ripple pattern forms and the In droplets continue to migrate across this uneven surface. The surface likely becomes uneven because of local instabilities caused by local changes in curvature and composition due to In enrichment. Eventually some of the In droplets reach the apexes of the ripple pattern and become constrained within the area of the apex (figure 3.5(b)), masking the underlying film and allowing nanospikes to form (figure 3.5(c)). Droplets are likely driven toward and held at apexes in the rippled InAs film in order to reduce their contact area with the InAs and so reduce their interfacial surface energy. Tilting the sample off normal relative to the FIB resulted in nanospikes being produced tilted by the same amount, further verifying that an etch-masking mechanism is responsible for nanospike creation. Figure 3.6 shows nanospikes created by tilting an InAs/InP heterostructure surface 30° from the direction normal to the ion beam. In the case of formation on homoepitaxial InAs, nanospikes grow under stationary In droplets so long as the In droplet is maintained. The In droplet "etch-mask" is likely resupplied by excess indium atoms from preferential sputtering of the III-V material, preventing it from being quickly sputtered away. This group III "self-sustained etch-mask" mechanism has previously been proposed in order to explain the formation of Ga capped cones on ion irradiated GaSb [16,22]. There may be an upper limit to nanospike height imposed by the ability of excess In atoms to reach the droplet at the top of the spike faster than the droplet is being sputtered away. For a homoepitaxial InAs film, additional nanospikes can form in the irradiated region at later times as more In droplets become stationary and act as masks. This is not the case for an InAs/InP heterostructure. Experimentally it has been shown that once the underlying InP is exposed the location of the InAs/InP interface and the different FIB sputtering behaviors of InAs and InP control the locations at which large In droplets can be present to form nanospikes. As the InAs/InP surface is eroded the large In droplets needed for nanospike formation are driven from the InAs/InP interface in order to remain on the InAs. This likely indicates that the interfacial surface energy of a droplet on InAs is likely lower than on InP.

Additionally, large In droplets were only able to form and persist on the InAs. As has been previously reported in chapter 2 of this dissertation, FIB sputtering of InAs is expected to produce more excess In atoms per ion (see Table 2.3) and produce much larger In droplets than sputtering of InP [20]. Indeed, only small group III droplets (<45 nm) were observed on regions of exposed InP, while larger droplets (>70 nm) which could create nanospikes where produced on the InAs films. This along with the absence of any new nanospike formation on InP indicates that sputtering of InP alone is unable to produce or sustain In droplets large enough for nanospike formation. The result is that exposure of the underlying InP substrate acts as a local inhibitor for nanospike formation, and movement of the InAs/InP interface as the InAs film erodes acts to constrain the regions in which new nanospikes can form. Any initial film roughness causes the InAs to ripple and become uneven more quickly and exposes the InP substrate sooner, thus playing a significant role in determining final nanospike location. For the heterostructure case, once the InAs film is milled through nanospike height increase slows and eventually stops (figure 3.5(d)). This is again likely because the InP substrate etches more slowly and produces fewer excess In atoms than InAs [20], and so is incapable of re-supplying the droplet etch-mask faster than it is being sputtered by the ion beam. Upon exposure of the InP substrate, nanospikes may grow for a limited time while their masking droplet still protects them, but as their droplet is sputtered away they cease to grow and also begin to be sputtered away. As a result, the thickness of the InAs film present when nanospike formation starts acts to control the maximum height a nanospike can reach.

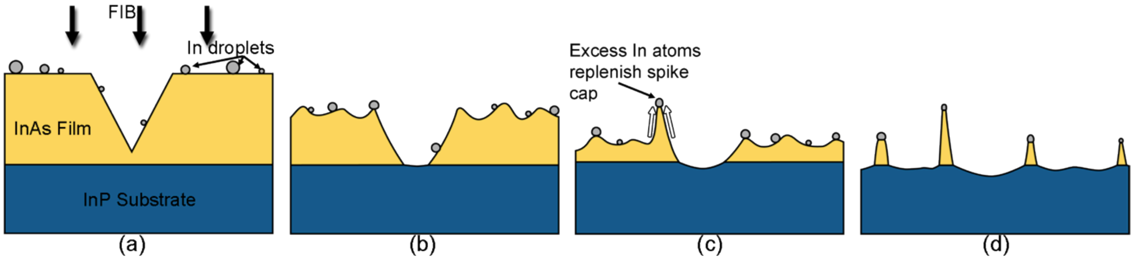

Figure 3.5: Schematic depicting the process of nanospike formation. (a) FIB irradiation causes In droplets to form on a rough InAs film. (b) As irradiation continues the InAs surface becomes uneven and rippled. (c) An In droplets becomes stationary at an apex of the film, allowing a nanospike to form. (d) More nanospikes will form as other In droplets become stationary until the InAs film is eroded away and the underlying InP substrate is fully exposed.

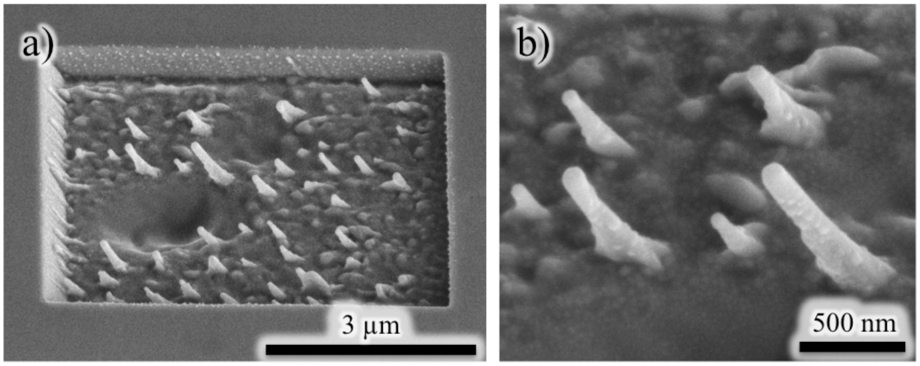

Figure 3.6: SEM images of tilted nanospikes produced by tilting an InAs/InP heterostructure to 30° off normal from the FIB.

3.4 Nanospike Templating

The mechanism for nanospike formation proposed above suggests that the locations at which nanospikes form may be controlled by templating the starting InAs surface to limit the locations where In droplets come to rest as FIB erosion proceeds. FIB pre-patterning of homoepitaxial InAs was observed to partially control the locations at which nanospikes form. Figure 3.7(a) shows a group of 1x1 μm mesas created by FIB milling an InAs sample. Figure 3.7(b) shows that same area following 9000 passes with a 7.3 pA FIB beam using a 100 ns spot dwell time, resulting in the formation of nanospikes in a pattern very roughly matching the original pre-patterned grid. The nanospikes formed do not sit in the original mesa centers but do sit in the original areas defined by the mesa rows, and in some cases more than one spike can be seen per mesa. This partially controlled placement is the result of the mesa pattern limiting the area over which In droplets can form and migrate and the result of more rapid sputtering from the mesa edges acting to create an inwardly receding boundary that drives In droplets towards the mesa interior. In the case of homoepitaxial InAs the surface in the patterned area remains rippled and new In droplets are produced as erosion continues both on the FIB patterned mesas and in the regions between them. As a result, prolonged FIB erosion causes secondary nanospike formation between the mesas of the original template, disrupting the nanospike pattern. This effect is particularly pronounced in cases where the original mesa pattern was milled less deeply than as pictured in Figure 3.7(a). In those experiments the mesa pattern was quickly removed by FIB milling and nanospike formation was able to take place unrestricted across the pre-patterned region. Thus pre-patterning and exposure of homoepitaxial InAs allows only limited nanospike templating to occur. A limited number of experiments were conducted where the spot dwell time and number of FIB passes used to generate mesa patterns were varied, but changing pre-patterning parameters did not significantly improve the degree of nanospike templating that could be achieved using homoepitaxial InAs alone.

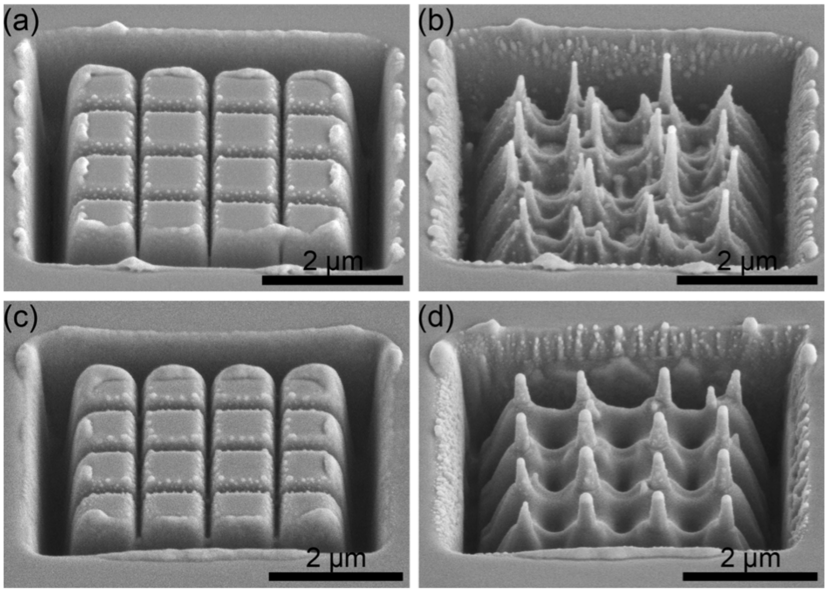

Figure 3.7: SEM images of areas of both homoepitaxial InAs and InAs/InP heterostructure intended for templated nanospike creation. (a) shows an array of raised mesas created by patterning homoepitaxial InAs. (b) shows that same array following 9000 FIB passes, with InAs nanospikes visible. (c) shows an array of raised mesas created by patterning a 500 nm InAs/InP heterostructure. (d) shows that same InAs/InP array following 9000 ion beam passes with nanospikes visible. In both cases the mesa templates were created using the same beam parameters and the templates were irradiated using the optimum beam parameters for nanospike creations specified earlier.

Nanospike formation using pre-patterned InAs/InP heterostructures allows for more accurate and reproducible nanospike templating. Figure 3.7(c) shows a group of 1x1 μm mesas created by FIB milling an InAs/InP sample, and figure 3.7(d) shows that same area following 9000 passes of a 7.45 pA FIB beam using a 100 ns dwell time, resulting in the creation of one large primary nanospike at each original mesa location. This is the best-case scenario, which results from using a deeply milled and sharply defined 1x1 μm mesa array. By pre-patterning and FIB irradiating InAs/InP it was found that nanospike formation can be repeatably confined to the center of those raised areas defined by the original mesa template, and the number of nanospikes per mesa center can be varied from approximately 1-3 depending on pre-patterning beam parameters and mesa size. Recessed areas in a FIB pre-pattern define the locations at which the InAs/InP interface and underlying InP substrate will first be exposed, and because nanospikes will not form on InP this acts to limit nanospike formation to the raised mesas which have thicker regions of InAs film initially present. During irradiation the mesa edges are rapidly milled away and the InAs/InP interface is driven towards the center of the mesa. This acts to drive any large In droplets that form to the mesa center and so directs nanospike formation to the center of each original mesa location. The pre-patterning process thins or completely removes the InAs film between the mesas, resulting in early exposure of the InP substrate and so prevents secondary nanospike formation in between mesas. These mechanisms for controlling nanospike location place an inherent limit on the size and types of pre-patterned features that may be used to produce accurately templated nanospikes. If the mesas are made increasingly large they will cease to effectively control the movement of the In droplets and multiple spikes at random locations within the mesa area may form. Likewise, if the mesa size is reduced too much, rapid milling from the mesa edges and a very small initial amount of InAs material per mesa from which to form nanospikes act to limit nanospike creation and the templating effect. Figure 3.8 shows some additional examples of attempts to template nanospikes using pre-patterned InAs/InP heterostructures. Figures 3.8(a) and (b) shows a template of approximately 400x400 nm mesas milled using a 50 µs spot dwell time before and after 8000 FIB passes respectively. This was the smallest mesa size used to successfully create nanospikes with some location templating, and as can be seen from Figure 3.8(b) the nanospikes produced are not uniform in size and there are not nanospikes at every mesa location. At this lower limit changing pre-pattering parameters slightly also has a large effect on templating. Figure 3.8(c) shows mesas of similar surface area to those in Figure 3.8(a) but milled more deeply and using more FIB passes and a shorter spot dwell time of 10 µs. Figure 3.8(d) shows that same mesa array following 5000 FIB passes. Spike structures are present matching the mesa template, but those structures were created only by rapid recession of mesa edges inward rather than due to the self-masking nanospike formation process. Figures 3.8(e) shows an array of 1x1 μm mesas milled less deeply than those pictured in Figure 3.7. Figure 3.8(f) shows those mesas following 9000 FIB passes. In this case there are nanospikes corresponding to each original mesa location, but because of the shallower original mesa pattern there are multiple spikes on many of the mesa sites and more variance in nanospike size. Further optimization of the templating process may result in a method for creating more uniformly sized and closely spaced nanospike arrays.

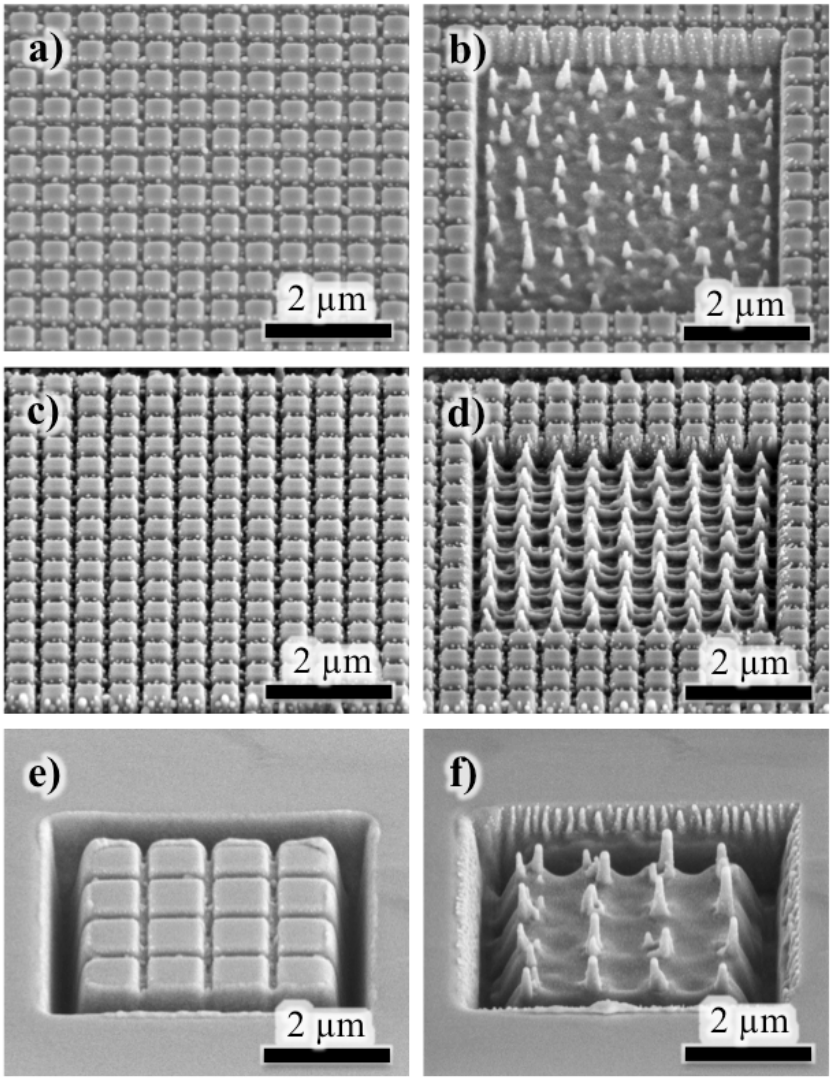

Figure 3.8: SEM images of regions of InAs/InP patterned with mesa arrays before and after FIB irradiation to create templated nanospikes. Images (a), (c), and (e) show regions before FIB blanket irradiation, and (b), (d), and (f) respectively show those same regions after irradiation.

3.5 Characterization of Nanospike Structure

In order to better understand their structure and later their electrical properties, nanospikes created both with homoepitaxial InAs films and InAs films grown on InP were characterized in cross-section by TEM. [110] BF, HRTEM, and HAADF STEM imaging revealed that the InAs and InAs/InP nanospikes have very similar structures. TEM imaging of non-templated, randomly placed InAs and InAs/InP nanospikes revealed that all the spikes examined were capped with an amorphous or partially crystalline In metal tip, and many of the spikes were decorated with additional In droplets. All the nanospikes possessed a heavily ion damaged outer layer that was amorphous with small regions of local crystallinity. The cores of the nanospikes below the outer damaged layer ranged from highly damaged and only partially crystalline to single crystalline. The damaged shell is due to ion irradiation and could likely be recrystallized by annealing under an arsenic overpressure [23,24]. However attempts to do this by placing nanospikes in an arsenic overpressure in the MBE chamber used in this study resulted in large changes in nanospike shape and loss of material. It is possible in these experiments that the annealing temperatures during As_4 exposure, which ranged from 200 to 450 ˚C, were too high and caused material loss. Disrupted and partially crystalline cores may occur in cases where the In droplet at the top of the nanospike did not remain completely stable in size and location during nanospike creation, resulting in intermittent exposure of the nanospike core to ion irradiation and damage.

Figure 3.9 shows a series of [110] BF images taken from two different TEM samples of nanospikes with a range of core structures created using homoepitaxial InAs, with darker areas in the spikes indicative of regions of crystallinity that scattered the electron beam strongly. Both TEM samples were created using nearly identically grown homoepitaxial InAs films and the same TEM preparation method. Figure 3.9(a) shows a lower magnification image of many InAs nanospikes. The taller InAs nanospike in Figure 3.9(b) shows a highly damaged and fully disrupted core, the taller nanospike in Figure 3.9(b) shows a core that is partially crystalline up its length, and Figure 3.9(d) shows a nanospike that has single crystalline lower half (dark contrast) and fully disrupted upper half (light contrast). Figure 3.10 shows another nanospike with a partially single crystalline core along with several HRTEM images showing (b) that spike's partially crystalline In droplet cap, (c) the disrupted region directly below the cap, and (d) a boundary between the ion damaged sidewall and single crystalline region of the nanospike. Figure 3.11 shows a series of [110] BF images taken of nanospikes created using InAs/InP heterostructures displaying a range of spike core structures similar to the InAs case. The primary nanospike in Figure 3.11(a) has a fully disrupted core, the primary spike in (b) has an only partially disrupted core, and most of the cores of the two nanospikes in (c) are single crystalline. In cases where a nanospike core was single crystalline it retained the original zinc blende structure of the starting film and was free of extended defects such as the twin boundaries or stacking faults commonly observed to span the width of semiconductor nanowires produced by VLS growth [25]. However, the boundaries between the crystalline cores and outer damaged layers were locally ringed with defects. In cases where the bases of the InAs/InP nanospikes were visible in transmission they were found to be at or below the InAs/InP interface, which remained sharp and free of defects.

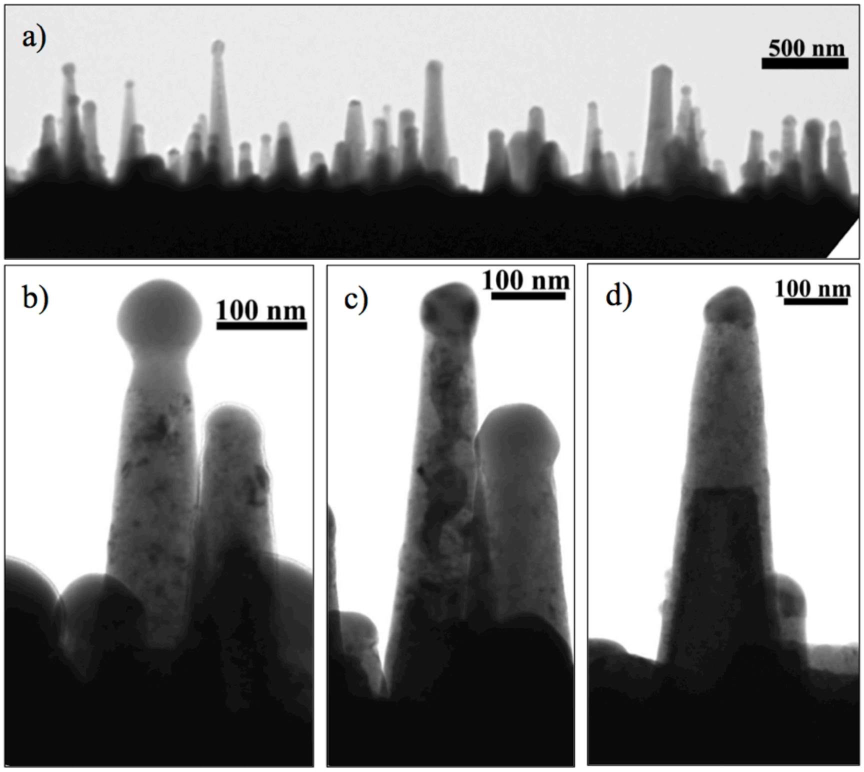

Figure 3.9: [110] BF TEM images of homoepitaxial InAs nanospikes. (a) shows a low magnification image of a region with many nanospikes. (b), (c), and (d) show InAs nanospikes with fully disrupted, partially disrupted, and partially single crystalline cores respectively.

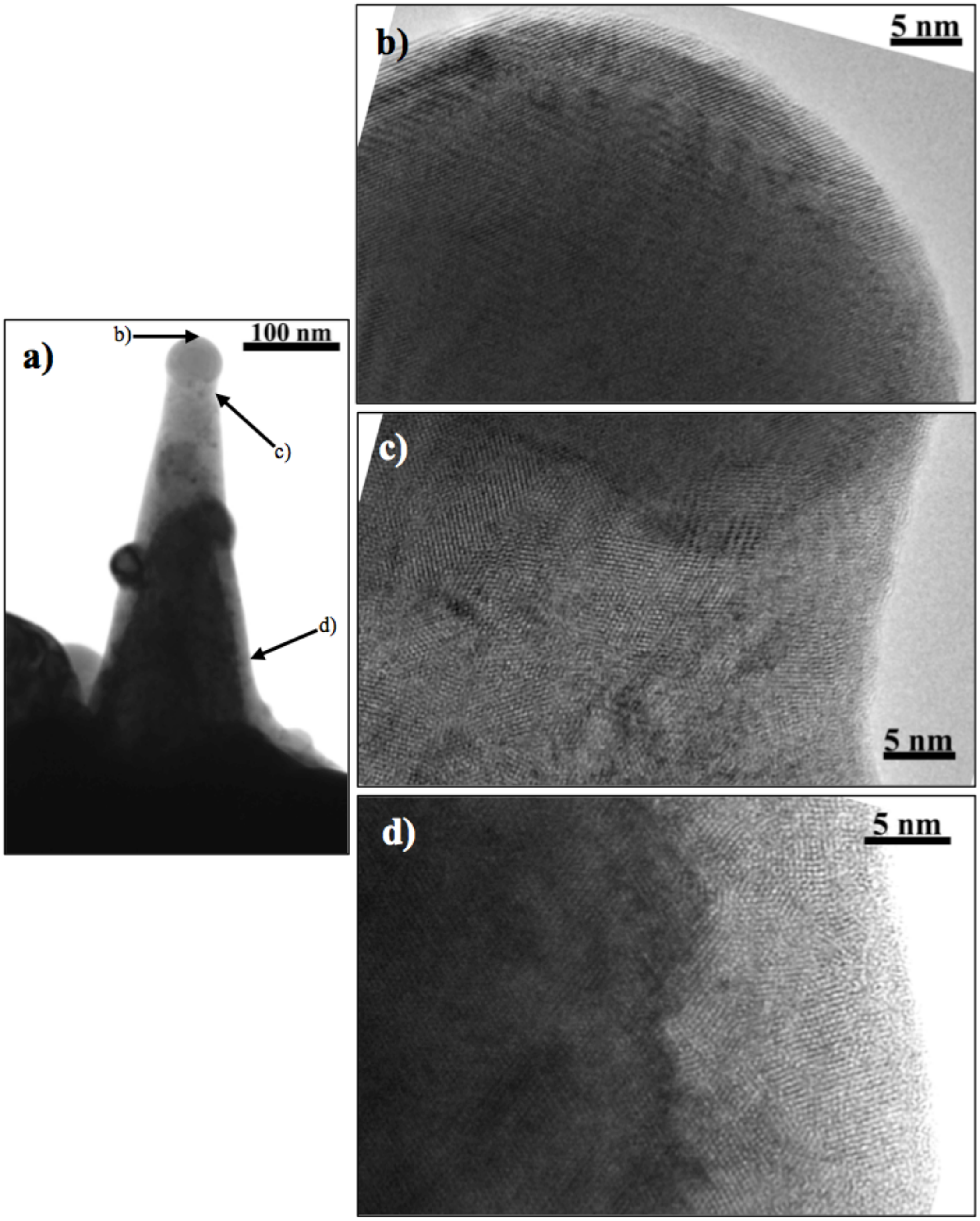

Figure 3.10: [110] BF and HRTEM images of an InAs nanospike. (a) shows a BF image of a nanospike with lower single-crystalline core and ion damaged upper region. (b) shows a HRTEM image of the spike cap, (c) shows a HRTEM image of the ion-disrupted region directly below the cap, and (d) shows the ion damaged sidewall and single crystalline core of the spike's lower half.

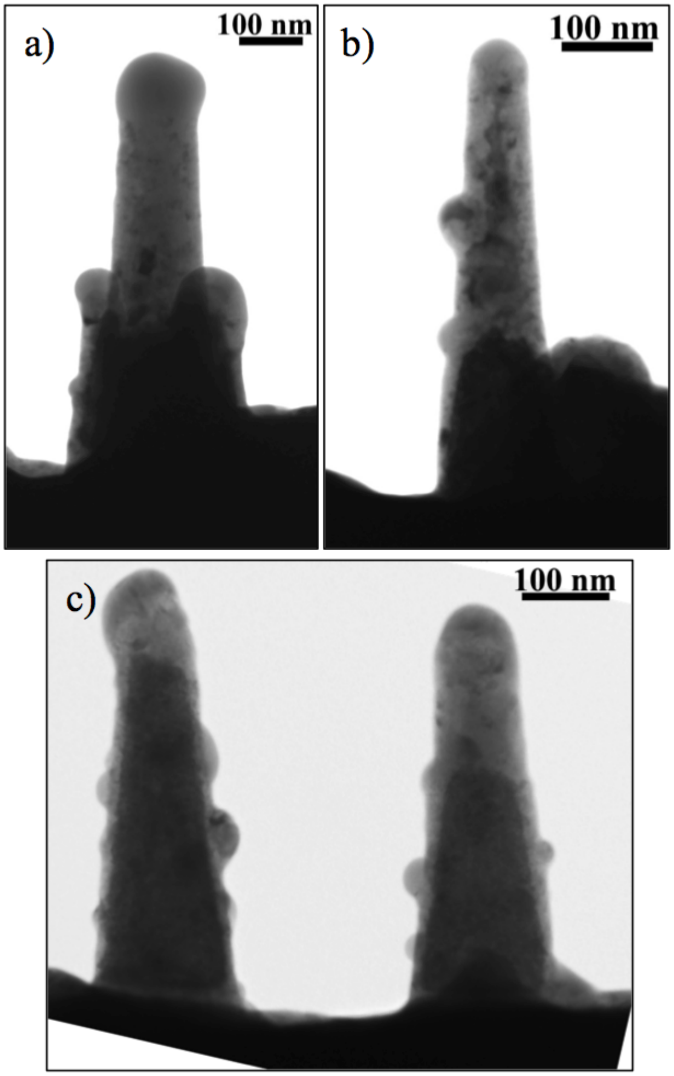

Figure 3.11: [110] BF TEM images of nanospikes formed by irradiation of an InAs/InP heterostructure. (a), (b), and (c) show InAs/InP nanospikes with fully disrupted, partially disrupted, and primarily single crystalline cores respectively.

InAs/InP templated nanospikes created by FIB irradiation of a single row of 1x1 μm mesas pre-patterned in the thinned region of the same TEM specimens used to examine randomly placed nanospikes were also imaged in cross-section. No templated homoepitaxial InAs nanospikes will be described here, as too few were successfully generated on TEM specimens to allow for accurate description as a group. The templated InAs/InP nanospikes possessed the same general structural features, such as a capping In droplet and ion-damaged out layer, as the non-templated randomly placed InAs/InP nanospikes, with the exception that all of the templated nanospikes examined by TEM possessed single crystalline cores. Figures 3.12 (a), (b), and (c) show [110] BF images of templated InAs/InP nanospikes with clearly visible crystalline cores. Figure 3.12(d) shows a HAADF STEM image of the spike pictured in (c). In that HAADF image bright features indicate areas that scattered the electron beam more strongly, and the crystalline core, In cap, and InAs/InP interface are readily visible. Figure 3.13 shows images of the same templated nanospike pictured in Figure 3.12(c) and (d). Figure 3.13(a) shows a BF image of the nanospike with the major structural features labeled, Figure 3.13(b) shows a HRTEM image of the top of the spike's crystalline core, and Figure 3.13(c) shows a HRTEM image of the sidewall boundary between the spike's crystalline core and ion damaged out layer. The long-range order of the lattice fringes visible in darker region of Figure 3.13(c) clearly indicate that the core is single crystalline, and defects in that core can be seen at the boundary with the outer layer. As was the case with the non-templated nanospikes, the single crystalline cores of the templated InAs/InP nanospikes retained the zinc blende structure and orientation of the original InAs film and were free of extended defects. STEM/EDS chemical analysis was also carried out on templated InAs/InP nanospikes to verify the composition of their various structural components. Figure 3.14(a) shows a HAADF image of the same templated spike shown in the previous figure, and (b)-(e) show STEM/EDS elemental maps of different atomic species, with the element and electron shell used to create the map indicated on each image. Figure 3.15 shows the raw results of a STEM/EDS line scan of 200 evenly spaced collection points taken down the length of that same spike. Elemental counts are plotted versus point down the spike and the location and direction of the line scan are shown in the inset HAADF image. The EDS results in Figures 3.14 and 3.15 indicate that droplet cap is Indium, that the spikes are composed of InAs, and that the InAs/InP boundary remains sharp following FIB irradiation. Based on EDS line scans across the width of the same templated nanospike it appears that the ion damaged nanospike shell may be slightly As depleted relative to stoichiometric InAs, which might be expected as As preferentially sputters from InAs under FIB irradiation [19,26]. However, due to the extremely low EDS signal from those scans, this could not be determined conclusively. All of the EDS data presented here is qualitative, and due to the low EDS signal obtained no attempts to quantitatively determine nanospike composition by STEM/EDS were made.

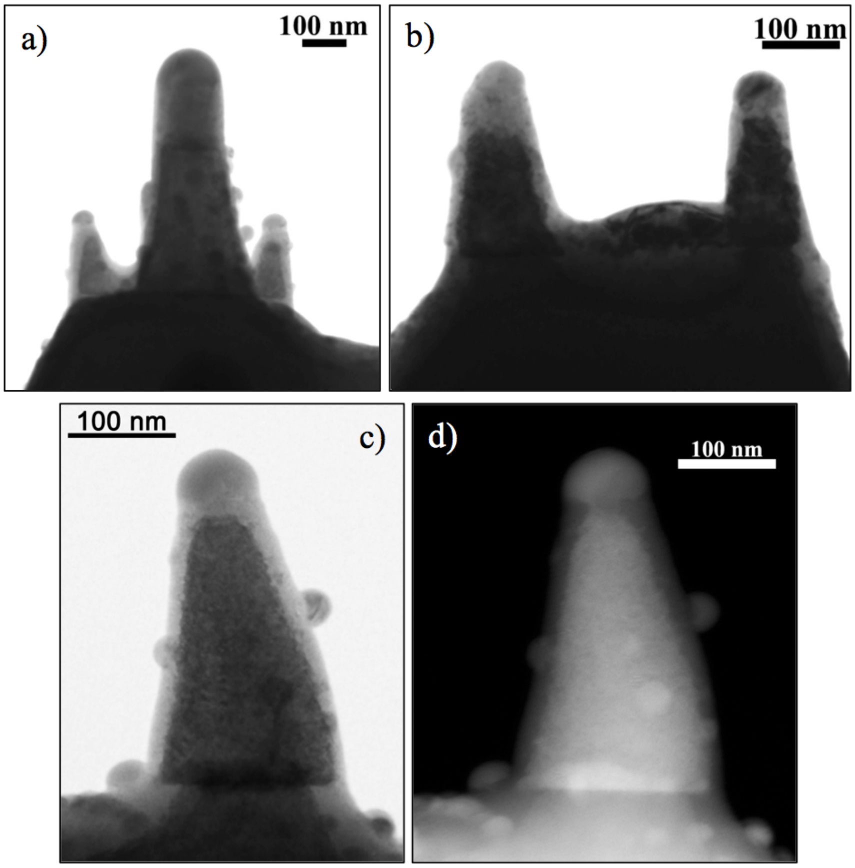

Figure 3.12: [110] TEM images of templated nanospikes formed by irradiation of an InAs/InP mesa pattern. (a), (b), and (c) show BF images of nanospikes with single crystalline cores. (d) shows a HAADF STEM image of the same nanospike shown in (c).

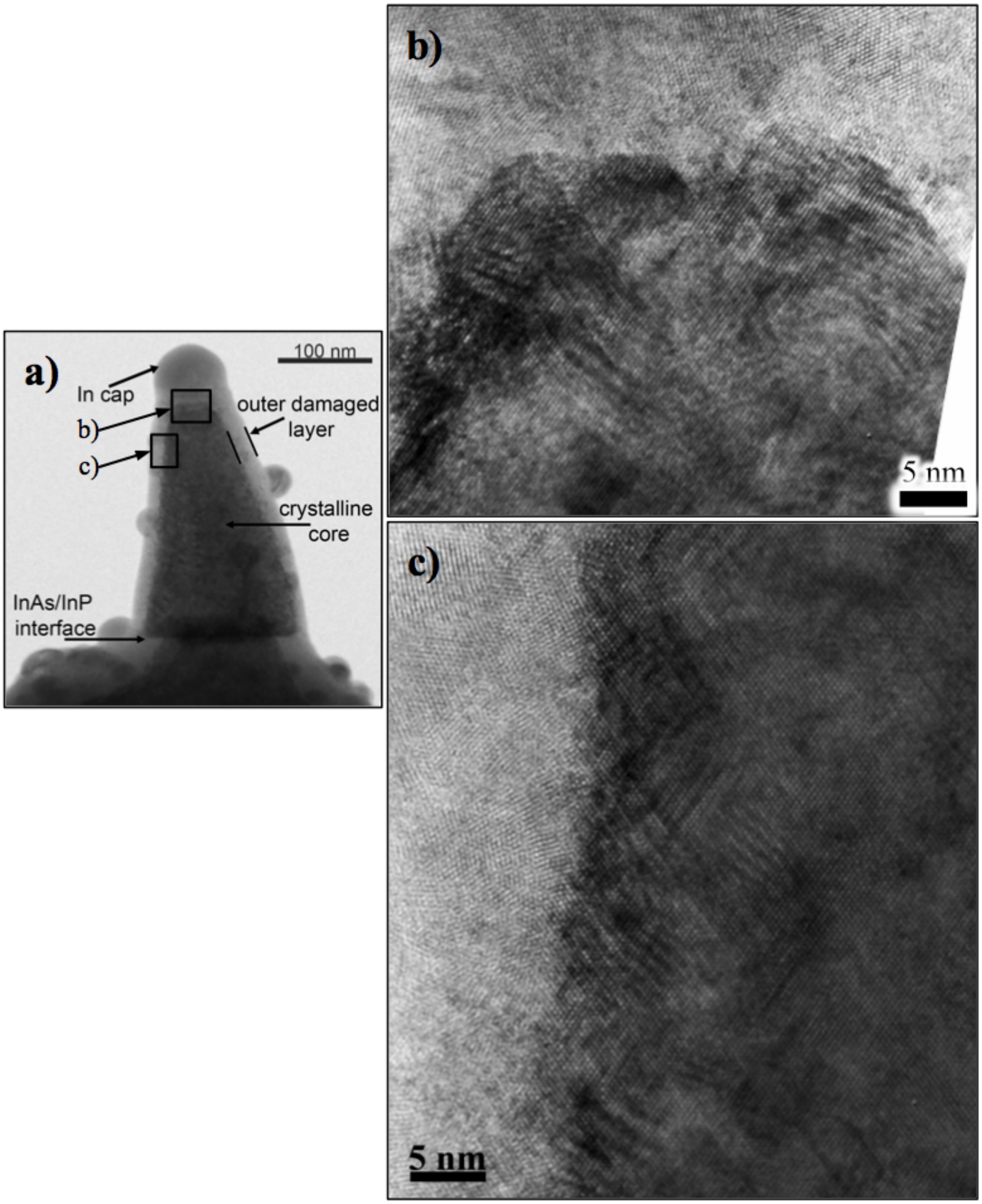

Figure 3.13: [110] TEM images of a templated InAs/InP nanospike. (a) shows a BF image of the spike with its major structural features labeled and the locations that images (b) and (c) were taken. (b) shows a HRTEM image of the interface at the top of nanospike's single crystalline core. (c) shows a HRTEM image of the nanospike's core sidewall and ion damaged outer layer.

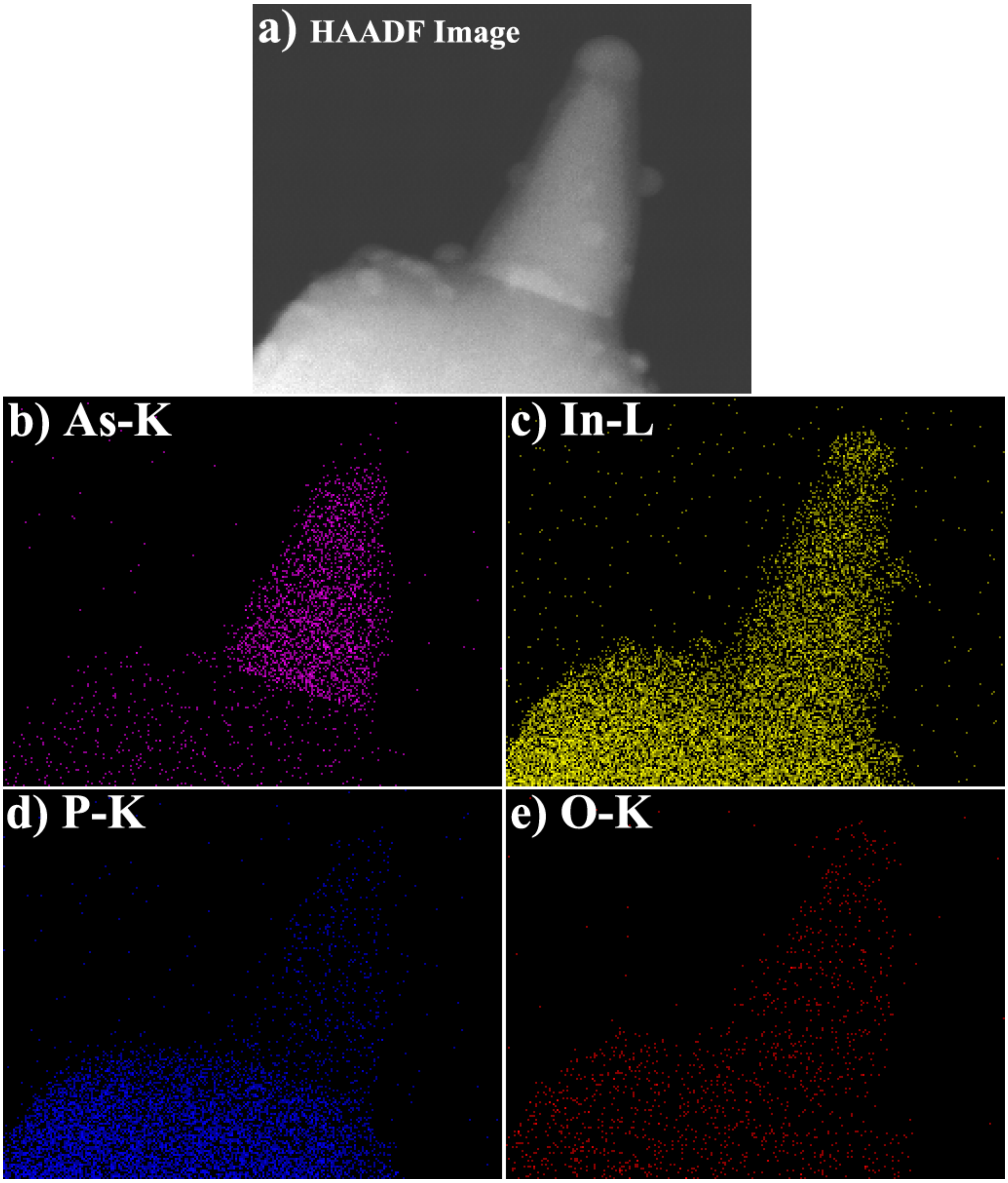

Figure 3.14: (a) shows a STEM HAADF image of the same templated InAs/InP nanospike pictured in Figure 3.13. (b)-(e) show STEM/EDS elemental maps of that nanospike. The element and electron energy shell used to create each map are indicated in the upper left-hand corner of each image, with the number and brightness of the colored pixels indicating the relative concentration of that element at each location.

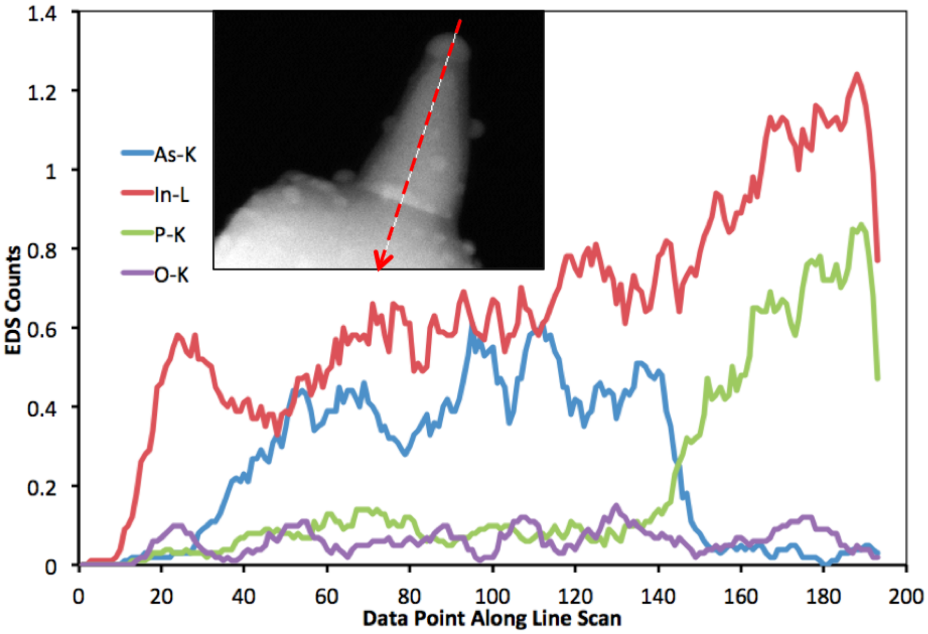

Figure 3.15: Plot showing the results of a 200 point STEM/EDS line scan taken down an InAs/InP templated nanospike starting at the In cap and moving towards the InP substrate. Raw EDS counts for each elemental peak examined are plotted versus scan point, and the physical length and direction of the line scan are indicated in the inset HAADF image by the dotted-line arrow.

3.6 Nanospike Electrical Characterization

With the goal of determining the suitability of nanospikes for nanoscale electronic and thermoelectric applications, following structural characterization the electrical properties of the nanospikes were examined using an in-situ TEM nanoprobe technique. As mentioned in the experimental methods section above, electrical characterization was carried out using a specialized TEM holder capable of directing a sharp tungsten nanoprobe into contact with individual nanospikes. The voltage of the probe relative to the holder could then be ramped and the electrical current passed from the probe through the sample to the TEM holder could be measured. This TEM technique was made necessary by the inhomogeneous structure of the nanospikes discovered during TEM characterization. In order to understand any nanospike electrical response it is necessary to know which structural element of the nanospike is being contacted by the electrical probe, as the electrical response of a nanospike might be expected to vary depending on whether the probe is put into contact with its In cap, the ion damaged sidewall, or driven into contact with a crystalline region. For this reason other nanoprobe electrical testing techniques, such as nanoprobe testing conducted in a SEM, would be unsuitable for examining the nanospikes, as without a way to unambiguously observe nanospike structure it is impossible to accurately interpret test results. By conducting electrical testing while simultaneously observing a nanospike's structure through BF TEM imaging, it was possible to direct the probe with great accuracy into contact with the desired feature on each spike and to be sure that contact was maintained during testing. TEM imaging during testing also allowed the structure of each tested nanospike to be recorded and any changes in nanospike structure due to electrical testing to be observed.

3.6.1 InAs/n+ InAs nanospike electrical testing results

Results from electrical characterization of nanospikes formed by FIB irradiation of undoped InAs films homoepitaxially grown on degenerately doped n+ InAs substrates will be presented and discussed first, as that system is electronically simpler and thus its results are more readily interpreted relative to the case of nanospikes created using undoped InAs heteroepitaxially grown on n+ InP. For all TEM nanoprobe testing, the W probe was intentionally driven into the In droplet cap at the top of each nanospike, and only directed into contact with other parts of the nanospike when that In cap had been destroyed or otherwise removed. For each InAs nanospike tested, multiple scans consisting of voltage ramps from zero to both positive and negative voltages were conducted, allowing the current (A) versus voltage (V) response (IV response) of the spike to be recorded. The first few voltage scans were limited to low values, generally ±1-2 V, and correspondingly low currents in order to allow the collection of data without inducing any structural changes in the nanospikes. Keeping nanospike current low also allowed the electrical system to remain in a lower current range with a correspondingly lower background noise level. By repeating low voltage scans more than one time it was possible to verify the repeatability of the electrical results obtained. Later voltage scans on each spike were run to higher voltages and currents. This often produced structural changes in the nanospikes, and at high enough currents the InAs nanospikes would either decompose or be destroyed outright. In many cases the nanospikes were destroyed so suddenly and violently that the process appeared instantaneous even when observed with a 30 fps camera. Quantitative analysis of InAs nanospike electrical response carried out here uses the results from the first low voltage scans with good electrical contact for each tested nanospike, which are assumed to be representative of the pristine spike.

An example of InAs electrical test is given in Figure 3.16. Figure 3.16(a) shows a plot of the raw IV data from an InAs nanospike with partially disrupted core that underwent three voltage scans. The first and second voltage scans to -1 and +1 V respectively produced smooth IV curves that were considered the electrical response of the unadulterated nanospike and were suitable for later quantitative analysis. The third voltage scan consisted of a ramp to +2 V, and during that test the nanospike underwent a structural disruption of its interior and partially decomposed. The point at which the nanospike began to decompose is visible in the IV data from scan 3 as a sharp discontinuity and sudden increase in current, as indicated on the plot. Figures 3.16 (b)-(e) show BF images taken of the spike at various points before and during the electrical testing process, including after the nanospike had been damaged. Figure 3.16(b) shows the W nanoprobe approaching the nanospike, and (c) shows the probe in contact with the nanospike's In cap before voltage ramping. The minimal change in nanospike diffraction contrast between Figures 3.16 (c) and (d), taken before and after voltage scans 1 and 2 respectively, indicates that those two voltage scans caused little change in nanospike structure. However, in Figure 3.16(e) taken after the third voltage scan it can be seen that the top half of the nanospike chemically decomposed, producing an In droplet which attached to the nanoprobe tip, and the lower half of the spike underwent structural changes as indicated by the large alterations in BF contrast visible in Figures 3.16(e) and (f). The electrical behavior shown by the InAs nanospike of Figure 3.16 is typical of the InAs nanospike electrical tests conducted in this work. In all cases where nanospike damage due to electrical testing occurred slowly enough to be observed, the structure of the spike would either disrupt along the spike core and then the spike would decompose starting at the region directly below the In cap, or the spike would decompose or be damaged starting in the area directly below the In cap. When a spike was decomposed or entirely destroyed it often left behind a thin shell of what was presumably an outer oxide or carbon contamination layer. Figure 3.17 shows two more examples of InAs nanospikes before and after a voltage scan that caused spike damage. Figures 3.17(a) and (b) show a nanospike with a ion disrupted core that underwent structural changes due to electrical testing, and Figures 3.17(c) and (d) show a nanospike with a partial single crystal core that decomposed at the tip.

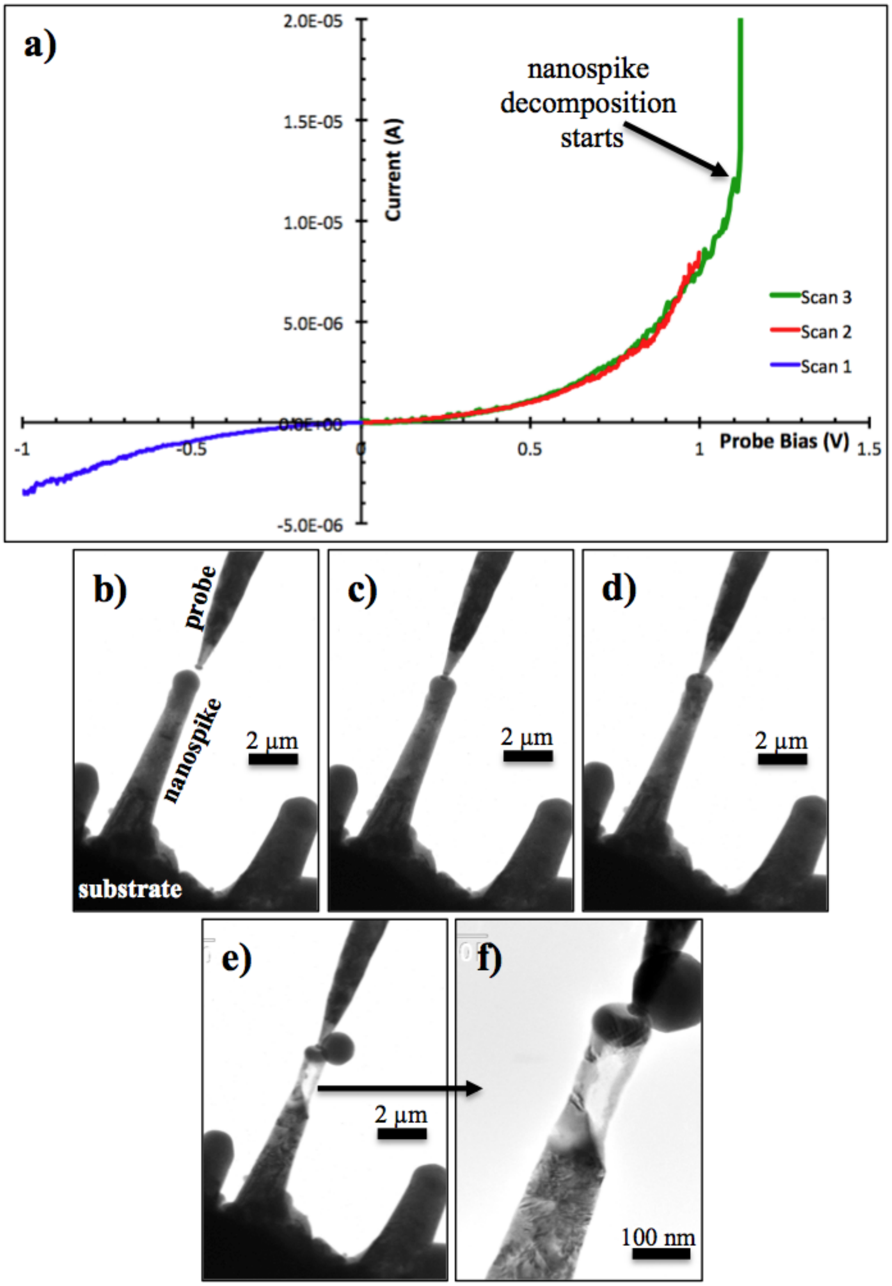

Figure 3.16: Full data set of IV curves and TEM images for the electrical testing of an InAs nanospike. (a) shows the raw IV data collected during testing. Image (b) shows the nanospike before the probe has made contact, (c) shows after the probe is in contact but before any voltage scans had been run, (d) shows after voltage scans 1 and 2 had been completed, (e) shows the nanospike after voltage scan 3, and (f) shows a higher magnification image of the damaged nanospike after scan 3. Data and images taken in collaboration with J. Jokisaari and Prof. X.Q. Pan.

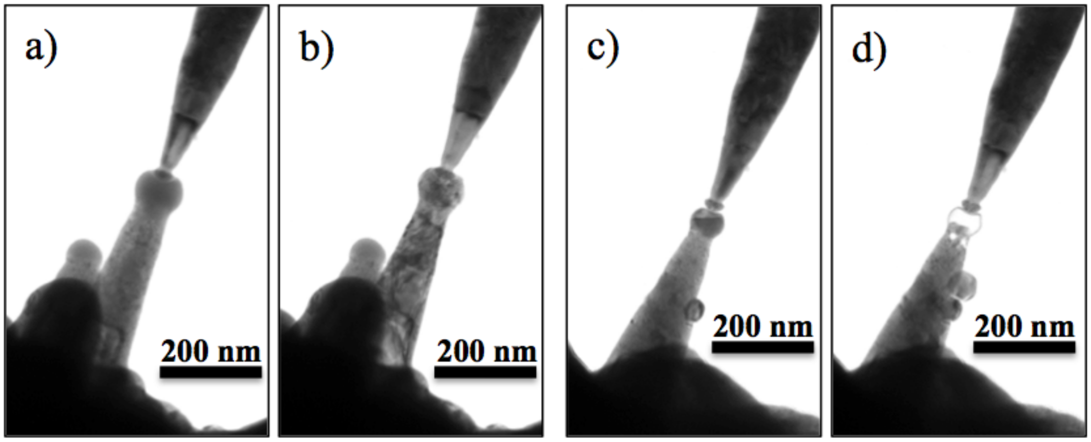

Figure 3.17: BF TEM images of InAs nanospikes before and after voltage scans in which the spikes were heavily damaged. (a) and (b) show a nanospike before and after undergoing internal structural changes, and (c) and (d) show a nanospike before and after it decomposed near its tip. Images taken in collaboration with J. Jokisaari and Prof. X.Q. Pan.

Figure 3.18 shows a plot of the raw current-voltage data from all the InAs nanospikes tested by inserting the W nanoprobe into their In droplet cap, and in general they all exhibit the same type of IV response during their first few representative voltage scans. For all of the nanospikes in Figure 3.18, the probe voltage was first ramped from 0 to -1 V and then from 0 to +1 V, and these two scans have been combined into one curve. In some cases the current data does not extend all the way to the ±1 V point, corresponding to cases where the measured current exceeded the maximum current limit allowed for that test. Noise in the data generally resulted from poor probe to nanospike contact. From Figure 3.18 it can be seen that as contacted all the nanospikes show a non-linear (non-Ohmic) IV response that is either nearly symmetric or asymmetric across voltage polarity. The data for nanospike 4 in that plot shows an example of nearly symmetric positive and negative voltage response, while nanospike 2 shows an asymmetric response. Nanospike 8 is something of an outlier, as it was the only InAs nanospike tested with a primarily single crystalline core and was much more conductive than the other nanospikes. All the other spikes examined had fully disrupted cores or had cores that were only partially single crystalline.

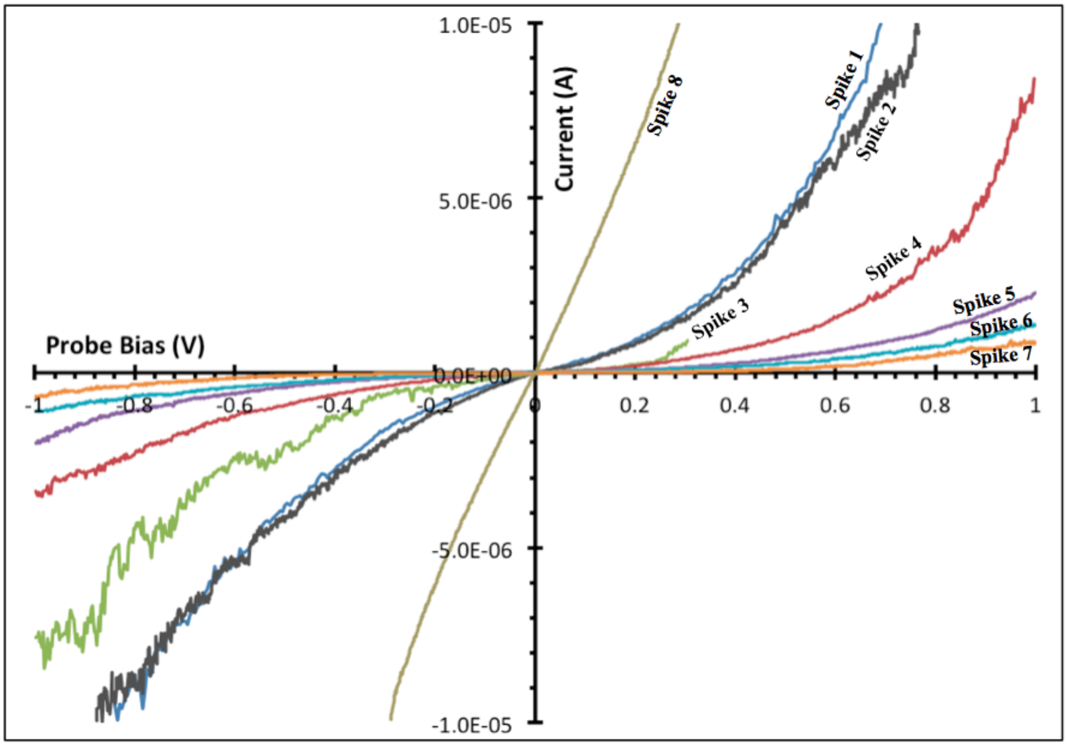

Figure 3.18: A plot of the raw IV data from the first voltage scans taken during TEM nanoprobe testing of eight different homoepitaxial InAs nanospikes. Data taken in collaboration with J. Jokisaari and Prof. X.Q. Pan.

As can also readily be seen from Figure 3.18, there is significant spread in the magnitude of the IV responses of the different spikes. However, it is not valid to compare the IV response of different nanospikes using the raw IV data, as the different physical size of each nanospikes influences the result. To compensate for differences in nanospike size it is necessary to normalize the current (A) and voltage (V) data by relevant physical dimensions, which allows current density (J, A/m^2) vs. electric field strength (E, V/m) to be plotted instead. To accomplish this, a variety of nanospike dimensions were measured based on TEM images of the electrically tested spikes. Figure 3.19 shows a schematic of an idealized nanospike structure with the experimentally measured dimensions labeled. Table 3.1 gives those measurements taken from each of the InAs nanospikes whose IV data is plotted in Figure 3.18. Crystalline core measurements are not included for nanospike 7 because the nature of its core was not clear in the BF TEM images of it. The choice of length to normalize voltage data by is fairly straightforward. Assuming that each nanospike's In droplet cap is fully metallic and conductive, then the height of the InAs semiconductor portion of the spike (In droplet height subtracted from full spike height) is the relevant dimension to use in calculating electric field strength at each data point. Choice of cross-section to use in determining current density is somewhat less straightforward, as the widths of the nanospikes change down their length. Again assuming the In droplet at the top of each spike is fully conductive, the idealized In droplet contact area, calculated by finding the area of the circle with the droplet contact width as its diameter, was selected. Droplet contact area was chosen because it represents the narrowest part of the conduction path and so was assumed to be the conduction-limiting cross-section. The semiconductor length and droplet contact area for each InAs nanospike are given in Table 3.2. The IV data from Figure 3.18 is replotted in Figure 3.20 divided by those spike dimensions to give J vs. E. Furthermore, using the droplet contact area and the semiconductor length the relative responses of the nanospikes can be compared by calculating nanospike resistivity at specific voltages. Nanospike resistivity values at -0.5, -0.2, +0.2, and +0.5 V are given in Table 3.2. Resistivities were also calculated using the spike cross-sectional areas at FWHM height and the nanospike base, but the effect of choosing those alternative cross-sections on the final resistivity values and J vs. E plot was minimal. By examining the values in Table 3.2 it can be seen that nanospike resistivity varies over several orders of magnitude. Variation in nanospike electrical response is also clear in the plot of Figure 3.20, where despite using the physical dimensions of the nanospikes to convert their IV response to J and E there is still significant variation between the curves plotted for each InAs nanospike.

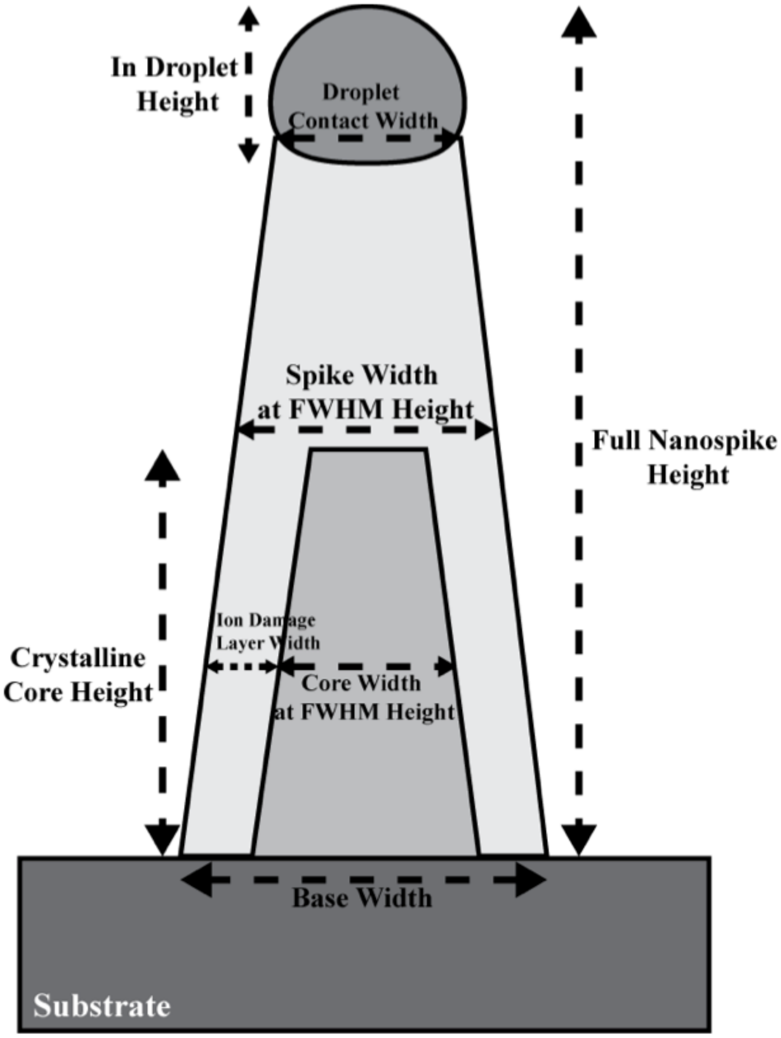

Figure 3.19: Schematic of an idealized nanospike structure showing the locations of features measured experimentally.

Table 3.1: Measurements of the InAs nanospike dimensions specified in Figure 3.19. In the cases where a nanospike did not have any single crystalline core volume, the values pertaining to that crystalline core were left as zero.

Nanospike #	**Spike Identifier**	**Full Nanospike Height (nm)**	**Base Width (nm)**	**Spike Width at FWHM (nm)**	**Crystalline Core Height (nm)**	**Core Width at FWHM Height (nm)**	**Ion Damaged Layer Width at Core FWHM (nm)**	**In Droplet Height (nm)**	**Droplet Contact Width (nm)**
1	EA5-1	409	150	96	84	88	21	86	71
2	EA4-4	606	184	126	317	121	15	56	71
3	EA1-3	276	149	90	0	0	0	69	70
4	EA1-1	703	176	116	180	121	14	79	95
5	EA3-1	455	235	140	0	0	0	77	129
6	EA3-2	324	158	103	107	111	14	61	77
7	EA4-3	346	114	113	Indeterminate	Indeterminate	Indeterminate	77	101
8	EA4-2	512	199	138	338	128	19	58	78

Table 3.2: Table giving the InAs nanospike physical parameters chosen for converting I vs. V data into J vs. E and giving the nanospike resistivity values calculated using those dimensions.

Nanospike #	**Spike Identifier**	**Length of Semiconductor Section (Full Height-Droplet Height) (nm)**	**Idealized Droplet Contact Area (nm^2)**	**Resistivity at -0.5 V (Ohm*m)**	**Resistivity at -0.2 V (Ohm*m)**	**Resistivity at +0.2 V (Ohm*m)**	**Resistivity at +0.5 V (Ohm*m)**
1	EA5-1	324	3956	0.0016	0.0025	0.0025	0.0013
2	EA4-4	550	3979	0.0009	0.0013	0.0018	0.0008
3	EA1-3	207	3865	0.0045	0.0096	0.0157	N/A
4	EA1-1	624	7073	0.0062	0.0112	0.0113	0.0057
5	EA3-1	378	13152	0.0422	0.0823	0.0775	0.0397
6	EA3-2	263	4606	0.0286	0.0508	0.0484	0.0317
7	EA4-3	269	7985	0.1567	0.3534	0.8833	0.1433
8	EA4-2	454	4814	N/A	0.0003	0.0003	N/A

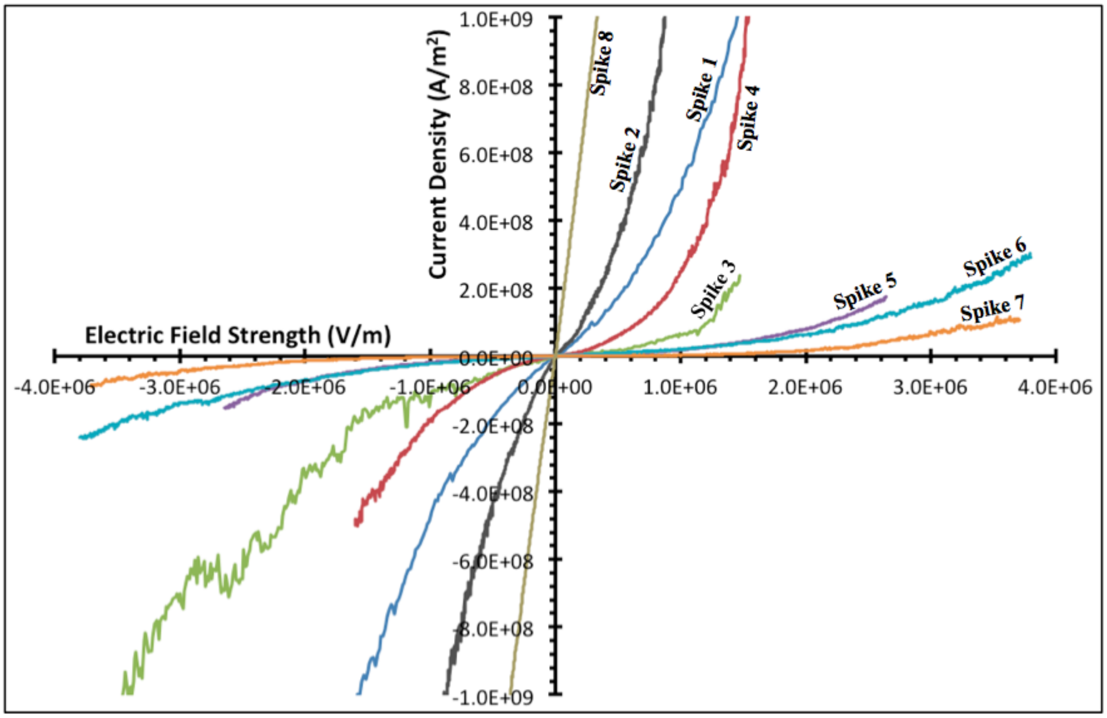

Figure 3.20: A plot of current density (J) vs. electric field strength (E) created using the current vs. voltage data shown in Figure 3.18 from the same eight InAs nanospikes. For each nanospike J was found by dividing I by the In droplet contact area and E was found by dividing V by the length of the semiconductor section of the nanospike body.

Based on the different electrical responses of the InAs nanospikes as plotted in Figures 3.18 and 3.20, **two questions regarding the nanospike electrical data need to be addressed in order to provide a clear picture of what controls nanospike conduction:**

1. **Why does electrical response vary so much between nanospikes?**

   and

2. **Why do the nanospikes exhibit a non-linear IV response?**

The first question may be partially answered by examining the effects that differences in nanospike structure are expected to have on electrical transport. Structural variation represents the primary difference between each nanospike once variations in nanospike dimension have been accounted for by converting to J and E or by calculating nanospike resistivity. As noted during TEM characterization, there are large differences between the internal structures of each spike. All the nanospikes have an In droplet cap and outer ion-damaged layer, but the cores of the nanospike vary from fully disrupted amorphous and polycrystalline material to continuous single crystals. Assuming that carrier transport occurs at least partially through the nanospike cores, then core structure will affect nanospike conduction. This assumption is partially justified by the earlier observation that in cases where changes to nanospike internal structure occurred during electrical testing at higher voltages the changes occurred first in the core of the nanospike. This indicates that current was passing through the core at the time that the damage occurred. It is difficult to quantify the degree of ion disruption present in the regions of nanospike core that are amorphous or polycrystalline, as all of those areas are heavily ion damaged and inhomogeneous on the nanoscale. However, the extent of each InAs nanospike core that is a continuous single crystal is readily observable and thus the degree to which each nanospike core is crystalline may be compared to its resistivity. This was done here by first calculating an idealized crystalline core volume by multiplying the height of the crystalline core by the crystalline core cross-sectional area found using the core width at its full-width-at-half-maximum (FWHM) height. The crystalline core volume was then divided by the idealized total nanospike volume found by multiplying the full nanospike cross-sectional area at FWHM height by the length of the semiconductor section of the nanospike. This produces an approximate nanospike single crystalline volume fraction. All the values necessary to carry out this calculation are given in Table 3.1, and nanospike 7 was excluded from analysis because the structure of its core could not be determined. Figure 3.21 shows a plot of nanospike +0.2 and -0.2 V resistivity values versus single crystalline volume fraction. Because data from only seven nanospikes are represented in that plot and there is considerable scatter in the data it is not reasonable to fit a specific resistivity vs. crystalline fraction trend curve to the data in Figure 3.21. However, the data in the plot shows that in general nanospikes with the lowest resistivity also had the highest single crystalline volume fraction and that nanospikes with lowest crystalline volume fraction have a higher resistivity. That a large single crystalline volume fraction would lower nanospike resistivity is not unexpected. Ion damage would be expected to raise the resistivity of a III-V semiconductor, and so single crystalline regions that still match the structure of and are in good contact with the InAs substrate should be more conductive than ion disrupted regions. The resistivity values of the two highest crystalline volume fraction nanospikes approach or are lower than the resistivity of bulk intrinsic InAs (approximately 0.002 Ω*m [27]) depending on voltage. Based on the data shown in Figure 3.21 it appears that nanospikes with a high volume fraction of single crystalline core are more conductive, while those with ion disrupted structures are less so. Thus some of the spread in the InAs nanospike electrical response data can be attributed to these structural differences between the spikes. There is still variation in the resistivity of those nanospikes that all have ion-disrupted cores, and that variation may also be due to structural differences. TEM characterization showed that the disrupted nanospike cores consisted of intermixed amorphous material and small regions of local crystallinity, and it may be that the unique structure of each disrupted nanospike core is responsible for the additional variation in nanospike conductivity. In cases where a nanospike has a partially disrupted and partially single crystalline core, the conduction path through the disrupted region may be so poor that it influences total conductivity more than the single crystalline region. This explanation may account for the cases in Figure 3.21 where a significant fraction of the nanospike core volume was crystalline but the spike still had a high resistivity.

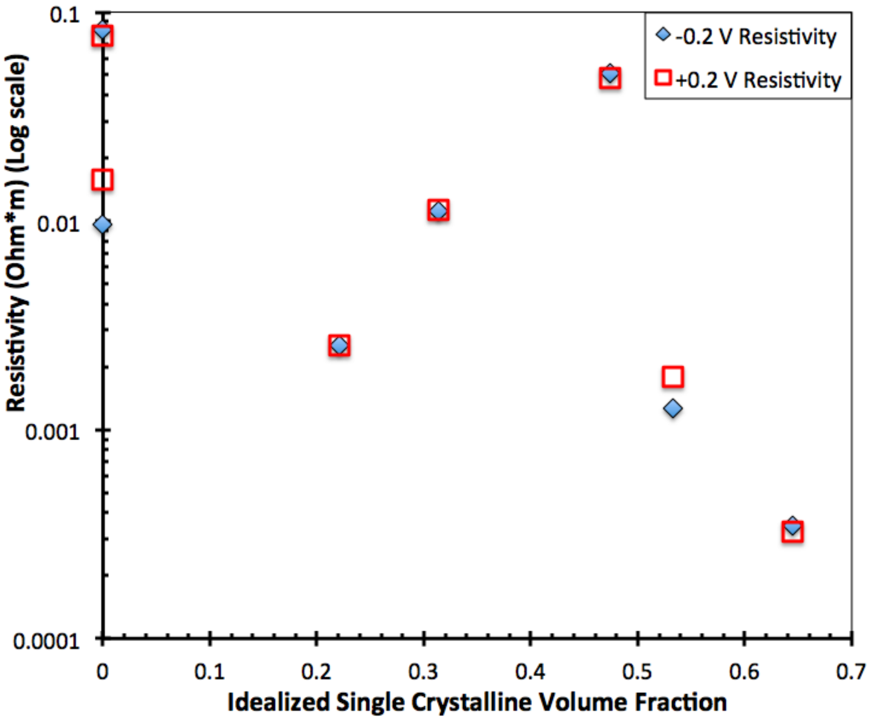

Figure 3.21: InAs nanospike +0.2 and -0.2 V resistivity values plotted versus their idealized single crystalline core volume fraction.

Structural differences may explain why the nanospikes show different levels of conductivity, but the reason for the non-linear IV response of the InAs nanospikes still needs to be determined. Individually the positive and negative polarity IV responses of the InAs nanospikes plotted in 3.18 show a smooth non-linear voltage dependence across the entire plotted range, with no sudden changes in slope evident. This was verified visually and by plotting the instantaneous linear slope between every pair of points in each IV data set and noting the absence of any inflection points or sharp changes in those dI/dV vs. V plots. However, at very low biases (<0.1 V) noise in the data makes analysis difficult and may have obscured a transition. Experiments where the W nanoprobe was driven into unirradiated, undoped InAs film near the thinned region of the TEM sample resulted in a linear IV response, indicating that the non-Ohmic nanospike response is characteristic of the nanospikes and not the homoepitaxially grown undoped-InAs/n+ InAs film structure used to produce the nanospikes.

Other authors have previously studied electrical transport in semiconductor nanowires, including examinations of III-V nanowires, and a number of those literature examples contain electrical data that resembles the nanospike IV behavior reported here. The electrical properties of individual nanowires are often probed using a field-effect transistor (FET) contact geometry, and the electrical properties of InAs nanowires specifically have been examined using this method [28-30]. However, FET type tests use a significantly different experimental set-up compared to the nanoprobe contact tests performed in this work, and correspondingly the information extracted from FET tests must be analyzed differently. Thus the discussion here will be limited to examples of other nanowire electrical studies that employ a simple 2-probe or nanoprobe contact experimental geometry and show results resembling the homoepitaxial InAs nanospike behavior seen in this work. Those studies identify a number of different mechanisms that limit conduction in different nanowires junctions and cause them to exhibit non-linear/non-Ohmic IV behavior. A series of 2-contact and SEM nanoprobe experiments have identified space-charge limited (SCL) conduction in the body of the wires as a cause of non-linear IV response in GaAs [31], GaN [30,32,33], and InAs nanowires [9,30]. SCL conduction is characterized by a transition from $I \alpha V$ behavior at low bias to $I \alpha V^2$ behavior at higher biases and a symmetric positive-negative polarity IV response characteristic of transport limited by process in the nanowire. Other studies of GaAs nanowires have identified carrier trap-limited behavior in the body of the nanowires [31,34]. This behavior is characterized by symmetric IV response and very low conduction at small bias followed by a sharp turn-on at biases high enough to allow carriers to escape their traps. Finally, another series of 2-contact and TEM nanoprobe studies have identified contact barrier limited (also called injection limited) conduction as a cause of non-Ohmic IV response in nanowires [35-38]. In those studies non-Ohmic IV behavior was concluded to be the result of Schottkey barriers at the two metal-nanowire junctions, with conduction controlled by thermionic emission of carriers over the barriers and tunneling through the barriers. Schottkey barrier limited conduction does not show a transition in voltage dependence and may produce symmetric, nearly symmetric, or asymmetric IV results depending on whether the two contacts and barrier heights are the same, slightly different, or largely different respectively. 2-contact Schottkey barrier limited behavior is well described by the "metal-semiconductor-metal" (MSM) model [39].

Because the InAs nanospike IV response reported here does not show symmetric IV behavior, a transition from $I \alpha V$ to $I \alpha V^2$ dependence, any sharp changes in IV slope, or a sharp turn on point, the cause of the non-Ohmic IV response of the InAs nanospikes cannot be attributed to SCL or trap-limited behavior. However, the general form of the InAs nanospike IV response does closely resemble the form of the experimental IV results attributed to Schottkey barrier limited conduction in references [35], [36], and [37]. Thus the nanospike electrical response will be examined with barrier limited conduction in mind. Figure 3.22(a) shows a simplified schematic of the TEM nanoprobe junction type used to test InAs nanospikes in this study, consisting of a nanospike created from the undoped InA film, the n+ InAs substrate with carrier concentration of N_D=2x10^{18} cm^{-3} as specified by the wafer manufacture, the In droplet at the top of the nanospike as the metal contact to the spike, and the junction between the n+ InAs and the conductive carbon paint applied to the TEM sample to ensure good electrical contact to the Mo TEM grid and TEM holder. The undoped InAs film was likely grown unintentionally n-doped, but its carrier concentration was not determined. Figure 3.22(b) shows a simplified possible band-structure to match that junction. The relevant metal work functions, φ_m, and bandgaps, E_g, necessary to generate that band structure are listed on the figure and were taken from references [40] and [41] respectively. Schottkey barriers heights, φ_b, above the Fermi level at the In and Carbon contacts were found using

$$\varphi_b = \varphi_m - \chi_s \tag{3.1}$$

where χ_s is the semiconductor electron affinity, taken as χ_s=4.9 eV for InAs [42]. Taking the carbon paint φ_m as approximately 5.0 (corresponding to the value reported for bulk polycrystalline carbon) and the In φ_m as 4.09 eV, Equation (3.1) predicts barriers of 0.1 eV and -0.81 eV at the C/n+InAs and InAs nanospike/In junctions respectively. The properties of the nanospike were assumed to be those of bulk InAs, with an intrinsic carrier concentration of N_D=~1x10^{15} cm^{-3} [27]. It is likely that the nanospike is more resistive than bulk InAs due to ion damage. The Fermi level, E_f, of the undoped InAs nanospike at 300 K was found assuming that Boltzman statistics apply and using the equation [43]

$$E_f = \frac{E_g}{2} + \frac{kT}{2} ln\left(\frac{N_V}{N_C}\right) \tag{3.2}$$

where k is the Boltzman constant, T is absolute temperature, N_v is the effective density of states in the valence band, and N_c is the effective density of states in the conduction band. The Fermi level of the n+ InAs wafer was found using [43]

$$E_c - E_f = kTln\left(\frac{N_C}{N_D}\right) \tag{3.3}$$

where E_c is the conduction band energy, here taken as equal to the intrinisic bandgap, and N_D is the donor concentration taken as the manufacturer provided carrier concentration. The n+ InAs used in this work is degenerately doped, and so Boltzman statistics cannot be used to accurately calculate its Fermi level. Thus equation (3.3) only gives an estimate of the n+ InAs Fermi level. The size of the depletion regions and band bending at the different junctions were not calculated exactly and are only approximated in Figure 3.22(b). No interface effects such as pinning of the Fermi level at the contacts due to surface states were included in development of band structures. Contact resistances were likely present at the junctions to the nanospike and n+ InAs, but those contact resistances were also unknown and so likewise not incorporated into this model.

Based on the band structure developed in Figure 3.22(b), there are small barriers to electron transport for both positive and negative probe bias predicted in the electronic structure of the nanospike system. These barriers may account for the non-Ohmic IV response of the InAs nanospikes. However, the barriers at each contact are relatively low and the InAs/nanospike junction is predicted to have a negative barrier height and to be nearly Ohmic. If instead of the n+ InAs/carbon paint contact a n+ InAs/Mo metal contact is considered, that junction is predicted to be Ohmic as well. Electrons should be able to cross over the predicted barriers in the electronic structure at low forward or reverse biases. So while the conduction behavior of the InAs nanospikes does appear to be barrier limited, it is not clear if the relevant barriers are due to the metal contacts in the system or something else. Given that the resistivity of ion damaged InAs is expected to be higher than single crystalline bulk InAs and all of the nanospikes tested had at least some ion damaged material between their single crystalline core and their In droplets, it is possible that the ion damaged regions of InAs act as a barrier to electron transport and so help to produce the high resistivity and non-linear conduction behavior found for the nanospikes. The inhomogeneity of the ion-damaged region may either be scattering carriers or providing a large number of traps. Figure 3.23(a) shows a schematic of an InAs nanospike junction now with single crystalline core and ion damaged structural regions included in the nanospike. Figure 3.23(b) shows a band structure corresponding to that junction with a hypothetical insulating barrier included due to the ion damaged material in the conduction path. The actual nature of the barrier may be different than depicted, but regardless a barrier or barriers of some type in the nanospike would limit electronic transport and might produce non-linear IV behavior like that seen in this work. The ion damaged regions of each spike are also inhomogenous and of different size, and differences between those damaged regions and the resulting effect on conduction explains why there is still spread in the IV response of nanospikes that all have full-length ion disrupted cores or similar amounts of undamaged core material. The electrical analysis conducted here is extremely basic and makes a number of assumptions about the electronic structure of the nanospike junctions tested, and thus cannot be used to quantitatively model transport through the nanospikes. Much more analysis and accurate modeling of transport in the nanospikes will be necessary to demonstrate conclusively that nanospike conduction is limited by internal barriers to electron transport and what the identities of those barriers are.

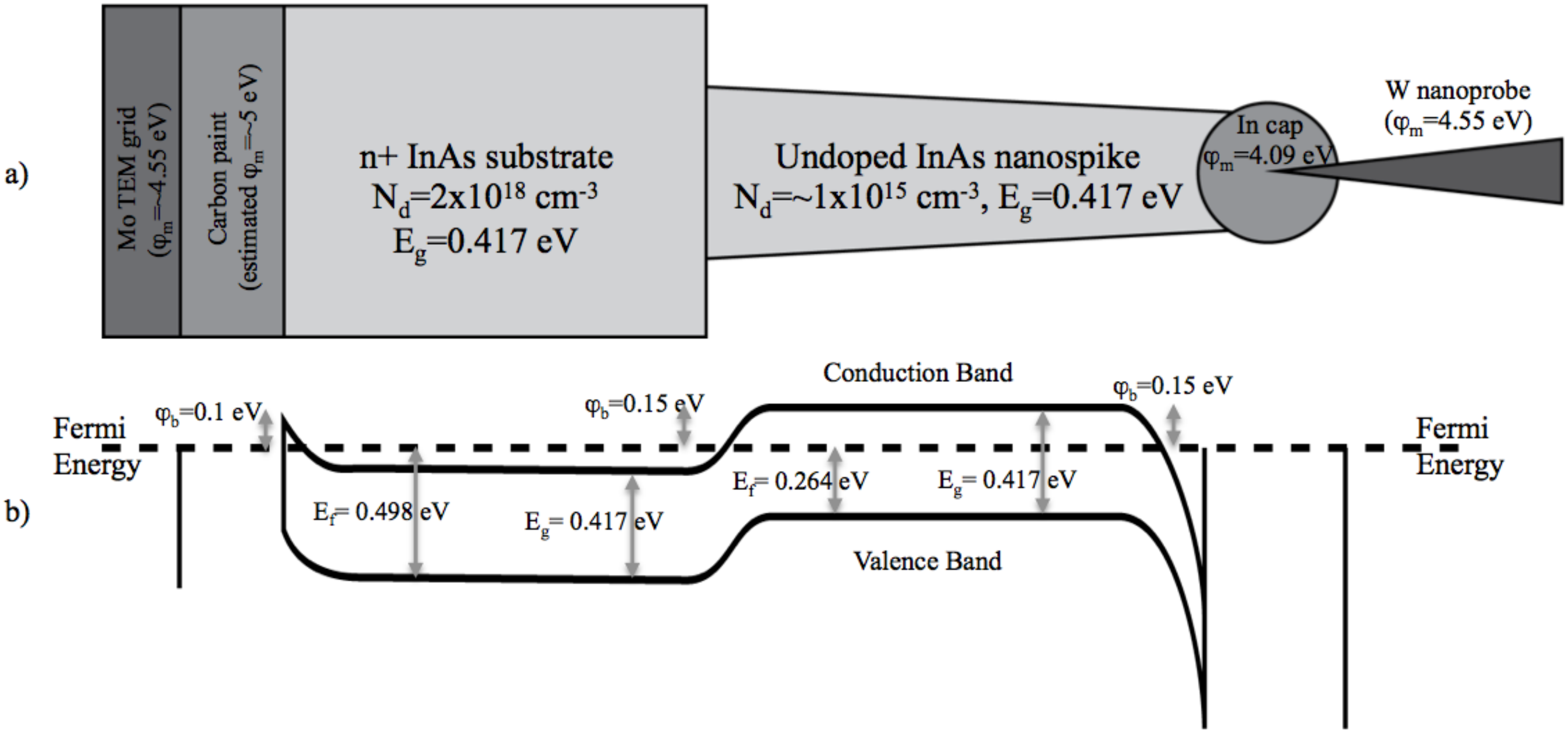

Figure 3.22: (a) shows a schematic of a simplified InAs nanospike junction, with the relevant structural elements and some electrical properties labeled. (b) shows a simple electronic band-diagram to match the junction in (a). The calculated energies of varies features are labeled in (b). Please note that the size of the depletion regions were not calculated and as shown are only a rough estimate.

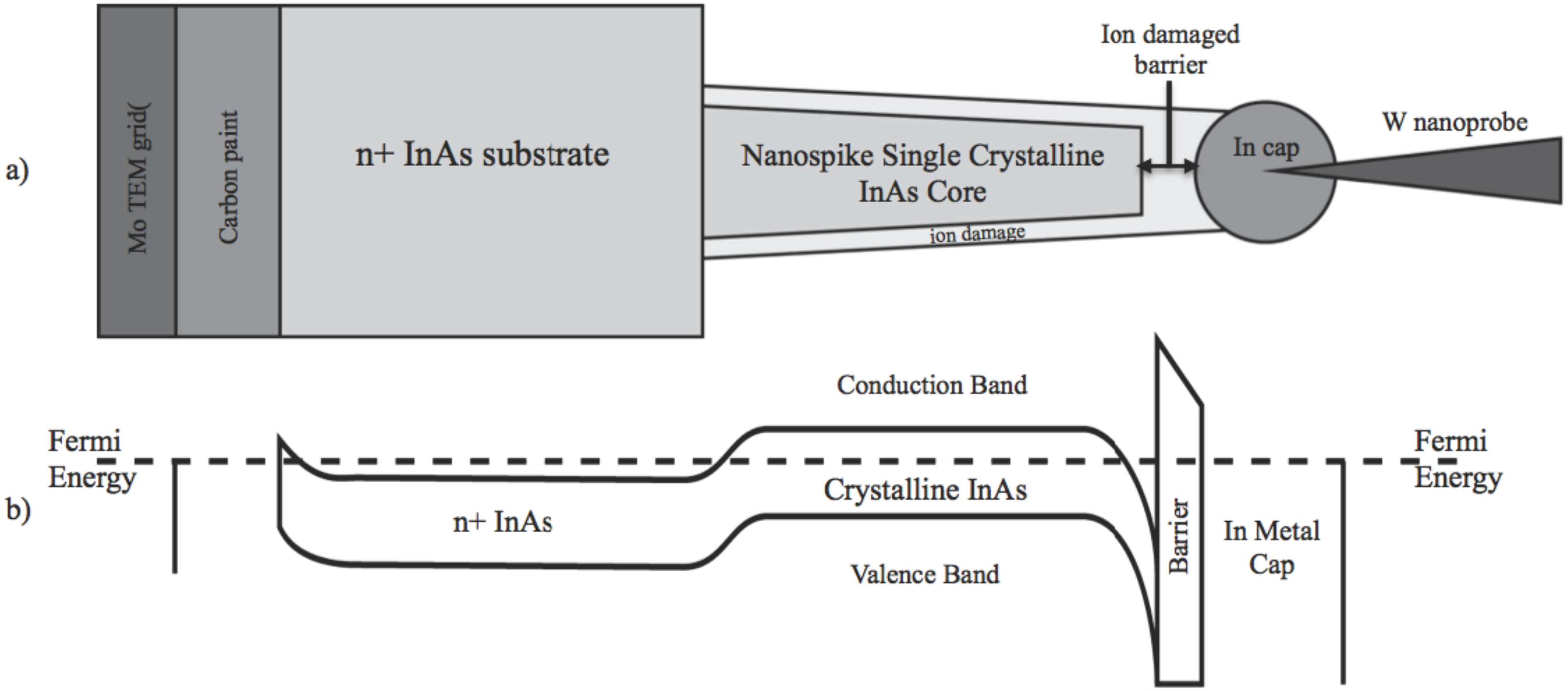

Figure 3.23: (a) shows a schematic of a simplified InAs nanospike junction that includes the internal structural features of the nanospike. (b) shows a simple electronic band-diagram to match the junction in (a) with a hypothetical barrier added near the In droplet junction to account for the effect of the ion-damaged region in the nanospike.

3.6.2 InAs/n+ InP nanospike electrical testing results

Nanospikes created by FIB irradiating InAs films grown on n+ InP substrates were electrically tested by TEM nanoprobe in the same manner as the homoepitaxial InAs nanospikes, and as such the results from their testing may be discussed in much the same way. The only major material differences between the InAs and InAs/InP cases are the presence of the InAs/InP heterostructure and that both randomly placed and templated InAs/InP nanospikes were tested. A minor difference in testing method is that many IV scans of the InAs/InP nanospikes were run from negative to positive voltage in one continuous test instead of split into two scans from zero to positive and negative voltage. However, testing in one scan instead of two did not alter the electrical response of the spikes. The low voltage (±1-2 V) portions of IV test curves were used to obtain data for quantitative analysis, and testing to higher voltages and currents resulted in damage or outright destruction of the InAs/InP nanospikes. All tests were conducted by contacting a W nanoprobe to the In droplet at the top of each nanospike. In some cases repeated lower voltage scans that did not cause readily visible damage to the nanospike would result in IV curves that maintained the same general shape as the earlier scans but were shifted to higher currents/conductivities. Increased conductivity was assumed to be due to changes in the contact between the probe and In nanospike tip or changes in the nanospike itself brought about by the previous scan. Thus these later curves do not reflect the response of the pristine nanospike and were not used for the following analysis. As in the InAs nanospike case, the first voltage scans with good probe-nanospike contact were used for quantitative analysis. For some of the randomly placed InAs/InP nanospike electrical tests, there was considerable noise at very low biases.

An example of the electrical response of a randomly placed InAs/InP nanospike with a fully ion disrupted core can be seen in Figure 3.24. Figure 3.24(a) shows a plot of the raw IV data from an initial scan from 0 to -3 V followed by a second scan from 0 to +3V. The nanospike was damaged during the second scan, so no additional scans were run. Figures 3.24 (b), (c), and (d) are BF TEM images that show respectively the InAs/InP nanospike before the W probe was brought into contact, after the probe was in contact but before any testing, and after both voltage scans. In Figure 3.24(d) damage to the lower-middle portion of the nanospikes core can be seen which occurred at the point indicated on the IV plot. The general behavior shown in Figure 3.24 is characteristic of the IV response of all the randomly placed and templated InAs/InP nanospikes tested. When driven to higher voltages and currents, just as the InAs nanospikes did, the InAs/InP nanospikes would either undergo structural damage in their core, visibly decompose, or be very suddenly destroyed. However, in the InAs/InP nanospike case there were more instances in which the nanospike was suddenly destroyed. Figure 3.25 contains three sets of BF images of InAs/InP nanospikes before and after voltage scans that suddently destroyed them. Figures 3.25(a) and (b) show a randomly placed nanospike, while Figures 3.25(c) and (d) and Figures 3.25 (e) and (f) show templated nanospikes. The templated InAs/InP nanospikes all were able to survive much higher voltages without suffering damage or being destroyed than the randomly placed InAs/InP or InAs nanospikes. This may have been due to their primarily crystalline core structures.

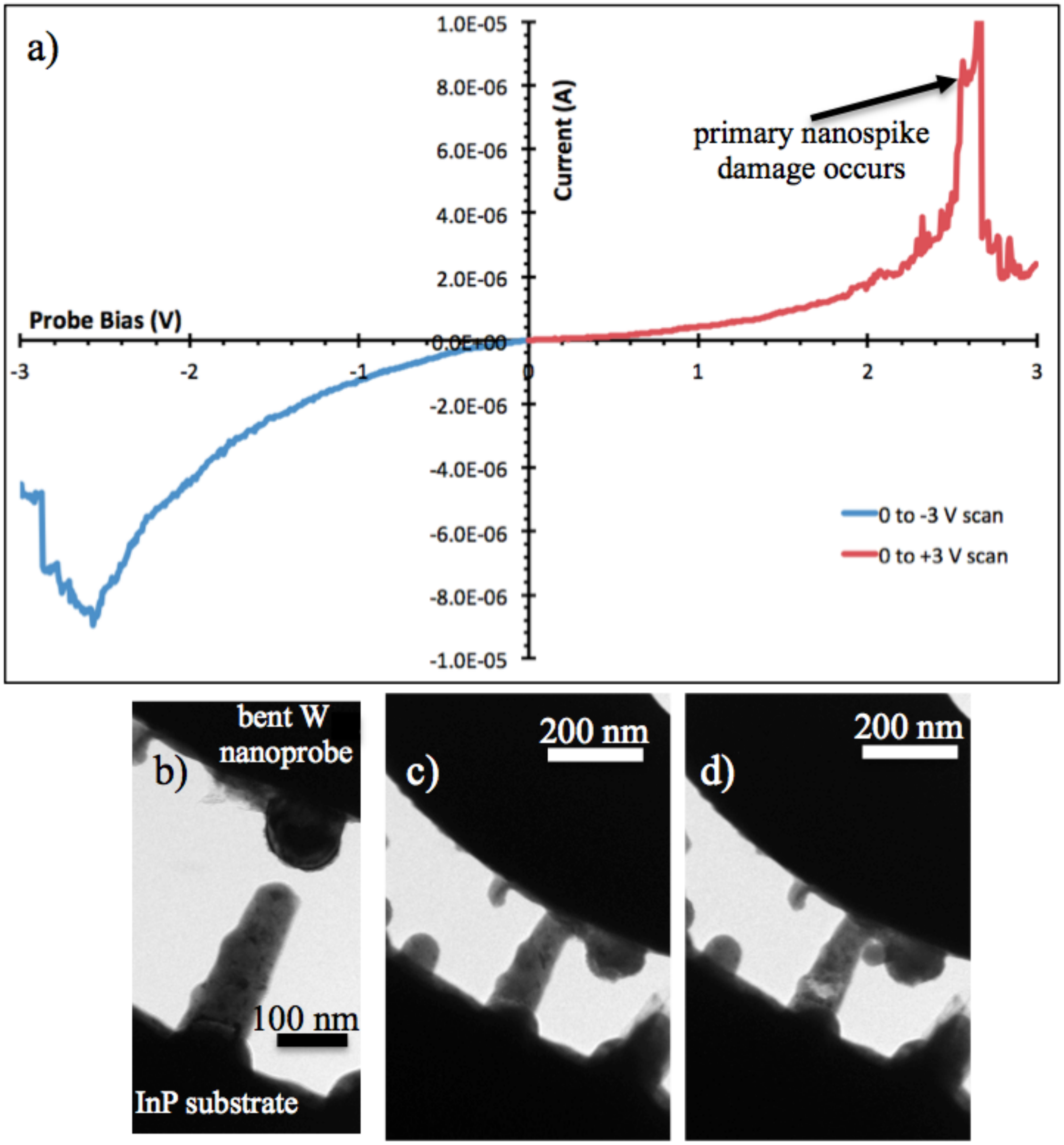

Figure 3.24: Full data set of IV curves and TEM images for the electrical testing of a randomly placed InAs/InP nanospike. (a) shows the raw IV data collected during testing. Image (b) shows the nanospike before the bent W probe had made contact, (c) shows after the probe was in contact but before any voltage scans had been run, and (d) shows the nanospike after two voltage scans had been completed. The nanospike was damaged by electrical testing at the point indicated on plot (a). Data and images taken in collaboration with J. Jokisaari and Prof. X.Q. Pan.

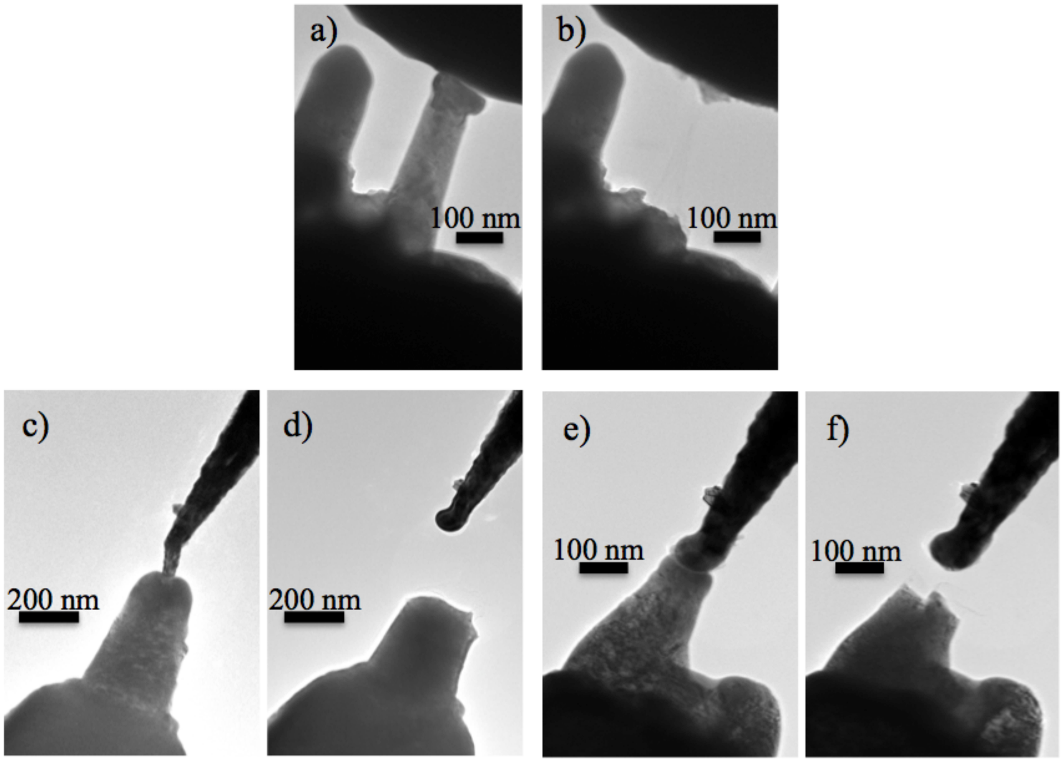

Figure 3.25: (a) and (b) show BF TEM images of a randomly located InAs/InP nanospike before and after a high voltage test that damaged it. (c)-(d) and (e)-(f) show templated InAs/InP nanospikes before and after electrical tests that damaged them. Images taken in collaboration with J. Jokisaari and Prof. X.Q. Pan

Figures 3.26(a) and (b) show the first scans with good electrical contact from nanoprobe electrical tests of several randomly placed and several templated InAs/InP nanospikes respectively. The core structures of the randomly placed nanospikes whose data are plotted in Figure 3.26(a) ranged from fully ion-disrupted to nearly fully single crystalline. All of the templated InAs/InP nanospikes electrically tested had full-length single crystalline cores. From Figure 3.26 (a) and (b) it can be seen that both the randomly placed and templated InAs/InP nanospikes show non-linear IV behavior that was either nearly symmetric or asymmetric across voltage polarity. The response of templated nanospike 1 is non-linear and only appears linear in Figure 3.26(b) because of the y-axis scale.

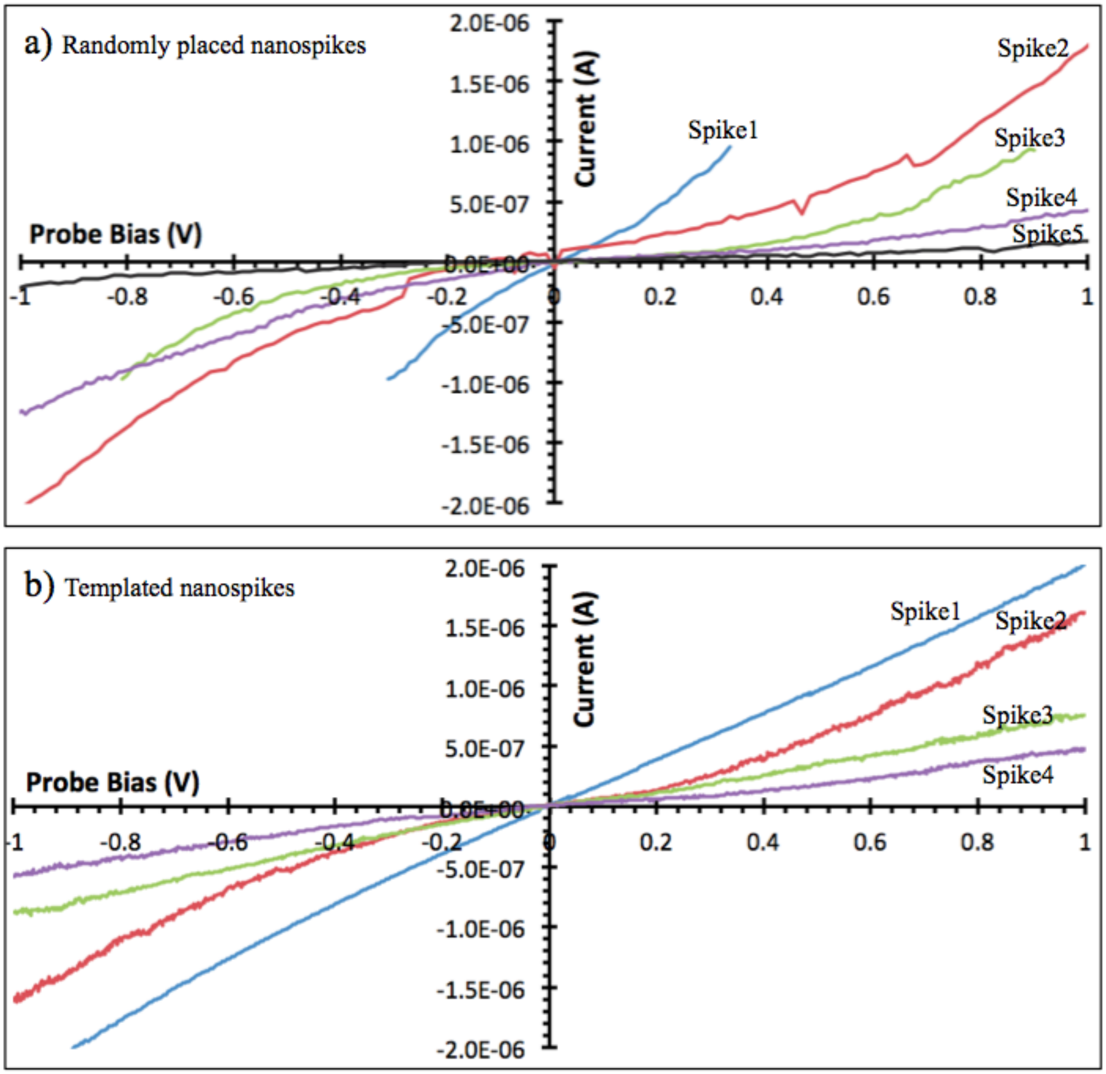

Figure 3.26: (a) gives a plot of the raw IV data from the first voltage scans of five randomly located InAs/InP nanospikes. (b) gives a plot of the raw IV data from the first voltage scans of four templated InAs/InP nanospikes. Data taken in collaboration with J. Jokisaari and Prof. X.Q. Pan

As with the homoepitaxial InAs nanospikes, to be able to usefully compare the responses of different InAs/InP nanospikes to each other requires that their raw IV data be normalized in a way that takes into account the physical dimensions of the nanospikes. This was done here using the same method as for the InAs case. The dimensions indicated in Figure 3.19 were measured for each InAs/InP nanospike from TEM images of those spikes. Table 3.3 gives those measurements for each randomly placed and templated InAs/InP nanospike whose IV data is plotted in Figure 3.26. The lengths of the semiconductor section of the nanospike and idealized droplet contact areas were then used to calculate nanospike resistivity values at -0.5, -0.2, +0.2, and +0.5 V, which are given in Table 3.4. Those dimensions were also used to convert and re-plot the InAs/InP IV data as J versus E. J vs. E plots for the randomly placed and templated InAs/InP nanospikes are given in Figure 3.27(a) and (b) respectively. Examining the values in Table 3.4 it can be seen that InAs/InP nanospike resistivity varies over several orders of magnitude, and there is significant spread in the J vs. E data for each spike plotted in Figure 3.27. It should be noted that some of the randomly placed InAs/InP nanospike electrical tests had significant noise at very low biases, and this accounts for some of the asymmetry and scatter in the -0.2 and +0.2 V resistivity values.

Table 3.3: Measurements of the InAs/InP nanospike dimensions at the locations specified in Figure 3.19.

Nanospike #	**Spike Identifier**	**Full Nanospike Height (nm)**	**Base Width (nm)**	**Spike Width at FWHM Height (nm)**	**Crystalline Core Height (nm)**	**Core Width at FWHM Height (nm)**	**Ion Damaged Layer Width at FWHM Core Height (nm)**	**In Droplet Height (nm)**	**Droplet Contact Width (nm)**
Random 1	EA2-1	442	139	108	80	79	13	88	91
Random 2	EA4-1	302	200	127	238	103	16	55	82
Random 3	EA3-1	383	159	123	175	98	18	88	113
Random 4	EA3-3	262	107	83	0	0	0	32	65
Random 5	EA3-4	628	248	135	436	111	18	57	99
Templated 1	PA2-1	194	124	115	130	96	11	46	92
Templated 2	PA4-1	231	220	134	137	119	12	87	113
Templated 3	PA5-2	191	159	116	131	109	15	52	97
Templated 4	PA5-3	503	330	249	391	228	17	124	211

Table 3.4: Table giving the InAs/InP nanospike physical parameters chosen for converting I vs. V data into J vs. E and giving the nanospike resistivity values calculated using those dimensions.

Nanospike #	Spike Identifier	Length of Semiconductor Section (Full Height- Droplet Height) (nm)	Idealized Droplet Contact Area (nm^2)	Resistivity at -0.5 V (Ohm*m)	Resistivity at -0.2 V (Ohm*m)	Resistivity at +0.2 V (Ohm*m)	Resistivity at +0.5 V (Ohm*m)
Random 1	EA2-1	354	6498	N/A	0.0065	0.0078	N/A
Random 2	EA4-1	247	5262	0.0177	0.0871	0.0196	0.0184
Random 3	EA3-1	295	9990	0.0627	0.1381	0.1128	0.0695
Random 4	EA3-3	229	3343	0.0163	0.0196	0.0522	0.0577
Random 5	EA3-4	571	7666	0.1023	0.5175	0.1086	0.1105
Templated 1	PA2-1	149	6617	0.0215	0.0226	0.0227	0.0232
Templated 2	PA4-1	143	10013	0.0661	0.1030	0.1042	0.0598
Templated 3	PA5-2	139	7392	0.0615	0.0706	0.0921	0.0765
Templated 4	PA5-3	379	35095	0.2002	0.2260	0.2987	0.3920

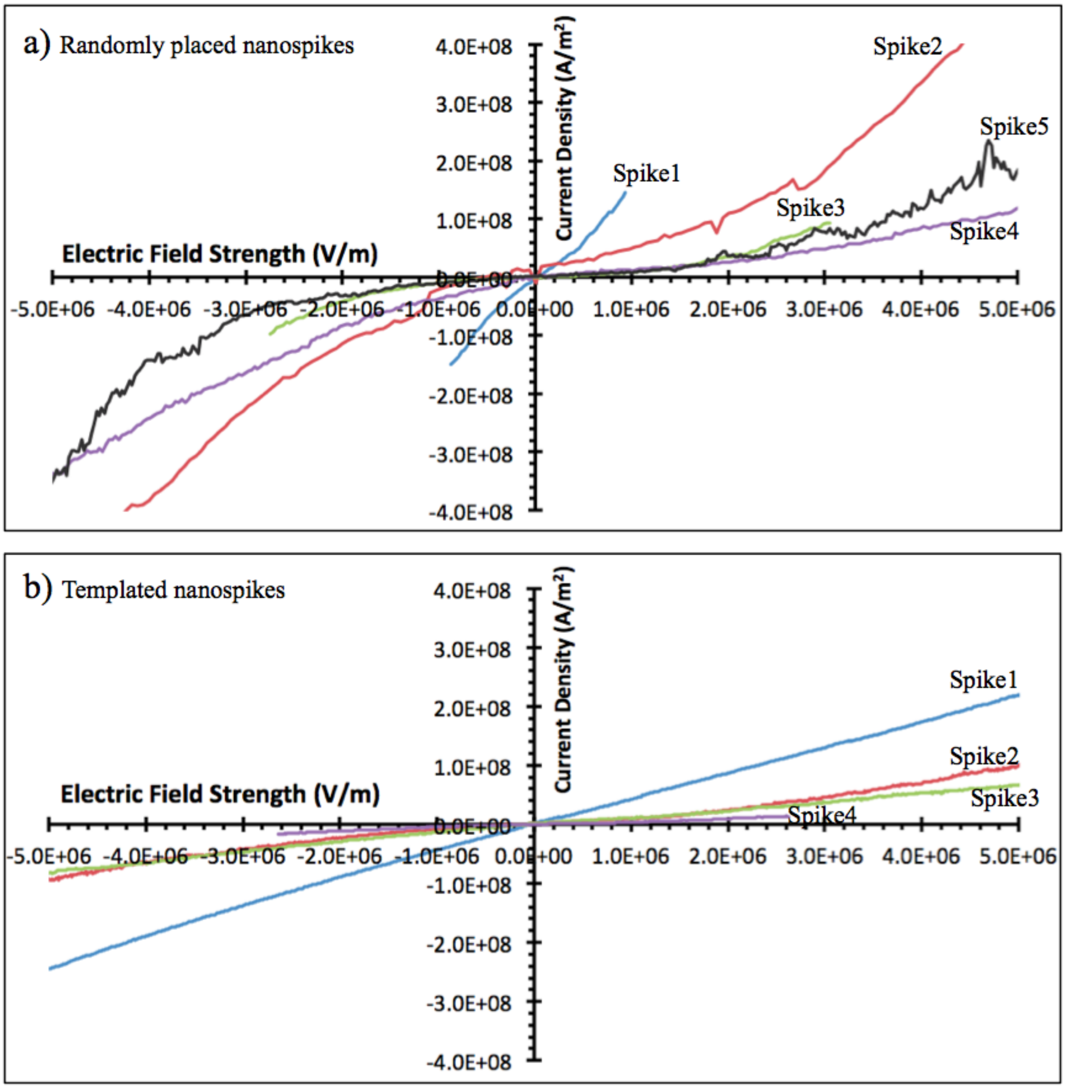

Figure 3.27: Plots of current density (J) vs. electric field strength (E) from electrical testing of the (a) randomly located and (b) templated InAs/InP nanospikes. J and E were found respectively by dividing I by the droplet contact area and dividing V by the length of the semiconductor section of the nanospike body.

Variation in the electrical response of the InAs/InP nanospikes can be discussed in much the same way as it was for the InAs nanospike case. Once the differences in the physical dimensions of the nanospikes have been accounted for, the primary remaining difference between the nanospikes is the variation in their internal structure, and structural differences in the nanospike cores may account for much of the spread in their electrical response. As was done for the homoepitaxial InAs nanospikes, the height and FWHM width of the InAs/InP randomly placed and templated nanospike single crystalline cores were used to generate an idealized crystalline core volume. This was divided by the similarly idealized volume of the semiconductor portion of each nanospike to produce an estimate of the single crystalline volume fraction of the nanospikes. Figure 3.28 shows a plot of InAs/InP randomly placed and templated nanospike -0.2 and +0.2 V resistivity values versus single crystalline volume fraction. No trend between resistivity and single crystalline volume fraction is evident in that scatter plot, and some of the nanospikes with higher crystalline volume fractions are also the most resistive. This does not change if the -0.5 V and +0.5 V resistivity values are plotted against single crystalline volume fraction. The lack of a clear trend and the scatter in Figure 3.28 may indicate that either the crystalline portion of the nanospike core is not the primary conduction path in the InAs/InP nanospikes or that the crystallinity of the core structure of the InAs/InP nanospikes is controlling conduction less than some other feature of the nanospike junction, such as defect density in the core. It is likely that structural variation in the nanospike core still accounts for at least some of the spread in the InAs/InP nanospike electrical response, but may not be the primary controlling factor in this case.

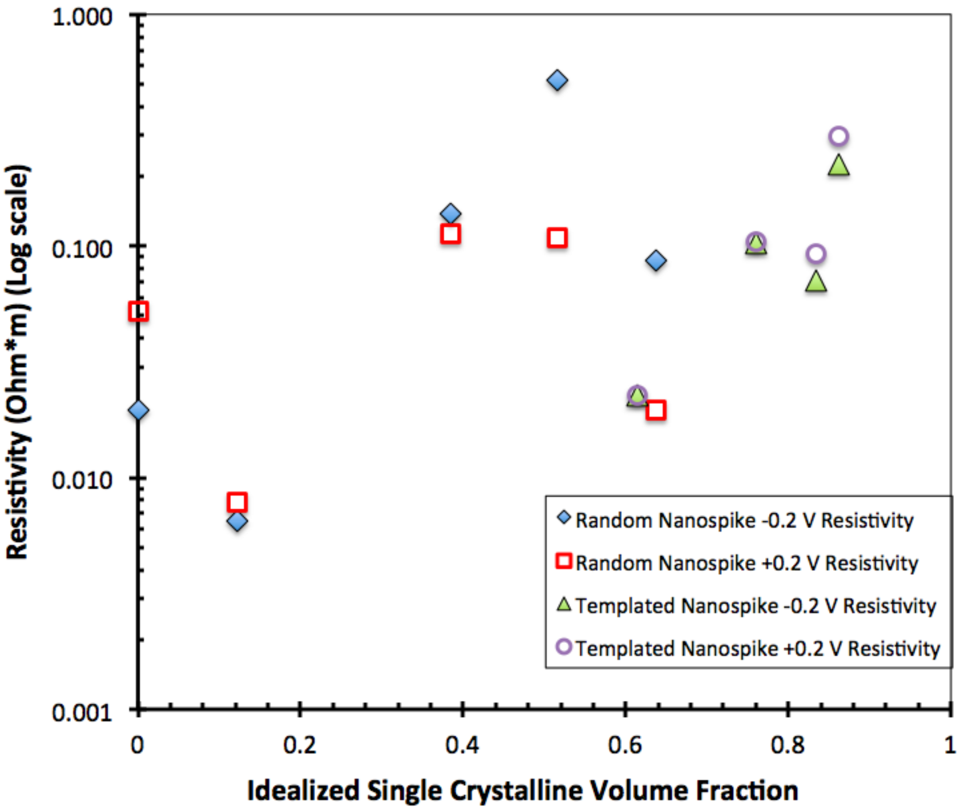

Figure 3.28: Randomly located and templated InAs/InP nanospike +0.2 and -0.2 V resistivity values plotted versus their idealized single crystalline core volume fraction.

Because the InAs/InP nanospike IV response reported here does not show symmetric IV behavior, a transition from I α V to I α V^2 dependence, any sharp changes in IV slope, or a sharp turn on point, SCL and trap-limited conduction behavior can again be ruled out as the cause of the non-Ohmic IV response of the InAs/InP nanospikes. The general form of their IV response does, as it did for the InAs nanospikes, resemble the cases of barrier-limited conduction found in the literature. In order to account for the non-Ohmic response of the InAs/InP nanospikes, the electronic band structure of an InAs nanospike/n+ InP junction was examined in much the same way that the InAs nanospike/n+ InAs junction was considered earlier. Figure 3.29(a) shows a simplified schematic of a junction corresponding to a TEM nanoprobe test of an InAs/InP nanospike, consisting of the nanospike created from undoped InAs film, the n+ InP substrate with carrier concentration of N_D=4.8x10^{18} cm^{-3}, the In droplet at the top of the nanospike, and the junction between the n+ InP and conductive carbon paint providing contact to the TEM grid. Figure 3.29(b) shows a simpe possible band-structure to match that junction. The relevant φ_m and E_g values necessary to create that diagram were taken from the same references used for the InAs nanospike case. The electron affinity of InP was taken as χ_s=4.35 eV [42]. Barrier heights at the contacts were again calculated using Equation (3.1), and the intrinsic InAs Fermi level and extrinsic Fermi level for the degenerately dope n+ InP were found using Equations (3.2) and (3.3) respectively. The bandgap offset at the InAs/InP interface was taken as type I with a 70/30 split giving a conduction offset of ~0.743 eV and valence offset of ~0.319 eV. The size of the depletion regions and band bending at the different junctions were not calculated exactly and are only approximated in Figure 3.29(b). Again, no trap states or interface effects such as pinning due to surface states were considered when developing the electronic structure in Figure 3.29(b). Based on that structure, barriers to electron conduction are predicted at the contacts to the In and carbon paint and at the InAs/InP heterointerface. The barriers at the InP/Carbon contact is predicted to be φ_b=0.65 eV and the band-offset barrier at the InAs/InP interface is predicted as φ_b=~0.3 eV. Both of these barriers are higher than any of the barriers predicted in the homoepitaxial InAs nanospike electronic structure, and may be the reason the InAs/InP nanospikes appear to exhibit barrier-limited conduction behavior. Those higher barriers may also explain why the resistivity values of the InAs/InP nanospikes given in Table 3.4 are as a set higher than the resistivity values of the InAs nanospikes given in Table 3.2, and why the resistivity of the InAs/InP nanospike junctions appears to be less dependent on nanospike internal structure than the InAs nanospike junctions were. There may be still be some form of barrier in the electronic structure due to ion damaged nanospike material in the conduction path as proposed for the InAs nanospikes, but if the InP/C and InAs/InP junction barriers are higher then they will control conduction in the InAs/InP nanospikes. Without more complex modeling and analysis of the InAs/InP nanospike electronic structure, it is not possible to determine which barriers to electron transport play the largest role in determining the conduction behavior of the InAs/InP nanospikes.

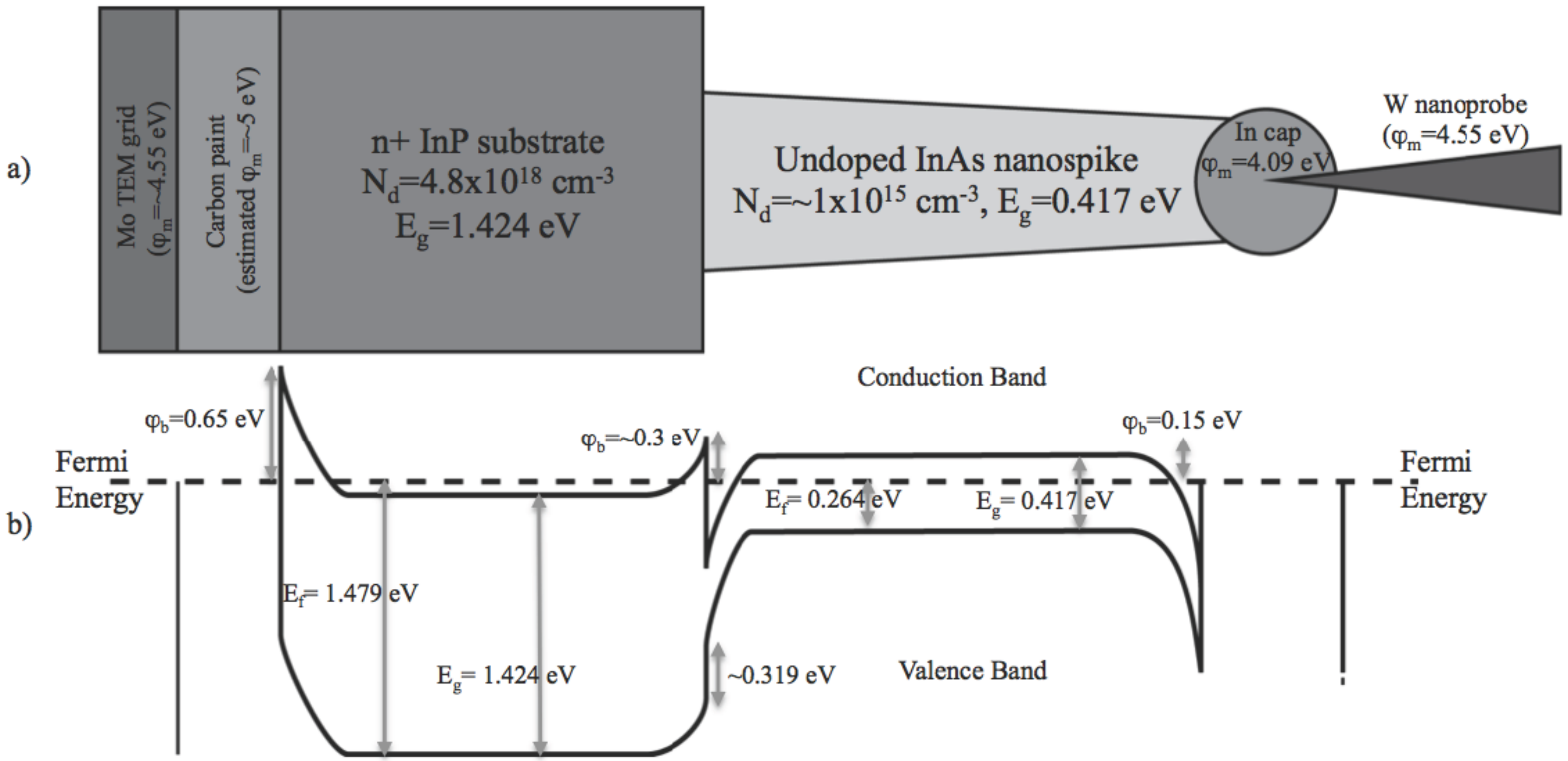

Figure 3.29: : (a) shows a schematic of a simplified InAs/InP nanospike junction, with the relevant structural elements and some electrical properties labeled. (b) shows a simple electronic band-diagram to match the junction in (a). The calculated energies of varies features are labeled in (b). Please note that the size of the depletion regions were not calculated and as shown are only a rough estimate

However, even without a complete understanding of conduction in the InAs/InP nanospikes, their level of conductivity can still compared to other similar structures. As one example, Figure 3.30 compares the behavior of the InAs/InP nanospikes to a somewhat similar example of an InAs nanowire junction taken from the literature. In that work the authors used gold catalyst particles and a VLS method to grow undoped InAs nanowires on a (111) GaAs substrate, and then tested those nanowires by contacting them with a W nanoprobe inside a SEM [30]. They reported the InAs nanowires as having an average length of 15 μm and diameters ranging from 50 to 150 nm. While this case in the literature does not exactly match the InAs/InP nanospike study conducted here, both it and this study examined long, undoped InAs nanostructures grown on a dissimilar III-V substrate with a wider bandgap. Thus it is sufficiently similar to allow for a useful if not direct one-to-one comparison. Figure 3.30(a) was taken from that literature example and shows a plot of the positive voltage IV response of three InAs nanowire [30], with a SEM image of their nanoprobe contacting a nanowire inset. By extracting the nanowire current at +0.2 V from that plot and using the nanowire dimensions reported in that work, the resistivity of those InAs nanowires can be estimated to range from approximately 0.0002 to 0.007 Ω*m. Figure 3.30(b) shows a similarly scaled plot of the positive IV response of the five randomly placed InAs/InP nanospikes included in this work's analysis. Their +0.2 V resistivity values range from approximately 0.008 to 0.11 Ω*m (see Table 3.4). By comparing both plots it can be seen that across the voltage range displayed both the InAs nanowires reported on in the literature [30] and the InAs/InP nanospikes from this work show similar levels of conductivity. Despite the inconsistencies of this comparison, that is a promising result. The InAs/InP nanospikes examined in this work were produced by FIB irradiation and have inhomogenous and ion damaged structures, and were not created by the one of the growth methods commonly used to create nanowires. Yet despite their different structures and means of production compared to the InAs nanowires reported on in the literature, they still appear to show comparable levels of conductivity. This is promising, as it indicates that the nanospikes may be electrically suitable for applications similar to those being considered for nanowires. In particular, they may be useful for thermoelectric applications, which require high electrical conductivity and poor thermal conductivity [5]. The disrupted, partially non-crystalline structure of the nanowires may assist in scattering phonons and so lower the thermal conductivity of the full nanowire junction relative to a similar nanowire based one.

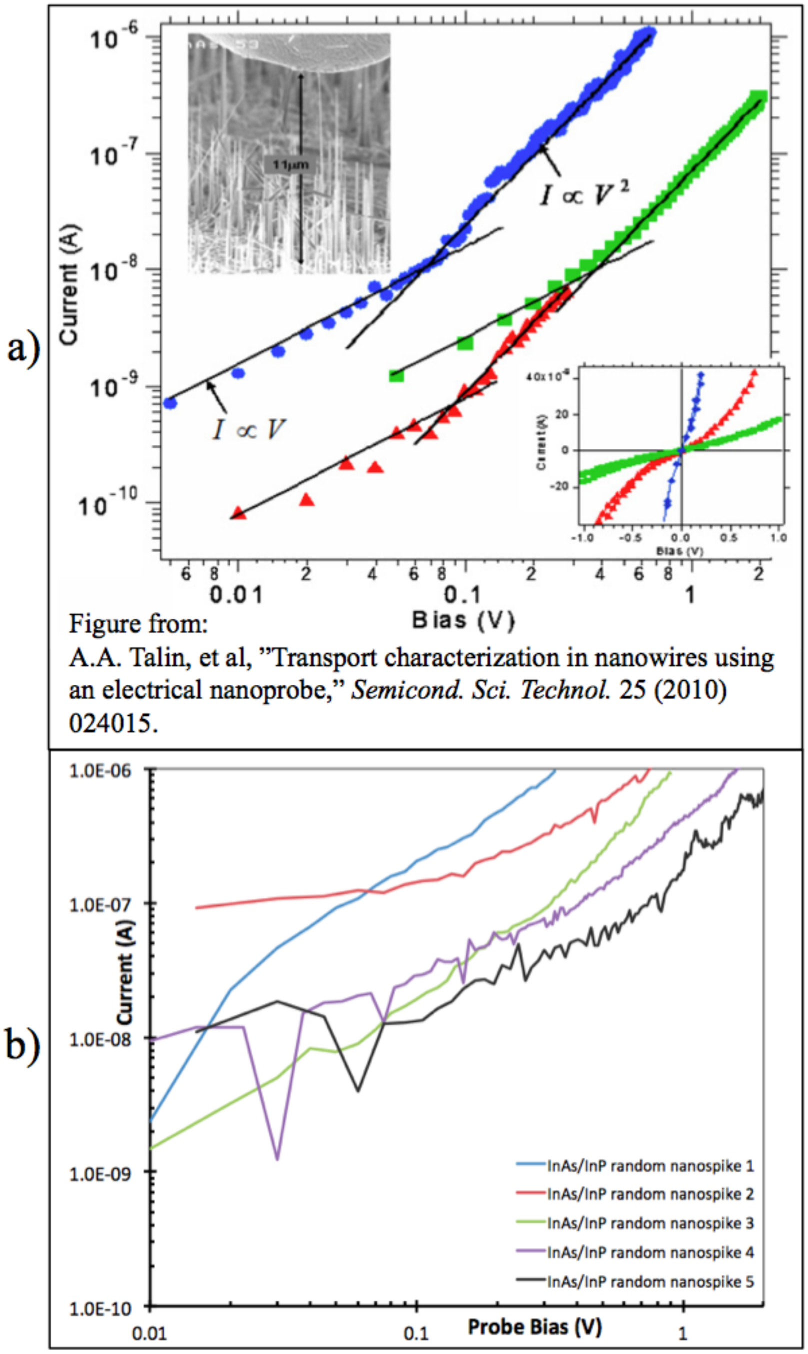

Figure from:
A.A. Talin, et al, "Transport characterization in nanowires using an electrical nanoprobe," *Semicond. Sci. Technol.* 25 (2010) 024015.

Figure 3.30: (a) shows an IV plot taken from reference [30] showing the results of SEM nanoprobe electrical testing of InAs nanowires, with an image of the probe in contact with a wire inset. (b) shows a plot of the IV results from this work's randomly placed InAs/InP nanospike tests, scaled to match (a). The data in (b) was taken in collaboration with J. Jokisaari and Prof. X.Q. Pan

3.7 Conclusions and Future Work

This work has demonstrated a 30 kV Ga^+ FIB erosion method for creating tall, nanowire-like InAs spike structures from both homoepitaxial InAs films and InAs/InP heterostructures. By varying FIB irradiation parameters it was found that lower beam currents and shorter spot dwell times produce nanospikes most effectively, with the optimum beam parameters used in this study being a ~7 pA beam current and 100 ns spot dwell time. Using those optimum conditions InAs nanospikes up to ~975 nm tall and InAs/InP nanospikes up to ~875 nm tall could be created using a 500 nm thick InAs film. The mechanism of nanospike formation was determined to be a self-assembled In etch-mask process. Indium droplets formed due to FIB irradiation protect the underlying material, allowing nanospikes to form as the surrounding material is milled away and controlling where they form. In the InAs/InP heterostructure case, no new nanospike formation was observed on regions of exposed InP substrate, such that the time available for nanospikes to form and grow taller is controlled by the initial InAs film thickness. Additional, because no nanospikes will form on the InP, the location of the InAs/InP interface affects the locations at which nanospikes are able to form. Nanospike formation and the effect of the InAs/InP interface on nanospike formation are the result of the unique responses of the III-V materials, and may be understood in terms of the differences in the FIB response of each material present.

A method for controlling nanospike location was also demonstrated. It was found that by pre-patterning the InAs film to control surface morphology the location of nanospikes produced using homoepitaxial InAs could be controlled in a limited manner. However, in the InAs case, continued irradiation will cause additional nanospike formation and disrupt the templating effect. Pre-patterning an InAs/InP heterostructure was used to more reliably control nanospike placement. Nanospikes will not form on the exposed regions of InP substrate, and because FIB pre-patterning defines the areas of InP that will be exposed earlier in the irradiation process it is able to effectively limit where nanospikes can form. Using an InAs/InP heterostructure with a known InAs film thickness provides an additional degree of control over the nanospike creation process by determining where and how tall those nanospikes may be. If nanospike arrays are to be used for device applications, reliably controlling nanospike location and size will be necessary.

TEM characterization of the nanospikes revealed that they have an inhomogeneous, ion-damaged structure. All of the nanospikes possessed an In droplet cap at their tip and an ion damaged outer layer composed of amorphous material and small regions of crystallinity. The cores of the nanospikes vary in structure. Some nanospikes cores were fully disrupted from ion damage and composed of many small crystalline regions and amorphous material. Others were only partially disrupted, containing discontinuous regions of crystallinity. Finally, some of the nanospike possessed single crystalline cores that maintained the orientation of the original film structure and that extended partially or almost entirely up the length of the nanospike. All of the templated InAs/InP nanospikes examined by TEM had almost entirely single crystalline cores. The crystallinity and orientation of those cores was verified by HRTEM. The identities of the various nanospike structural components were verified by STEM/EDS analysis.

With the nanoscale electrical and thermoelectric device applications in mind, the electrical responses of homoepitaxial InAs, randomly located InAs/InP, and templated InAs/InP nanospikes were examined using an *in-situ* TEM nanoprobe technique. In all cases where the probe was put into contact with the In droplet at the spike top the nanospikes showed a non-linear IV response. The dimensions of the nanospikes were measured and used to account for the effect of nanospike size on electrical response by generating J vs. E and resistivity values for each spike. Despite these attempt to normalize the nanospike electrical response with respect to nanospike size, there was still significant spread in the IV data, with different nanospikes showing very different levels of conductivity. It is likely that much of this variation in electrical response can be attributed to variations in nanospike structure. In an attempt to understand this, an approximate single crystalline core volume fraction was calculated for each nanospike and compared to it resistivity. In the case of the homoepitaxial InAs nanospikes, those with a greater volume of crystalline core generally had a lower resistivity. In the case of the randomly located and templated InAs/InP nanospikes there was no apparent trend between crystalline volume fraction and degree of resistivity. This may indicate that core structure plays less of a role in controlling electronic transport in the InAs/InP case.

In an attempt to further understand the non-linear nanospike electrical response, the nanospike IV data was compared to cases of semiconductor nanowires tested in a similar manner in the literature. The electrical behavior of the nanospikes appeared to most closely match other reported cases of contact barrier limited behavior. To examine that form of behavior, simplified band structures were constructed for the InAs and InAs/InP nanospike junctions. While very rudimentary, those structures allow examination of the expected barriers to electron transport in the nanospike system. For the case of InAs nanospikes, only very low barriers to electron conduction were predicted at the junction contacts and InAs/n+ InAs interface. However, it is possible that another electronic barrier exists in the system due to more resistive ion damaged nanospike regions in the conduction path, and this may be what is limiting InAs nanospike conduction. This agrees with the observation that InAs nanospikes with a large volume of crystalline core and correspondingly smaller amount of ion-damaged material were more conductive. Because ion damaged core structure varies from nanospike to nanospike, this may also helps explain why there is so much variation in electrical response between nanospikes with similar core types. For the InAs/InP junction case, a higher barrier was predicted at one electrical contact and the offset at the InAs/n+ InP interface also acts as a significant barrier. These higher barriers to electron transport may be part of what limits conduction in that system in addition to any effect from the ion damaged portion of the nanospike. Significantly more analysis will be needed to thoroughly understand the factors that control transport through the nanospikes created in this work.

Overall this study has reported on a new process for creating unique high-aspect ratio InAs nanostructures using a non-growth, FIB erosion method. A novel heterostructure pre-patterning technique for controlling nanospike location was also demonstrated. The nanospike formation mechanism and enhanced templating effect from use of an InAs/InP heterostructure highlight how the unique FIB responses of the III-V semiconductors may be exploited in novel ways to create unique nanostructures. In a first-of-its-kind study of electrical transport through ion erosion created nanostructures, the structure and electrical response of the nanospikes were characterized by using an in-situ TEM nanoprobe approach. The nanospikes were shown to possess a level of conductivity on par with at least one other example of VLS grown nanowires. These results are promising from the standpoint of considering the nanospikes for nanoscale device applications that will require both reasonable conductivity and the ability to reliably control nanostructure formation. In particular, the nanospikes may be useful for thermoelectric applications, which will require structures with high electrical conductivity and low thermal conductivity. The conductivity of the nanospikes has already been demonstrated here, and the nanospikes have an inhomogeneous and ion disrupted structure that may scatter phonons effectively and result in low thermal conductivity. However, in order to determine the ultimate feasibility of using nanospikes in any application and thermoelectric applications specifically, more testing and analysis of their transport properties needs to be conducted.

Of primary importance in evaluating the usefulness of the nanospikes for device application will be to determine if the nanospikes can be created over wider areas. In this work nanospikes were created only over 5x5 µm areas in serial fashion. In order to be useful in any manufactured device, nanospikes will need to be created over much larger macro-scale areas. It is possible this may be accomplished using a broad-beam ion implantation system and high ion current densities close to those achieved by FIB systems to irradiate and sputter material from larger areas. A study examining the feasibility of using other ion irradiation techniques to create nanospikes over broader areas needs to be conducted. Assuming that nanospike may be created over macro-scale areas, the optimum conditions for reliable nanospike creation will again need to be determined and the efficacy of templating nanospikes across large areas will need to be studied. If a method cannot be found for creating nanospikes in a controllable way over larger areas, it seems unlikely that the nanospikes will be considered for broad use in devices.

The transport properties of the nanospikes also need to be more thoroughly characterized to determine if they will ultimately be useful for devices. Those features of nanospike structure that control their conductivity need to be more thoroughly determined. This will require additional electrical testing, and may require testing ensembles of nanospikes to examine their properties on average. Specifically for consideration in thermoelectric applications, nanospike thermal properties and the structural features that control them will need to be characterized. On the individual nanospike level this may pose a significant experimental challenge, as probing the thermal properties of an individual nanospike and decoupling that result from the influence of the nanospike's substrate and surrounding features may be difficult. It may be easier and ultimately more useful to examine thermal transport in a nanospike ensemble. Once the electrical and thermal properties of the nanospikes have been thoroughly characterized, it may be possible to optimize their properties by varying production parameters to more carefully control their structure. Then ways in which nanospikes may be beneficially incorporated into nanostructure-based devices may be more directly examined.

3.8 References

[1] Yoffe, A. D. *Advances in Physics* **50**, 1-208 (2001).

[2] Hu, J., Odom, T. W. & Lieber, C. M. *Acc. Chem. Res* **32**, 435-445 (1999).

[3] Gudiksen, M. S., Lauhon, L. J., Wang, J., Smith, D. C. & Lieber, C. M. *Nature* **415**, 617-620 (2002).

[4] Xia, Y. et al. *Advanced Materials* **15**, 353-389 (2003).

[5] Dresselhaus, M. S. et al. *Physics of the Solid State* **41**, 679-682 (1999).

[6] Dresselhaus, M. S. et al. *Advanced Materials* **19**, 1043-1053 (2007).

[7] Li, D. et al. *Applied Physics Letters* **83**, 2934 (2003).

[8] Zhou, F., Moore, A., Bolinsson, J. & Persson, A. *Physical Review B* (2011).

[9] Katzenmeyer, A. M. et al. *Ieee Transactions On Nanotechnology* **10**, 92-95 (2011).

[10] Dick, K. A. *Progress in Crystal Growth and Characterization of Materials* **54**, 138-173 (2008).

[11] Tanemura, M., Aoyama, S., Fujimoto, Y. & Okuyama, F. *Nuclear Instruments and Methods in Physics Research Section B: Beam Interactions with Materials and Atoms* **61**, 451-456 (1991).

[12] Nozu, M., Tanemura, M. & Okuyama, F. *Surface Science* **304**, L468-L474 (1994).

[13] Chini, T., Kato, J. & Tanemura, M. *Nuclear Instruments and …* (1995).

[14] Yuba, Y., Hazama, S. & Gamo, K. *Nuclear Instruments and Methods in Physics Research Section B: Beam Interactions with Materials and Atoms* **206**, 648-652 (2003).

[15] Nerbø, I. S. et al. *Applied optics* **47**, 5130-5139 (2008).

[16] Le Roy, S., Barthel, E., Brun, N., Lelarge, A. & Søndergård, E. *Journal of Applied Physics* **106**, 094308 (2009).

[17] Wei, Q., *Self-organized Nanoscale Patterning under Ion Beam Irradiation,* PhD Thesis, University of Michigan, Ann Arbor, 2009.

[18] Szot, J., Hornsey, R., Ohnishi, T. & Minagawa, S. *Journal of Vacuum Science & Technology B: Microelectronics and Nanometer Structures* **10**, 575 (1992).

[19] Lugstein, A., Weil, M., Basnar, B., Tomastik, C. & Bertagnolli, E. *Nuclear Instruments and Methods in Physics Research Section B: Beam Interactions with Materials and Atoms* **222**, 91-95 (2004).

[20] Grossklaus, K. A. & Millunchick, J. M. *Journal of Applied Physics* **109**, 014319 (2011).

[21] Bradley, R. M. & Harper, J. M. E. *J. Vac. Sci. Technol. A* **6**, 2390-2395 (1988).

[22] Le Roy, S., Søndergård, E. & Plapp, M. *Physical Review B* **81**, 161401 (2010).

[23] Pearton, S. J. et al. *Journal of Applied Physics* **64**, 629-636 (1988).

[24] Wesch, W. *Nuclear Instruments and Methods in Physics Research Section B: Beam Interactions with Materials and Atoms* **68**, 342-354 (1992).

[25] Glas, F., Harmand, J. C. & Patriarche, G. *Physical Review Letters* **99**, 146101 (2007).

[26] Lugstein, A., Basnar, B., Smoliner, J., Bertagnolli, E. & Weil, M. *Journal of Vacuum Science & Technology B: Microelectronics and Nanometer Structures* **22**, 2995 (2004).

[27] Oda, O. *Compound Semiconductor Bulk Materials and Characterization,* (World Scientific Publishing Co., Singapore, 2007).

[28] Schroer, M. D. & Petta, J. R. *Nano Letters* **10**, 1618-1622 (2010).

[29] Dayeh, S. A. *Semiconductor Science and Technology* **25**, 024004 (2010).

[30] Talin, A. A. et al. *Semiconductor Science and Technology* **25**, 024015 (2010).

[31] Schricker, A. D., Forrest III, M. D., Wiacek, R. J. & Korgel, B. A. *Nanotechnology* **17**, 2681 (2006).

[32] Talin, A. A., Léonard, F., Swartzentruber, B. S., Wang, X. & Hersee, S. D. *Physical Review Letters* **101**, 76802 (2008).

[33] Talin, A. A., Swartzentruber, B. S., Léonard, F., Wang, X. & Hersee, S. D. *Journal of Vacuum Science & Technology B: Microelectronics and Nanometer Structures* **27**, 2040-2043 (2009).

[34] Katzenmeyer, A. M., Léonard, F., Talin, A. A., Wong, P. S. & Huffaker, D. L. *Nano Letters* 3067-3072 (2010).

[35] Zhang, Z. Y., Jin, C. H., Liang, X. L., Chen, Q. & Peng, L. M. *Applied Physics Letters* **88**, 073102-073102-3 (2006).

[36] Zhang, Z. et al. *Advanced Functional Materials* **17**, 2478-2489 (2007).

[37] Liu, Y., Zhang, Z. Y., Hu, Y. F., Jin, C. H. & Peng, L. M. *Journal of Nanoscience and Nanotechnology* **8**, 252-258 (2008).

[38] Liu, B., Bando, Y., Wang, M. & Golberg, D. *Journal of Nanoscience …* (2010).

[39] Sze, S. M., Coleman, D. J. & Loya, A. *Solid-State Electronics* **14**, 1209 (1971).

[40] Haynes, W. M. (ed) *CRC Handbook of Chemistry and Physics, 92nd* (CRC Press, Cleveland, 2011).

[41] Vurgaftman, I., Meyer, J. R. & Ram-Mohan, L. R. *Journal of Applied Physics* **89**, 5815 (2001).

[42] Bhattacharya, P. *Semiconductor optoelectronic devices, 2nd Edition* (Prentice Hall, Upper Saddle River, NJ, 1997).

[43] Sze, S. M. & Ng, K. K. *Physics of Semiconductor Devices, 3rd Edition* (John Wiley & Sons, Inc., Hoboken, NJ, 2007).

Chapter 4

3-D Focused Ion Beam Patterning of III-V Substrates

4.1 Introduction and Background

Of the compound semiconductor materials the III-V semiconductors have seen the broadest use [1], specifically in the areas of optoelectronics, high electron mobility applications, and solar power generation. Part of the reason why the III-V semiconductors have seen such wide application and continue to see intense development is because the different III-V binary compounds may be readily alloyed together, allowing access to a wide range of bandgaps [2], and they may be grown epitaxially on one another as single-crystalline thin films, allowing for many different heterostructure combinations. These capabilities allow for the creation of a wide range of different heteroepitaxially grown thin film structures, in turn allowing design of a broad range of different electronic and device structures. However, the lattice parameters of the different III-V compounds and alloys also span a wide range (see Figure 1.1) and many III-V heterostructure combinations with otherwise promising electronic band structures are not used due to the deleterious effects of lattice mismatch strain. Mismatch strain arises when a growing heteroepitaxial film distorts its equilibrium structure in order to accommodate the lattice parameter of the material it is being grown upon. This strain increases with film thickness, and once the growing film exceeds some critical thickness it will relax through surface roughening or the creation of defects such as misfit and threading dislocations [3,4]. Threading dislocations, surface roughness, and other defects such as stacking faults and twins are extremely deleterious to the electronic properties of the film [5], and high defect densities will render an active layer unusable for applications requiring high optical efficiency or high carrier mobility. As lattice matched substrates for many III-V combinations are not available, growth is carried out upon readily obtainable GaAs and InP substrates. When growing device layers, the damaging effects of lattice mismatch require that strain in the growing film be carefully controlled or mitigated in some fashion.

A number of methods have been devised to allow the growth of smooth, low-defect density films in lattice-mismatched semiconductor systems. These include growth on metamorphic buffer layers [6-8], growth of threading dislocation filtering structures [9,10], and layer transfer techniques [11,12]. While successful, these approaches require growth of additional thick layers that are time consuming to produce and greatly add to the complexity of the fabrication process. Metamorphic buffer layers may also cause roughness and cross-hatching on the film surface [13]. Because of these drawbacks the development of other methods for controlling strain and defect densities in mismatched films is an active area of research. An alternative method that has seen some success in both the Si-Ge (group IV) and III-V systems is growth upon patterned substrates. Improvement in the quality of films grown upon a 3-D patterned or otherwise modified substrates has been reported for both the Si-Ge system [14,15] and a limited number of III-V heterostructure systems [16-18]. These previous studies have been limited in the types of patterns and material combinations they explore, and did not attempt to optimize pattern geometry to achieve the largest improvement in film quality possible.

III-V growth on patterned substrates has previously shown promise as a general method for reducing strain and controlling defect densities in lattice mismatched systems, but more complex studies examining the effects of different patterning parameters on film quality have not been carried out. This study was conducted to explore the use of FIB substrate irradiation and 3-D patterning to engineer strain relaxation and control defect formation in lattice mismatched III-V heteroepitaxial films. FIB patterning was chosen as the method for substrate modification to allow for rapid examination of the effects of different patterning types and geometries on mismatched film growth. The effects of FIB irradiation and milling on GaAs and InP, the most common III-V substrates for device applications, were characterized. Patterning results were found to depend strongly on the specific pattern designs used and the different FIB responses of each material. Lattice-mismatched InAs and InGaAs films were grown on a variety of FIB created patterns milled into InP and GaAs wafers respectively, and the films grown on the FIB patterned regions were characterized to identify any changes caused by the patterns and to determine film quality. Growth on patterned substrates was found to significantly alter the diffusion of adatoms and resulting film morphology, and it was found that by altering 3-D feature size the regularity and size of the film islands grown on them could be manipulated. TEM analysis revealed growth on patterned regions did not reduce the film defect density, and growth on FIB damaged areas containing group III nanodots was found to be detrimental to film quality. As a result patterning strategies were developed to limit the influence of group III nanodot formation and ion damage. In the end it was determined that the FIB method of patterning and the FIB response of the III-V materials were responsible fort the observed poor film quality, and not inherently the patterned growth approach itself that produced this negative result. This conclusion is discussed with regards to the FIB response of the III-V materials, and suggestions for possible ways to improve film relaxation and quality are made. While the goal of using FIB 3-D substrate patterning to improve film quality was not met, this work still may provide valuable insight into the effect of FIB irradiation on the III-V materials and the ways in which substrate topography controls film growth.

4.1.1 *<u>The effects of mismatch strain on epitaxial thin films</u>*

The aim of this work and previous studies of substrate patterning as a method for controlling strain in heterostructures has been to limit the damaging effects of lattice mismatch strain on growing films. In practice this means preventing surface roughness and the formation of crystalline defects damaging to film properties, in particular threading dislocations, stacking faults, and twins which cut through the thickness of active device layers. Mismatch strain in the III-V semiconductors builds up as a film is grown epitaxially on a substrate with a different lattice parameter. In order for epitaxial growth to occur, the crystalline structures of the film and substrate must elastically strain to accommodate their difference in lattice parameter. In most cases the substrate is much thicker than the film, and so the atoms of the growing film are the ones displaced and the film takes up most of the strain necessary to accommodate the lattice mismatch. The degree of lattice mismatch, f, and consequently the amount of in-plane strain required to match the film in-plane lattice parameter to that of the substrate, is defined as [1]

$$f = \frac{a_s - a_f}{a_f} \tag{4.1}$$

where a_s is the lattice parameter of the substrate and a_f is the lattice parameter of the film. Distortion of the film lattice in plane also produces tetragonal distortion out of plane. Initially the film will grow coherently strained to fully match the in-plane lattice parameter of the substrate, a mode of growth referred to as pseudomorphic. As the film continues to grow the elastic strain energy in it increases with film thickness, increasing the energy of the system. Eventually that strain energy reaches a critical point past which the energy of the system may be lowered through a strain release mechanism. This relaxation mechanism often takes the form of either misfit dislocation formation at the heterointerface, surface roughening, or a transition to a 3-D growth mode. Figure 4.1 shows this process schematically. The film thickness at which these strain-relieving processes occur is called the critical thickness, h_c. Misfit dislocations alone may not be damaging to film properties. However misfit dislocation formation is linked to the formation of threading dislocations and other through-film defects. Thus identifying and controlling the physical phenomena which lead to strain creation and drive the creation of dislocations is of paramount importance to understanding how the number of defects may be limited or defects prevented from forming in the film altogether.

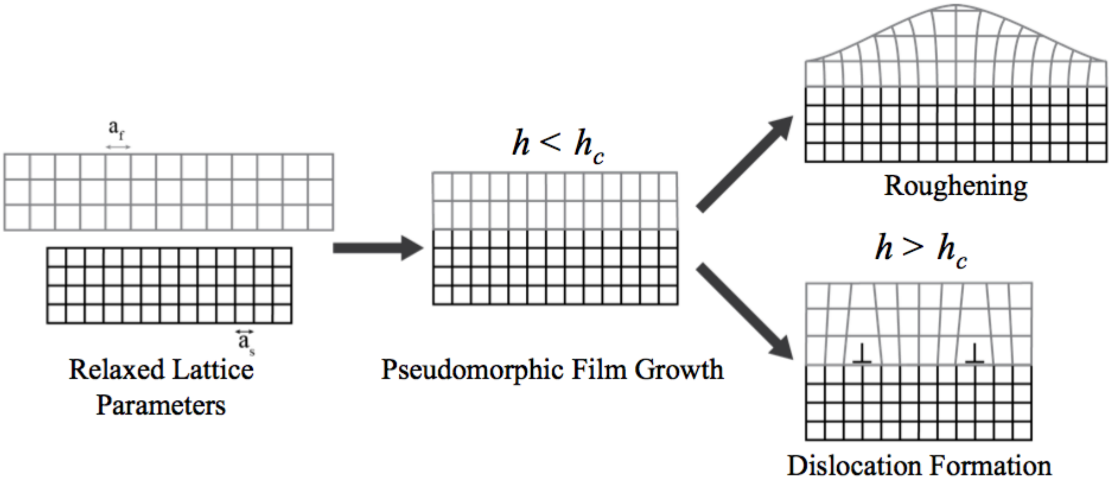

Figure 4.1: Schematic showing an epitaxial film with a larger parameter than its substrate first growing psuedomorphically strained to match the substrate and then above the critical thickness relaxing by roughening or forming dislocations.

The critical thickness, as corresponding to the point at which misfit dislocations initially form, was first theoretical calculated for the Ge_xSi_{1-x} system by Van der Merwe

[19]. That theory predicts that misfit dislocations form when the areal strain energy of the growing film exceeds a critical value, past which the strain energy relieved by creation of a dislocation is greater than the energy of the dislocation itself. Van der Merwe's theory and predictions were later refined by the work of People and Bean [4]. Both sets of authors clearly identify strain energy generated at the interface and in the film as the driving force for misfit dislocation nucleation. Another well-known theory describing h_c and dislocation generation in a strained film is that of Matthews and Blakeslee [3], which relies on a mechanical equilibrium rather than energy balance approach to predict h_c. That theory requires the presence of pre-existing threading dislocations in the film, and defines the critical thickness as the point at which stress due to mismatch becomes great enough to drive the pre-existing dislocations through the film. Then as those threading dislocations travel they create new misfit dislocation length along the film/substrate interface, relieving strain. This process is illustrated schematically in Figure 4.2. New defects may also be created when moving dislocations interact to form new threading dislocations or dislocation loops [14]. The Van der Merwe and Matthew and Blakeslee theories regarding critical thickness identify strain energy in the film and dislocation movement respectively as the factors that control defect generation in a strained epitaxial film. By identifying these two mechanisms they provide routes for designing strategies to preventing defect generation.

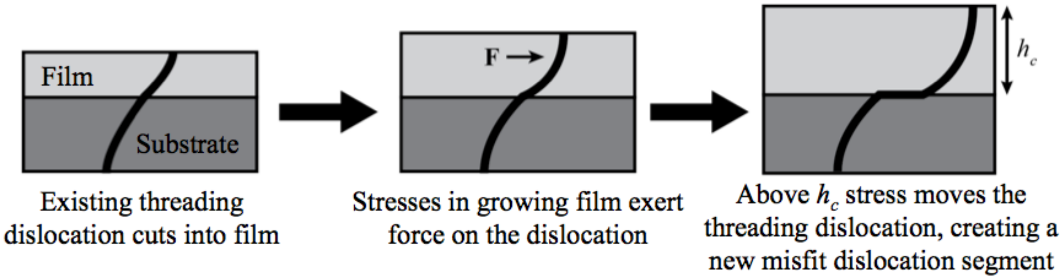

Figure 4.2: Schematic depicting the Matthew-Blakeslee mechanism of misfit dislocation production.

4.1.2 Patterning to reduce strain and threading defect density

Luryi and Suhir first proposed that lattice mismatched film growth on patterned substrates might be used to reduce strain in the film and reduce or eliminate defect formation [20]. They predicted that by growing on a series of "seed" pads separated by regions where the film is not in rigid contact with the substrate that the film will be able to periodically relax over those regions. The areas between pads may be anything that allows film growing over it to freely slip and so prevent strained growth. Stress and strain in the growing film will then be concentrated at the seed pads with a maximum at the pad center and minimums at the pad edges. If the seed pads are widely enough separated that the stress fields from neighboring pads do not overlap and small enough such that the maximum strain at their center does not exceed the critical energy for dislocation formation then no new defects will be formed as the film grows. This in principle would allow for a film to be grown far thicker than its standard h_c without nucleating new defects, assuming growth is dominated by the pads. In order for a film to be grown arbitrarily thick without reaching a critical thickness, the pad spacing needs to be near the equilibrium misfit dislocation spacing of the normal continuous interface. As a test case, Luryi and Suhir predicted that a maximum pad width of ~20 nm and minimum pad separation of ~3.2 nm would be required to allow for growth of arbitrarily thick Ge films on Si (a 4.0% lattice mismatch) without new dislocation nucleation. Even for cases where the required pattern dimensions for arbitrarily thick growth are not attainable, films grown on nanoscale patterns may still be able to partially relax and see some improvement in defect density. In the time following Luryi and Suhir's proposal several groups have had success reducing defect densities in mismatched III-V films using growth on substrates patterned with 3-D features on the sub-micron and nanoscale, and so have demonstrated the viability of the patterning approach [18,21].

Luryi and Suhir's theory addresses the strain energy driven mechanism for dislocation creation, but does not directly address the problem of new defect creation by dislocation movement and interaction. However, growth on 3-D patterns has been demonstrated to reduce the creation of new defects due to the strain driven movement of pre-existing defects as well. Fitzgerald et al grew 350 nm of $In_{0.05}Ga_{0.95}As$ on 2 μm high GaAs pillars of various lateral sizes down to 2 μm [22]. They reported a significant drop in the dislocation density on the pillars and attributed this to dislocation movement being constrained and halted at the pillar edges and a reduced number of active dislocations sources present in the limited growth area. As an alternative approach to dislocation blocking, Hull et al fabricated an array of 2 μm diameter oxide pillars on a silicon substrate and then grew Ge_xSi_{1-x} (x=0.15-0.20) films up to several microns in thickness on the remaining silicon area between the pillars [23]. They saw a two order of magnitude drop in dislocation density due to the pillars blocking dislocation movement. Thus growth on patterned substrates may be used to both relieve strain and prevent dislocation nucleation and to prevent the movement of dislocation generating defects.

4.2 Experimental Methods

In this work creation and characterization of FIB milled patterns was carried out using both the FEI Nova Nanolab dual-beam FIB/SEM system and the UHV FEI Magnum ion column chamber attached to the MBE growth chamber. All patterning of substrates for subsequent film growth was carried out using the UHV FEI Magnum column. This was done so those samples could be transferred *in-vacuo* to the MBE growth chamber without fear of exposure to air and oxidation, and because carbon contamination deposited by SEM imaging in the dual-beam system was found to negatively affect film growth. [100] n+ InP and n+ GaAs substrates were irradiated using a 30 kV Ga^+ FIB kept at normal incidence to the sample surface in order to either blanket irradiate square regions or ion mill specific patterns. The majority of irradiation and patterning was carried out using a 10 pA beam defining aperture, corresponding to a 12 nm beam diameter and actual measured beam currents in the range of approximately 7.5 to10 pA. Occasionally to decrease the time necessary to generate a larger pattern, a 30 pA aperture, corresponding to beam diameter of 16 nm and beam currents in the range of 28 to 30 pA, or larger was used. However, as the FIB patterning resolution of the UHV Magnum FIB system was limited not by its optics but by chamber vibration to 50-60 nm, increasing ion beam current and probe diameter did not have a noticeable effect on patterning resolution. A beam spot overlap of 50% was used for all FIB experiments to ensure even ion dose was delivered to all irradiated areas. Number of beam passes, spot dwell time, and total ion dose were varied between experiments to achieve the desired degree of irradiation or milled pattern depth. As a general rule it was found that using a longer spot dwell time and a lower number of beam passes produced patterns with more sharply defined edges. Specific pattern types were milled by inputting the pattern as a bitmap (24-bit .bmp) image into the FIB control software and then scanning the FIB to match the image. On each FIB modified substrate for characterization or film growth many different patterned regions were created, with each different pattern separated by a minimum distance of 10 μm.

The III-V films grown on patterned substrates were produced by MBE using the EPI 930 MBE system attached to the FEI Magnum FIB system. For more information on that growth system see section 1.5.1 of this dissertation. For this study InAs films were grown on locally patterned InP substrates and InGaAs films were grown on locally patterned GaAs substrates. In the InP case, the substrates were first patterned in the FIB system and then transferred to the growth chamber for oxide desorption and InAs film growth. In the GaAs case, either the substrate was patterned first, then desorbed, and finally had InGaAs grown on it, or the wafer was first desorbed, had a 500 nm GaAs buffer layer deposited, was then patterned, and finally had InGaAs grown on it. InAs films on InP were grown at temperatures ranging from 460-470 ˚C, with an InAs growth rate of ~0.25-0.3 ML/s, and an As_4 overpressure. InGaAs films were grown on GaAs with compositions ranging from ~33-45% In, at a temperature of 480 ˚C, with a combined InGaAs growth rate of ~0.54-0.99 ML/s, and under an As_4 overpressure. In the InAs case, films were grown to equivalent mass thicknesses of 50-500 nm. InGaAs films were grown either 200 or 500 nm thick.

Characterization of FIB patterned areas on both wafers patterned in the dual-beam FIB/SEM and wafers patterned using the UHV Magnum ion beam system was carried out by SEM and AFM. Wafers patterned in the UHV system were also characterized by ion-induced secondary electron (ISE) imaging using the ion beam immediately following their production. Characterization of the patterned areas was conducted to verify pattern creation, examine milling depths, examine pattern features such as edge sharpness, and to look for the presence of FIB created group III nanodots or droplets. InAs and InGaAs films grown on regions of FIB patterned substrate and the surrounding area were characterized by SEM and BF, DF, and high-resolution TEM imaging of cross-sectional samples.

Because individual patterned regions were on the order of 10x10 μm and entire groups of patterned regions never covered an area greater than 110x110 μm, examining the patterns in cross-section by TEM could not be accomplished using traditional film cross-section preparation techniques. Instead a FIB lift-out method was used to extract thin cross-sectional lamellae from individual patterned regions. FIB lift-out was accomplished using the FEI Nova Nanolab dual-beam with Pt GIS and the FEI Quanta 200 dual-beam with Pt GIS and Omniprobe nanomanipulator. Figure 4.3 shows a single patterned area throughout the FIB lift-out process. During lift-out both the ion beam and electron beam were used to provide views of the sample area from different perspectives. The FIB lift-out process first involves protecting the surface of the area to be examined from later ion milling steps with a layer of deposited Pt. This protective mask was created using the GIS in the dual-beam instruments to first deposit a thin (<100 nm) layer of Pt using the electron beam, and then to deposit an additional thicker layer of Pt (200-500 nm) using the ion beam on top of the original e-beam Pt (Figure 4.3 (a)). If the thin e-beam Pt layer was not deposited before the ion-beam Pt, then the top surface of the samples had an approximately 20 nm deep ion damaged layer across their surface. After Pt deposition trenches were milled out to either side of the sample using a high current 30 kV FIB and cross-section patterns. After trenches were milled, the area of interest was further thinned to <5 μm thick using cleaning cross-section patterns. Then "U-cuts" were made along the bottom and up the sides of the thinned area, resulting in a thin cross-section lamella attached to the sample only by two small bridges near the material surface (visible in Figure 4.3(c)). In the FEI Quanta system the sample could then be tilted to >40° relative to the SEM beam and the Pt GIS needle and Omniprobe nanomanipulator tungsten probe could be inserted (Figure 4.3(b)). The W probe was then brought close to the sample (Figure 4.3(c)) and then carefully brought into contact with the top of the thinned lamellae. The probe was then attached to the sample using ion-beam deposited Pt, and the lamella was cut free from the sample by ion milling through the two thin bridges of material at either side of it (Figure 4.3(d)). The lamella, now attached to only the W probe, was lifted out of the sample and transferred over to a Cu Omniprobe TEM grid designed with a stepped backside for lift-out specimen attachment (Figure 4.3(e)). The lamellae was carefully directed into contact with the grid along one of its sides (Figure 4.3(f)) and attached to the grid with ion-beam deposited Pt. The sample could then be cut free from the W probe and left attached to the Cu grid (Figure 4.3(g)). In the FEI Nova Nanolab FIB/SEM system the sample could then be tilted normal to the ion beam and thinned further to electron transparency. This was accomplished by first thinning the sample to <500nm thick using the 30 kV ion beam and cleaning cross-section patterns on both sides of the sample, and then thinning the sample to a final thickness of <100 nm in the area of interest using a low current 10 kV ion beam (Figure 4.3(h)). A lower accelerating voltage is used for the final thinning steps to decrease the depth of the ion damaged region on both sides of the sample. At this point samples could be transferred to the TEM for imaging. Because no effort was made to orient patterned regions or lift-out specimens relative to the major crystallographic directions of the sample wafer, during TEM imaging samples were tilted to whichever low-index zone-axis could be most easily reached.

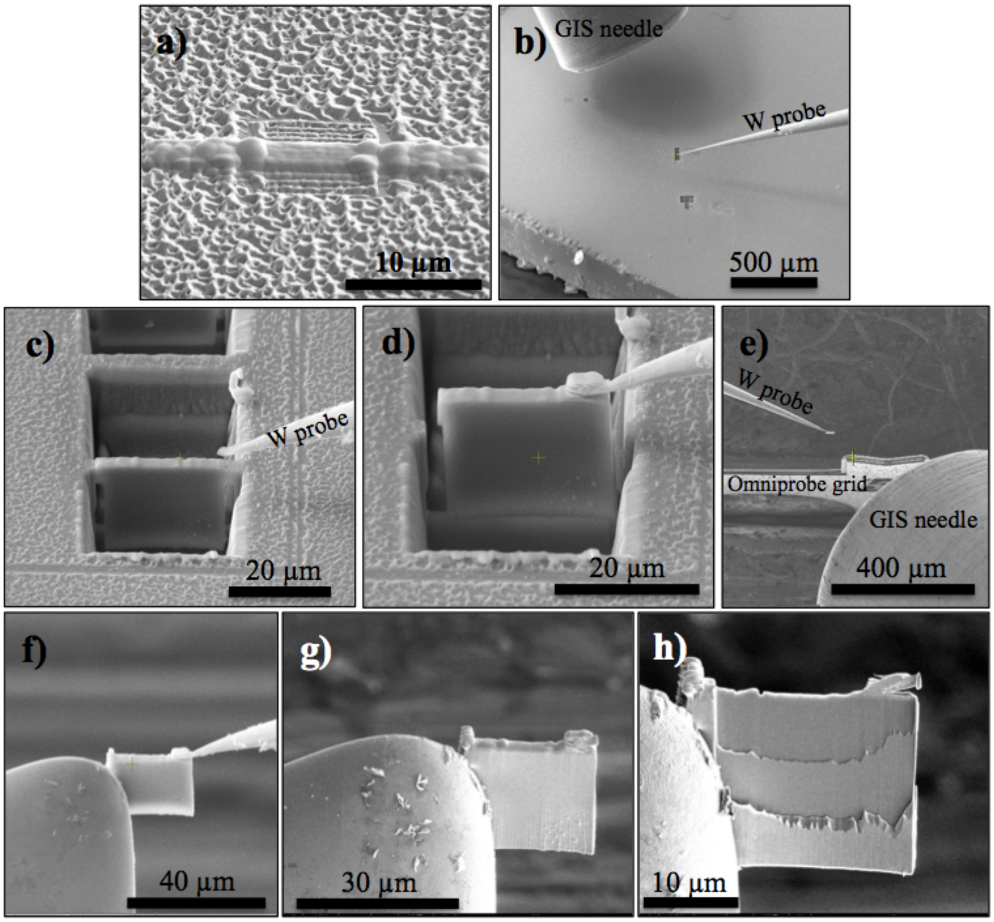

Figure 4.3: A series of images showing a sample throughout the FIB lift-out preparation process. (a) shows the patterned area following electron and ion beam Pt deposition, (b) shows the inserted GIS needle and W probe on approach to the sample, (c) shows the W probe approaching the sample lamella, (d) shows after the probe has been attached and the lamella has been cut free, (e) shows the probe with attached sample approaching the Cu Omniprobe grid, (f) shows the sample in contact with the grid, (g) shows the sample after being attached to the grid before final thinning, and (h) shows the sample after being thinned along its top surface to electron transparency for TEM imaging.

4.3 FIB Pattern Generation

Prior to and in between film growth experiments a variety of different 3-D pattern types were created by normal incidence 30 kV FIB milling of InP and GaAs substrates and then characterized. This was done to identify the best conditions for pattern creation, to identify those pattern designs that might be optimum for film growth, and to examine the features of those patterns that might affect film growth. For those purposes a variety of different pattern types were designed and milled using different FIB parameters. These included arrays of raised square mesas separated by trenches, square recess arrays separated by thin walls, arrays of small holes, rectangular mesa arrays, isolated pillars, and other pattern types. The advantage of using FIB milling to create those patterns was that it allowed many different pattern types to be created quickly using different FIB parameters over a relatively small area, allowing rapid and easier examination of many different patterning variables using only a few samples overall. SEM images of a number of different pattern types milled into InP and GaAs along with their FIB milling parameters can be seen in Figures 4.4 and 4.5 respectively. Figures 4.4(a) and 4.5(b) show low magnification SEM images of areas with fiducial marks and a group of several different patterns. In the end to limit the number of experimental variables, the majority of testing was carried out using only raised square mesa (as shown in Figures 4.4(d), 4.5(c), and 4.5(d)), square recess (Figure 4.5(b)), and hexagonal hole array (Figure 4.4(b)) patterns. The mesa size, trench depth, and trench spacing of the mesa patterns were varied, while the recess size, depth, and wall thickness of the recess patterns were varied. For the hole array patterns, hole size was kept at the minimum achievable diameter allowed by the FIB resolution while hole depth and spacing were varied.

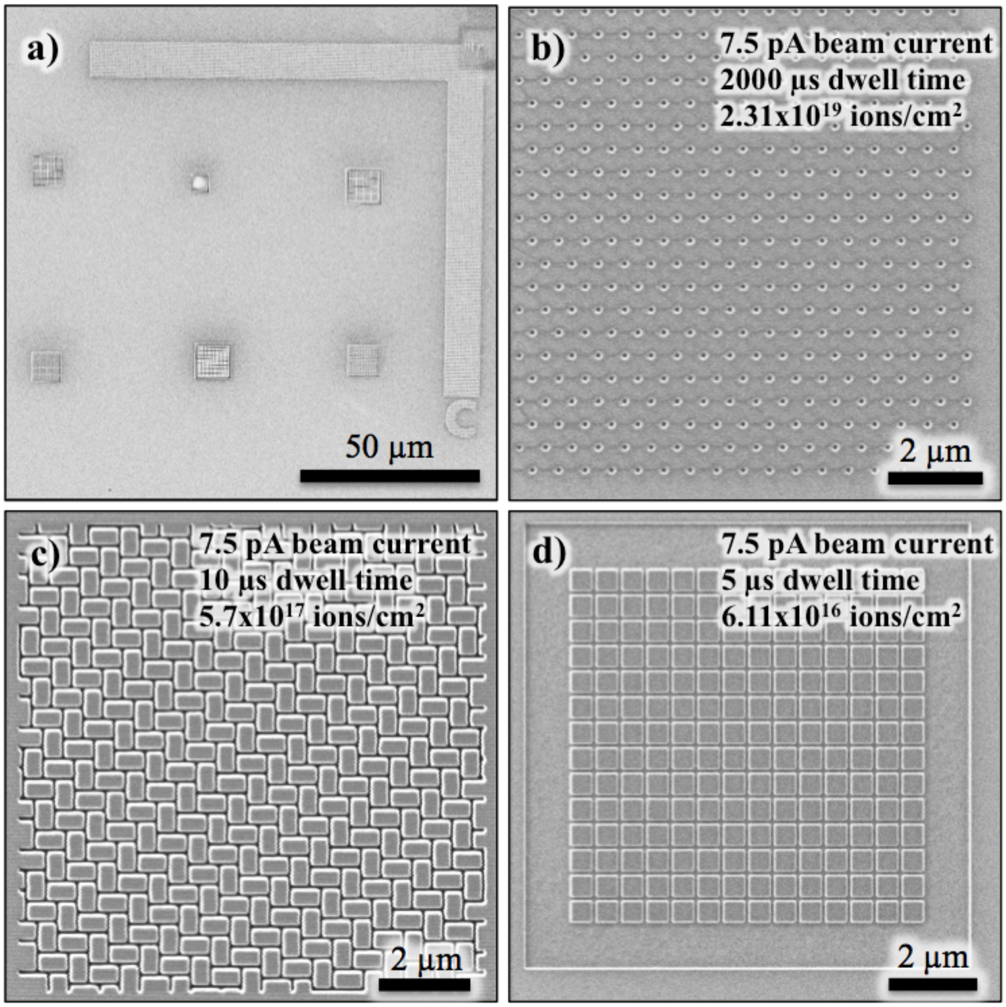

Figure 4.4: Images showing patterned regions of InP. (a) shows an SEM image of an area contained several patterns and identifying fiducial mark. (b), (c), and (d) show ISE images of different patterns. The basic FIB parameters used to create each pattern are given at the top right-hand side of each image.

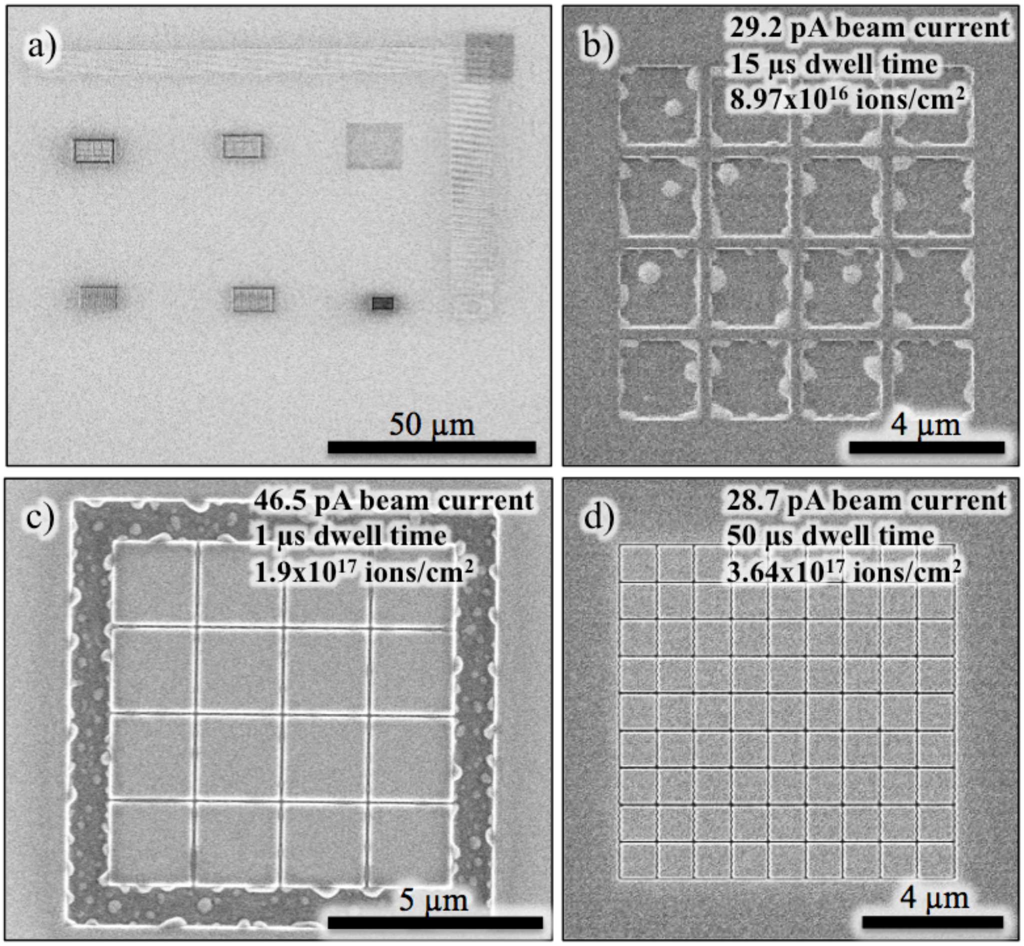

Figure 4.5: Images showing patterned regions of GaAs. (a) shows an SEM image of an area contained several patterns and identifying fiducial mark. (b) and (d) show ISE images and (b) shows an SEM image of different patterns. The basic FIB parameters used to create each pattern are given at the top right-hand side of each image.

As patterns were milled into both InP and GaAs it was found that the FIB spot dwell time and correspondingly the number of FIB passes necessary to mill each pattern affected how well the edges of pattern features were defined and matched to the original image file. The default spot dwell time for the FIB instruments used was 1 μs, but it was generally found that longer dwell times in the range of 5-50 μs produced better defined pattern features, depending on pattern type. The minimum well-defined pattern feature size that could be produced was limited by the resolution of the chosen FIB probe and by vibration in the FIB vacuum systems. Figure 4.6 shows arrays of (a) 2x2 μm, (b) 0.5x0.5 μm, and (c) 250x250nm square mesas milled into InP. It can be seen that as the desired mesa size decreases the mesas become less well defined, with the mesas in Figure 4.6(a) having clear, square edges while the mesas in Figure 4.6(c) are rounded and poorly defined. It was assumed that smooth layer-by-layer film growth and trench overgrowth would be promoted by flat patterns with well-defined features, so for film growth experiments FIB milling parameters and pattern types that produced features with those qualities were selected for pattern creation.

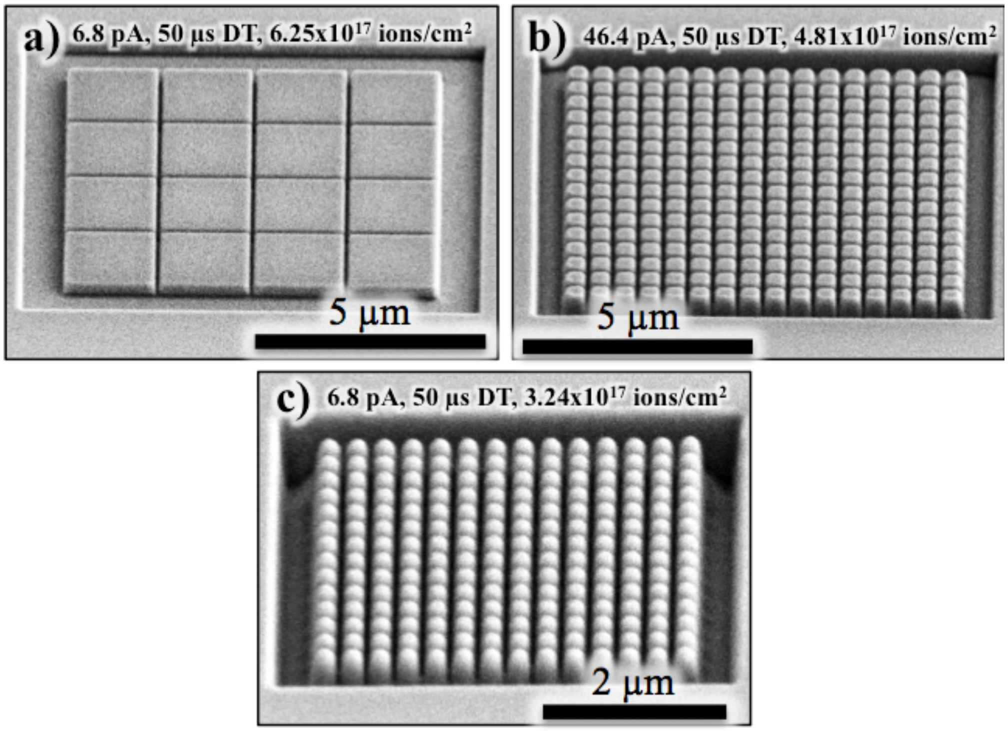

Figure 4.6: SEM images showing square mesa array patterns with mesas of different sizes. The basic FIB parameters used to create each pattern are given along the top of each image.

FIB milling to create patterns was also observed to produce group III droplets or nanodots in the FIB irradiated regions and along the edges of ion milled features. The phenomenon of FIB-induced group III nanodot formation is discussed thoroughly in chapter 2 of this dissertation. Figures 4.7(a) and (b) respectively show In nanodots on an InP raised mesa array and Ga droplets on a GaAs raised mesa array. Before any film growth on patterned areas had been carried out it was assumed that metallic nanodots on those portions of a pattern intended for film growth or overgrowth would be detrimental to film quality, and the detrimental effect of growth on nanodot containing FIB milled areas was later confirmed by TEM examination. With this in mind, a number of patterning strategies were developed to limit the creation or influence of group III nanodots. One such strategy is to limit the ion dose used for pattern creation to below the threshold for group III droplet formation. As reported in Table 2.1, this corresponds to an ion dose of ~$1.7\text{x}10^{16}$ ions/cm^2 and milling depth of ~21 nm for GaAs and an ion dose of ~$1.7\text{x}10^{15}$ ions/cm^2 and milling depth of ~3 nm for InP. Figure 4.8(a) shows a recessed square in GaAs milled to a depth less than that necessary to produce droplets. Patterning below the droplet threshold dose may be a viable option for creating patterns on GaAs, but the threshold dose of InP is too low for that strategy to be employed. Another strategy to limit droplet formation is to mill patterns that require very little material to be locally sputtered away such that there are not enough excess group III atoms produced to form nanodots. Arrays of small, widely separated holes are one obvious pattern type that fits this strategy, and Figure 4.8(b) shows an array of holes milled into InP with no obvious In nanodot formation in between the holes. However, limiting the volume of milled material to below that necessary to form nanodots may also be accomplished by milling only very narrow trenches. Figure 4.8(c) shows a square mesa array with narrow trenches milled into GaAs with no Ga droplets present. In cases where the chosen pattern geometry requires significant material removal, another final strategy to limit the effect of group III droplets on the growth area of the pattern may be employed. By milling patterned features deeply into the substrate the presence of nanodots may be restricted to only the deeper portions of the pattern, and so kept away from those portions of the pattern designed for film growth and overgrowth. Figure 4.8(d) shows an array of square mesas with very deep trenches milled into GaAs in order to isolate any Ga droplet formation to the bottom of the milled regions. These strategies for limiting the formation or influence of group III nanodots on the patterned regions were used whenever possible when creating patterns for the later film growth experiments.

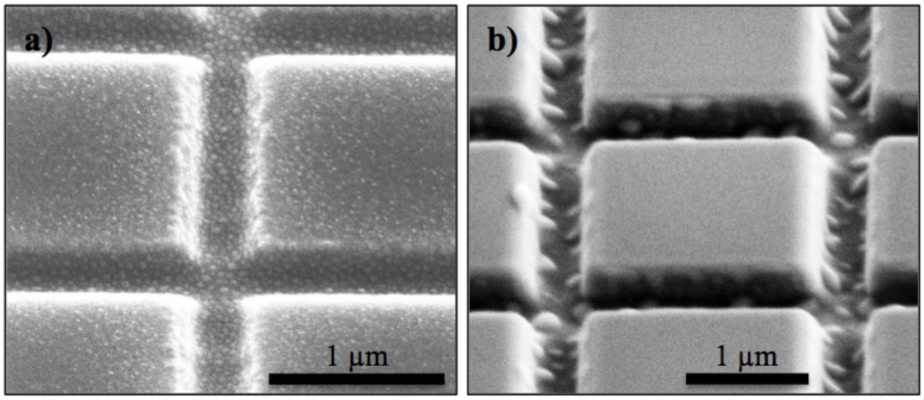

Figure 4.7: SEM images showing nanodot formation on FIB milled raised mesas. (a) shows In nanodots on a pattern milled into InP. (b) shows Ga nanodots on a pattern milled into GaAs.

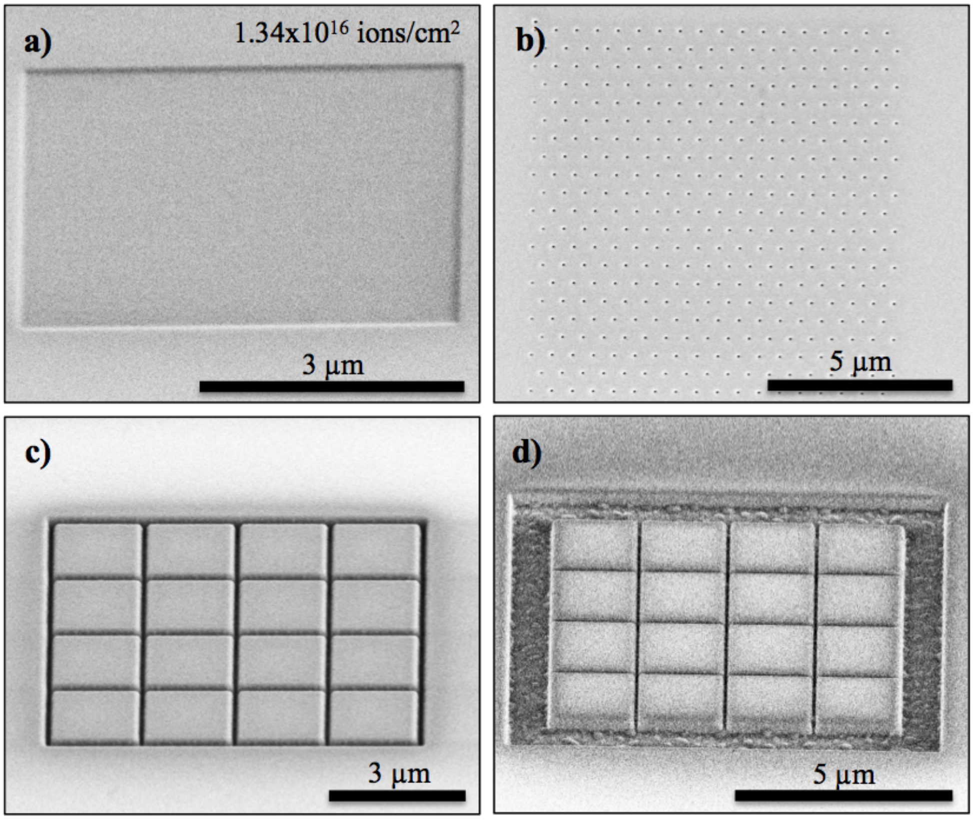

Figure 4.8: Images showing patterns that highlight different patterning strategies for limiting the effect of group III droplet formation on the patterned area.

4.4 Growth of InAs films on FIB patterned InP

InAs film grown on n+ InP wafers was chosen as a first test system for examining growth on FIB patterned areas. The InAs/InP system was chose because of the large lattice strain between the InAs film and InP (a compressive strain of 0.031 as defined by Equation (4.1)). This large mismatch resulted in very rough film morphology in the unpatterned areas, and it was hoped it would make the effects of growth on the patterned region immediately obvious. InAs films of equivalent mass thicknesses of 50, 200, and 500 nm were grown for this study, of which SEM images are shown in Figures 4.9(a), (b), and (c) respectively. Changing the InAs film thickness only altered the amount of InAs material present and film coverage in the patterned areas, and did not significantly alter the general effects of the patterns on the film. Thus the results of experiments using the different InAs film thickness will be discussed somewhat interchangeably. All of the InAs film grown on unpatterned regions of InP was very rough, poorly coalesced or islanded, and faceted. Facets were aligned to the <111> and <110>-type crystallographic directions of the film, as determined by noting their orientation relative to the cleaved <110> edges of the InP wafer and the [001] out of plane direction.

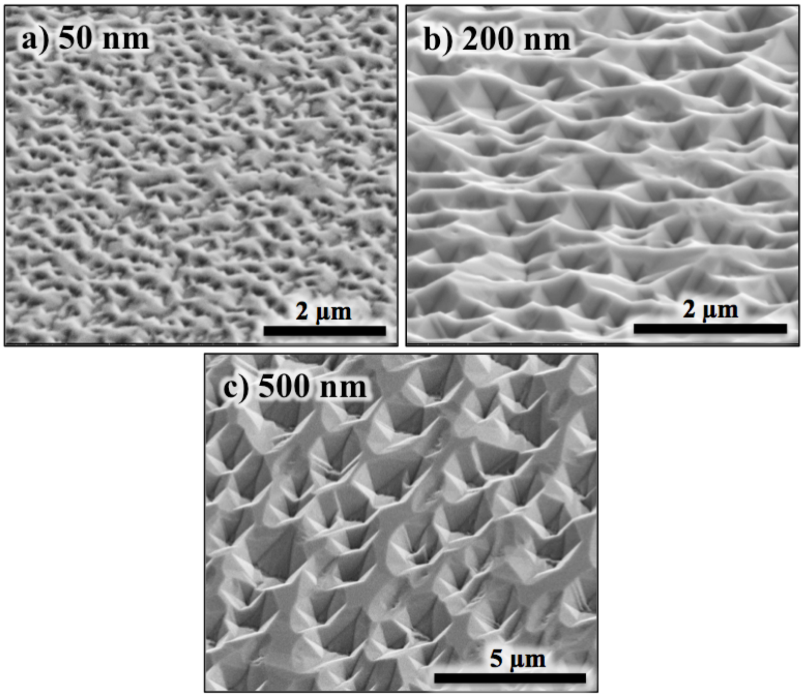

Figure 4.9: SEM images taken with the sample tilted off-normal form the electron beam showing regions of (a) 50 nm, (b) 200 nm, and (c) 500nm mass equivalent thickness InAs film grown on unpatterned areas of InP.

InAs growth on all of the different 3-D pattern types FIB milled into InP had an effect on InAs film morphology that was easily visible by SEM. ISE imaging after pattern creation or to characterize the patterns before film growth does seem to have affected film morphology around the patterns. However, comparison of film grown on identical patterns that were and were not imaged with the ion beam showed that the effects of the pattern on local InAs film morphology overwhelmed any effect of the ISE imaging, such that ISE imaging had no observable influence on final patterned area film morphology. Growth on 3-D patterned regions affected the distribution of InAs material in the region of the pattern, affected the morphology of InAs islands in the patterned area, and affected the faceting of the film. In general, the edges of 3-D patterned features appear to have acted as sinks for adatoms, which preferentially diffused to them. This resulted in regular InAs island growth at the patterned features, with island and facet arrangements repeating across the patterned features. This preferential diffusion of adatoms to the patterned features also resulted in areas denuded of InAs around those features. These effects are readily visible in Figure 4.10, which shows two different regions from the same sample patterned with hexagonal hole patterns before and after growth of a 50 nm InAs film. Figures 4.10(a) and (b) show a region patterned with closely spaced holes, and the Figure 4.10(b) SEM image of that region after film growth shows regularly repeating and faceted InAs islands centered on the hole locations, with no InAs material in between. Figures 4.10(c) and (d) show a region patterned with more widely spaced holes. In that case the SEM image of Figure 4.10(d) shows regular InAs islands centered on the holes and additional InAs material between the holes. This indicates that in this case the holes were widely enough spaced that they could not capture all of the incoming adatoms and completely deprive the area in between of InAs. Similar effects were visible in areas patterned with arrays of raised square mesas and square recesses. Figure 4.11 shows three areas with different types of square mesa patterns before and after growth of 200 nm of InAs films. Figures 4.11(a), (b), and (c) show images of a region patterned with ~500x500 nm square mesas with ~70 nm wide trenches. From Figure 4.11(b) and (c) it can be seen that while the film in that area is still rough, growth on the patterned region caused the faceting and morphology of the film to become regular and repeating. Those images also show that the edges of the patterned region affected film morphology, resulting in long evenly faceted straight lines of InAs along each edge. Figures 4.11(d), (e), and (f) show a region patterned with 2x2 μm square mesas with ~650 nm wide trenches, and Figures 4.11(g), (h), and (i) show a region patterned with 2x2 μm square mesas with narrower ~50 nm wide trenches. Both patterns resulted in a local shift in film morphology to regularly repeating and faceted InAs islands. However, in the case of the pattern with wider trenches the mesas were spaced too far away for the InAs film to overgrow the trenches, and so regularly faceted InAs islands were created on the mesas. In the narrower trench case, the trenches captured the incoming adatoms, resulting in growth of InAs along and out from the trenches themselves. Figure 4.12 shows two different regions patterned with arrays of square recesses before and after 200 nm of InAs film growth, with Figures 4.12(a), (b), and (c) showing a region patterned with 500x500 nm recesses and Figures 4.12(d), (e), and (f) showing a region patterned with 2x2 μm recesses. Again the patterns altered the morphology of the InAs film, causing it to grow in regularly space islands aligned to the features of the pattern. As visible in Figures 4.12(e) and (f), large InAs islands formed along the walls between recesses, indicating that adatoms preferentially diffused there during growth. Figures 4.10, 4.11, and 4.12 all serve as examples of how substrate patterning locally controlled adatom diffusion and InAs film morphology. However, the defect density of the InAs film in the patterned regions relative to the unpatterned areas could not be inferred from morphology alone.

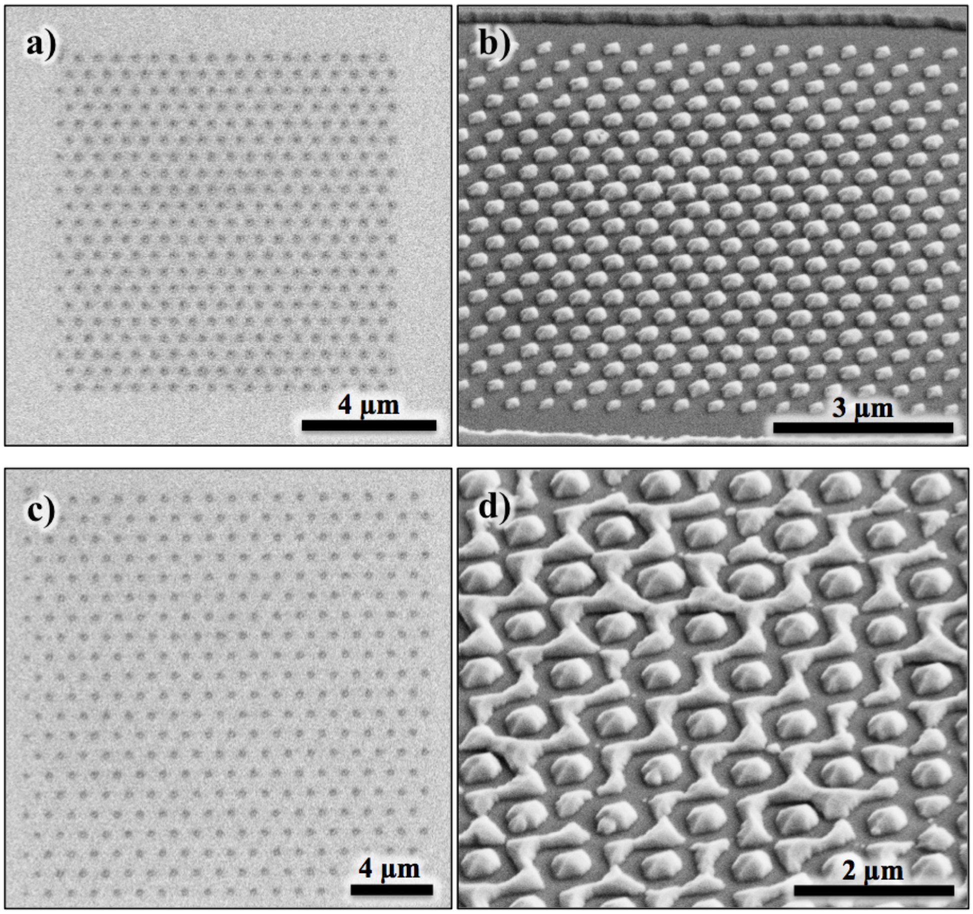

Figure 4.10: (a) and (c) show ISE images of two InP regions on the same sample patterned with arrays of hexagonally arranged holes. (b) and (d) respectively show SEM images from the areas shown in (a) and (c) following 50 nm of InAs film growth. (b) and (d) were taken with the sample tilted relative to the SEM beam normal.

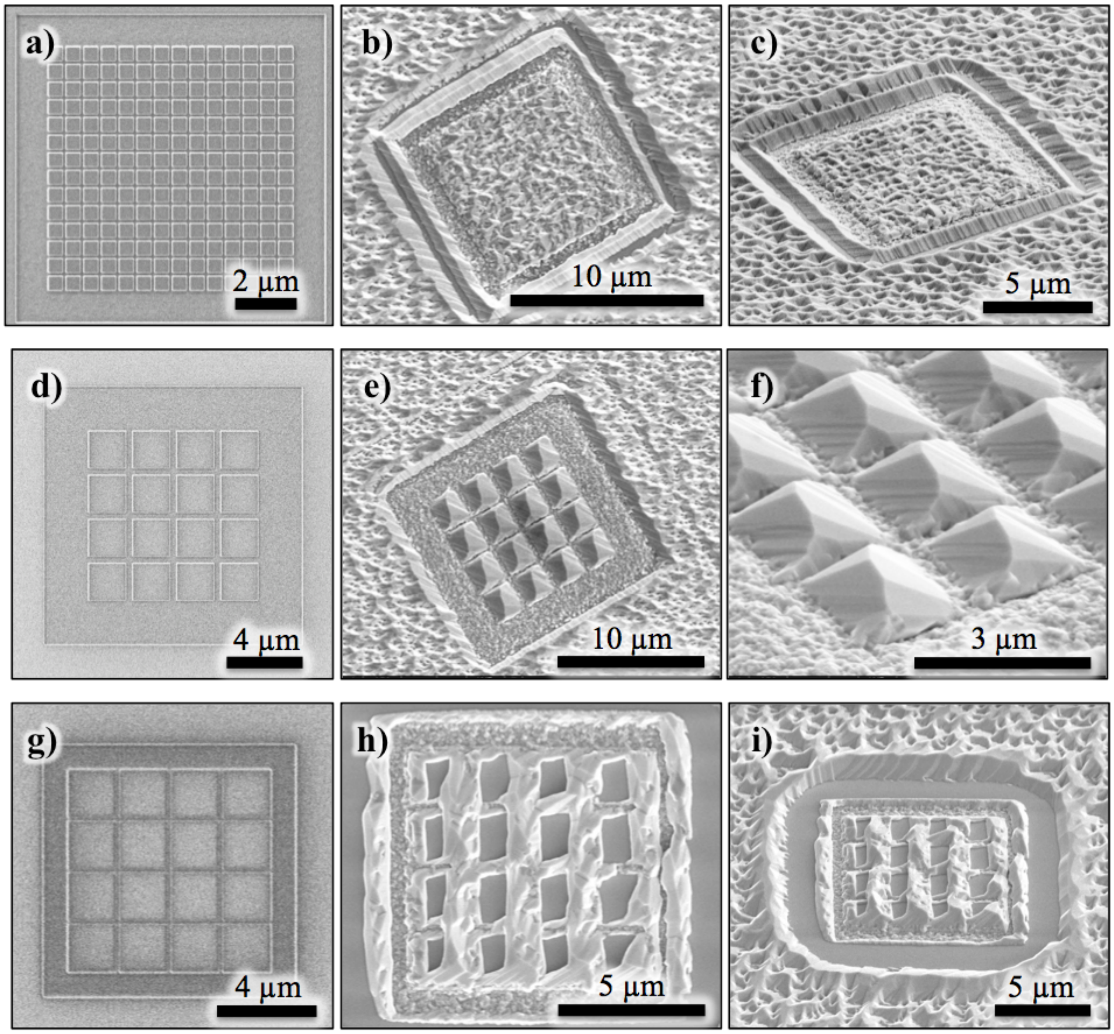

Figure 4.11: (a), (d), and (g) show ISE images of InP regions patterned with arrays of square mesas before InAs film growth. (b)-(c), (e)-(f), and (h)-(i) respectively show SEM images of the patterns in (a), (d), and (g) following growth of 200 nm of InAs. Images (c), (f), and (i) were taken with the sample tilted off the SEM beam normal.

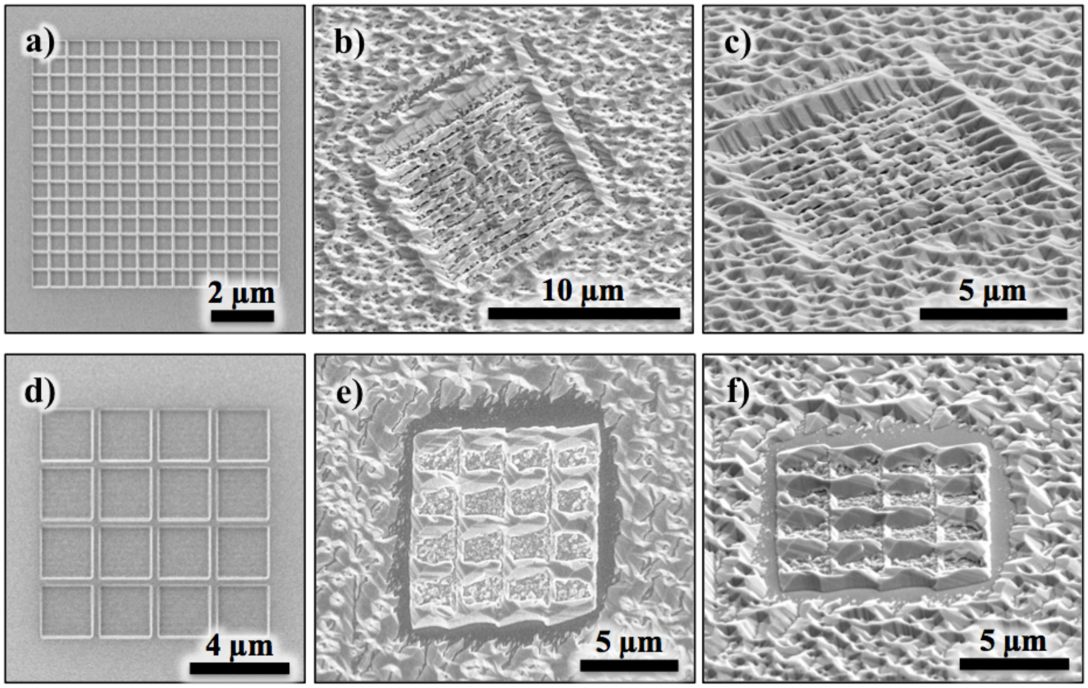

Figure 4.12: (a) and (d) show ISE images of InP regions patterned with arrays of square recesses. (b)-(c) and (e)-(f) respectively show SEM images of the areas in (a) and (d) following growth of 200 nm of InAs. (c) and (f) were taken with the sample tilted off the SEM beam normal.

FIB blanket irradiation also had a significant effect on InAs film morphology. This is visible in FIB border region milled around the 2x2 μm square mesa patterns in Figure 4.11 and in the 2x2 μm recesses in Figure 4.12. To examine this effect, a series of InP areas were blanket irradiated with ion doses both below and including the range used to mill 3-D patterns. Figure 4.13 shows three regions of blanket irradiated InP following growth of 200 nm of InAs film, with the ion dose received listed on each image. As visible in those images, FIB irradiation caused the morphology of the InAs film to locally develop laterally smaller islands and a lower overall feature height. At higher doses like those used to create the square mesa patterns, irradiation also caused a loss of clear InAs surface faceting, as shown in Figures 4.13(a) and (b). Lower doses below those used for 3-D pattern generation still resulted in changes to film morphology, but not a complete loss of faceting, as shown in Figure 4.13 (c).

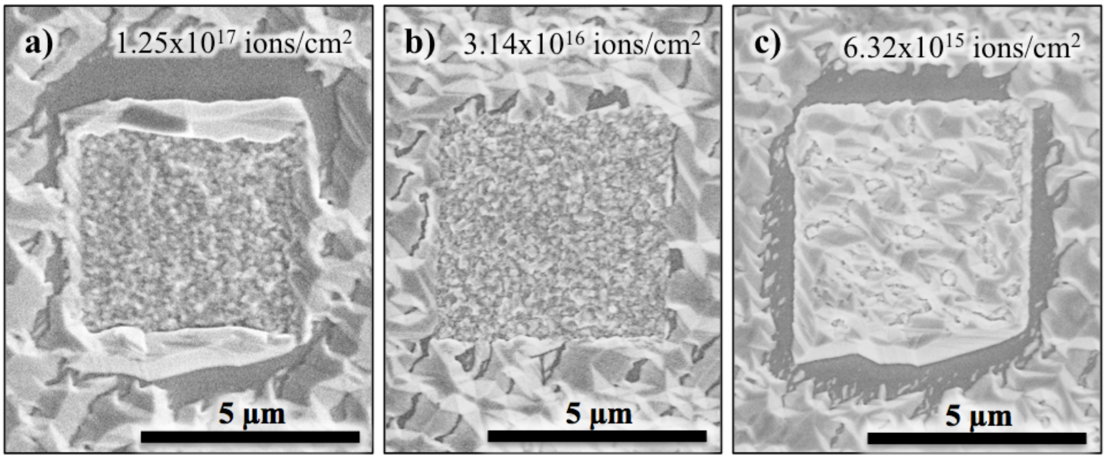

Figure 4.13: SEM images showing three regions of InP that were blanket irradiated by the FIB before growth of 200 nm of InAs. The blanket dose each area received is given on the image.

In order to determine what effect FIB patterning had on the structure and defect density of the InAs films, film grown on patterned and unpatterned regions of InP was examined by cross-sectional TEM imaging. All TEM samples were produced by the FIB lift-out method, and so had a protective Pt layer deposited along their top surface. The lift-out sample preparation method was time consuming, and so only a small number of patterned area cross-section samples were examined. Figure 4.14 shows four BF TEM images of InAs islands from unpatterned, unirradiated regions of 200 nm InAs films, with the InP substrate and Pt layer labeled in each image. TEM examination of unpatterned regions showed that the InAs islands in those areas contained threading dislocations and other defects which cut through their thickness and misfit dislocations along the InAs/InP interface with an average spacing of ~18-20 nm. The linear threading defect density of the InAs islands was measured near the heterointerface and found to be approximately 5.5 per µm of interface.

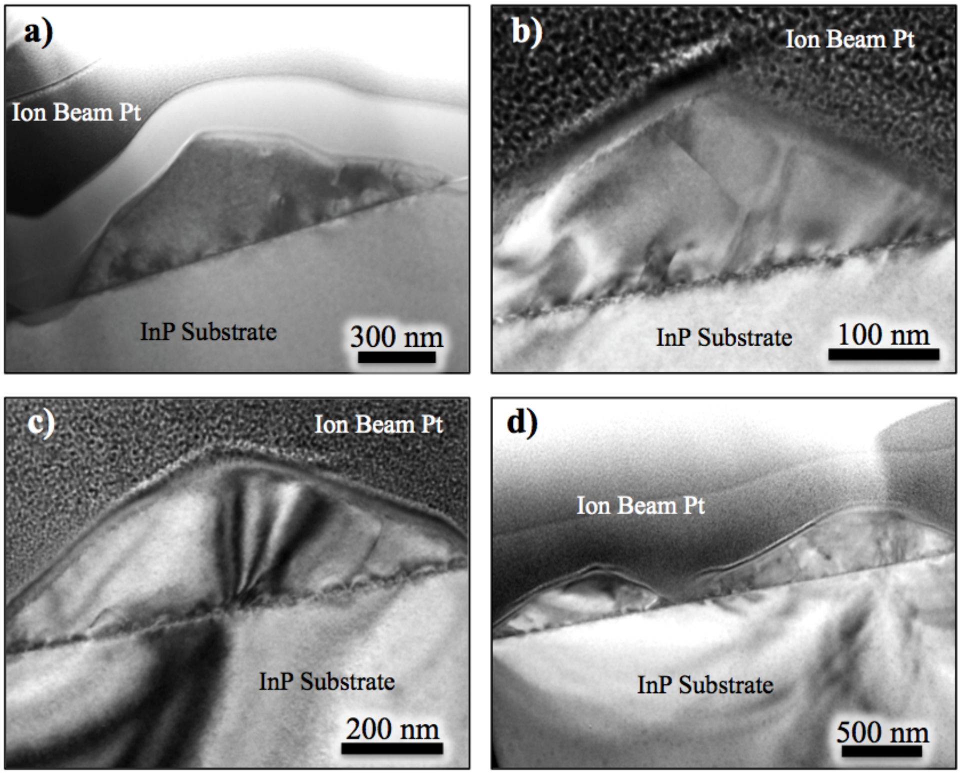

Figure 4.14: BF TEM images of InAs islands from unpatterned regions of a 200 nm InAs films grown on InP. (a) was taken with the sample oriented near a [130]-type zone-axis, while the other three images were taken with the sample oriented to a [110]-type zone-axis.

Figure 4.15 shows a series of images taken from an area blanket irradiated with an ion dose of 1.87x10^{16} ions/cm^2 before growth of a 200 nm thick InAs film, with morphology characteristic of high dose blanket irradiated regions. Figure 4.15(a) shows a SEM image of that region of InAs film, and Figure 4.15(b) shows an assembled montage of BF TEM images taken of a cross-section from the middle of the blanket irradiated area. Figures 4.15(c) and (d) show higher magnification matched BF and DF images of a section of the InAs film pictured in (b). BF, DF, and HRTEM imaging of the irradiated region shown in Figure 4.15(b) revealed that the InAs film was highly defective and polycrystalline. The heterointerface between the InAs and InP was also uneven and rough, as is visible in Figure 4.15(c). TEM examination of the FIB irradiated regions of other recess and mesa patterns showed similar defected and polycrystalline structures with rough interfaces. Based on SEM examination of other FIB blanket irradiated InP regions (see Figure 4.7(a) and Chapter 2 of this dissertation), FIB milling would have caused the InP wafer surface to roughen and produce InP nanodots. The FIB irradiation would also have created ion damage in the near-surface region of InP. It is likely the rough, damaged InP surface and the presence of In nanodots during film growth caused the InAs in the irradiated regions to grow polycrystalline and non-epitaxially and also provide nucleation sites for crystalline defects. Regardless of mechanism, it can be clearly seen that FIB irradiation of InP is extremely detrimental to the quality of films grown in the irradiated areas.

Figure 4.16 shows a series of images taken from a region patterned with an array of 2x2 μm square recesses before growth of a 200 nm mass equivalent thickness InAs film. Figures 4.16(a) shows an ISE image of the patterned InP before film growth, and Figure 4.16(b) shows a SEM image of that same area following film growth. Figure 4.16(c) shows a montage of BF TEM images taken from a cross section through a row of four recessed areas at the location indicated by the dotted line in (b). Figures 4.16(d) and (e) show higher magnification BF images of some of the large, faceted InAs islands that grew over the walls of the recessed areas. TEM images revealed that the InAs in the ion milled recesses was again polycrystalline and defective. The large InAs islands at the recess walls were single crystalline and maintained the orientation of the InP substrate. However, they contained a high density of linear crystalline defects. Higher magnification images of those islands showed that the majority of their defects appeared to have originated in the ion milled recesses and propagated into the islands. Based on this observation it appears likely that the ion damage, rough heterointerface, or defective material in the recessed regions were responsible for nucleating and injecting defects into the larger single crystalline InAs islands.

Figure 4.17 shows a series of images taken from a region patterned with an array of raised 2x2 μm square mesas with ~650 nm wide trenches before growth of a 200 nm thick InAs film. Figures 4.17(a) shows an ISE image of the patterned InP before film growth, and Figure 4.17(b) shows a SEM image of that same area following InAs growth. Figure 4.17(c) shows a montage of BF TEM images taken from a cross section through the faceted InAs islands on two of the mesa tops at the location indicated by the dotted line in (b). Figure 4.16(d) shows a higher magnification BF image of the InAs at one of the mesa edges. TEM examination of the cross-section through this patterned area shows that the InAs material between the mesas was again defective and polycrystalline, that the

InAs material on the mesa edges contained a high density of linear threading defects, and that the InAs material in the mesa center contained a lesser number of threading defects. The large InAs islands on the mesas were single crystalline and epitaxially oriented to the InP substrate. The linear threading defect density of the InAs islands on the mesas but away from the mesa edges was measured near the heterointerface and found to be approximately ~6.4 per µm of interface. So the InAs threading defect density in the mesa interiors approximately matches the threading defect density of InAs grown on unpatterned, unirradiated regions of InP within the experimental error of the measurement method. Examination of the material at the mesa edges again showed a high density of linear defects which appear to have been injected into that material from the poor quality InAs in the ion milled trenches (see Figure 4.17(d) as an example).

Overall, based on the limited cross-sectional TEM results presented above, InAs growth on patterned InP does not appear to improve the defect density of the InAs films relative to unpatterned areas, and growth in or near FIB irradiated areas appears to be extremely detrimental to film quality. InAs growth on patterns of smaller mesas might better help relax the film and promote overgrowth of the trenches, but smaller mesa patterns were not examined by TEM to confirm this. However, based on SEM images of the smaller mesa patterns and the observed effect of growth near FIB milled regions, it seems unlikely that the defect density or film quality of the smaller mesa regions would be much improved. TEM characterization of patterns created to minimize the effect of In nanodots on the patterned region, like those pictured in Figure 4.8, was also not carried out. By growing InAs on 3-D patterns designed to minimize the ability of FIB irradiation to influence the regions of the pattern intended for film growth it might be possible to minimize the detrimental effects of FIB irradiation.

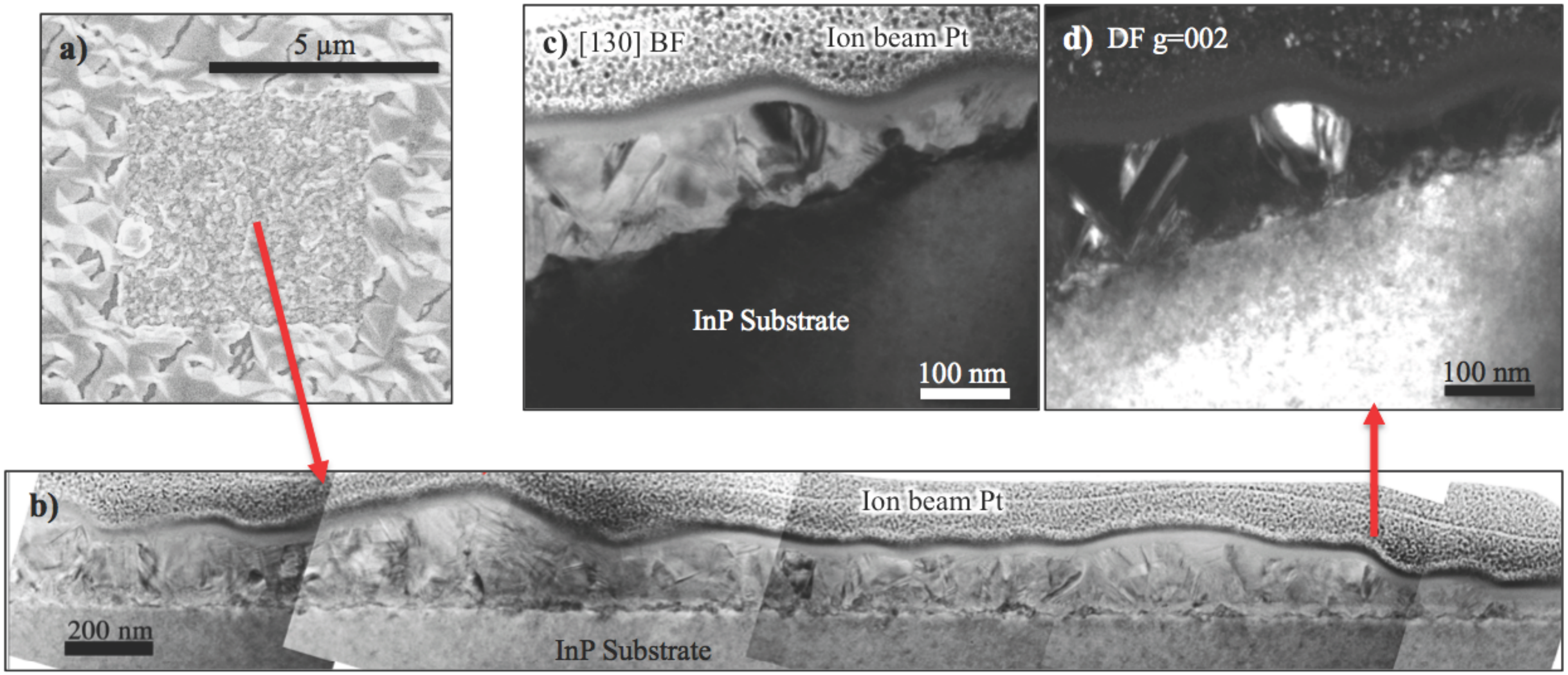

Figure 4.15: (a) shows a SEM image of a 200 nm InAs grown on a region of FIB blanket irradiated InP. (b) shows a BF TEM image montage of a cross-section through the InAs film in the irradiated area. (c) and (d) show matched [130] zone-axis BF and g=002 DF images respectively of the location indicated in (b).

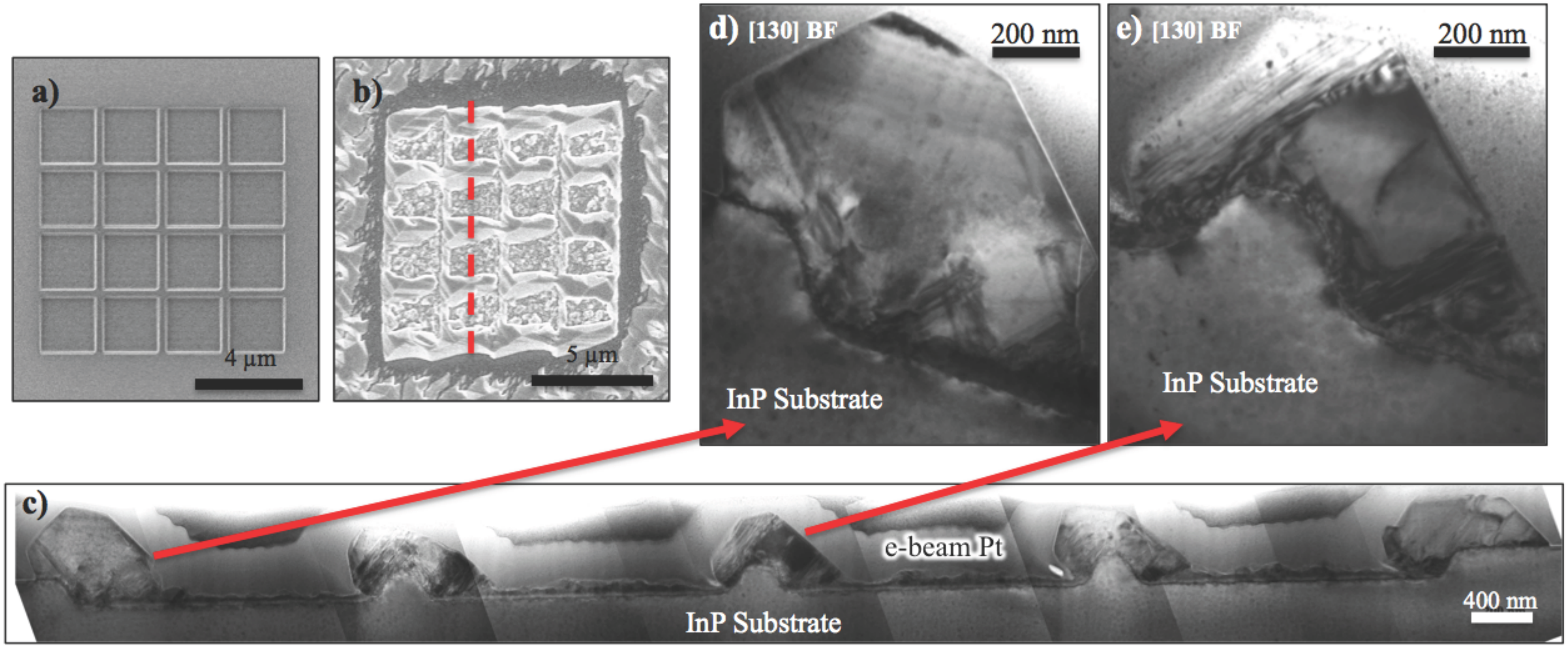

Figure 4.16: (a) shows an ISE image of a region of InP patterned with an array of 2x2 µm recesses before InAs film growth. (b) shows a SEM image of that same area following growth of 200 nm of InAs. (c) shows a BF TEM image montage of a cross-section through the InAs film in the patterned at the location indicated by the dotted line in (c). (d) and (e) both show higher magnification [130] zone-axis BF images of InAs islands at recess walls.

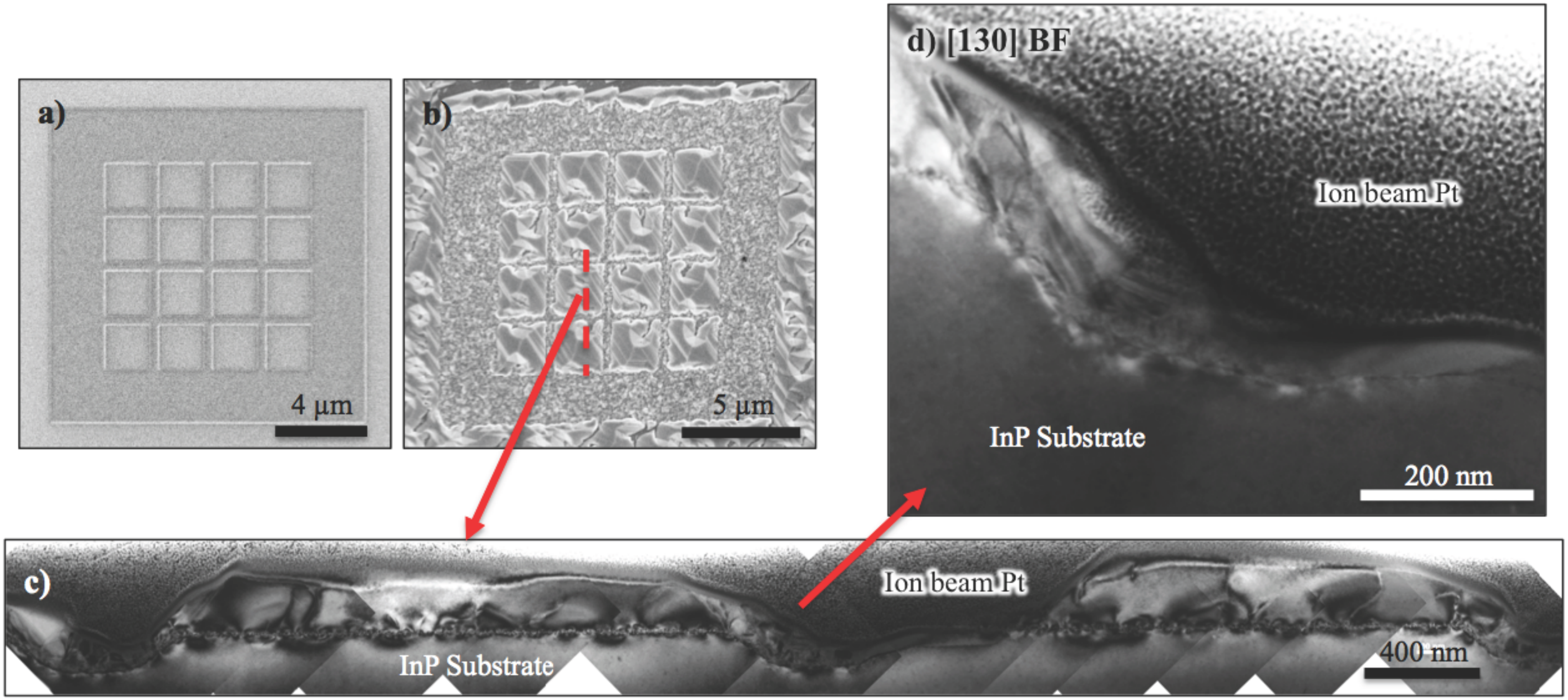

Figure 4.17: (a) shows an ISE image of a region of InP patterned with an array of 2x2 µm raised mesas with ~650 nm wide trenches. (b) shows a SEM image of that same area following growth of 200 nm of InAs. (c) shows a [130] zone-axis BF TEM image montage of a cross-section taken through two InAs islands on the mesas at the location indicated by the dotted line in (b). (d) shows a [130] zone-axis BF image of the edge of a mesa taken at the location indicated.

4.5 Growth of InGaAs films on FIB patterned GaAs

Following the examination of InAs films grown on InP, a limited number of experiments examining InGaAs grown on FIB patterned GaAs were conducted. The InAs/InP system produced very rough and discontinuous films, and it was hoped that by switching to a lower mismatch system with a correspondingly smoother and more continuous film morphology that pattern overgrowth and relaxation over the pattern would be promoted. Two InGaAs film on patterned GaAs samples were produced, one with a film composition of $In_{0.45}Ga_{0.55}As$ and thickness of 200 nm, and the other with composition $In_{0.33}Ga_{0.67}As$ and a 500 nm thickness. In the $In_{0.33}Ga_{0.67}As$ case the GaAs substrate was desorbed and had a 500 nm GaAs buffer grown on it before being transferred to the UHV FEI Magnum FIB chamber for patterning. In the case of both InGaAs film experiments, the results of film growth on surface morphology were characterized, but no cross-sectional TEM or defect density characterization was conducted. This was because in the case of both films the growth on patterned areas did not improve film morphology and generally resulted in locally rougher film, and using the results of the InAs/InP study as a guide it was judged unlikely that any improvement in InGaAs film quality had been achieved. Both InGaAs film samples showed similarly negative responses to FIB patterning, so for the sake of brevity results from only the $In_{0.33}Ga_{0.67}As$ sample will be shown in greater detail here. The 500 nm thick $In_{0.33}Ga_{0.67}As$ film grown on unpatterned regions of GaAs buffer had a surface morphology consisting of relatively low, elongated islands aligned parallel to one of the [110]-type cleavage planes of the sample, giving its surface a ridge-like pattern. Figure 4.18 shows two SEM images taken of that film surface. The composition of the film was determined by taking 004 and 224 glancing exit HRXRD Ω-2θ scans.

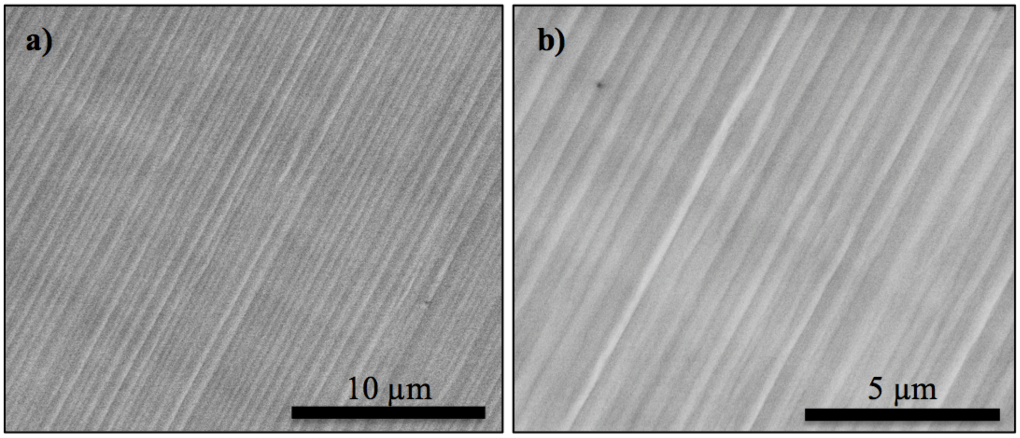

Figure 4.18: SEM images taken of a 500 nm thick $In_{0.33}Ga_{0.67}As$ film showing regions where the underlying GaAs substrate had not been FIB patterned.

The $In_{0.33}Ga_{0.67}As$ film's GaAs substrate was patterned with a variety of square raised mesa array patterns, square recess array patterns, hexagonally arranged hole patterns, and a few other less regular pattern types. To varying degrees all of the patterns detrimentally affected the InGaAs film surface. Figures 4.19(a) and (b) show low magnification SEM images of two regions containing nine FIB milled patterns each, and each pattern in those images had a visible effect on film morphology. Figure 4.20 shows two different regions patterned with hexagonally arranged holes before and following InGaAs film growth. Figures 4.20(a), (b), and (c) show a region patterned with closely spaced holes, and Figures 4.20(d), (e), and (f) show a region patterned with more widely spaced holes. For both cases, the film grown on the hole patterns showed increased roughness and surface defects. Figure 4.21 shows examples of regions patterned with arrays of square mesas before and after InGaAs film growth. Figures 4.21(a), (b), and (c) show a region patterned with approximately 500x500 nm square mesas. The images in (b) and (c) show that the underlying pattern roughened and disrupted the film on it relative to the smoother surrounding InGaAs. Figures 4.21(d), (e), and (f) show a region patterned with 2x2 μm square mesas and a trench width of ~650 nm. This pattern was milled using an ion dose of 4.7×10^{16} ions/cm^2, which is greater than the ion dose necessary to initiate the formation of Ga droplets on GaAs. The images in Figures 4.21(e) and (f) show that the underlying patterned resulted in the creation of repeating InGaAs islands of pseudo-regular shape on the patterned GaAs mesas. This result is similar to that seen in the InAs/InP system using the same pattern type, and again indicates that 3-D substrate features are controlling adatom diffusion and capture. Figures 4.21(g), (h), and (i) show a region patterned with 2x2 μm square mesas and a trench width of ~650 nm. However to create this second pattern a lower ion dose of 1.6×10^{16} ions/cm^2 was used, below the threshold for FIB induced Ga droplet formation. In this case the images in Figures 4.21(h) and (i) show that the InGaAs film was able to overgrow the mesa array and produce a single continuous island of InGaAs film. While still rougher than the film in the surrounding unpatterned region, the film in this final case does show improved morphology relative to the previous two mesa patterns shown in Figure 4.21. This indicates that the presence of FIB created Ga droplets in a patterned region contributes to and increases the roughness of its InGaAs film, and that by preventing their formation film morphology may be marginally improved. Figure 4.22 shows examples of regions containing recess patterns before and after film growth. Figures 4.22(a), (b), and (c) show an area patterned with an array of 2x2 μm square recesses, while Figures 4.22(d), (e), and (f) show an area patterned with block-M shaped recesses of different sizes. In both cases InGaAs growth over the recesses altered the morphology of the InGaAs film. Similar to the InAs/InP system, InGaAs film growth over heavily FIB irradiated or milled regions of GaAs produces film morphology with laterally smaller features and no oriented surface texture. Based on the similar result seen in the InAs/InP case, it seems likely that the film in this area has been effected by growth on heavily ion damaged regions of GaAs which contained Ga droplets. The InGaAs film in these regions may be polycrystalline, as was the case for the InAs films (see Figure 4.15), but no TEM analysis was conducted to determine the film structure for the InGaAs case. Overall InGaAs growth on regions of patterned GaAs increased film roughness, and based on surface morphology did not improve the quality of the InGaAs film relative to film grown on unpatterned regions. Because of this initial negative result and similar results in the InAs/InP system, no further experimentation or analysis was conducted on InGaAs films grown on FIB patterned GaAs.

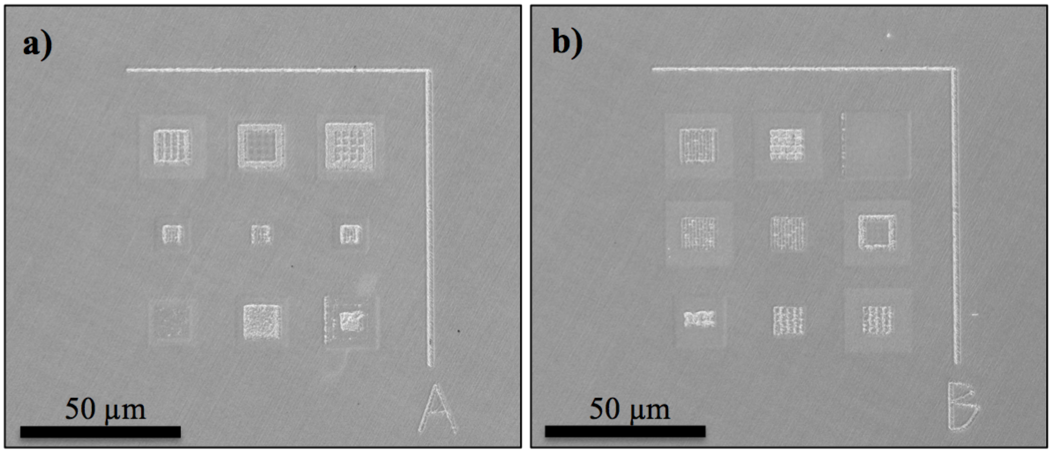

Figure 4.19: Low magnification SEM images of two regions each containing nine different patterns milled into GaAs with 500 nm of $In_{0.33}Ga_{0.67}As$ grown on them.

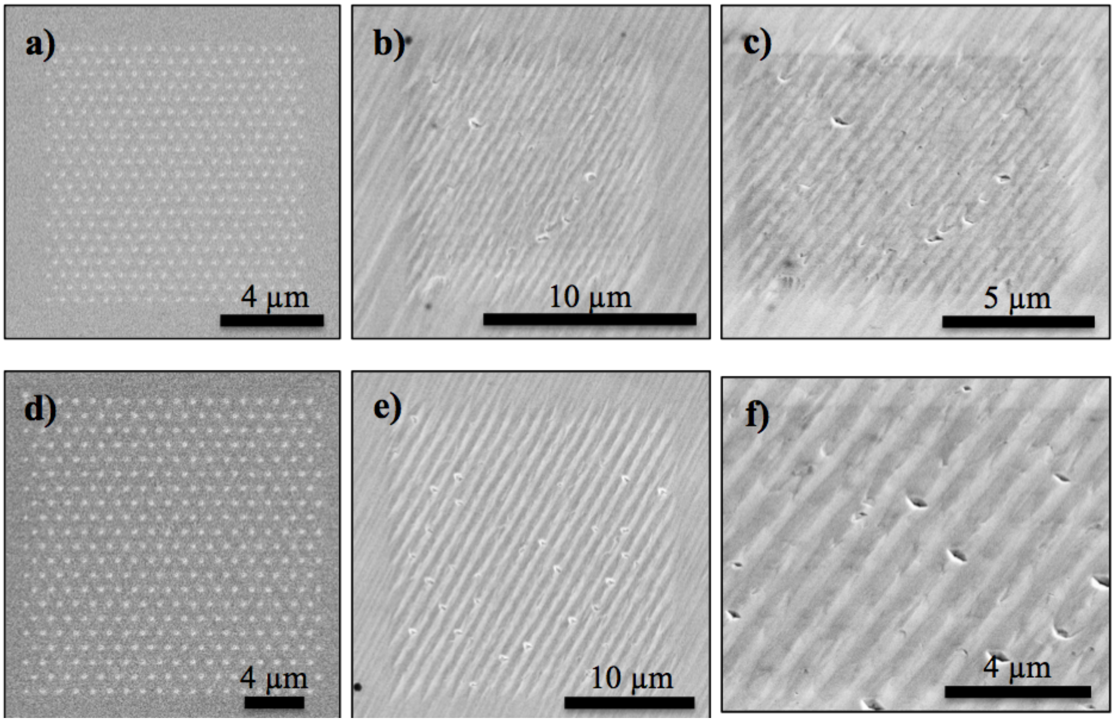

Figure 4.20: (a) and (d) show ISE images of GaAs regions patterned with hexagonally arranged holes before InGaAs growth. (b)-(c) and (e)-(f) respectively show SEM images of the patterns in (a) and (d) following growth of 500 nm of $In_{0.33}Ga_{0.67}As$. Images (c) and (f) were taken with the sample tilted relative to the SEM beam normal.

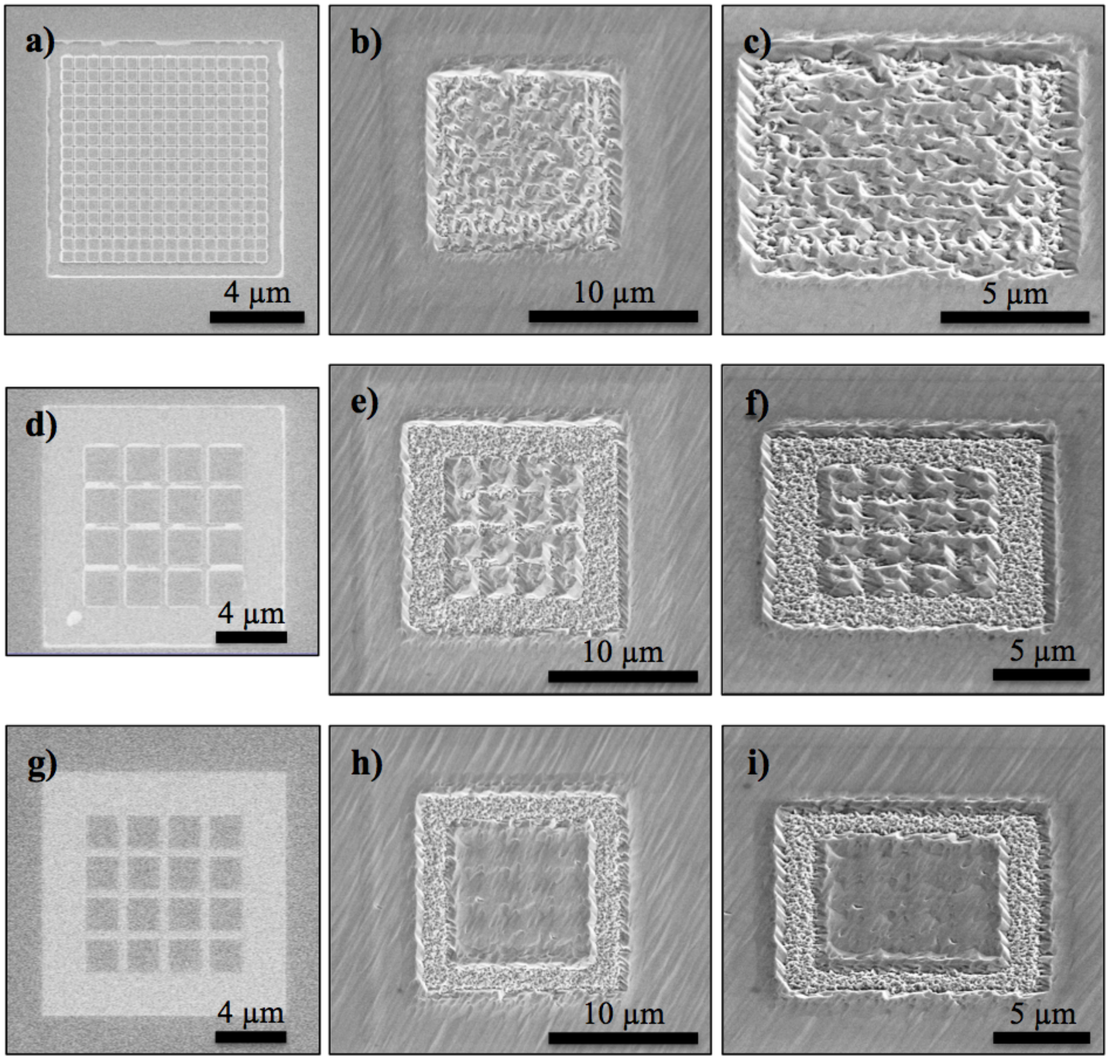

Figure 4.21: (a), (d), and (g) show ISE images of GaAs regions patterned with arrays of square mesas before film growth. (b)-(c), (e)-(f), and (h)-(i) respectively show SEM images of the patterns in (a), (d), and (g) following growth of 500 nm of $In_{0.33}Ga_{0.67}As$. *Images (c), (f), and (i) were taken with the sample tilted relative to the SEM beam normal.*

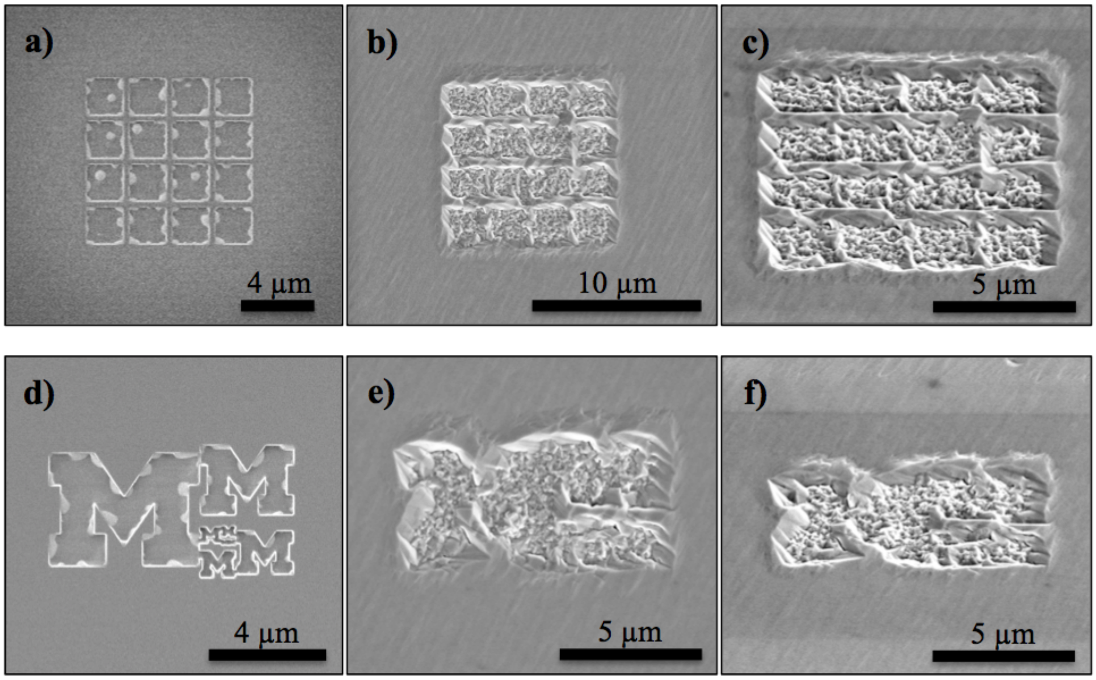

Figure 4.22: (a) and (d) show ISE images of GaAs regions patterned with a series of recesses. (b)-(c) and (e)-(f) respectively show SEM images of the areas in (a) and (d) following growth of 500 nm of $In_{0.33}Ga_{0.67}As$*. (c) and (f) were taken with the sample tilted relative to the SEM beam normal.*

4.6 Conclusions and Future Work

This study examined the effect of using FIB milling to pattern InP and GaAs substrates with 3-D features before film growth, and was conducted in the hope of reducing the defect density and improving the quality of lattice mismatched films grown on these common III-V substrate materials. Initially 3-D patterns on both InP and GaAs were created and characterized with the goal of determining the patterning capabilities of the FIB systems used and to characterize the effects of FIB milling on the surface of each material. Creation and characterization of square mesa array, square recess array, and hexagonally arranged hole patterns was the primary focus of these efforts. The minimum feature size of each pattern type was ultimately set by the vibration limited milling resolution of the FIB instruments, and how well the features of a given pattern were defined depended on feature size and the FIB parameters used to create them. The FIB milling method used to produce the 3-D patterns for this study resulted in the creation of group III nanodots in the FIB milled portions of each pattern at higher doses. Later examination of film grown on the ion milled regions indicated that those nanodots were detrimental to film quality, and so several pattern creation strategies were developed to minimize the effect of ion damage and nanodot formation in the patterned regions.

InAs films grown on InP were chosen as the heterostructure system for initially examining the result of film growth on 3-D patterns. SEM examination showed that FIB patterned features act as strong sinks for adatoms during film growth, and the InAs film in the patterned regions was observed to have significantly altered morphology compared to the unpatterned regions. Growth on patterns resulted in the creation of regularly spaced and regularly shaped faceted InAs islands while denuding the surrounding area of InAs. Purely from the standpoint of surface features it was unclear if those morphological changes in the InAs films represented an improvement in overall film quality. Film growth on the heavily ion damaged regions also resulted in significant changes to film morphology, with film growth in those areas resulting in a loss of faceting or other visible alignment relative to the substrate orientation.

TEM examination of cross-sections taken through regions of InAs film grown on patterned InP revealed that growth on the patterned regions was universally detrimental to film quality. Film grown on FIB milled regions was found to be polycrystalline and heavily defective. This may have been due to the presence of a rough InP surface and In nanodots produced by high dose FIB irradiation. Films grown on patterns of recesses or mesas produced large single crystalline InAs islands epitaxially oriented to the InP substrate, but the nearby FIB milled regions produced defects which propagated into those large islands. As a result, InAs grown on the patterned regions was found to have approximately the same or a higher threading defect density compared to the surrounding rough InAs film grown on unpatterned InP. Overall, FIB milling and proximity to FIB milled material was observed to have an extremely detrimental effect on film quality. It is possible that by switching to FIB milled patterns designed to minimize the influence of FIB milling on surfaces intended for film growth and with a smaller feature size to better encourage local film relaxation, the defect density of the patterned regions could be improved. However, based on the results of this study it seems unlikely that film quality would be improved sufficiently to justify the use of FIB created patterns over other strain relaxation and defect reduction strategies.

In order to examine the effects of FIB 3-D substrate patterning on a less highly mismatched system, a limited number of experiments were conducted examining InGaAs films grown on FIB patterned GaAs. Examination of InGaAs film morphology in the patterned regions showed that patterning and FIB irradiation had in all instances resulted in a detrimental effect on film morphology. Film roughness in the patterned areas was somewhat improved by use of patterns milled using ion doses below the threshold necessary to create Ga droplets, but lower dose patterns still resulted in film with rougher surface morphology than film grown over unpatterned substrate. Based on this result no TEM evaluation of existing samples was conducted and no additional InGaAs on patterned GaAs samples were produced.

The results of this study have shown that 3-D surface features act as strong sinks for adatoms during film growth, and that patterning may be used to manipulate the regularity and morphology of III-V islands grown on them. Growth on FIB irradiated and milled areas was found to produce very defective film, and that defects formed in the FIB milled regions may propagate into adjacent film grown on patterned features. This detrimental effect is likely due to the manner in which the III-V substrates respond to FIB irradiation and due to the presence of FIB created group III nanodots. Based on this observation several patterning strategies were developed which minimize the nanodot formation or the influence of FIB irradiation and damaged on the areas of each pattern intended for film growth. Results in the InGaAs/GaAs system indicate that limiting group III nanodot formation in the patterned region does produce a marginal improvement in film morphology.

This study indicates that the poor quality of the mismatched films grown on FIB patterned regions is due to the use of FIB milling as the chosen substrate modification method and the unique response of the III-V materials to FIB irradiation rather than a failure of the patterning and strain relaxation approach proposed by Luryi and Suhir [20] as a whole. Previously other authors have reported success in improving lattice mismatched III-V film quality by growing over patterns produced by other methods [18,21], indicating that substrate patterning may still be a defect reduction approach worth pursuing using other substrate modification techniques. A published study examining in-depth the effect of different pattern types, feature sizes, and pattern orientations on mismatched film quality is still lacking, and might be conducted using another patterning method that does not inherently have a detrimental effect on III-V film quality. One possible approach that will allow for creation of many different 3-D pattern variations on a small number of samples is to employ electron beam lithography and reactive-ion etching (RIE) to pattern III-V substrates. Such an e-beam lithographic and RIE approach will avoid the ion damage and group III droplet formation problems associated with FIB milling. From the standpoint quickly of varying pattern parameters and dimensions, e-beam lithography may not match the ease of FIB milling. However, compared to other available techniques for generating small 3-D substrate features, such as optical lithography and etching, masked deposition of material, or micro-machining, e-beam lithography will provide a relatively quick way to create many different pattern types with nanoscale features over small areas and using a low total number of samples.

4.7 References

[1] Bhattacharya, P. *Semiconductor optoelectronic devices, 2nd Edition* (Prentice Hall, Upper Saddle River, NJ, 1997).

[2] Vurgaftman, I., Meyer, J. R. & Ram-Mohan, L. R. *Journal of Applied Physics* **89**, 5815 (2001).

[3] Matthews, J. W. & Blakeslee, A. E. *Journal of Crystal Growth* **27**, 118-125 (1974).

[4] People, R. & Bean, J. C. *Applied Physics Letters* **47**, 322 (1985).

[5] Ohring, M. *Materials Science of Thin FIlms, 2nd Edition* (Academic Press, San Diego, 2002).

[6] Lubyshev, D. et al. *Journal of Vacuum Science & Technology B: Microelectronics and Nanometer Structures* **19**, 1510-1514 (2001).

[7] McGill, L. M. et al. *Journal of Vacuum Science & Technology B: Microelectronics and Nanometer Structures* **22**, 1899 (2004).

[8] Lee, M. L., Antoniadis, D. A. & Fitzgerald, E. A. *Thin Solid Films* **508**, 136-139 (2006).

[9] Gourley, P. L., Drummond, T. J. & Doyle, B. L. *Applied Physics Letters* **49**, 1101-1103 (1986).

[10] Dodson, B. W. *Journal of Electronic Materials* **19**, 503-508 (1990).

[11] Fitzgerald, E. A. *Materials Science and Engineering B* **124-125**, 8-15 (2005).

[12] Isaacson, D. M. et al. *Journal of the Electrochemical Society* **153**, G134 (2006).

[13] Sawano, K. et al. *Applied Physics Letters* **85**, 2514 (2004).

[14] Fitzgerald, E. A. et al. *Journal of Applied Physics* **65**, 2220 (1989).

[15] Hull, R. et al. *Applied Physics Letters* **60**, 1468 (1992).

[16] Matyi, R. J., Shichijo, H. & Tsai, H. L. *Journal of Vacuum Science & Technology B: Microelectronics and Nanometer Structures* **6**, 699 (1988).

[17] Guha, S., Madhukar, A., Kaviani, K. & Kapre, R. *Journal of Vacuum Science & Technology B: Microelectronics and Nanometer Structures* **8**, 149 (1990).

[18] Lee, S. C. et al. *Applied Physics Letters* **85**, 4181 (2004).

[19] van der Merwe, J. H. *Journal of Applied Physics* **34**, 123 (1963).

[20] Luryi, S. & Suhir, E. *Applied Physics Letters* **49**, 140 (1986).

[21] Guha, S., Madhukar, A. & Chen, L. *Applied Physics Letters* **56**, 2304 (1990).

[22] Fitzgerald, E. A. et al. *Applied Physics Letters* **52**, 1496 (1988).

[23] Hull, R. et al. *Applied Physics Letters* **56**, 2445-2447 (1990).

Chapter 5

Ion Beam Pre-Implantation of III-V Substrates

5.1 Introduction and Background

Their direct bandgaps, high carrier mobilities, and ability to access a wide range of electronic properties through alloying and heterostructure creation have resulted in broad application and intense development of the III-V compound semiconductors. However, lattice mismatch strain and its detrimental effects on film quality limit the practical applications of many III-V semiconductor heterostructure combinations with otherwise promising electronic structures. Mismatch strain and the mechanisms of mismatch strain driven defect creation are discussed in section 4.1.1 of this dissertation. Briefly, mismatch strain is produced when a growing heteroepitaxial film distorts its equilibrium structure in order to accommodate the lattice parameter of the material it is being grown upon. This strain increases with film thickness, and once that strain exceeds some critical point it will relax through surface roughening or the creation of defects such as misfit and threading dislocations. Threading dislocations, surface roughness, and other defects such as stacking faults and twins are extremely deleterious to the electronic properties of a film [1], and preventing their presence in active device layers is critical for many applications.

Due to the importance of mitigating the effects of lattice mismatch strain on device properties, a number of methods have been developed for reducing strain in growing heteroepitaxial films or for preventing defects from propagating into the active layers of a device. Examples include growth on metamorphic buffer layers [2-4] and growth of threading dislocation filtering structures [5,6]. While effective, both metamorphic buffer layer growth and the creation of dislocation filtering structures require the growth of thick, non-device related layers and increase the complexity of the growth process. They may also result in a rough film surface that is detrimental to the properties of subsequently grown films. An alternative method that has seen some success in both the Si-Ge (group IV) and III-V systems is the use of broad beam ion implantation to promote relaxation of substrates or buffer layers. Mismatched growth on ion irradiated buffer layers has been demonstrated as a method for controlling defect location and promoting stress relaxation in the III- V semiconductors [7,8]. Similarly beneficial effects have been observed for Si-Ge layers grown on irradiated group IV buffer layers [9,10] and Si substrates pre-implanted before film growth [11-13]. However, recent work in the III-V material system has focused primarily on swift, heavy ion irradiation [8,14-16], and no work has been published on the effects of pre-implantation of common III-V wafer substrates before film growth.

Pre-implantation of substrates before growth may provide a method for promoting strain relaxation and reducing threading defect densities in mismatched films that does not add much complexity to the growth process or require the use of thick additional buffer layers. This work examines the use of broad beam ion pre-implantation of GaAs wafers as a route to engineering film relaxation and defect placement in lattice mismatched III-V heterostructures. Substrate implantation before film growth has been shown to improve film defect density in the Si-Ge system [11-13]. As the effect of a similar pre-implantation approach on the III-V systems has not been reported in the literature, this study is a novel extension of the pre-implantation technique into the III-V material system. In this study the effects of both In^+ and Ar^+ pre-implantation of GaAs substrates on subsequent InGaAs film growth are examined using a variety of different implantation conditions. From a device processing standpoint, pre-implantation of substrates before film growth may prove to be a simpler way of reducing strain and defect density in III-V film substrates than the methods proposed above. The effects of implantation on GaAs substrates were first characterized for both ion species. Following substrate characterization, InGaAs films were grown on both pre-implanted and unimplanted substrates for comparison and characterized with regards to film roughness, % relaxation, and defect density. In^+ substrate pre-implantation was found to not affect InGaAs film quality. This was concluded to be due to the nature and depth of ion damage induced in GaAs by In^+ implantation, which may not interact with the growing film sufficiently to affect film properties. Ar^+ pre-implantation was found to have an effect on InGaAs film quality, causing the films to relax more completely towards their unstrained lattice parameter and to develop a smoother surface. However, their dislocation density was either increased or unchanged by Ar^+ implantation. Ar^+ pre-implantation was demonstrated as a method for improving film roughness and relaxation by ion beam controlled enhancement of dislocation creation. Possible strategies for improving InGaAs film quality by using Ar^+ pre-implantation combined with dislocation-filtering heterostructures will be discussed, and future work examining pre-implantation of the III-V materials will also be proposed. By combining a pre-implantation and adislocation filtering approach it may be possible to design a simple method for generating buffer layers for lattice mismatched film growth that are smooth, relaxed, and threading dislocation free.

5.1.1 Ion Irradiation for Strain Relaxation and Defect Reduction

Growth on ion irradiated substrates or buffer layers has been demonstrated as a method for controlling strain and defect density in both III-V [7,8,14,15,17,18] and Si-Ge [9,10,19-22] heterostructures. The effect of ion implantation on both semiconductor systems is complex, with the end effect on film strain and film defect density depending on a number of variables, including ion energy, ion species, ion dose, and target composition. The Si-Ge system is being included in this overview because the manner in which energetic ions interact with the Si-Ge system is similar in some aspects to how they interact with the III-V materials, and work in the Si-Ge system has helped to motivate this study. Much of the work in the SiGe system has involved implantation of Si-Ge heterostructures with keV range ions followed by a thermal anneal [9,10,19-22]. All of those studies identify ion damage created defects near the heterointerface as the cause of any implantation induced relaxation. One proposed mechanism for how ion damage produces relaxation is that defects created by ion damage below the heterointerface may alone or condensed into larger voids serve as misfit dislocation nucleation sites in the substrate. During annealing dislocations generated from the damage in the substrate may propagate to the heterointerface and allow mismatch strain there to be partially relieved without generation of more defects in the film itself [9,10,20,22].

Studies using keV range ions implanted into III-V heterostructures have also successfully demonstrated ion induced strain relaxation and threading dislocation reduction. Myers et al. grew compressively strained InGaAs/GaAs strained-layer-superlattice (SLS) structures on GaAs substrates and then implanted the heterostructure with 300 keV Ar_+ ions [7,17]. They observed a marked decrease in SLS stress as a result of ion implantation. They attributed this stress decrease to an initial ion damage induced increase in compressive stress at the implant depth, which served to facilitate dislocation generation and eventual film relaxation. Defects were confined near the ion implantation depth in the SLS buffer layer but allowed the entire SLS structure to relax with few defects present in the film layers nearer the surface. The mechanism proposed in these studies is similar to the mechanism proposed above for the Si-Ge case. Swift heavy ion (SHI) irradiation studies in the III-V system using ions with energies in the MeV range have revealed another relaxation mechanism that may be active in compound semiconductors. High-energy ion irradiation of already grown strained layers may result in ion induced mixing and ion enhanced diffusion near the film/substrate interface [8,14,15]. The resulting mixing near the interface creates a region of intermediate composition that may function as an ion created buffer layer and allow partial film relaxation. In heavily irradiated compound semiconductor heterostructures film relaxation is likely due to a combination of both ion-induced compositional changes and ion created defect sources, and it is unclear which effect is dominant.

All previous ion-induced strain relaxation studies in the III-V system have focused on irradiation of already grown buffer or SLS structures. Of greater interest to this work is the pre-implantation of semiconductor substrates before film growth. While no previous studies have been published examining pre-implantation of III-V substrates, a pre-implantation approach for improving strain relaxation and lowering threading defect densities has seen some success in the group IV system [11-13]. As an example, Sawano et al. implanted Si substrates with 25 keV Ar^+ ions, grew a SiGe buffer layer on the implanted Si, and then annealed the heterostructure [11]. Doing this produced a significant increase in SiGe film relaxation compared to the unimplanted case, and they observed no threading dislocations in the topmost layer of their Si-Ge structure. Group

IV pre-implantation studies again identify strain relaxation at the heterointerface as resulting from dislocation generation in the substrate at ion damage created sources.

5.2 Experimental Methods

GaAs wafer substrates were implanted for this study with either In^+ or Ar^+ ions using a National Electrostatics Corp. (NEC-Middleton WI, USA) 400 kV Ion Implanter. That instrument can be referred to as broad-beam implantation system, as it is capable of implanting areas up to 6 in^2. [001] oriented n+ doped GaAs epi-ready wafer pieces were implanted with their surfaces at normal incidence to the ion beam, under vacuum, and at room temperature using a range of ion energies and ion doses. Large samples (1/4 of a 3 inch GaAs wafer) were implanted and then cleaved into smaller pieces along the [110] easy cleavage planes to generate samples with identical implantation conditions for multiple experiments. In^+ ions were generated using a solid Indium-Tin-Oxide (ITO) target ion source. Samples were In^+ implanted with a total ion dose of approximately $1x10^{14}$ ions/cm^2 at energies of either 50, 100, or 200 keV using a beam current of 50 nA/cm^2. Ar^+ ions were generated using a gas source. GaAs wafer samples were Ar^+ implanted with a total ion dose of either $1x10^{14}$ or $1x10^{15}$ ions/cm^2 at energies of 25 or 50 keV using a beam current of 75 nA/cm^2. All sample implantations were carried out by Dr. Fabian Naab at the Michigan Ion Beam Laboratory (MIBL). Samples implanted at every In^+ and Ar^+ implantation condition were characterized in their as-received state by AFM, HRXRD, and cross-sectional TEM.

InGaAs film growths were carried out by MBE using the EPI 930 MBE system. InGaAs films of thicknesses varying from 50 nm to 1 μm were grown on both pre-implanted and unimplanted wafers. Film growth samples first had their oxide desorbed by heating under an As_4 overpressure to 595-625 ˚C as recorded by optical pyrometer. All film growth steps were also carried out under an As_4 overpressure. For the case of InGaAs films grown on In^+ implanted GaAs, samples were cooled to ~590 ˚C and had a either a 20 nm or 2 nm thick GaAs buffer layer grown on them followed by cooling to ~500 ˚C for $In_xGa_{1-x}As$ growth. A 1 μm film of $In_xGa_{1-x}As$ was then grown on each In^+ implanted sample at InGaAs growth rates of 0.9-1.0 ML/s , using an V:III ratio of ~3, and with compositions ranging from approximately x=0.12 to 0.34 as determined after growth by HRXRD. The buffer layer thicknesses and compositions of specific samples will be given in the relevant portion of the results section. Following InGaAs film growth the samples were quenched to <200 ˚C. $In_xGa_{1-x}As$ films grown on unimplanted GaAs for comparison to films grown on In^+ pre-implanted GaAs were produced in a similar manner. Following oxide desorption the unimplanted GaAs substrates were cooled to ~590 ˚C for growth of a 500 nm GaAs buffer, then cooled to ~500 ˚C for growth of a 1 μm InGaAs layer, and finally quenched to <200 ˚C. Not all comparison samples were grown on the same day as their respective pre-implanted sample. However, their InGaAs growth rates and targeted In compositions were chosen to match the InGaAs films grown on In^+ implanted substrates as closely as possible to allow for as close a comparison of InGaAs film quality as possible. For $In_xGa_{1-x}As$ films grown on Ar^+ pre-implanted GaAs substrates, following oxide desorption samples were in one case cooled to ~590 ˚C for growth of a 2nm GaAs buffer and then cooled to 500 ˚C, and for all other samples had no buffer grown and were cooled directly to 500 ˚C. Once sample temperature was stabilized at 500 ˚C, $In_xGa_{1-x}As$ films ranging in thickness from 1 μm to 50 nm were grown using InGaAs growth rates of 0.95-0.98 ML/s, a V:III ratio of ~3-3.5, and compositions ranging from approximately x=0.20 to 0.25. Following InGaAs growth the samples were immediately quenched to <200 ˚C. $In_xGa_{1-x}As$ films grown on unimplanted GaAs substrates for comparison to the Ar^+ pre-implanted samples were grown either immediately before or after their respective pre-implanted sample whenever possible and using the same growth conditions and either a 200 nm thick buffer for thicker InGaAs films or no at all buffer for thinner InGaAs films. This allowed for as close a direct comparison as possible between InGaAs films grown on Ar^+ pre-implanted GaAs and unimplanted GaAs.

As-recevied In^+ and Ar^+ pre-implanted GaAs wafer samples were also desorbed and annealed under an As_4 overpressure using the EPI 930 MBE system in a manner meant to mimic the thermal conditions seen by the InGaAs film growth samples described in the preceding paragraph. Pre-implanted samples were heated to 595-625 ˚C to desorb their oxide. Then both the In^+ and Ar^+ pre-implanted film samples were cooled to and stabilized at 500 ˚C, held at that temperature for an hour, and then quenched to <200 ˚C.

The as-received Ar^+ and In^+ implanted GaAs samples, implanted and annealed samples, InGaAs films grown on pre-implanted GaAs, and the InGaAs films grown on unimplanted GaAs were characterized by AFM, HRXRD, and cross-sectional TEM. Tapping mode AFM scans of every sample's surface were taken using either the Digital Instruments (Veeco) Nanoscope IIIa AFM or Veeco Dimension Icon AFM. These AFM surface scans were used to examine surface morphology and roughness. Root-mean-squared (RMS) surface roughness values for each InGaAs film sample were found using 10x10 μm AFM scans and the free and open source Gwyddion scanning probe microscopy visualization and data analysis software program (version 2.24, gwyddion.net). The general film morphology seen in the 10x10 μm AFM scans was verified as representative of the film using larger area scans up to 50x50 μm. For most scans some degree of data "flattening" was needed to correct tilt of the sample and account for non-linearities or other issues inherent in the piezoelectric elements driving the scan head. Flattening was accomplished by using an automated function in either the AFM instrument's software or Gwyddion to fit a polynomial of order 0-4 to every trace in the image and then subtracting the background defined by that fit from the image. The flattening process was observed for every image and the lowest order polynomial possible that resulted in a satisfactory fit was used in order to avoid the introduction of unnecessary artifacts. Additional flattening was sometimes accomplished after polynomial fitting by matching each scan line to the median height. This helped to eliminate sharp irregularities between neighboring horizontal scan lines. Unfortunately, judging the success of an image flattening routine's ability to correct the image while still preserving the accuracy of the data in the AFM scan is subjective, as it is up to the user to identify the relevant features in each AFM scan and ensure that they are preserved.

HRXRD was used to examine the as-received and annealed implanted GaAs substrates and to examine the InGaAs films grown on implanted and unimplanted substrates. All XRD work was carried out using the Bede D1 triple-axis diffractometer and copper $K\alpha_1$ radiation. In the case of the as-received implanted GaAs substrates, Ω-2θ scans were taken about their 004 diffraction peak to observe how ion damage had broadened it. Amorphized material in a sample could be detected in the Ω-2θ scans as a low, broad peak or hump to the lower angle (larger lattice spacing) side of the 004 peak.

In the case of the annealed samples, their Ω-2θ 004 scans were compared to the unannealed implanted substrates to see how annealing had affected their peak width and the presence of any amorphous material. In the case of InGaAs films grown on GaAs substrates, 004 and 224 glancing exit (GE) geometry Ω-2θ scans were taken about the sample's substrate peak to observe the separation between the peaks corresponding to the substrate and film. By comparison to the known lattice spacing of the GaAs substrate the out-of-plane lattice parameter of the film could be determined from its 004 peak location and its in-plane lattice parameter from its 224 peak location. By comparing the scans from films of the same composition grown on pre-implanted and unimplanted substrates any differences in film relaxation could be seen as a shift in the film peak location. InGaAs film composition and percent relaxation back toward equilibrium lattice parameter (% relaxation) were determined using the in and out-of-plane lattice parameters found for the film, the elastic constants of the relevant III-V materials, and assuming a simple rule-of-mixtures relationship between film composition and lattice parameter. The actual calculations to determine film composition and % relaxation were carried out using an automated routine in the XRD instrument software. That routine took the 004 and 224 GE Ω-2θ experimental data, fitted curves to the diffraction peaks to find peak location, and then using the separation between film and substrate peaks calculated the relevant lattice parameters, film composition, and % relaxation. For InGaAs films <200 nm thick, the number of counts in the film 224 GE peak was often extremely low, in the range of 10-100 counts per point. Scans with greater resolution and more count time per point were used to better resolve these low peaks. However, because the signal to noise ratio was very low, the error in the calculated compositions and % relaxation for these thin films was greater. As the total counts in a HRXRD data set are somewhat arbitrary, in that they depend not only on the sample but also the total x-ray intensity and instrument alignment on any given day, all HRXRD results reported here have been normalized relative to the number of counts in the highest point of a sample's substrate peak.

Cross-sectional TEM analysis of as-received and annealed implanted substrates was used to determine the nature and extent of the damage created in them by ion implantation. TEM of InGaAs thin film samples was used to examine the threading defect density of the films, the condition of the InGaAs/GaAs heterointerface, and the effect of ion damage on it. BF, DF, and HRTEM imaging techniques were used for analysis. SAD was used primarily to orient samples to the [110] zone-axis for BF and HRTEM imaging or to a selected 2-beam condition for BF and DF imaging. Linear threading defect densities in InGaAs films were determined by taking a continuous series of images along a stretch of the InGaAs/GaAs interface and counting the number of defects intercepting a line placed a small distance above the interface. This measurement distance from the interface was set by strain-contrast, which obscured features right at the interface itself. Samples for cross-sectional TEM examination were prepared using a combined mechanical wedge polishing and Ar^+ ion-polishing method. First two thin cross-sectional slices through each sample were created by cleaving with a diamond scribe along the [110] type easy cleavage planes parallel to the sample edges. The top surface of those samples containing the features of interest were then epoxied together and allowed to cure for at least 12 hours at room temperature. The paired cross-section sample was then attached to a glass block along a flat edge using a stiff, low-melting point wax (sometimes referred to as "crystal-wax") with the epoxied interface perpendicular to the flat of the glass block. Then using a tri-pod or "T-tool" polishing tool to hold and level the glass block one exposed side of the sample was polished down a small amount first using 600 grit SiC polishing paper followed by polishing with 1200 grit SiC paper to ensure a mirror smooth surface. The fixing wax was then melted to allow the sample to be flipped to the opposite side and reattached to the glass block. The sample cross-section was then polished to a height of less than 2 mm using 600 grit SiC polishing paper, and then polished to a thickness of less than 100 μm using 1200 grit SiC paper. The point at which to stop mechanically polishing was determined by visually observing sample thickness, and polishing was ceased at the point when the unavoidable slight tilt of the sample relative to the polishing wheel caused it to wedge in from one side and visibly erode. At this point a Mo ring grid was attached with more epoxy to the sample with the epoxied interface centered in the ring, and the sample still attached to the glass block by wax was allowed to cure for at least 12 hours at room temperature. The sample attached to its Mo grid was then removed from the glass block by placing the block in acetone to dissolve the fixing wax. The freed sample was then taken to a Gatan

Prescision Ion Polishing System (PIPS) instrument for final thinning. The PIPS instrument used two low energy Ar^+ ion guns aimed at the sample at an angle to slowly mill the sample from both sides in vacuum. Each sample was first milled using 4-4.5 kV ion beams directed at the sample center at an angle of 4-6° off the sample surface. Once the sample had been thinned enough that one side had eroded to the epoxy interface or a hole had formed at the epoxy interface (generally taking 2-6 hours), the milling conditions were changed to a 2-3 keV beam energy and a 3-4° degree gun angle and milling was resumed for 10 minutes. This final lower energy mill was meant to remove some of the ion damaged material resulting from the initial, more aggressive mill. Following the final low energy mill, the sample could be removed from the PIPS system. The finished sample thinned to electron transparency was then ready for TEM imaging and could be placed in a double-tilt TEM holder for insertion into the TEM instrument.

5.2.1 SRIM Simulation

The freely available software package SRIM (The Stopping Range of Ions in Matter, version 2008.05, [23]) was used to simulate and predict the effects of In^+ and Ar^+ ion implantation into GaAs. The calculations and algorithm SRIM uses to predict ion interactions were developed primarily by J. F. Ziegler and J. P. Biersack [24]. SRIM uses a monte carlo method to simulate the implantation of ions into an amorphous target along with the associated ion-target interactions, and in its default configuration produces most accurate results for elemental or simple compound targets implanted in the linear cascade regime with ions of energy in the keV to MeV range. In this work, SRIM was used to roughly estimate the ion range distribution and damage distribution produced when implanting GaAs with Ar^+ and In^+ ions of various energies and doses. For a given ion dose the damage was estimated by find the displacements per atom (DPA) or damage energy density (keV/cm^3) based on the total number of atomic replacement and vacancy creating events predicted by SRIM as a function of depth and the displacement energy of GaAs. The GaAs target was setup in SRIM as amorphous with the density and stoichiometry of bulk crystalline GaAs. The energy necessary to displace a Ga or As atom from its site (displacement energy, E_d) was input as 15 eV based on other studies examining GaAs implantation and ion damage in the literature [25,26]. 10000 ion SRIM simulations of ion range and damage were used to guide the choices made in this study about which ion doses and energies to use when pre-implanting GaAs substrates and to better understand the distribution of ion damage that implantation produced.

5.3 In^+ Pre-Implantation of GaAs Substrates

5.3.1 Characterization of In^+ implanted GaAs

GaAs substrates were implanted with In^+ ions at energies of 50, 100, and 200 kV to a dose of $1x10^{14}$ ions/cm^2, then characterized and compared to unimplanted GaAs pieces taken from the same wafer that GaAs for implantation was taken from. Following implantation, the surfaces of samples implanted at each energy were examined by AFM and found not to show any significant difference in surface roughness relative to the unimplanted case. Figure 5.1 shows AFM surface scans of each In^+ implanted GaAs type and the unimplanted GaAs. Figure 5.2 shows HRXD 004 Ω-2θ scans taken from all three types of In^+ implanted samples. Each implantation sample's XRD data shows a broad shoulder to the lower angle, higher lattice parameter side of the GaAs substrate, with the effect being most pronounced in the 200 kV case. This hump is indicates that ion implantation disrupted or amorphized a portion of the GaAs substrate, resulting in a disordered region with a distribution of atomic spacings that were on average larger than the GaAs (004) lattice spacing.

The presence of these amorphous regions was confirmed by cross-sectional TEM. Figures 5.3(a), (b), and (c) show TEM images of the near-surface ion damaged region of the 50, 100, and 200 kV implanted substrates respectively, oriented such that the epoxy used in the sample preparation process is at the top of the image and the GaAs beneath the amorphous material is at the bottom. The amorphous regions are the bands of intermediate contrast between the light epoxy and darker crystalline GaAs. Those bands were confirmed to be amorphous by HRTEM and by noting the presence of diffuse rings in SAD patterns which correspond to amorphous material. The amorphous regions were not completely without structure, as confirmed by centering of the amorphous rings in SAD patterns and in fast Fourier transforms (FFTs) of HRTEM images directly at the GaAs (111) plane spacing. The amorphous region extended to an average depth below the sample surface of 28, 59, and 98 nm for the 50, 100, and 200 kV samples respectively. The boundary at the transition from amorphous back to crystalline GaAs at those depths was uneven and contained a large number of crystalline defects. Below the transition were additional ion induced defects in the crystalline GaAs, visible as dark lines and spots in the images of Figure 5.3. The amorphous region of the 50 kV sample extended to its top surface and the amorphous region of the 100 kV as-received sample extended to its top surface with a few very small isolated GaAs crystallites at the surface. The 200 kV sample had an approximately 10 nm thick layer of crystallites all along its top surface. HRTEM images of the 200 kV top surface and amorphous to crystalline GaAs lower boundary are shown in Figure 5.4. This top surface layer of crystallites and the deeper amorphous layer of the 200 kV sample indicate that the higher implantation energy allowed In^+ ions in its case to penetrate into the sample a short distance before beginning to lose energy to atomic collisions, after which the higher energy ions were able to inflict more damage to a greater depth in the GaAs substrate. Figure 5.5 shows the results of 10000 ion SRIM simulations estimating the ion ranges and damage distribution in GaAs of 50, 100, and 200 kV In^+ ions. The average depths of amorphization for each implantation energy are shown by the vertical dotted lines on the damage plot. By taking the SRIM predicted damaged at the amorphous depth to be the threshold for amorphization, the GaAs amorphization threshold was found to be 0.80 DPA ($5.3\text{x}10^{20}$ keV/cm^3), 0.43 DPA ($2.9\text{x}10^{20}$ keV/cm^3), and 0.54 DPA ($3.6\text{x}10^{20}$ keV/cm^3) for the 50, 100, and 200 kV cases respectively. These values are in relatively good agreement with the GaAs damage threshold of $3.3\ \text{x}10^{20}$ keV/cm^3 reported in the literature by a study using a similar SRIM and cross-sectional TEM method to examine Si^+ implantation of GaAs [25].

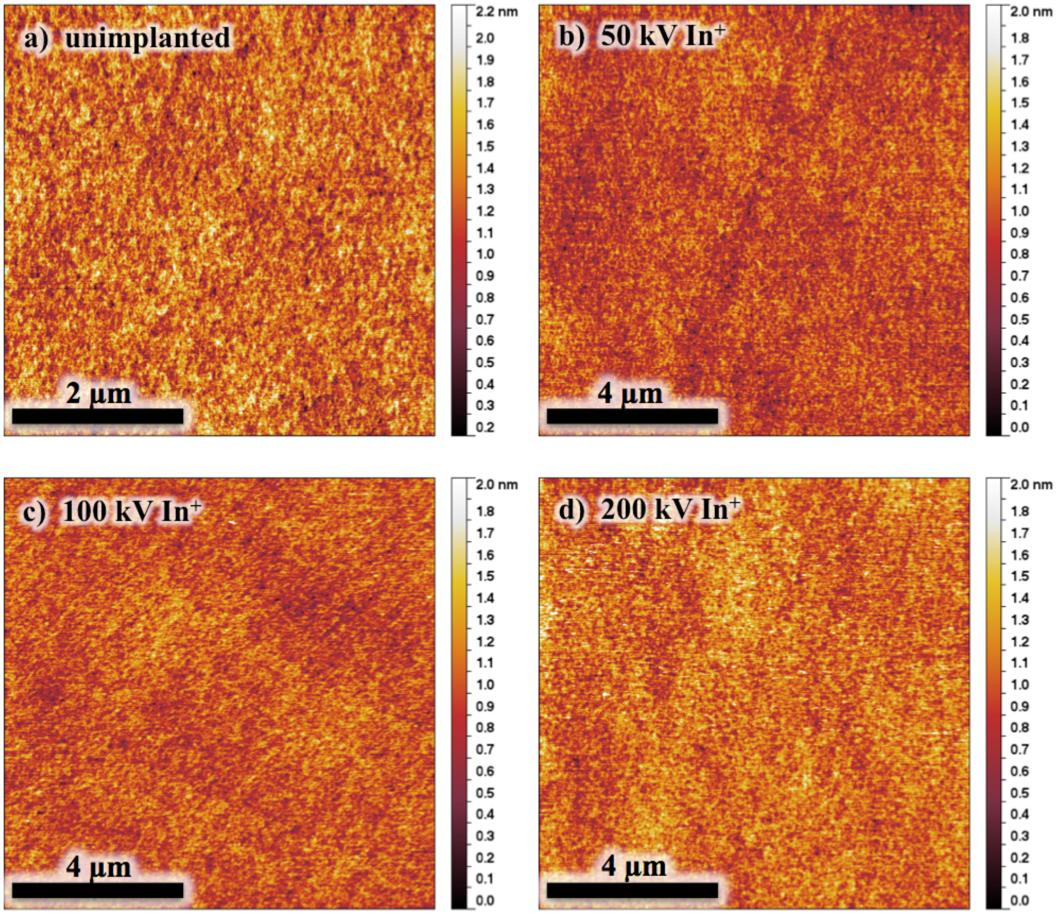

Figure 5.1: AFM scans taken of (a) an unimplanted GaAs wafer and as-received (b) 50 kV, (c) 100 kV, and (d) 200 kV In$^+$ implanted samples. The field of view (FOV) in (a) is 5 µm and 10 µm in the other images. The vertical height range is 2 nm for all the images.

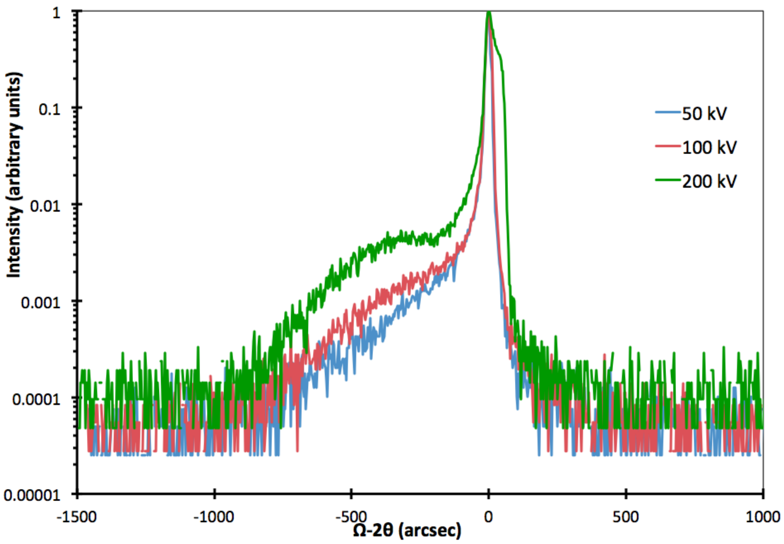

Figure 5.2: HRXRD 004 Ω-2θ scans for the 50, 100, and 200 kV as-received In$^+$ implanted samples.

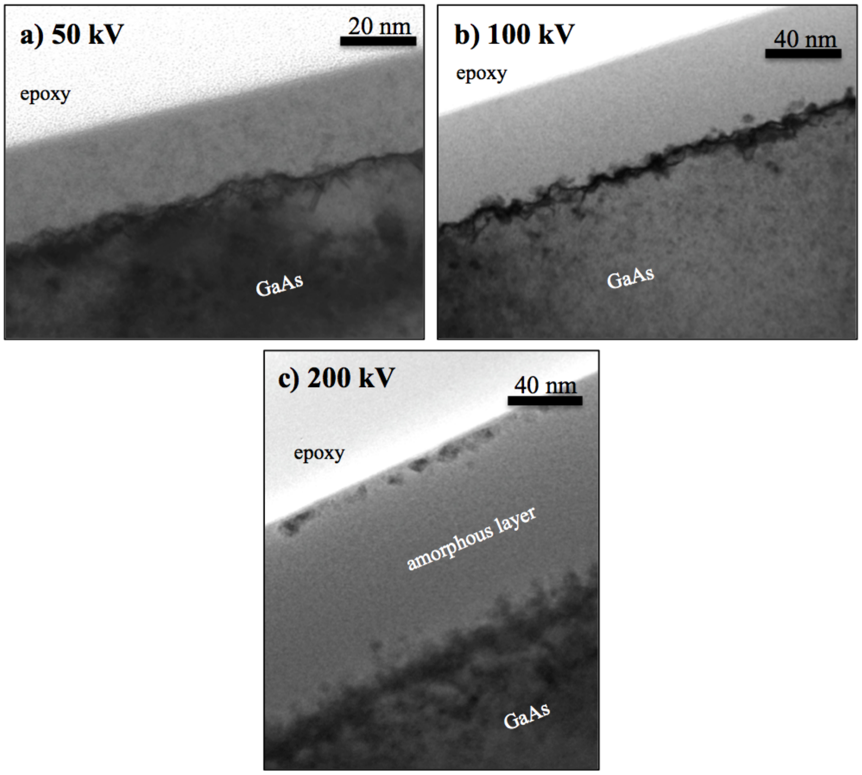

Figure 5.3: [110] BF TEM images showing the ion damaged regions of the as-received (a) 50 kV, (b) 100 kV, and (c) 200 kV In$^+$ implanted samples.

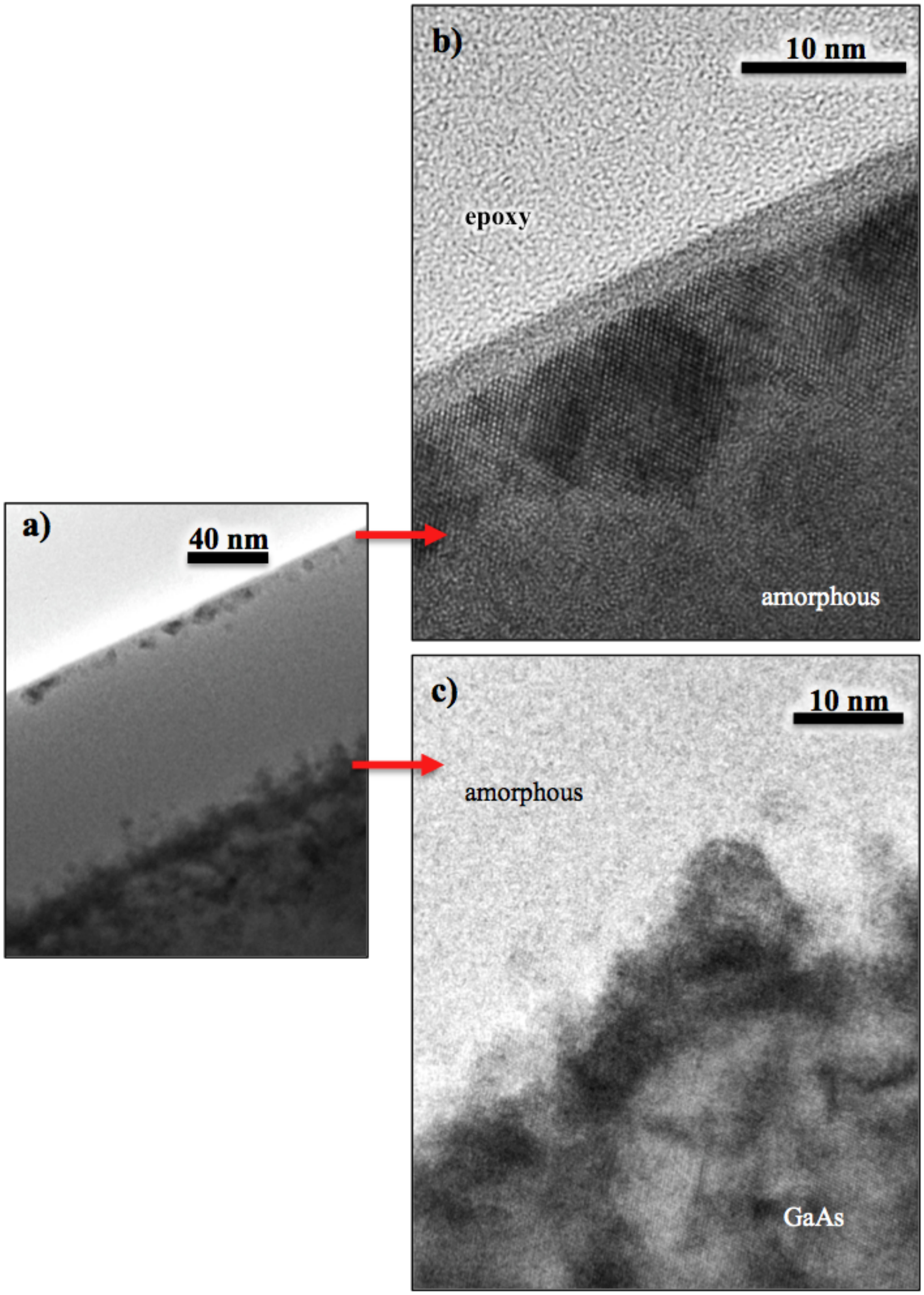

Figure 5.4: TEM images showing the damaged region of the 200 kV In$^+$ implanted GaAs sample. (a) shows a BF image of the entire damaged region. (b) shows a HRTEM image of the top surface of the sample, and (c) shows a HRTEM image of the damaged and defective material at the bottom of the amorphous region.

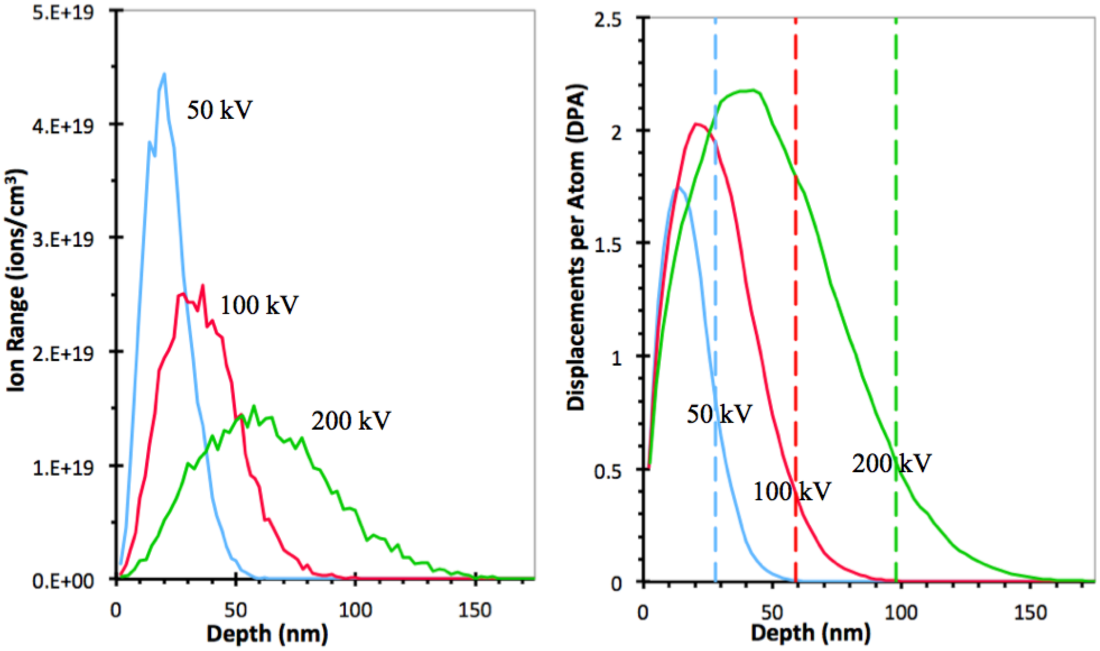

Figure 5.5: Plots showing 10000 ion SRIM simulations of ion range (left) and 1x10^{14} ions/cm^{2} damage distribution (right) for In^{+} ion implantation of GaAs. The vertical dotted lines in the damage plot show the experimentally determined average depth of amorphization for each implantation energy.

Samples of 50 and 200 kV In^{+} implantated GaAs were annealed by heating them under an As_4 overpressure to desorb their oxide, then holding them at the 500 ˚C InGaAs growth temperature for an hour. This was done to mimic the thermal history of an InGaAs film growth and so allow examination of the implanted substrates in a condition similar to that present during later InGaAs film growth experiments, and specifically to allow examination of the types of ion-induced defects present in the near surface region. Figure 5.6 shows AFM surface scans of (a) a desorbed and quenched unimplanted sample and desorbed and annealed (b) 50 kV implanted and (c) 200 kV implanted samples. In all cases desorption and annealing resulted in a rougher and pitted sample surface, presumably from the loss of GaAs material during time at elevated temperature. The unimplanted example is less pitted than the 50 and 100 kV implanted samples, but this is likely because the implanted samples were annealed for an hour at 500 ˚C and had time to degrade further while the unimplanted sample was brought to 500 ˚C after desorption and then immediately quenched. HRXRD comparison of the implanted samples before and after annealing indicates that some of the amorphous and ion damaged material was recrystallized and healed during annealing. As an example, Figure 5.7 shows 004 Ω-2θ scans from the 200 kV implanted GaAs before and after annealing, with recrystallization of amorphous material indicated by loss of most of the amorphous shoulder. However the annealed sample's 004 diffraction peak is still broad with lower intensity shoulders still present, indicating that ion damage is also still present in the sample.

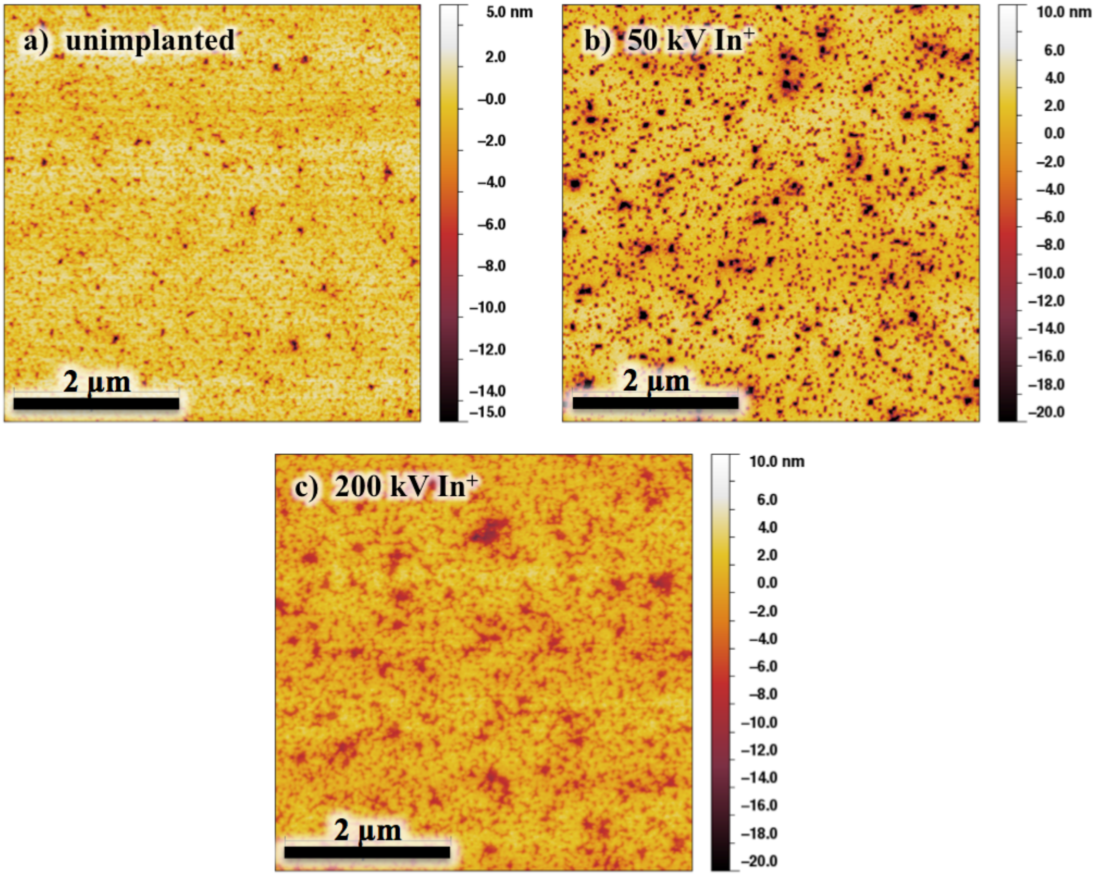

Figure 5.6: AFM scans taken of (a) an unimplanted GaAs wafer and (b) 50 kV and (c) 200 kV In^+ implanted samples following oxide desorption and annealing. The FOV of each image is 5 µm.

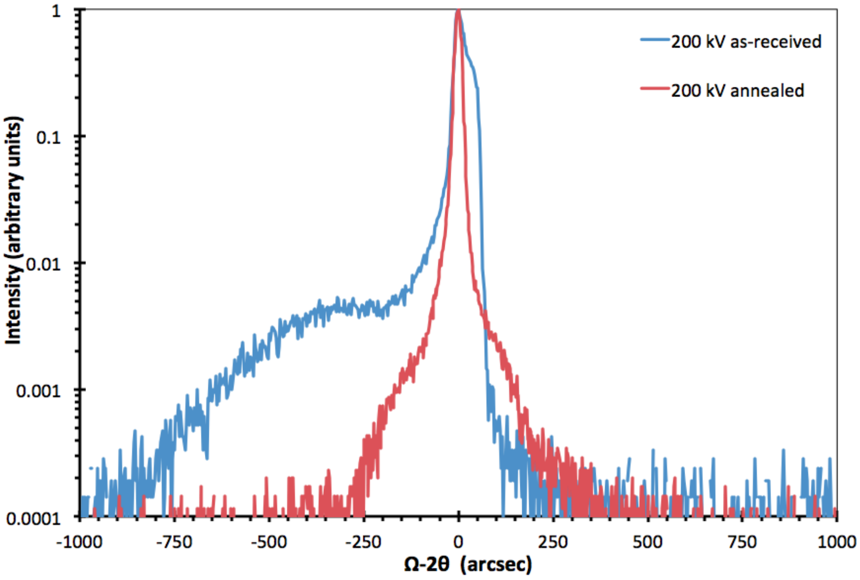

Figure 5.7: HRXRD 004 Ω-2θ scans for 200 kV In$^+$ *implanted samples in the as-received and desorbed/annealed conditions.*

Cross-sectional TEM of the 50 and 200 kV In$^+$ implanted and annealed samples was used to examine the distribution and type of ion damage in the samples as a function of depth below their desorbed surfaces. Figure 5.8 shows TEM images of In$^+$ ion induced defects in the 50 kV annealed sample. As shown by Figures 5.8(a) and (b), all of the amorphous damage in the samples epitaxially recrystallized and left defects ranging in location from the GaAs surface down to a depth of ~40 nm. The defects in those images were either triangle shaped defects or blobs of dark contrast, which had no structure obviously visible using [110] HRTEM imaging and were assumed to be collections of vacancies. Triangle defects were by far the most common defect seen. Figure 5.8(c) shows a HRTEM image of several triangle defects. They are bounded by linear crystalline defects, which might be stacking faults or anti-phase boundaries. The strain contrast from the triangle defect does not extend past the bounding linear defects. The triangle defects might be tetrahedral stacking fault zones seen in projection. No additional analysis was conducted to determine the identity of the triangle defects more completely. Figure 5.9 shows TEM images of ion induced defects in the 200 kV annealed sample. As shown in Figures 5.9(a) and (b), all of the amorphous damage in the sample recrystallized epitaxially, leaving a distinct band of defects below the surface. The majority of those defects lie in a range of 50-175 nm below the sample surface, putting the defect band over the location of the original amorphous-to-crystalline GaAs boundary found at a depth of 98 nm in the as-received sample. Defects in the 200 kV sample included regions of dark contrast without obvious structure which were assumed to be coalesced vacancies, defects showing “coffee-bean” diffraction contrast with an clear linear defect at their center which could be a dislocation loop, and triangle defects like those found in the 50 kV sample. Examples of these defect types are shown at higher magnification in Figures 5.9(c) and (d).

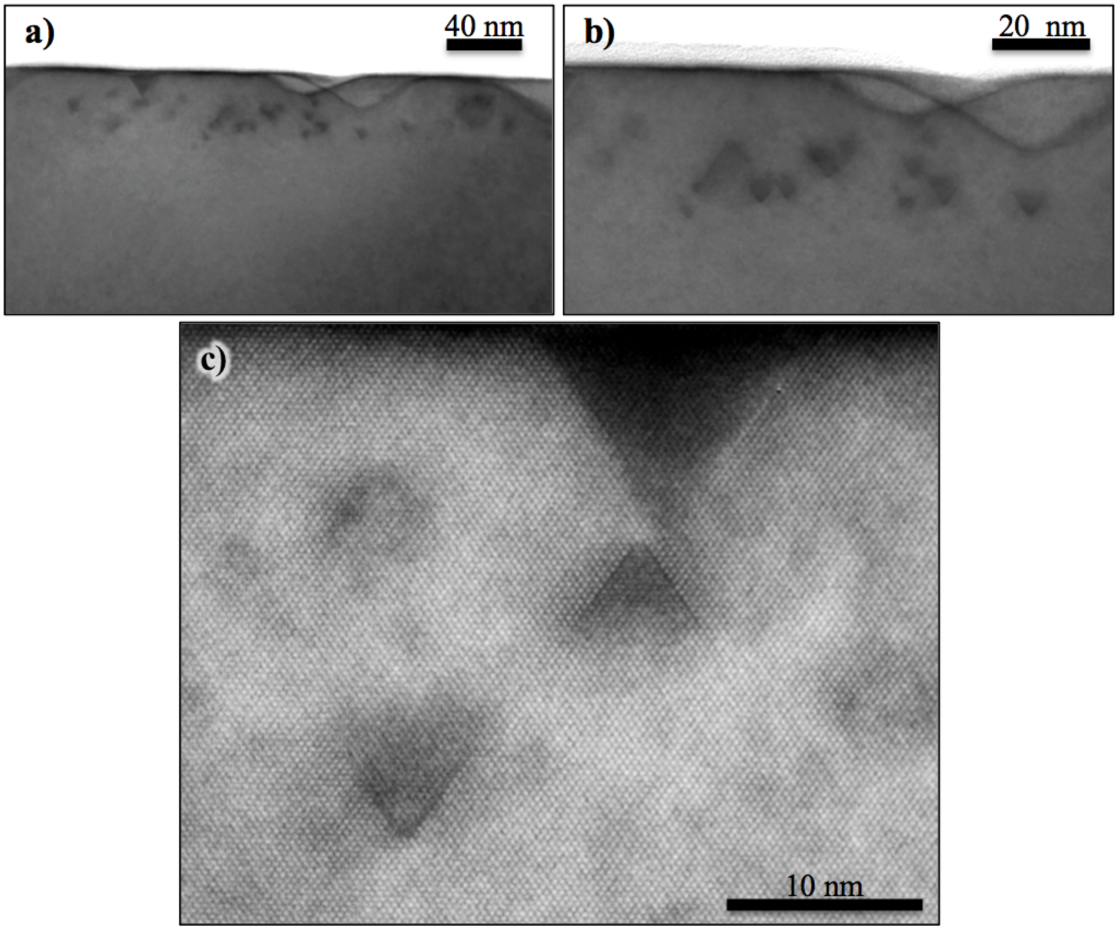

Figure 5.8: TEM images of ion induced defects in an annealed 50 kV In^+ implanted GaAs substrate. (a) and (b) show [110] BF images of defects near the sample surface. (c) shows a HRTEM image of triangle shaped defects near the surface.

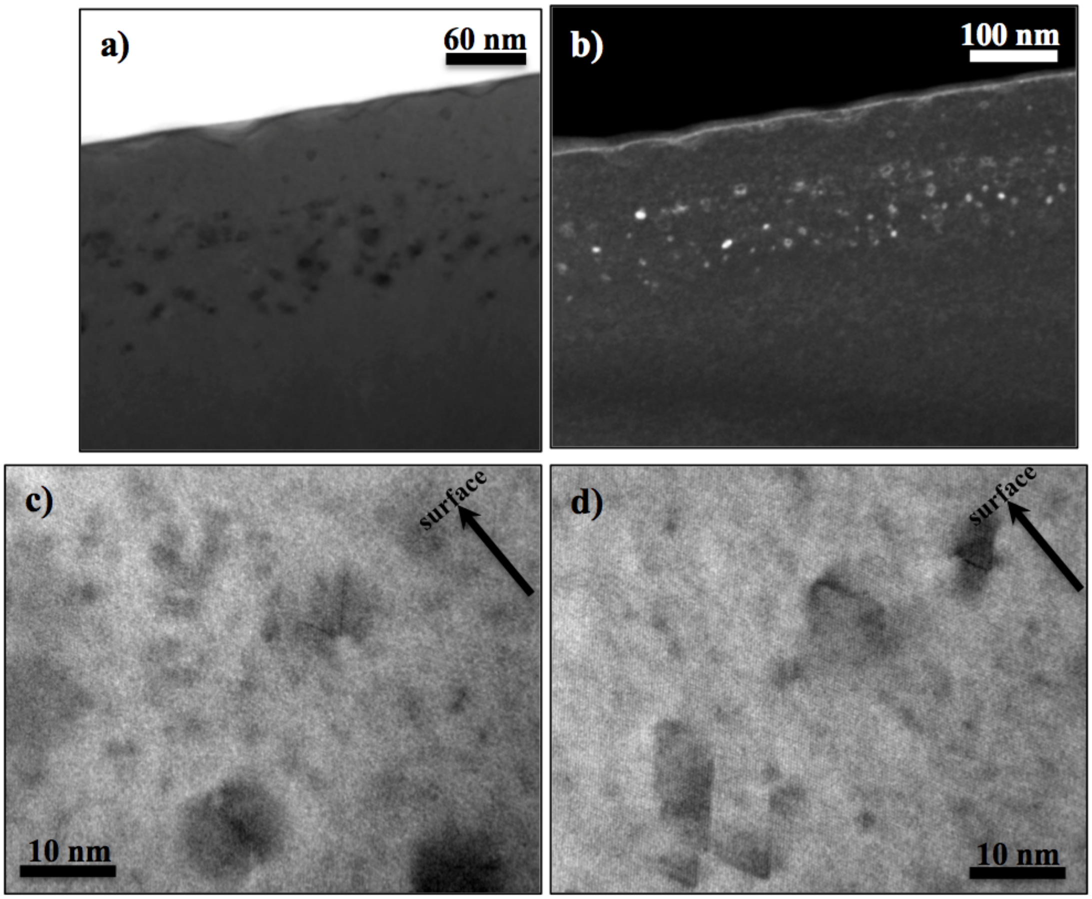

Figure 5.9: TEM images showing ion induced defects in an annealed 200 kV In$^+$ implanted GaAs substrate. (a) shows a [110] BF image of defects in a band beneath the sample surface. (b) shows a g=004 DF image of a similar area taken with the sample tilted to a 2-beam condition near the [110] zone-axis. (c) and (d) show higher magnification [110] BF images of several different defect types.

5.3.2 Characterization of InGaAs films grown on In$^+$ pre-implanted substrates

Once the effects of In$^+$ implantation on the GaAs substrates had been characterized, InGaAs films were grown on pieces of 50 and 200 kV pre-implanted GaAs to observe the effect of pre-implantation on film quality. Matching InGaAs films were also grown on unimplanted material to provide a point of direct comparison. Pre-implanted and unimplanted samples for comparison were grown using nearly the same growth conditions but were not grown on the same day, and so there are slight variations in film composition between each comparison set. The relative quality of a film was determined by its roughness, % relaxation, and threading dislocation density. Only a few

InGaAs on In$^+$ pre-implanted substrate samples were produced because the initial samples did not show promising results.

The first InGaAs on In$^+$ pre-implanted sample grown was a 1 µm thick $In_{0.12}Ga_{0.88}As$ film grown on a 20 nm GaAa buffer on 200 kV implanted GaAs. A 1 µm thick $In_{0.12}Ga_{0.88}As$ film grown on a 500 nm GaAs buffer on unimplanted GaAs was produced to serve as a comparison sample. Both samples were characterized by AFM, HRXRD, and cross-section TEM. Figure 5.10 gives an AFM surface scan for each sample, along with the composition and % relaxation found using 004 and 224 GE Ω-2θ HRXRD scans. The $In_{0.12}Ga_{0.88}As$ film on 200 kV implanted GaAs was much rougher and only slightly more relaxed than the unimplanted comparison sample.

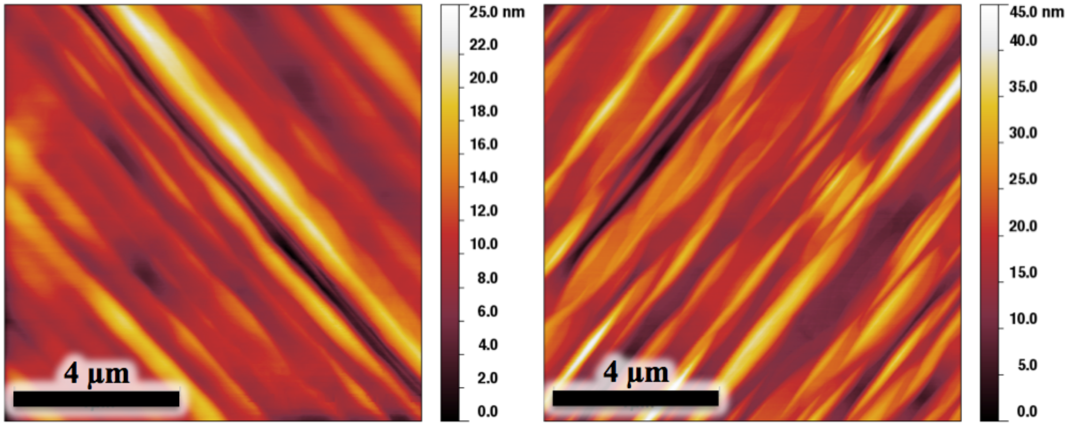

a) $In_{0.12}Ga_{0.88}As$ on unimplanted GaAs
200 nm GaAs buffer layer
RMS roughness= 3.5 nm
% relaxation= 91.6%

b) $In_{0.12}Ga_{0.88}As$ on 200 kV In$^+$ implanted GaAs
20 nm GaAs buffer layer
RMS roughness= 7.0 nm
% relaxation= 93.6%

Figure 5.10: AFM surface scans of $In_{0.12}Ga_{0.88}As$ films grown on (a) an unimplanted GaAs substrate and (b) a 200 kV In$^+$ pre-implanted GaAs substrate. The FOV of each image is 10 µm. Buffer layer thickness, RMS roughness, and % relaxation are given for each sample.

Figures 5.11(a) and (b) show BF images of the $In_{0.12}Ga_{0.88}As$ film grown on unimplanted GaAs. That InGaAs film was nearly threading dislocation free, with most of the defects extending into the GaAs buffer layer instead. Based on cross-sectional TEM images, that sample had linear threading dislocation densities of 0.75 µm^{-1} in the film and 6.2 µm^{-1} in the buffer layer. Figure 5.11(c) shows a BF image of the $In_{0.12}Ga_{0.88}As$ film grown on 200 kV implanted GaAs, and Figure 5.11(d) shows a DF image of its InGaAs/GaAs interface. The band of ion induced defects in that sample's substrate is visible in both images. In the 200 kV In$^+$ implanted case, threading dislocations were present in both the film and substrate, and those in the substrate did not appear to originate at ion-induced defects. The implanted case had a linear threading dislocation density in the film of 5.9 μm^{-1} and 5.4 μm^{-1} in the substrate. That higher threading dislocation density may account for why the implanted sample's film was able to relax slightly more. Results from characterization of both films showed that the 200 kV implanted sample was both rougher and had a higher threading defect density, and so it may be concluded that In$^+$ pre-implantation did not improve film quality.

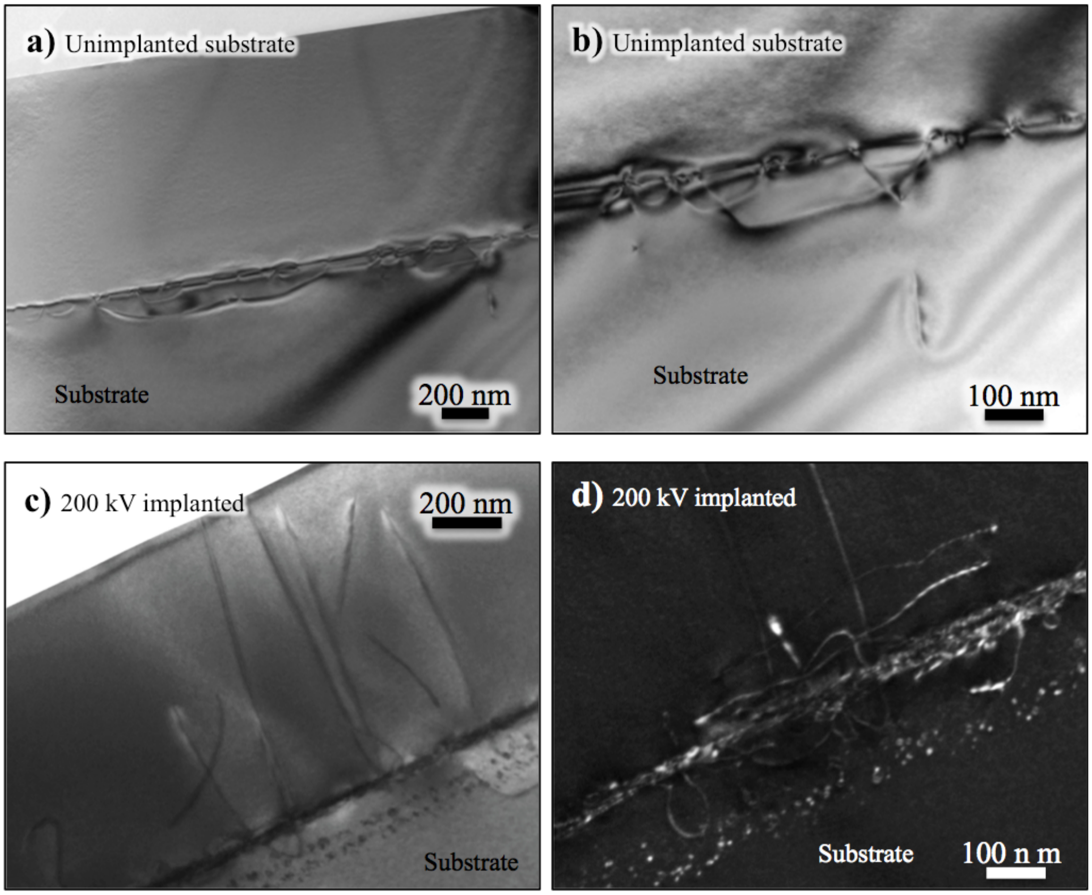

Figure 5.11: (a) and (b) show BF TEM images of an $In_{0.12}Ga_{0.88}As$ *film grown on unimplanted GaAs taken with the sample oriented to a [004]-type 2-beam condition near the [110] zone-axis. Dislocations are visible as the dark lines in the substrate. (c) shows a [100] zone-axis BF image and (d) shows a g=02-2 DF image of an* $In_{0.12}Ga_{0.88}As$ *film grown on a 200 kV* In$^+$ *pre-implanted substrate. Threading dislocations are visible as dark and white lines in images (c) and (d) respectively.*

Next $In_xGa_{1-x}As$ films with compositions near x=0.30 were grown on 200 kV pre-implanted, 50 kV pre-implanted, and unimplanted substrates in the hopes that a higher lattice mismatch strain would interact more strongly with the ion induced defects. A 1 μm thick $In_{0.34}Ga_{0.66}As$ film grown on a 20 nm GaAs buffer on 200 kV pre-implanted GaAs was first grown. Two films were grown on 50 kV pre-implanted GaAs: a 1 μm thick $In_{0.3}Ga_{0.7}As$ film on a 20 nm GaAs buffer and a 1 μm thick $In_{0.3}Ga_{0.7}As$ film on a 2 nm GaAs buffer. The composition of the first InGaAs film on 50 kV pre-implanted GaAs was not verified by HRXRD and is based off of growth rate calibrations. The buffer layer of the second film was reduced from 20 nm to 2 nm to sacrifice starting GaAs surface smoothness in favor of bringing the ion-induced defects as close to the InGaAs/GaAs interface as possible. A 1 μm thick $In_{0.32}Ga_{0.68}As$ film grown on a 200 nm GaAs buffer on unimplanted GaAs was produced to serve as a comparison sample. Figure 5.12 shows an AFM surface scan, composition, and % relaxation found using 004 and 224 GE Ω-2θ HRXRD scans for the 200 kV pre-implanted sample, the second 50 kV pre-implanted sample with 2 nm buffer, and the unimplanted sample. As indicated by that figure and the film property values given in it, the InGaAs films grown on In^+ pre-implanted substrates show a level of surface roughness similar to the unimplanted case and show little or no improvement in % relaxation. The slight improvement in % relaxation seen for the 200 kV sample is likely due to its higher In content. The first 50 kV pre-implanted sample is not shown in Figure 5.12. Its surface morphology resembled the other 50 kV sample, but it was rougher than the unimplanted sample with an RMS roughness value of 4.0 nm.

Figure 5.13 shows cross-sectional TEM images of the $In_{0.32}Ga_{0.68}As$ film grown on unimplanted GaAs. Figure 5.14 (a) shows a BF image of the $In_{0.34}Ga_{0.66}As$ film grown on 200 kV pre-implanted GaAs, and Figures 5.14(b) and (c) show TEM images of the $In_{0.3}Ga_{0.7}As$ film with a 20 nm buffer grown on 50 kV pre-implanted GaAs. Because of the very high dislocation densities in these samples and the poor quality of the images taken from the 200 kV sample, measuring linear dislocation densities was difficult and inaccurate. However, by comparing the images in Figure 5.13 and Figure 5.14 it can clearly be seen that the threading dislocation densities of the pre-implanted samples are similar to or higher than those of the unimplanted samples. So in summary, $In_xGa_{1-x}As$

x=~0.3 growth on 50 and 200 kV In$^+$ ion pre-implanted substrates did not produce significant improvements in film roughness, relaxation, or threading dislocation density compared to the unimplanted substrate case.

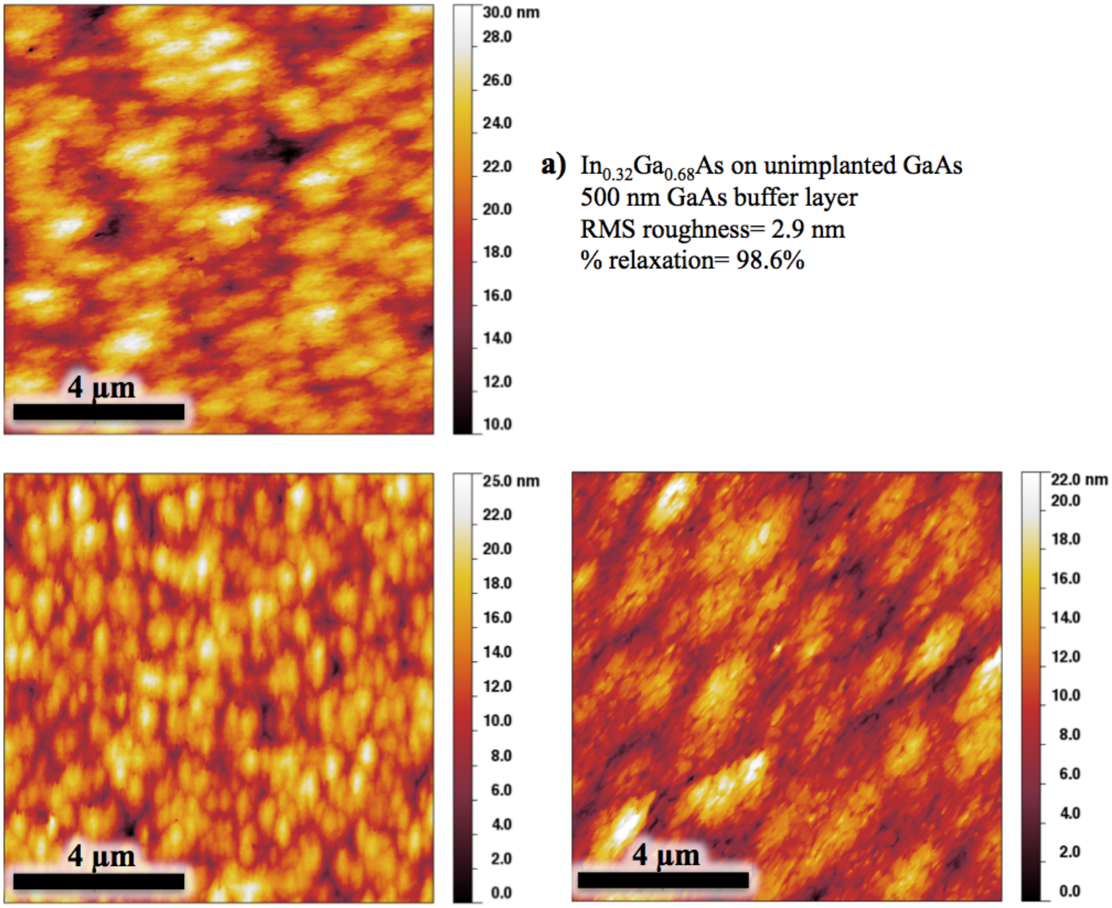

a) $In_{0.32}Ga_{0.68}As$ on unimplanted GaAs
500 nm GaAs buffer layer
RMS roughness= 2.9 nm
% relaxation= 98.6%

b) $In_{0.34}Ga_{0.64}As$ on 200 kV In$^+$ implanted GaAs
20 nm GaAs buffer layer
RMS roughness= 3.2 nm
% relaxation= 99.9%

c) $In_{0..30}Ga_{0.70}As$ on 50 kV In$^+$ implanted GaAs
2 nm GaAs buffer layer
RMS roughness= 3.0 nm
% relaxation= 95.8%

Figure 5.12: AFM surface scans of InGaAs films grown on (a) an unimplanted GaAs substrate, (b) a 200 kV In$^+$ pre-implanted GaAs substrate, and (c) a 50 kV In$^+$ pre-implanted substrate. The FOV of each image is 10 µm. Composition, buffer layer thickness, RMS roughness, and % relaxation are given for each sample.

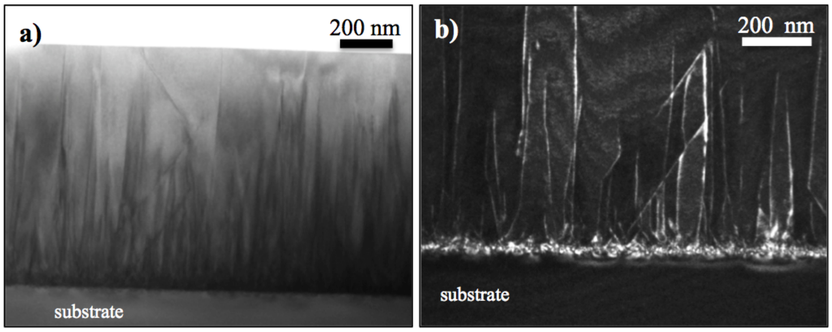

Figure 5.13: TEM images of an $In_{0.32}Ga_{0.68}As$ *film grown on an unimplanted GaAs substrate. (a) is a [110] BF image of the film, with dislocations in the film visible as dark lines. (b) is a g=004 DF image of the InGaAs/GaAs interface with dislocations visible as white lines.*

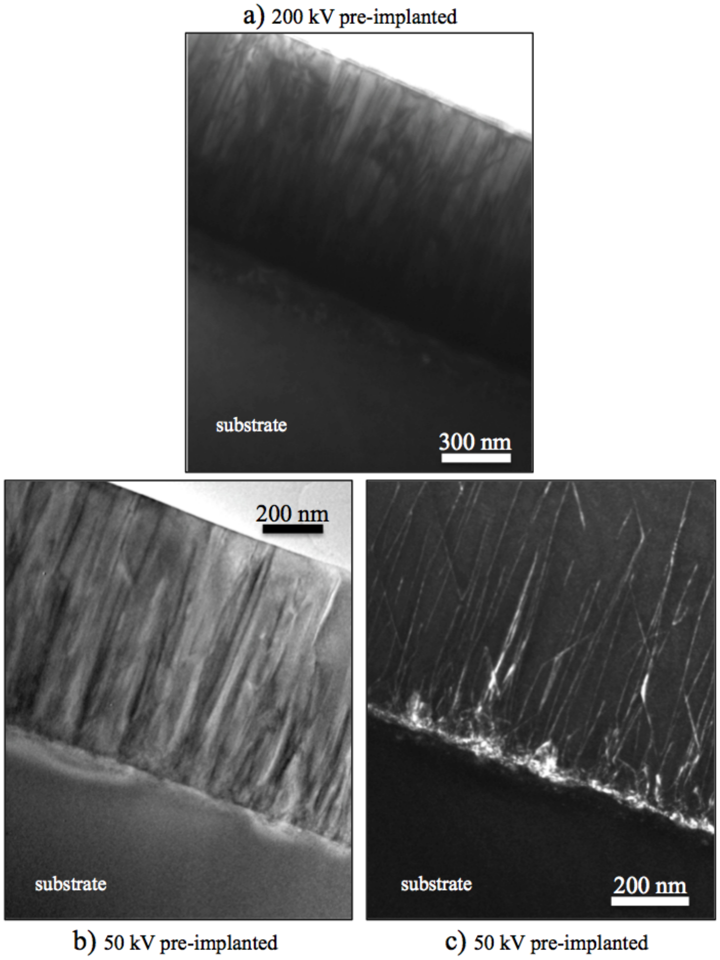

Figure 5.14: (a) shows a [110] BF TEM image of an $In_{0.34}Ga_{0.66}As$ *film grown on a 200 kV* In^+ *pre-implanted GaAs substrate. (b) shows a [110] BF image of an* $In_{0.3}Ga_{0.7}As$ *film grown on a 20 nm buffer on a 50 kV* In^+ *pre-implanted GaAs substrate. (c) shows a g=004 DF image of the InGaAs/GaAs interface from the same 50 kV sample.*

InGaAs growth on In^+ ion pre-implanted substrates produced no improvement in film quality relative to InGaAs films grown on unimplanted GaAs substrates. That lack of improvement may be due to several possible cause. First and foremost, it is possible no type of ion induced damage or defect will interact with a strained III-V heterointerface to improve film relaxation and lower threading defect density. However, the examples in the literature reported earlier in section 5.1.1 indicate that this is not the case. Another possibility is that the defects produced by In^+ implantation were placed too deeply beneath the GaAs substrate surface to interact with strain at the InGaAs/GaAs interface. This was likely the case with the 200 kV implanted samples, as their ion induced defects lay in a band >50 nm below the sample surface (see Figure 5.9(b)). For this reason buffer layers in later experiments would be reduced or eliminated in order to bring the interface as close to the ion induced defects as possible. In the 50 kV case however defects were seen in annealed samples extending up to the substrate surface. It is also possible that the types of defects produced by In^+ implantation were of the wrong type to interact with the strain-field produced at the lattice mismatched heterointerface. As an example, the triangle shaped defects seen in the 50 kV sample (see Figure 5.8(c)) had very little dark strain contrast associated with them in BF TEM images, possibly indicating that their presence does not heavily strain the surrounding lattice. In^+ implantation may produce defects with little strain because the In^+ ions may readily substitute into the Ga lattice once implanted and annealed. Finally, in all the In^+ implanted sample types an amorphous layer produced by ion damage was recrystallized upon heating as part of the film growth process. The process of recrystallization and annealing may have allowed much of the ion damage in the substrate to heal, and so removed a significant portion of any implantation-produced strain near the substrate surface which might interact with the strained InGaAs film. These possible reasons for why In^+ pre-implantation was unable to improve strained InGaAs film quality were taken into account when designing the Ar^+ pre-implantation experiments that followed.

5.4 Ar$^+$ Pre-implantation of GaAs Substrates

5.4.1 *Characterization of Ar$^+$ implanted GaAs*

A second round of pre-implantation experiments were carried out in which GaAs substrates were implanted with Ar$^+$ ions at energies of 25 or 50 kV to doses of 1x10^{14} or 5x10^{14} ions/cm^2, then characterized and compared to unimplanted GaAs material. Implantation energies, doses, and choice of Ar$^+$ as the implantation species were selected keeping in mind the possible causes for why In$^+$ pre-implantation failed to improve InGaAs film quality as discussed above and by using SRIM to predict the damage distribution of different Ar$^+$ implantation parameters. Figure 5.15(a) shows 10000 ion SRIM simulations of Ar$^+$ ion ranges in GaAs for implantation energies of 25 and 50 kV, and Figure 5.15(b) shows the damage distribution predicted for each implantation energy and dose combination. Ar$^+$ was chosen as the implantation species for this second round of pre-implantation experimentation because it will not readily incorporate into the GaAs lattice and is a lighter ion, allowing easier control of the degree of ion damage produced in the GaAs targets. The lower ion implantation energies of 25 and 50 kV were chosen in order to produce ion damage nearer to the substrate surface. Based on the GaAs amorphization threshold determined using the In$^+$ implantation results, Ar$^+$ ion doses of 1x10^{14} and 5x10^{14} ions/cm^2 were chosen to produce implanted GaAs substrates that both were and were not partially amorphized. It was hoped that by using Ar$^+$ ions with these changed implantation parameters that ion damage could be produced in the GaAs target substrates that would interact with and change a lattice mismatched film grown on them.

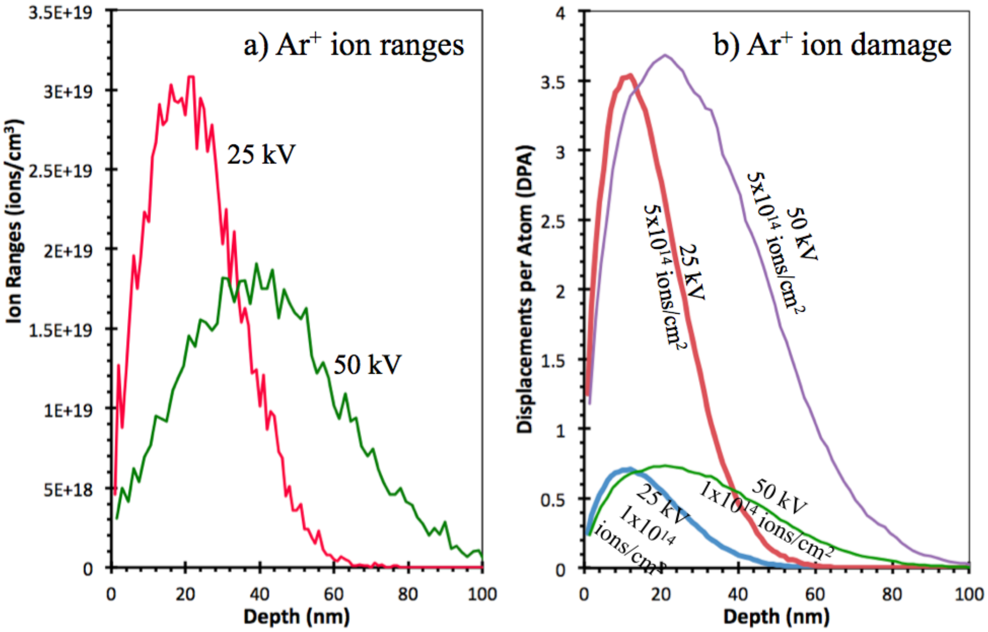

Figure 5.15: 10000 ion SRIM simulations predicting (a) ion ranges and (b) damage distributions for Ar$^+$ implantation into GaAs.

Samples implanted using each energy and dose combination were examined by AFM and found not to have any significant difference in surface roughness relative to the unimplanted case. Figure 5.16 shows AFM surface scans of each Ar$^+$ implanted GaAs type. Figure 5.17(a) shows HRXRD 004 Ω-2θ scans taken from both types of 25 kV implanted GaAs, and Figure 5.17(b) shows 004 Ω-2θ scans from both types of 50 kV implanted GaAs. Each implantation sample's XRD data shows a broad shoulder and one or more peaks to the lower angle, higher lattice parameter side of the GaAs substrate diffraction peak. As in the In$^+$ implantation case, these shoulders and peaks are taken to indicate the presence of ion damage and a disrupted GaAs structure. As might be expected from the SRIM predicted damage distributions in Figure 5.15(b), 50 kV Ar$^+$ implantation had a greater impact on the structure of the irradiated GaAs.

Cross-sectional TEM of the Ar$^+$ implanted samples was again used to examine the distribution and type of ion damage in each sample as a function of depth below their surfaces. The presence of amorphous regions in the more highly dosed samples was confirmed by cross-sectional TEM. Figures 5.18(a) and (b) show TEM images of the ion-damaged regions of the higher ion dose 25 kV 5x10^{14} ions/cm^2 and 50 kV 5x10^{14} ions/cm^2 samples respectively. Both of those samples have a region of amorphous GaAs beneath their surface, have in that amorphous region small islands of GaAs which remained crystalline, and have ion-damage induced defects in the remaining crystalline material beneath their amorphous layers. Full loss of long-range order in the amorphous regions was confirmed by HRTEM. The higher dose 25 kV sample was amorphized down to an average depth of ~20 nm, and the higher dose 50 kV sample was amorphized to an average depth of ~50 nm. Figure 5.19 shows TEM images of the ion damaged regions in the lower ion dose Ar^+ implanted samples. Figure 5.19(a) shows a low magnification image of the 25 kV $1x10^{14}$ ions/cm^2 sample's near surface ion damage, and Figure 5.19(d) shows a low magnification image of the 50 kV $1x10^{14}$ ions/cm^2 sample's damage. Both 25 and 50 kV low dose samples have a layer of ion induced defects visible as spots of dark contrast in those images, with the defects in a band extending from the surface to a depth of ~30-35 nm in the 25 kV case and to a depth of ~60 nm in the 50 kV case. Neither lower dose sample had an amorphous layer, though the XRD results in Figure 5.17 indicate they may have had regions with locally disrupted crystalline structure. Thus, by using Ar^+ as the implantation species and a lower dose of $1x10^{14}$ ions/cm^2 amorphization was avoided. The types of defects observed by BF and HRTEM imaging in the Ar^+ implanted samples included regions of dark contrast without obvious structure which were assumed to be coalesced vacancies, defects showing "coffee-bean" diffraction contrast with a clear linear defect at their center which may be a dislocation loop, and linear defects below the amorphous region in the higher dose implanted samples. Figures 5.19(b) and (c) show examples of the defects presumed to be coalesced vacancies in the 25 kV $1x10^{14}$ ions/cm^2 implanted sample. Figure 5.19(e) shows a BF image of the same type of defect and Figure 5.19(f) shows a HRTEM image of coffee-bean defects with a linear defect at their center in the 50 kV $1x10^{14}$ ions/cm^2 sample. No triangle shaped defects like those observed in the In^+ implanted samples were seen in the Ar^+ implanted samples.

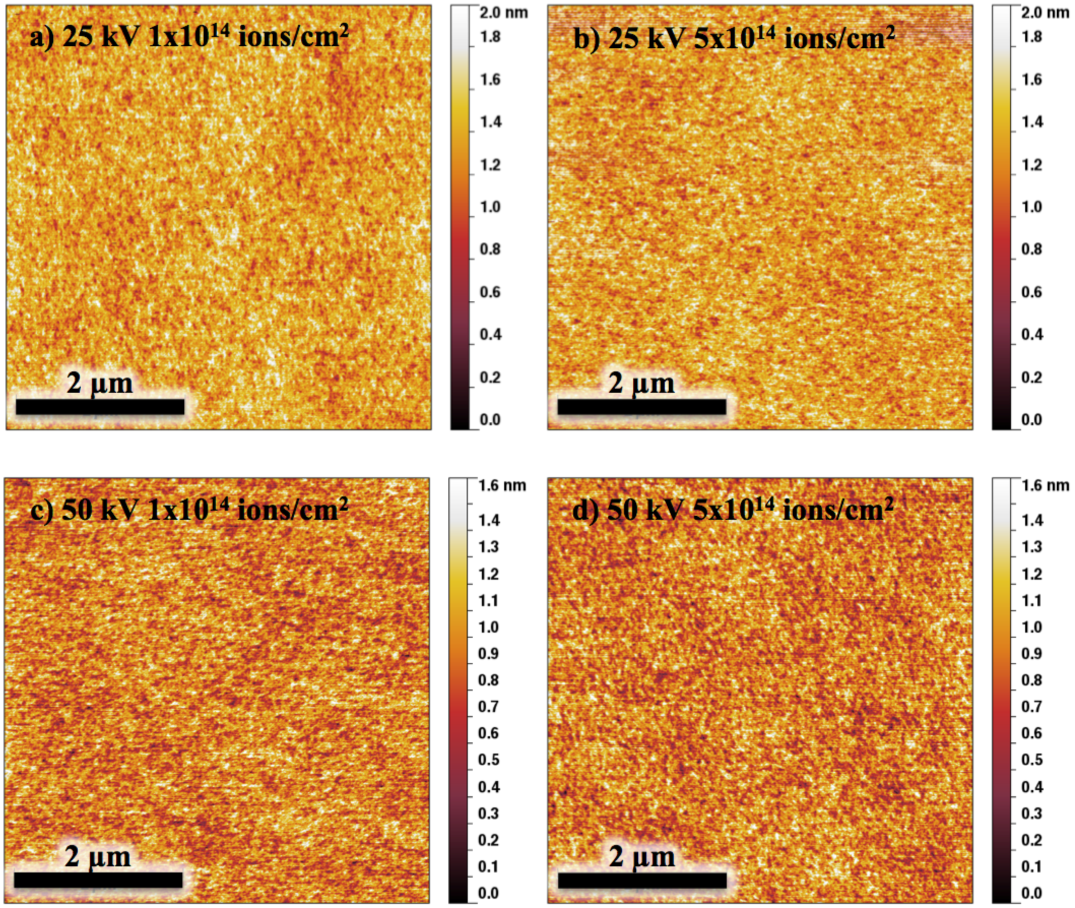

Figure 5.16: AFM scans taken of as-received (a) 25 kV 1x10^{14} ions/cm^2, (b) 25 kV 5x10^{14} ions/cm^2, (c) 50 kV 1x10^{14} ions/cm^2, and (d) 50 kV 5x10^{14} ions/cm^2 Ar$^+$ implanted samples. The FOV in each image is 5 µm.

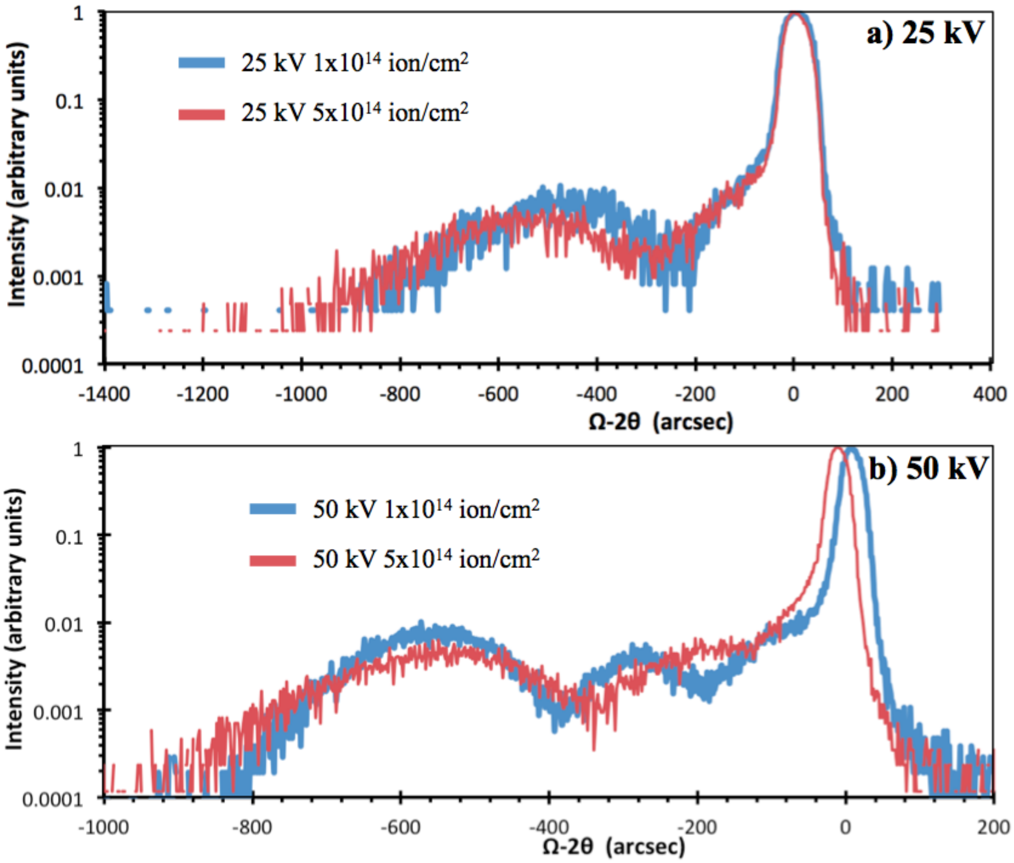

Figure 5.17: HRXRD 004 Ω-2θ scans taken from as-received (a) 25 kV and (b) 50 kV Ar^+ implanted GaAs samples.

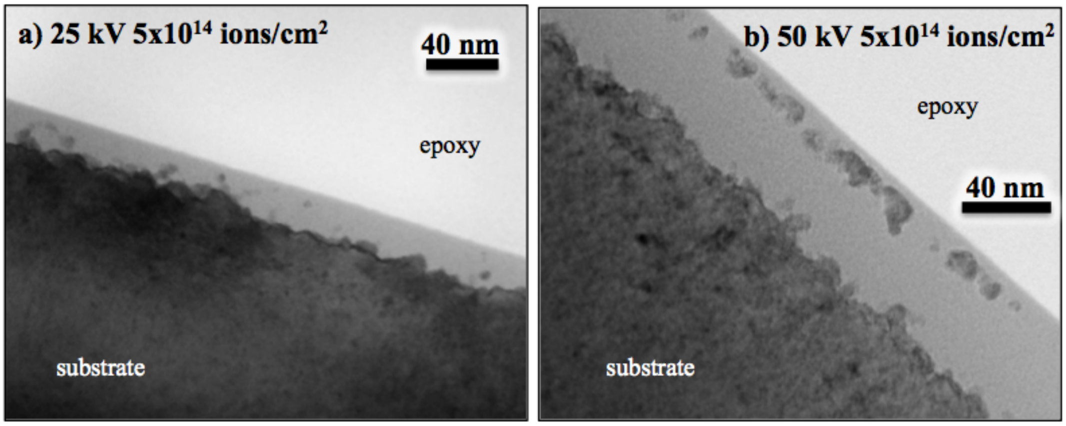

Figure 5.18: [110] BF TEM images taken of the higher ion dose as-received (a) 25 kV $5x10^{14}$ ions/cm^2 and (b) 50 kV $5x10^{14}$ ions/cm^2 Ar^+ implanted samples. Both samples have a surface layer of amorphous material.

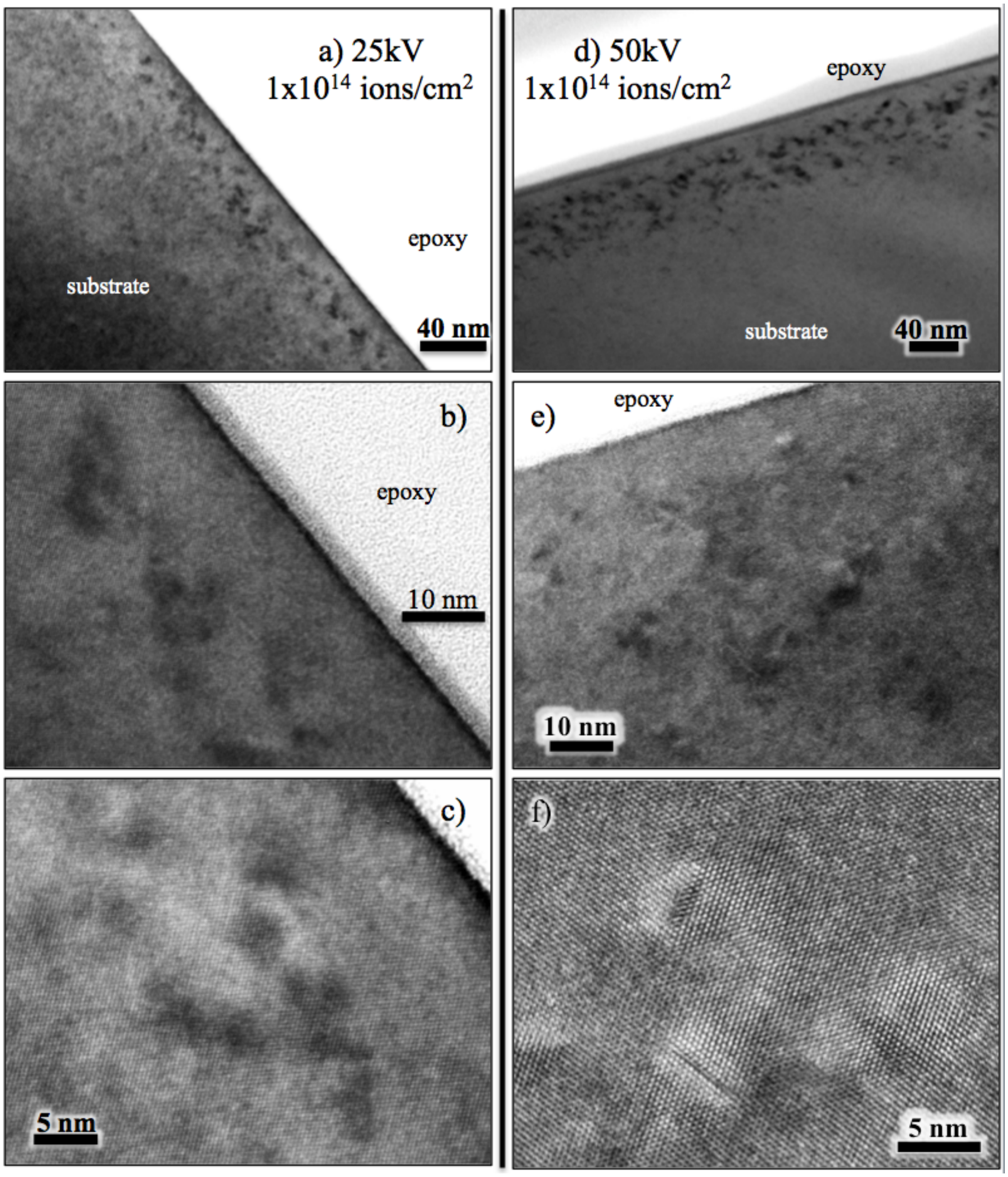

Figure 5.19: BF TEM images of the lower ion dose as-received Ar$^+$ *implanted GaAs samples. (a) shows a [110] BF image of ion damage below the surface of the 25 kV 1x10*^{14} *ions/cm*^{2} *sample, and (b) and (c) show higher magnification images of ion-induced defects in that same sample. (d) shows a [220] 2-beam condition BF image of ion damage below the surface of the 50 kV 1x10*^{14} *ions/cm*^{2} *sample, and (e) and (f) show higher magnification images of ion-induced defects in that same sample. Neither the 25 kV nor 50 kV low dose samples had a layer of amorphized material.*

A sample of each Ar$^+$ implantation energy and dose combination was annealed by heating under an As$_4$ overpressure to desorb its oxide and then held at 500 ˚C for an hour. This was again done to mimic the thermal history of an InGaAs film growth. AFM was then used to examine the surface condition of the annealed samples to provide a picture of the starting surface condition for InGaAs growth, and HRXRD was used to examine the effect of annealing on implantation damage. Figure 5.20 shows AFM surface scans of all four Ar$^+$ implanted sample types. In each case desorption and annealing resulted in surface roughening and pitting, comparable to the similarly annealed unimplanted and In$^+$ implanted sample surfaces shown in Figure 5.6.

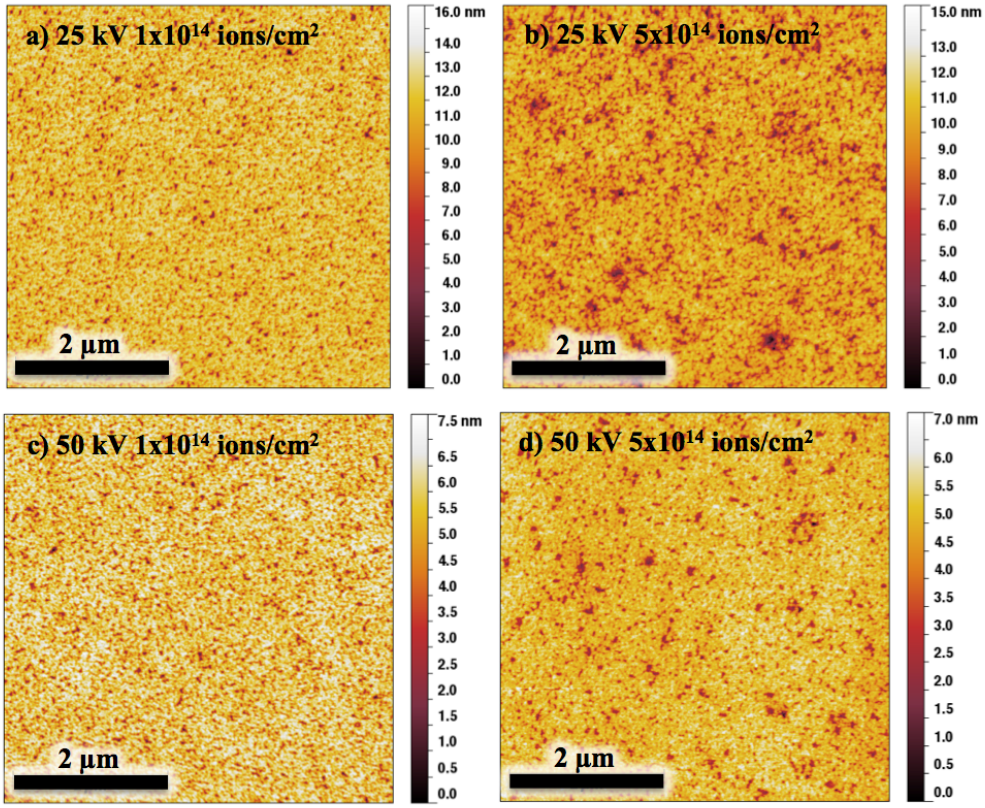

Figure 5.20: AFM scans taken of (a) 25 kV 1x10^{14} ions/cm^2, (b) 25 kV 5x10^{14} ions/cm^2, (c) 50 kV 1x10^{14} ions/cm^2, and (d) 50 kV 5x10^{14} ions/cm^2 Ar$^+$ implanted, desorbed, and annealed samples. The FOV of each image is 5 μm.

HRXRD examination of the annealed samples compared to the as-received Ar$^+$ implanted samples showed that annealing removed some but not all of the amorphous material and ion damage. Figure 5.21(a) shows HRXRD 004 Ω-2θ scans from both the as-received and annealed lower dose 50 kV 1x10^{14} ions/cm^2 implanted GaAs, and Figure

5.21(b) shows similar HRXRD scans for the higher dose 50 kV 5x10^{14} ions/cm^2 implanted material. Annealing lowered or removed most of the intensity from the broad peaks and substrate peak shoulders visible in as-received sample XRD data. However, in both Figure 5.21(a) and (b) the annealed sample substrate peaks are still broadened, indicating that not all ion damage was removed by annealing.

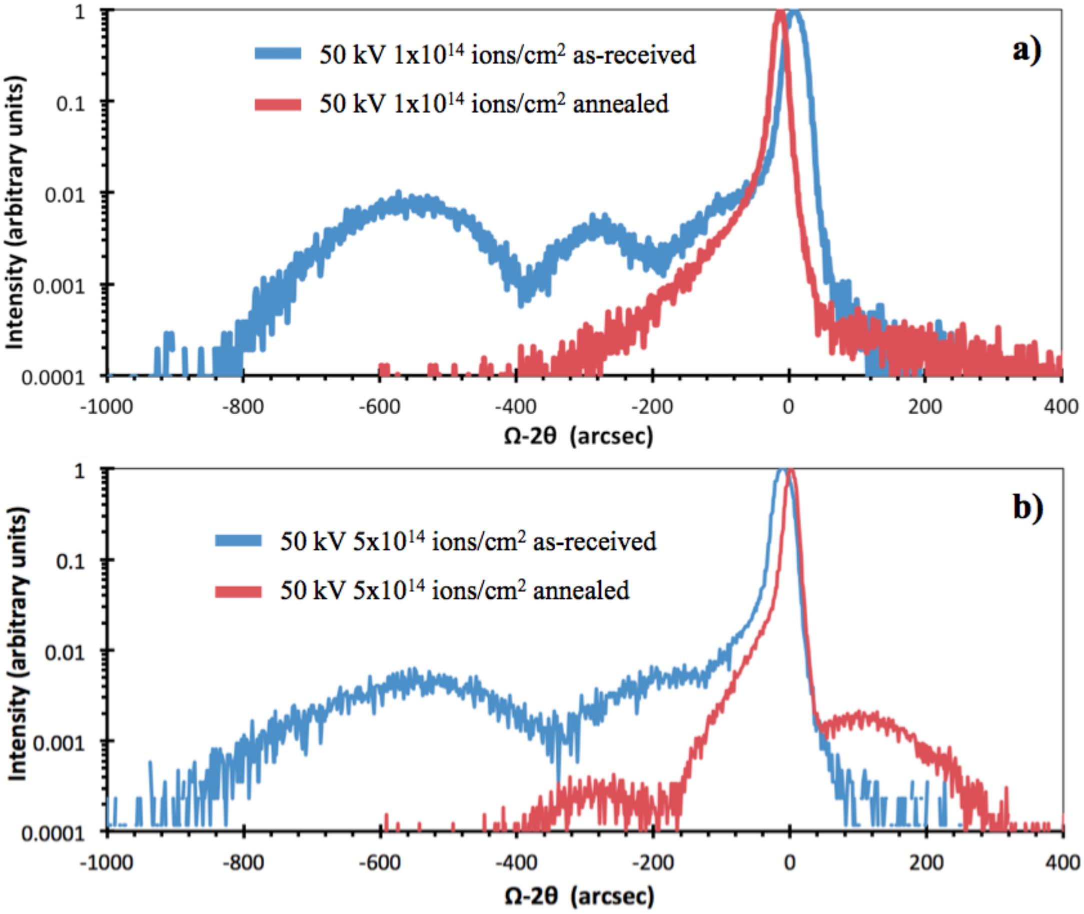

Figure 5.21: shows HRXRD 004 Ω-2θ scans of (a) 50 kV 1x10^{14} ions/cm^2 and (b) 50 kV 5x10^{14} ions/cm^2 Ar$^+$ implanted GaAs before and after annealing.

5.4.2 Characterization of InGaAs films grown on Ar$^+$ pre-implanted substrates

Following characterization of the effects of Ar$^+$ implantation on GaAs substrates InGaAs films were grown on only some of the different types of Ar$^+$ implanted substrates in order to observe the effects of pre-implantation on lattice mismatched film quality. Experimentation was focused on the lower dose 25 and 50 kV 1x10^{14} ions/cm^2 pre-implanted substrates that were not amorphized during implantation. InGaAs films were also grown directly on the Ar$^+$ pre-implanted substrates, with a 2 nm GaAs buffer in one case and no buffer whatsoever for all others. This was done to ensure that Ar^+ implantation damage remained as close to the heterointerface as possible. For each film grown on a pre-implanted substrate a comparison film of the same composition was grown on an unimplanted substrate using the same growth parameters. The relative quality of the InGaAs films was again judged by film roughness, % relaxation, and threading defect density.

The first InGaAs on Ar^+ pre-implanted substrate experiments conducted were the growth of 1 μm thick $In_{0.22}Ga_{0.78}As$ films on pre-implanted and unimplanted substrates. A 1 μm $In_{0.23}Ga_{0.77}As$ film on a 25 kV $5x10^{14}$ ions/cm^2 pre-implanted substrate with no buffer and a 1 μm thick $In_{0.22}Ga_{0.78}As$ film on an unimplanted substrate with a 200 nm GaAs buffer were grown one after another on the same day using exactly the same growth conditions. A 1 μm $In_{0.22}Ga_{0.78}As$ film on a 25 kV $1x10^{14}$ ions/cm^2 pre-implanted substrate with a 2 nm GaAs buffer was grown on a different day using matched but not exactly the same growth conditions as the other two 1 μm films. The surface condition of each film was determined by AFM, and film composition and % relaxation were determined by HRXRD. Figure 5.22 shows AFM scans of each 1 μm InGaAs sample surface, and the sample composition, RMS roughness, and % relaxation are listed with the corresponding image. The two films grown on Ar^+ pre-implanted GaAs were significantly smoother, with RMS roughness values of 2.5 nm, than the film grown on the unimplanted GaAs substrate, which had a RMS roughness of 10.24 nm. The films grown on pre-implanted substrates were also 3-4% more relaxed towards their bulk InGaAs lattice parameters than the film on unimplanted GaAs was.

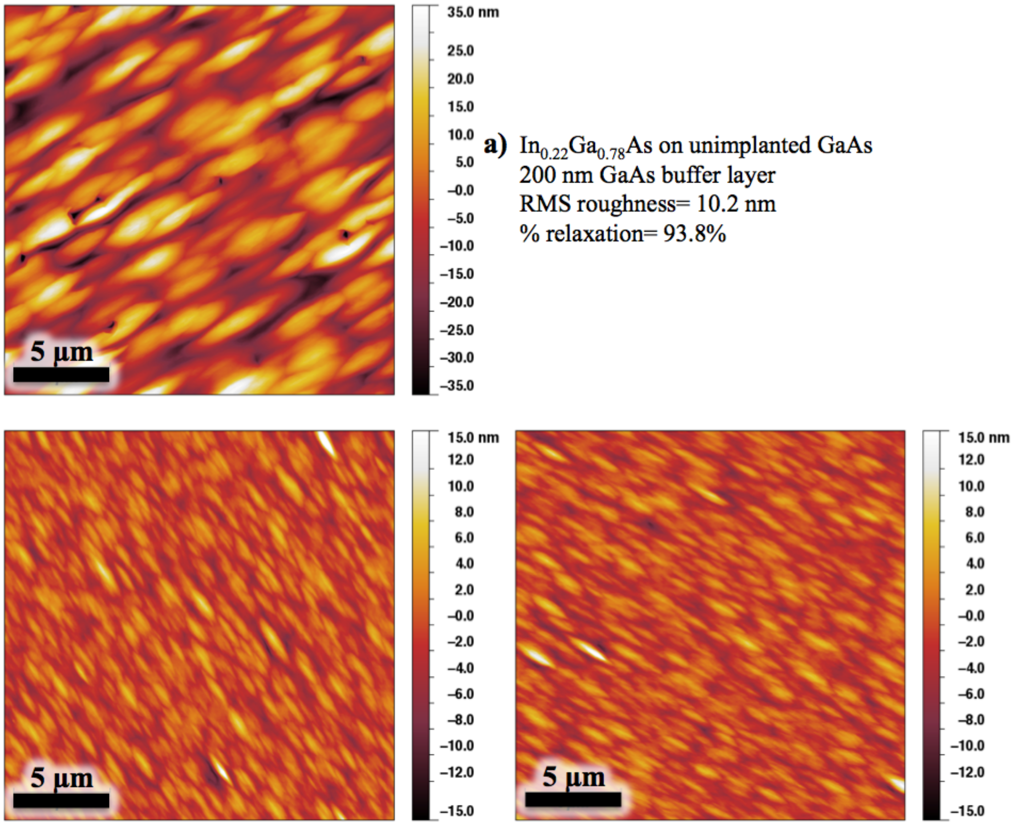

a) $In_{0.22}Ga_{0.78}As$ on unimplanted GaAs
200 nm GaAs buffer layer
RMS roughness= 10.2 nm
% relaxation= 93.8%

b) $In_{0.22}Ga_{0.78}As$ on 25 kV 1x10^{14} ion/cm^2 Ar$^+$
implanted GaAs, 2 nm buffer layer
RMS roughness= 2.5 nm
% relaxation= 98.0%

c) $In_{0.23}Ga_{0.77}As$ on 25 kV 5x10^{14} ion/cm^2 Ar$^+$
implanted GaAs, no buffer layer
RMS roughness= 2.5 nm
% relaxation= 96.8%

Figure 5.22: AFM surface scans of 1 µm thick InGaAs films grown on (a) an unimplanted GaAs substrate, (b) a 25 kV 1x10^{14} ions/cm^2 Ar$^+$ pre-implanted GaAs substrate, and (c) a 25 kV 5x10^{14} ions/cm^2 Ar$^+$ pre-implanted substrate. The FOV of each image is 10 µm. Composition, RMS roughness, and % relaxation are given for each sample.

Cross-sectional TEM specimens were prepared from the 1 µm InGaAs films grown on the unimplanted and the 25 kV 1x10^{14} ions/cm^2 Ar$^+$ pre-implanted substrates, and the cause of the difference in their roughness and relaxation values was immediately obvious. Figures 5.23(a) and (b) show a BF and DF image respectively of the InGaAs film grown on the unimplanted GaAs substrate, and Figures 5.23(c) and (d) show BF images of the film grown on the 25 kV 1x10^{14} ions/cm^2 Ar$^+$ pre-implanted substrate. The unimplanted sample had a low threading dislocation density, with threading dislocations injected into both the film and into the substrate. The 25 kV 1x10^{14} ions/cm^2 Ar$^+$ pre-implanted sample had a very high threading dislocation density in the InGaAs film, with no threading defects propagating through the ion damaged region of the substrate. The higher threading dislocation density in the Ar^+ pre-implanted sample indicates that in its case the InGaAs film relieved most of its lattice strain through dislocation formation rather than surface roughening, and its higher dislocation density allowed it to relax more completely. The unimplanted sample had very few dislocations, and so was able to relax less and roughened in response to strain in its InGaAs film.

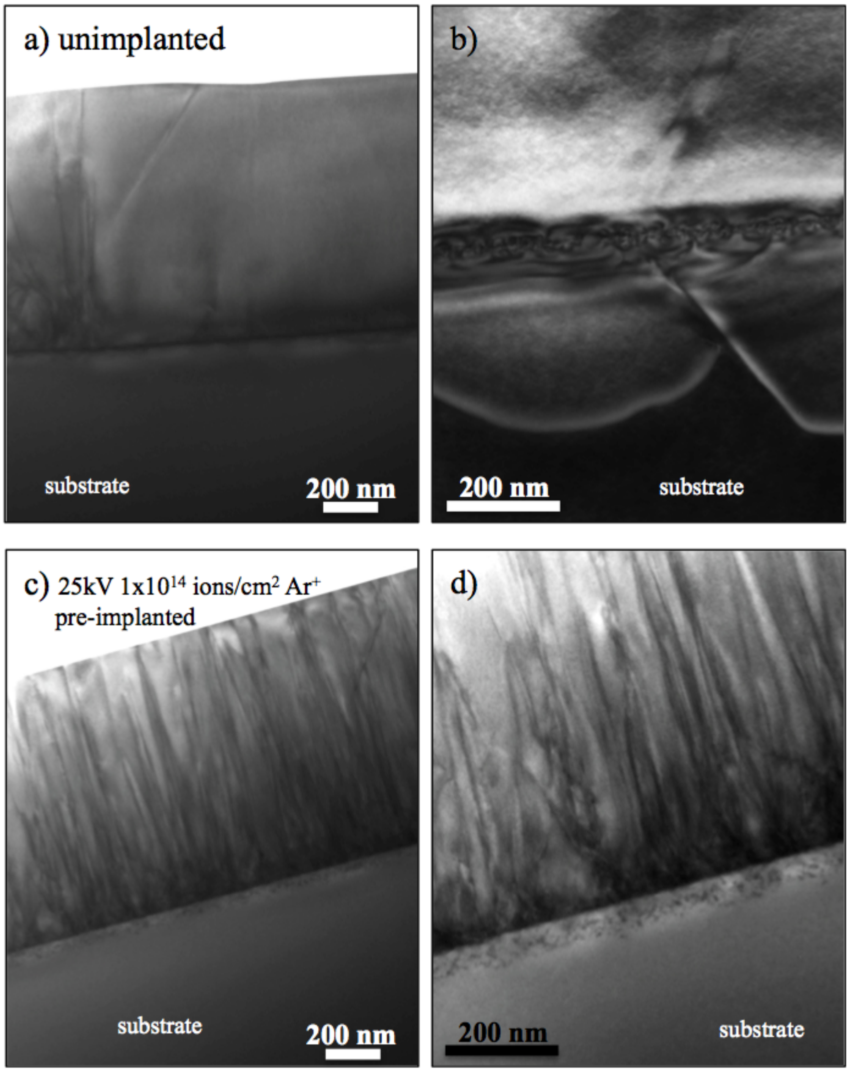

Figure 5.23: (a) shows a [110] BF image of an $In_{0.22}Ga_{0.78}As$ film grown on unimplanted GaAs, and (b) is a higher magnification g=004 DF image of that sample's InGaAs/GaAs interface showing threading dislocations in the GaAs substrate. (c) shows a [110] BF image of an $In_{0.22}Ga_{0.78}As$ film grown on 25 kV $1x10^{14}$ ions/cm^2 Ar^+ pre-implanted GaAs, and (d) shows a higher magnification BF image of that film's interface region.

Having observed the result of 1 μm thick InGaAs film growth on pre-implanted substrates, 50 nm and 100 nm thick films were grown to try to examine the effect of pre-implantation on thinner, less relaxed films. Three 100 nm thick $In_{0.25}Ga_{0.75}As$ films were grown one after another on the same day using exactly the same growth conditions on unimplanted, 25 kV $1x10^{14}$ ions/cm^2 pre-implanted, and 50 kV $1x10^{14}$ ions/cm^2 pre-implanted substrates with no buffer layers. The surface condition of each film was determined by AFM, and film composition and % relaxation were determined by HRXRD. Figure 5.24 shows AFM scans of each 100 nm InGaAs sample surface, and each sample's composition, RMS roughness, and % relaxation are listed with its corresponding image. The 100 nm InGaAs films grown on 25 and 50 kV Ar^+ pre-implanted GaAs substrates were significantly smoother, having RMS roughness values of 2.8 and 2.2 nm respectively, than the 100 nm film grown on unimplanted GaAs, which had a RMS roughness of 5.8 nm. Both of the films grown on pre-implanted GaAs substrates were >5% more relaxed than the unimplanted case. That large a relaxation difference is readily visible when comparing the HRXRD results from each sample, as shown by the 004 Ω-2θ scans in Figure 5.25. So in the 100 nm film case Ar^+ substrate pre-implantation again significantly improved InGaAs film roughness and relaxation.

Three 50 nm thick $In_{0.2}Ga_{0.8}As$ films were also grown one after another on the same day using exactly the same growth conditions on unimplanted, 25 kV $1x10^{14}$ ions/cm^2 pre-implanted, and 50 kV $1x10^{14}$ ions/cm^2 pre-implanted substrates with no buffer layers. The surface condition of each film was determined by AFM, and Figure 5.26 shows a scan of each 50 nm InGaAs sample surface. Signal in the 224 GE Ω-2θ scans from the 50 nm films was too low to allow a clear film peak to be resolved above the background, so HRXRD could not be used to determine the 50 nm InGaAs film composition and relaxation independently. The composition of the 50 films was instead determined using the ratio of the different group III growth rates used to produce them. As all three films were produced using exactly the same growth conditions, they may still be usefully compared to one another. Based on the AFM scans of each 50 nm sample, both 25 and 50 kV Ar^+ pre-implantation again significantly decreased film surface roughness relative to the unimplanted case.

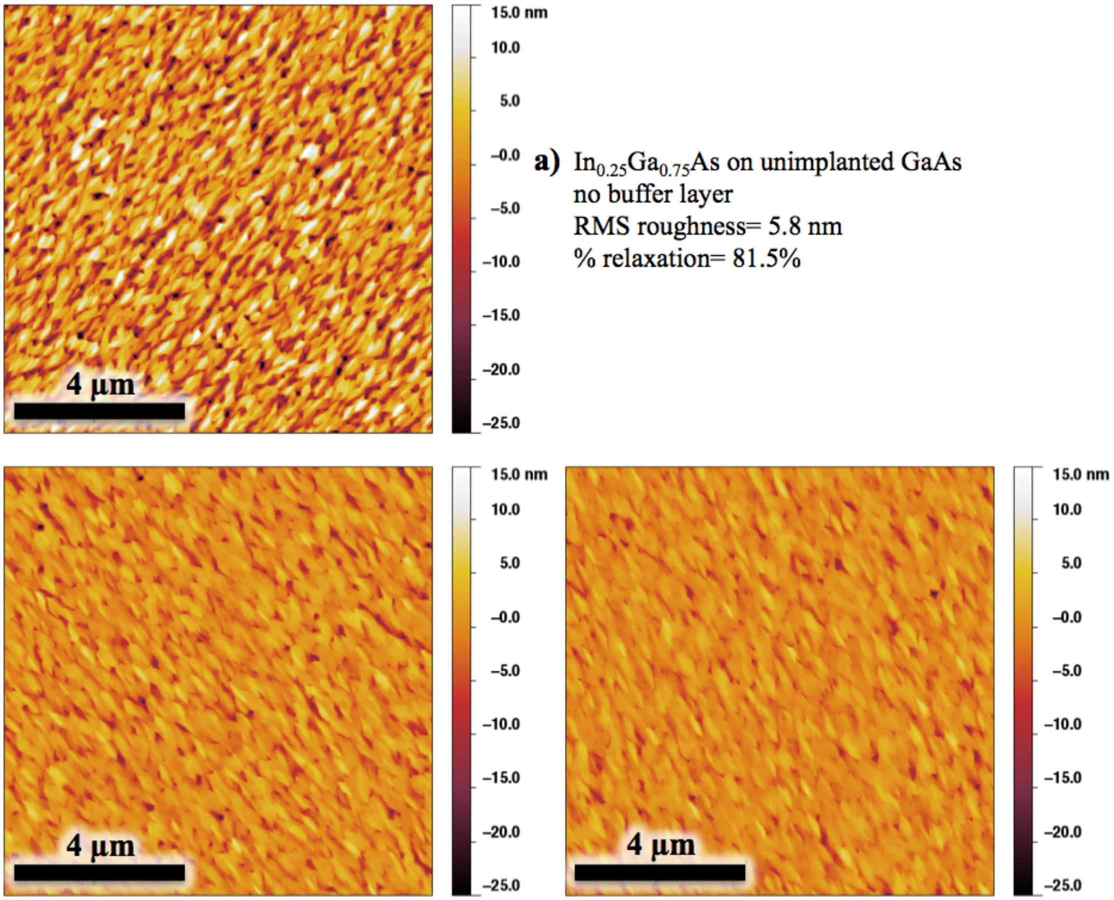

a) $In_{0.25}Ga_{0.75}As$ on unimplanted GaAs
no buffer layer
RMS roughness= 5.8 nm
% relaxation= 81.5%

b) $In_{0.25}Ga_{0.75}As$ on 25 kV 1x10^{14} ion/cm^2
Ar^+ implanted GaAs, no buffer layer
RMS roughness= 2.8 nm
% relaxation= 86.6%

c) $In_{0.25}Ga_{0.75}As$ on 50 kV 1x10^{14} ion/cm^2
Ar^+ implanted GaAs, no buffer layer
RMS roughness= 2.2 nm
% relaxation= 87.0%

Figure 5.24: AFM surface scans of 100 nm thick InGaAs films grown on (a) an unimplanted GaAs substrate, (b) a 25 kV 1x10^{14} ions/cm^2 Ar^+ pre-implanted GaAs substrate, and (c) a 50 kV 1x10^{14} ions/cm^2 Ar^+ pre-implanted substrate. The FOV of each image is 10 µm. Composition, RMS roughness, and % relaxation are given for each sample.

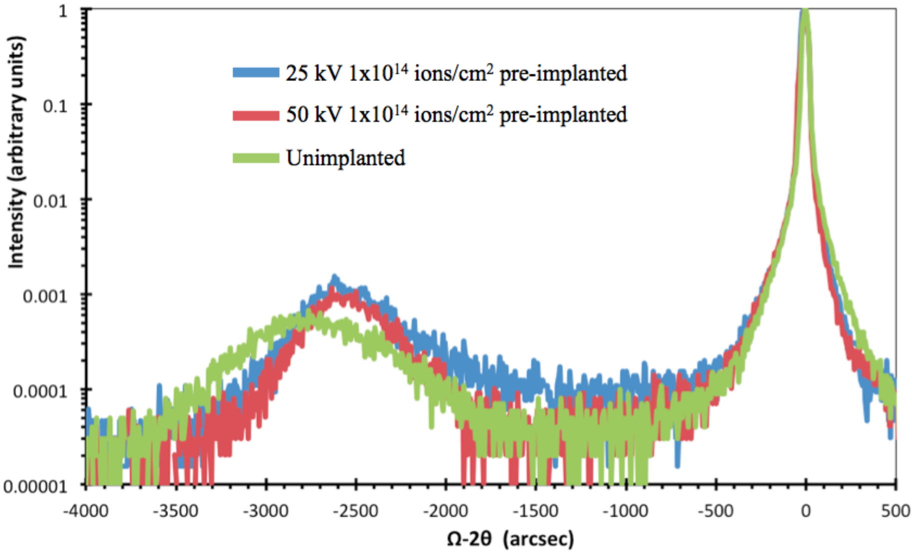

Figure 5.25: HRXRD 004 Ω-2θ scans taken of 100 nm thick $In_{0.25}Ga_{0.75}As$ films grown on unimplanted, 25 kV 1x10^{14} ions/cm^2 pre-implanted, and 50 kV 1x10^{14} ions/cm^2 pre-implanted substrates.

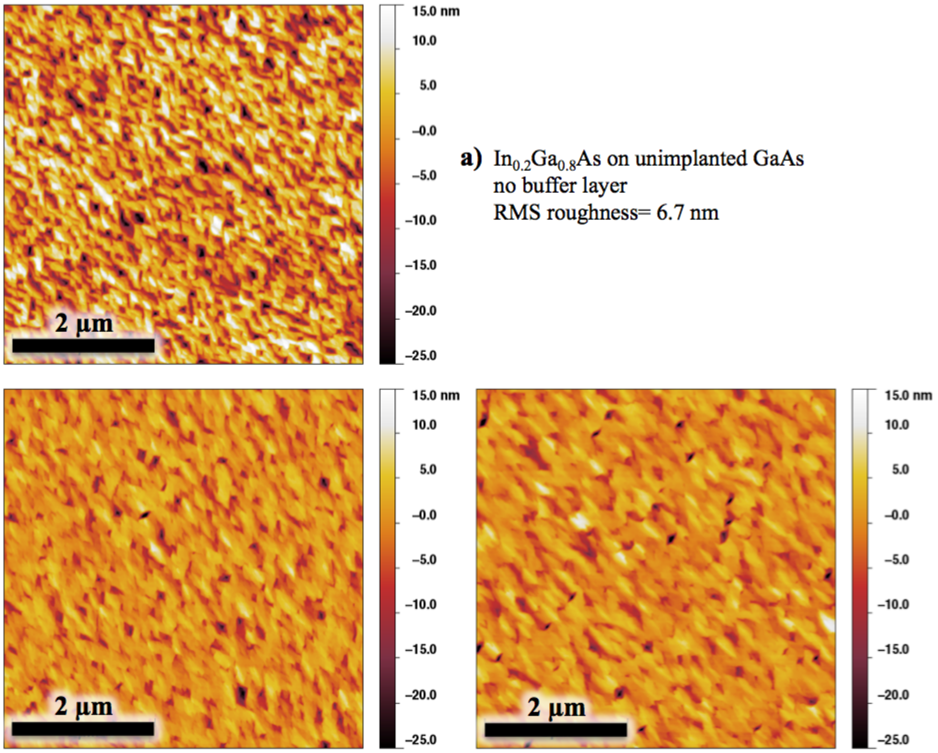

a) $In_{0.2}Ga_{0.8}As$ on unimplanted GaAs
no buffer layer
RMS roughness= 6.7 nm

b) $In_{0.2}Ga_{0.8}As$ on 25 kV 1x10^{14} ion/cm^2
Ar^+ implanted GaAs, no buffer layer
RMS roughness= 3.55 nm

c) $In_{0.2}Ga_{0.8}As$ on 50 kV 1x10^{14} ion/cm^2
Ar^+ implanted GaAs, no buffer layer
RMS roughness= 3.6 nm

Figure 5.26: AFM scans of 50 nm thick InGaAs films grown on (a) unimplanted GaAs, (b) 25 kV 1x10^{14} ions/cm^2 Ar^+ pre-implanted GaAs, and (c) 50 kV 1x10^{14} ions/cm^2 Ar^+ pre-implanted GaAs. The FOV of each image is 10 µm.

Cross-sectional TEM specimens were produced from each 100 nm InGaAs film sample and imaged to determine threading dislocation density. Figures 5.26(a) and (b) show BF and DF images respectively of the 100 nm $In_{0.25}Ga_{0.75}As$ film grown on unimplanted GaAs. Those images clearly show the rough surface of the film, and threading dislocations are visible in both images. Measurements of threading dislocation density using a series of TEM images along the InGaAs/GaAs interface put the linear threading defect density of that film at 24.5 μm^{-1}. Figures 5.26(c) and (d) show BF images of the 100 nm $In_{0.25}Ga_{0.75}As$ film grown on 25 kV $1x10^{14}$ ions/cm^2 Ar^+ pre-implanted GaAs, with threading dislocations visible in both images and ion induced defects beneath the InGaAs/GaAs interface visible in (d). The linear threading dislocation density of that film was found to be 21.4 μm^{-1}. Figures 5.26(e) and (f) show BF and DF images respectively of the 100 nm $In_{0.25}Ga_{0.75}As$ film grown on 50 kV $1x10^{14}$ ions/cm^2 Ar^+ pre-implanted GaAs, with threading dislocations and ion induced defects in the substrate visible in both images. The linear threading dislocation density of that film was found to be 35.0 μm^{-1}. Figures 5.26(c) and (e) both show that the Ar^+ pre-implanted samples are noticeably smoother than the unimplanted sample. Within the experimental error of the measurement method, the unimplanted and 25 kV $1x10^{14}$ ions/cm^2 implanted 100 nm film samples had approximately the same threading dislocation density, while the 50 kV $1x10^{14}$ ions/cm^2 sample was more dislocated. So Ar^+ pre-implantation did not significantly change InGaAs film threading dislocation density or increased it relative to the unimplanted case.

Table 5.1 summarizes the results of the InGaAs film growth on Ar^+ pre-implanted substrate and unimplanted substrate comparison experiments. Overall, Ar^+ pre-implantation of GaAs substrates before growth was shown to either not change or to increase the density of threading dislocations compared to growth on unimplanted samples, but it did improve film roughness and increase film relaxation. Theses results are likely the effect of roughness and relaxation being connected to dislocation formation. Ar^+ implantation seems to have promoted increased dislocation formation in the strained InGaAs films, and so allowed those films to more completely relax towards their equilibrium lattice parameter and to do so through dislocation generation instead of surface roughening. The lower number of dislocations in the films grown on unimplanted substrates forced those films to roughen and remain more strained when compared to the Ar^+ pre-implanted samples. By using Ar^+ pre-implantation it is possible to purposefully cause increased dislocation creation and relaxation in a strained film.

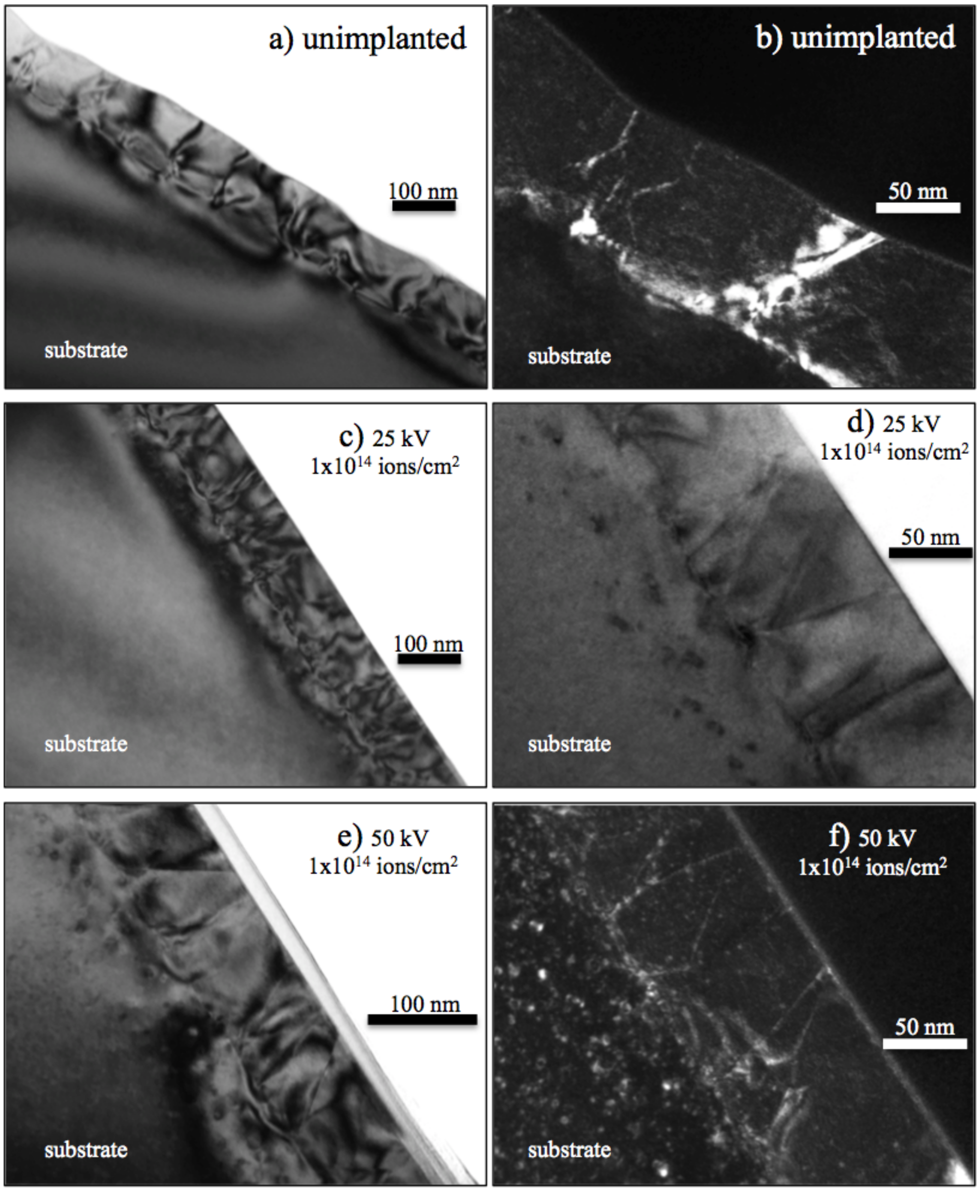

Figure 5.27: (a) and (b) show [110] BF and g=004 DF images respectively of a 100 nm $In_{0.25}Ga_{0.75}As$ film grown on unimplanted GaAs. (c) and (d) show a near [110] zone-axis [00-2] 2-beam BF image and a [110] BF image respectively of a 100 nm $In_{0.25}Ga_{0.75}As$ film grown on 25 kV $1x10^{14}$ ions/cm^2 Ar^+ pre-implanted GaAs. (e) and (f) show a near [110] zone-axis [00-2] 2-beam BF image and a g=004 DF image respectively of a 100 nm $In_{0.25}Ga_{0.75}As$ film grown on 50 kV $1x10^{14}$ ions/cm^2 Ar^+ pre-implanted GaAs.

Table 5.1: Summary of characterization results comparing InGaAs films of different thickness grown on unimplanted and Ar$^+$ pre-implanted GaAs substrates.

Sample Identifier	InGaAs Thickness (nm)	Implantation Energy (kV)	Ion Dose (ions/cm2)	Film composition (fraction In)	Film RMS roughness (nm)	Film % Relaxation	Linear Dislocation Density (#/µm)
M2905	1000	N/A	0	0.22	10.2	93.8	low
M2898	1000	25	1x10^{14}	0.22	2.5	98.0	very high
M2906	1000	25	5x10^{14}	0.23	2.5	96.8	
P2924	100	N/A	0	0.25	5.8	81.5	24.5
P2925	100	25	1x10^{14}	0.25	2.8	86.6	21.4
P2926	100	50	1x10^{14}	0.25	2.2	87.0	35
P2921	50	N/A	0	0.20	6.7	unknown	
P2922	50	25	1x10^{14}	0.20	3.5	unknown	
P2923	50	50	1x10^{14}	0.20	3.6	unknown	

5.5 Combined Ar$^+$ Pre-Implantation and Dislocation Filtering Approach

The ideal substrate for the epitaxial growth of thin film layers for device applications will be extremely smooth and free of threading dislocations that may propagate into any layers above it. Depending on the heterostructure to be grown, it may also be desirable for a substrate or buffer layer to be as unstrained and relaxed as possible. This work has shown that Ar$^+$ substrate pre-implantation may be used to grow lattice mismatched layers which are both smoother and more relaxed relative to a similar film grown on an unimplanted, normal substrate. However, they also have a higher threading dislocation density. So the films grown in this study satisfy some of the requirements for a high quality buffer layer, but from a defect density standpoint still leave much to be desired. However, if Ar$^+$ pre-implantation could be combined with another technique or structure designed to remove dislocations from the top layer of the film stack, it might be possible to produce a buffer on GaAs for lattice mismatched active layer growth that is smooth, relaxed and has a low dislocation density.

Several different types of dislocation filtering structures have been proposed and demonstrated in the literature that are compatible with the InGaAs/GaAs system. In particular, InAlAs based structures are well suited for use with GaAs and InGaAs because by varying In and Al composition $In_yAl_{1-y}As$ may be grown lattice matched to nearly the entire range of $In_xGa_{1-x}As$ alloys. This allows the growth of lattice matched or very low strain dislocation filtering structures or the purposeful inclusion of a small amount of mismatch strain to aid in dislocation filtering. InAlAs graded buffer layers grown on GaAs have been demonstrated as an effective method for preventing threading dislocations from entering active layers above them [27], and graded InAlAs buffer layers combined with an InAlAs inverse step layer, which is slightly in tension relative to the underlying buffer, have also been shown to be effective at relieving strain and preventing dislocation propagation into active layers [2,28]. Both strained and unstrained lattice matched InGaAs/InAlAs superlattice (SL) structures have also been shown to be effective at filtering dislocations and preventing their propagation into layers grown above them [5,29]. The exact mechanism by which the SL structures filter dislocations is not always clear. In the lattice matched case, the ability of the structure to filter dislocations has been attributed to the difference in the elastic constants of the InAlAs and InGaAs, with the stiffer InAlAs preventing dislocation propagation. In the lattice mismatched SL case and in studies using InAlAs inversion layers a small amount of tensile stress between the InAlAs and InGaAs has been suggested to prevent dislocation propagation while not being high enough to create additional dislocations by itself. For a more detailed look at how dislocation filtering works in the InAlAs system, please see the discussion in references [5] and [6].

It may be possible to use Ar^+ pre-implantation of GaAs substrates to purposefully increase dislocation generation in a thin sacrificial InGaAs layer, and so prevent film roughening and enhance relaxation. Then a dislocation filtering structure like those discussed above can be grown on that sacrificial layer to remove the threading dislocations from the system. Such a combined approach might be used to create a smooth and dislocation free substrate for growth of devices otherwise lattice mismatched to the GaAs substrate. From a device processing standpoint, substrate pre-implantation followed by dislocation filtering and device structure growth may be a simpler approach to improving substrate quality than the methods shown in previous III-V ion implantation studies, in which strained superlattice structures were grown first and then implanted to relax them [7,17].

As an initial proof of concept, a strained layer InGaAs/InAlAs SL structure was grown on Ar^+ pre-implanted GaAs. The structure consisted of a 50 kV $1x10^{14}$ ions/cm^2 Ar^+ implanted GaAs substrate, on which was grown a 200 nm thick $In_{0.22}Ga_{0.78}As$ layer, followed by growth of a 20 period 10 nm $In_{0.18}Al_{0.82}As$/10 nm $In_{0.22}Ga_{0.78}As$ superlattice, and finally followed by the growth of another 200 nm thick $In_{0.22}Ga_{0.78}As$ layer. All film growth was carried out at 500 ˚C under an As_4 overpressure using an $In_{0.22}Ga_{0.78}As$ growth rate of 0.65 ML/s and $In_{0.18}Al_{0.82}As$ growth rate of 0.76 ML/s. The composition of the InAlAs was chosen to produce a slight tensile strain of ~0.36% relative to the fully relaxed $In_{0.22}Ga_{0.78}As$ lattice parameter. The composition and % relaxation of the top $In_xGa_{1-x}As$ film were determined after growth by HRXRD to be x=0.226 and 94.9% respectively. Figure 5.28 shows an AFM scan of the top $In_{0.22}Ga_{0.78}As$ layer, which had an RMS roughness of 3.3 nm. Figure 5.29(a) shows a [110] BF TEM image of the entire filtering structure, and Figure 5.29(b) shows a g=004 DF two image montage of the entire film structure. At the bottom of both images the ion damaged GaAs substrate and very high dislocation density lower 200 nm $In_{0.22}Ga_{0.78}As$ layer can be seen. Ar^+ pre-implantation was purposefully used to increase the dislocation density and relaxation of that lower $In_{0.22}Ga_{0.78}As$ layer. The superlattice structure can be seen as layers of alternating light and dark contrast in the middle of both images. The top $In_{0.22}Ga_{0.78}As$ layer has fewer threading dislocations visible in it than the lower layer, indicating that the superlattice structure was able to filtering out some but not all of the threading dislocations. This first filtering structure was grown as a proof of concept, and not fully optimized. With additional optimization of growth conditions and strain in the superlattice structure, it may be possible to filter out more threading dislocations and do so with a thinner SL structure.

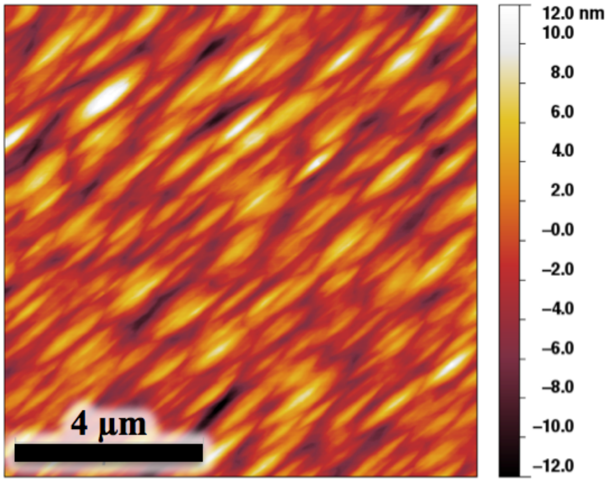

Figure 5.28: AFM scan of the top $In_{0.22}Ga_{0.78}As$ layer of an $In_{0.18}Al_{0.82}As/In_{0.22}Ga_{0.78}As$ filtering structure grown on a 50 kV 1x10^{14} ions/cm^2 Ar^+ pre-implanted GaAs substrate.

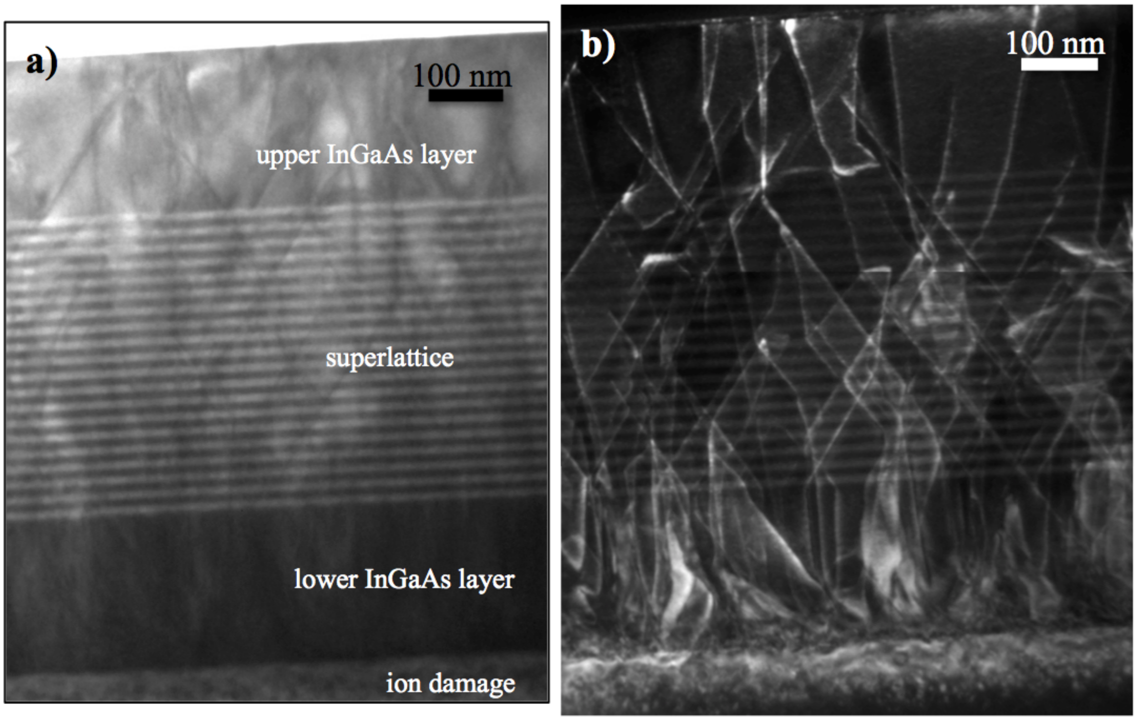

Figure 5.29: TEM images showing an $In_{0.18}Al_{0.82}As/In_{0.22}Ga_{0.78}As$ filtering structure grown on a 50 kV 1x10^{14} ions/cm^2 Ar^+ pre-implanted GaAs substrate. (a) shows a [110] BF image of the entire structure, and (b) shows two g=004 DF images that together show the entire structure.

5.6 Conclusions and Future Work

This work characterized the effects of In^+ and Ar^+ implantation on GaAs wafer substrates resulting from a variety of implantation parameters, and then examined the effect of both In^+ and Ar^+ substrate pre-implantation on lattice mismatched InGaAs film growth. 50-200 kV 1×10^{14} ions/cm^2 In^+ implantation was found to create a layer of amorphous and ion damaged material in GaAs substrates. That amorphous layer could be recrystallized upon annealing. Growth of 1 μm thick InGaAs layers on both 50 and 200 kV In^+ pre-implanted GaAs substrates did not significantly improve film roughness or relaxation when compared to similar films grown on unimplanted GaAs. Growth on In^+ pre-implanted substrates either increased or did not lower the threading defect density of InGaAs films grown on them. Thus by any of the metrics used in this study, In^+ pre-implantation did not improve InGaAs film quality. This may have been for one or more of several different reasons. In some cases the defects produced using the In^+ implantation conditions chosen may have been to far from the InGaAs/GaAs interface to interact with the growing film. The defects produced may also not have been of a type that could strongly interact with strain in the growing film. That might be because In will readily incorporate into the GaAs crystal structure, and so with annealing the implanted In^+ ions may have produced defects which did not strain the surrounding lattice enough to produce an effect. Epitaxial recrystallization of GaAs material amorphized by In^+ implantation may also have removed defects and strain created by implantation, and so prevented implantation from having a beneficial effect on the InGaAs films.

Based on results from the In^+ pre-implantation study, a second round of Ar^+ pre-implantation experiments were conducted with implantation species and conditions chosen to minimize the influence of the effects which may have caused In^+ to produce no beneficial change in InGaAs film quality. Ar^+ ions were implanted into GaAs substrates using ion energies of 25 and 50 kV and doses of 1×10^{14} ions/cm^2 and 5×10^{14} ions/cm^2. The higher dose implantation conditions were found to partially amorphize the GaAs substrate. The lower ion dose implantations did not produce an amorphous layer, instead creating a band of ion induced defects that stretched up to the substrate surface. 1 μm, 100 nm, and 50 nm thick InGaAs films were grown on Ar^+ pre-implanted GaAs substrates. Growth on the pre-implanted substrates was found to produce a decrease in film roughness and an increase in film relaxation relative to films grown on unimplanted GaAs. Ar^+ pre-implantation either increased or did not significantly change the threading defect density of the 1 μm and 100 nm thick InGaAs films. The films grown on the Ar^+ pre-implanted substrates were likely less rough and more relaxed because implantation enhanced the creation of defects in the InGaAs films, allowing them to relax without roughening. So Ar^+ pre-implantation has been shown to be a method for enhancing the creation of threading defects in lattice-mismatched films and to, as a trade-off, produce the beneficial effects of lowered roughness and increased film relaxation.

By combining Ar^+ pre-implantation with an InAlAs/InGaAs dislocation filtering structure it may be possible to create InGaAs substrates for device growth that are smooth, relaxed, and have a low threading defect density. An InAlAs/InGaAs superlattice dislocation filtering structure was grown on 50 kV Ar^+ pre-implanted GaAs as a proof of concept. It did filter out some but not all of the dislocations purposefully produced in a strained sacrificial InGaAs layer by substrate pre-implantation. Future work might focus on optimizing the growth conditions and design of similar structures to better filter threading defects. A possible change in filtering structure design that may improve results is to grow the InAlAs layers with lower In content, which would create more tensile strain in those layers and so better stop dislocation propagation. Through optimization it may be possible to filter out most of the threading dislocations using a thinner filter structure. This would provide a route for using Ar^+ substrate pre-implantation to produce useful high quality buffer layers for device growth. Using substrate pre-implantation to purposefully enhance dislocation creation in a sacrificial layer followed by dislocation filtering structure growth may, from a device processing standpoint, prove to be a simpler method for producing unstrained, threading dislocation free buffer layers than other methods such as ion implantation through a strained-layer-superlattice or thick metamorphic buffer layer growth.

In addition to improving the effectiveness of dislocation filtering structures, the GaAs substrate pre-implantation conditions could also be further optimized. Future work in this area might include varying Ar^+ implantation energy and dose or exploring the use of other implantation species. By further optimizing the pre-implantation process, it may be possible to lower the amount by which pre-implantation increases InGaAs film threading defect density while still providing an increase in film relaxation and lowered film roughness. As part of this process a thorough examination of the mechanism by which ion implantation enhances threading dislocation creation will provide a basis for the design of implantation experiments designed to minimize that effect.

5.7 References

[1] Ohring, M. *Materials Science of Thin FIlms, 2nd Edition* (Academic Press, San Diego, 2002).

[2] Lubyshev, D. et al. *Journal of Vacuum Science & Technology B: Microelectronics and Nanometer Structures* **19**, 1510-1514 (2001).

[3] McGill, L. M. et al. *Journal of Vacuum Science & Technology B: Microelectronics and Nanometer Structures* **22**, 1899 (2004).

[4] Lee, M. L., Antoniadis, D. A. & Fitzgerald, E. A. *Thin Solid Films* **508**, 136-139 (2006).

[5] Gourley, P. L., Drummond, T. J. & Doyle, B. L. *Applied Physics Letters* **49**, 1101-1103 (1986).

[6] Dodson, B. W. *Journal of Electronic Materials* **19**, 503-508 (1990).

[7] Myers, D. R., Arnold, G. W., Hills, C. R., Dawson, L. R. & Doyle, B. L. *Applied Physics Letters* **51**, 820 (1987).

[8] Pathak, A. P., Dhamodaran, S., Sathish, N. & Rao, N. S. *Radiation Effects and Defects in Solids* **162**, 131-150 (2007).

[9] Hull, R. et al. *Applied Physics Letters* **56**, 2445-2447 (1990).

[10] Holländer, B. et al. *Nuclear Instruments and Methods in Physics Research Section B: Beam Interactions with Materials and Atoms* **175**, 357-367 (2001).

[11] Sawano, K. et al. *Applied Physics Letters* **85**, 2514 (2004).

[12] Hsieh, Y. C. et al. *Applied Physics Letters* **90**, 083507 (2007).

[13] Sawano, K. et al. *Thin Solid Films* **517**, 87-89 (2008).

[14] Nageswara Rao, S. V. S. et al. *Nuclear Instruments and Methods in Physics Research Section B: Beam Interactions with Materials and Atoms* **212**, 442-450 (2003).

[15] Dhamodaran, S. et al. *Journal of Physics: Condensed Matter* **18**, 4135 (2006).

[16] Dhamodaran, S. et al. *Nuclear Instruments and Methods in Physics Research Section B: Beam Interactions with Materials and Atoms* **266**, 583-588 (2008).

[17] Myers, D. R. et al. *Superlattices and Microstructures* **4**, 585-589 (1988).

[18] Dhamodaran, S. et al. *Radiation Effects and Defects in Solids* **162**, 215-221 (2007).

[19] Holländer, B. et al. *Nuclear Instruments and Methods in Physics Research Section B: Beam Interactions with Materials and Atoms* **148**, 200-205 (1999).

[20] Luysberg, M. et al. *Journal of Applied Physics* **92**, 4290 (2002).

[21] Christiansen, S. H., Mooney, P. M., Chu, J. O. & Grill, A. *MATERIALS RESEARCH SOCIETY SYMPOSIUM PROCEEDINGS* **686**, 27-32 (2002).

[22] Cai, J. et al. *Journal of Applied Physics* **95**, 5347 (2004).

[23] http://www.srim.org/

[24] Ziegler, J. F., Biersack, J. P. & Littmark, U. *The Stopping and Range of Ions in Solids,* (Pergamon, New York, 1985).

[25] Jones, K. S. & Santana, C. J. *J. Mater. Res* **6**, (1991).

[26] Sayed, M., Jefferson, J. H., Walker, A. B. & Cullis, A. G. *Nuclear Instruments and Methods in Physics Research Section B: Beam Interactions with Materials and Atoms* **102**, 232-235 (1995).

[27] Cordier, Y., Zaknoune, M., Trassaert, S. & Chauveau, J. M. *Journal of Applied Physics* **90**, 5774-5777 (2001).

[28] Cordier, Y. & Ferre, D. *Journal of Crystal Growth* **201**, 263-266 (1999).

[29] Chu, P., Lin, C. L. & Wieder, H. H. *Thin Solid Films* **166**, 155-162 (1988).

Chapter 6

Conclusions and Future Work

Ion implantation has been used extensively in the electronics industry for quite some time to alter the electronic properties of the III-V and other semiconductor materials. However, the unique response of the III-V semiconductors to ion irradiation has let to the discovery of other applications for ion irradiation in that material system. This work is composed of four studies, each of which had the goal of studying some aspect of the response of III-V substrate materials to ion irradiation. Two of those studies examined different methods by which FIB irradiation of III-V materials could be used to create nanostructures that might have use in nanoscale device applications. The other two studies looked at ways that ion irradiation might be used to modify III-V substrate materials to improve the overall quality of lattice mismatched III-V films grown on them. This chapter will summarize the primary findings of each study, draw conclusions based on those findings, and suggest future work.

The basic response of GaAs, InP, InAs, and AlAs to Ga^+ FIB irradiation was characterized, and the ability of each of those materials to form group III nanodots under normal incidence FIB irradiation was examined in detail. This was accomplished by measuring the distribution of nanodot sizes produced as a function of FIB dose for each material. Each of the studied materials was found to respond differently to FIB exposure. With increasing ion dose the distribution of nanodots on GaAs was found to stabilize with an average nanodot diameter of ~150 nm. Similarly the distribution of nanodot sizes on InP was found with increasing ion dose to stabilize with an average nanodot diameter of ~33 nm. The nanodot size on InAs undergoes a transition past a critical dose to a bimodal size distribution. Thin films of AlAs were irradiated and not observed to form Al nanodots. In order to better understand these experimental results, a model was employed that combined sputtering theory and diffusive growth driven by Ostwald ripening. The final form of that model predicts that the competing effects of nanodot losses to sputtering and nanodot growth throug diffusive transport of excess group III adatoms to each dot control nanodots size. The model also predicts that average nanodot size will eventually reach a stable value when those competing effects balance. Final nanodot size is determined by the physical processes active in the system and the physical properties of the particular III-V material being irradiated. Materials which have a higher rate of group III adatom surface diffusion and a higher rate of excess group III atom production due to preferential sputtering will correspondingly have nanodots that are able to grow to larger sizes before growth is stopped by sputtering losses. In contrast, materials that have a high pure group III sputtering yield and a high group III surface tension will have nanodots that are stabilized at smaller relative sizes. All of these effects are in some capacity related to the relative atomic bonding strength of the III-V material or pure group III element, and the experimental results of this study qualitatively agree with the trends predicted by the model. This work represents the first reported investigation of the fundamental processes that drive the nanodot forming behavior of the III-V compounds. The results of this work reveal the physical parameters that may be used to control group III droplet production, and so have implications for the design of ion beam processes aimed at creating nanostructures for device applications using III-V materials.

A second nanostructure creation study was conducted examining the creation, templating, and characterization of unique semiconductor spike nanostructures. Those structures, termed “nanospikes,” were created using normal incidence FIB irradiation of homoepitaxial InAs grown on n+ InAs substrates or InAs films grown on n+ InP substrates. Low FIB currents and short spot dwell times were identified as the optimum beam parameters for nanospike creation. The mechanism of nanospike creations was identified as an In droplet self-assembled etch-masking process. In droplets created by FIB irradiation mask the underlying material from further erosion, allowing nanospikes to form at locations where In droplets stop to locally protect the InAs film. During experiments examining creation of nanospikes on InAs/InP heterostructures it was discovered that nanospikes and large In droplets are unable to form on InP, and the location of the InAs/InP interface as InAs film erosion proceeds limits further nanospike formation. Thus the relative FIB responses of In metal, InAs, and InP control nanospike creation and location. A novel InAs/InP heterostructure FIB pre-patterning method for controlling nanospike location was also demonstrated in this work. By pre-patterning an InAs film to control its morphology before nanospike creation, the location of In droplets and correspondingly nanospike formation could be partially controlled. By pre-patterning an InAs film on InP it was found that nanospikes could be reliably templated into arrays. This improved templating effect occurs because patterning an InAs/InP heterostructure to expose the underlying InP restricts the areas where nanospikes are able to form. TEM characterization of the nanospikes revealed that they all possess an In droplet cap at their top and an outer ion damaged layer. Their core structures may range from fully ion-disrupted to almost entirely single crystalline. The single crystalline cores of the nanospikes were found to maintain the zinc blende structure and crystallographic orientation of the substrate material. Templated nanospikes produced using an InAs/InP heterostructure were in all cases observed to possess primarily single crystalline cores. The electrical response of randomly located homoepitaxial InAs, randomly located InAs/InP, and templated InAs/InP nanospikes were examined using an *in-situ* TEM nanoprobe technique. Characterization of the electrical properties of ion erosion created nanostructures in this manner represents a first-of-its-kind examination. All three electrically tested nanospikes types showed a non-linear current-voltage (IV) response. There was significant spread in the nanospike IV data and resistivity values that could not be accounted for by normalizing the results with respect to the physical size of the spikes. It is likely that this variation in electrical response can be attributed to differences in nanospike core structure. Those homoepitaxial InAs nanospikes with a greater volume fraction of single crystalline core were generally found to have lower resistivity values than those with more completely ion-disrupted cores. However, no similar trend was observed for InAs/InP nanospikes. In an attempt to understand the non-linear IV behavior of the nanospikes, the electrical response of the nanospikes recorded in this work was compared to the results of similar nanowire electrical testing results reported in the literature, and was found to most closely match cases of nanowire electrical behavior attributed to contact barrier limited conduction. Simple band structure models were constructed for both the InAs/n+ InAs and InAs/n+ InP nanospike test junctions. Based on those models, only very low contact barriers to conduction were predicted for the InAs/n+InAs nanospike case, and it is possible another electronic barrier exists in the system due to the ion damaged nanospike material in the conduction path. In the InAs/n+ InP nanospike junction case, higher barriers to electron conduction were predicted to exist at one contact and at the InAs/InP interface, and it is possible that those barriers play a greater role in determining the electrical response of those spikes. This would help to account for why no trend was seen relating InAs/InP nanospike core structure and resistivity. Regardless of the factors that control nanospike conduction, the nanospikes tested in this work show promising levels of conductivity. Combined with their ion disrupted structure this may make the nanospikes useful for thermoelectric applications which will require nanostructures with high electrical conductivity and low thermal conductivity.

The effects of using FIB milling to pattern GaAs and InP substrates with 3-D features before film growth were examined with the goal of using 3-D substrate patterning to enhance lattice mismatched film relaxation and to reduce threading defect density in those films. A variety of FIB milled patterns were created on both GaAs and InP, with the primary focus being on the creation and characterization of square mesa array, square recess array, and hexagonally arranged hole patterns. Characterization of FIB created patterns showed that group III nanodots were being produced on the patterned features. Those nanodots would later be shown to be detrimental to film growth, and so several different patterning strategies were developed to limit the influence of ion damage and FIB produced nanodots on the portions of the patterns intended for film growth. InAs films were grown on patterned InP substrates. Growth on the patterns was found to significantly alter InAs film morphology, producing regularly faceted InAs islands at patterned features while denuding the surrounding area of InAs material. This affect was attributed to 3-D features acting as strong sinks for adatoms during film growth. InGaAs films were grown on patterned GaAs, and a similar effect was observed, with the patterned features locally controlling InGaAs film morphology. TEM cross-sections through regions of InAs film grown on patterned InP revealed that growth on the patterns had been universally detrimental to film growth. InAs material grown on FIB milled region of substrate was highly defective and polycrystalline. That defective material appeared to also inject defects into adjacent large, epitaxial InAs islands grown on patterned features. As a result the InAs film grown on the patterned InP substrate regions was found to have an unchanged or higher threading defect density than film grown on unpatterned substrate areas. The poor quality of the film grown on FIB patterned regions was attributed to the rough surface of the FIB milled areas and to the presence of group III nanodots produced by the FIB. This work demonstrates that 3-D features can be used to alter film morphology. The detrimental effects on film quality were the result of the FIB patterning technique, and not necessarily inherent to 3-D patterned features in general. It is possible that by patterning III-V substrates using another method growth on the 3-D patterns may be used to enhance strain relaxation and improve the film quality of lattice mismatched films.

The final study reported in this dissertation examined the effects of In^+ and Ar^+ ion pre-implantation of GaAs substrates on subsequently grown lattice mismatched InGaAs film quality, as is the first reported examination of substrate pre-implantation in the III-V system. GaAs substrates were In^+ and Ar^+ ion implanted using a broad beam implantation system and a variety of different beam energies and ion doses. 50-200 kV $1x10^{14}$ ions/cm^2 In^+ implantation was found to partially amorphize the GaAs substrates, and that amorphous layer was recrystallized by annealing or during the heating associated with film growth. Growth of 1 μm thick InGaAs layers on both 50 and 200 kV In^+ pre-implanted GaAs substrates did not significantly improve film roughness, increase film relaxation, or lower film threading defect density relative to similar films grown on unimplanted GaAs. This lack of improvement in film quality may have been due to a failure of In^+ implantation to produce ion damage that interacted with the strain at the InGaAs/GaAs heterointerface strongly enough to induce a change in the InGaAs films. With this in mind, a second round of experiments using Ar^+ pre-implantation were designed to increase the effect of ion implantation on mismatched film growth. Ar^+ ions were implanted into GaAs substrates using ion energies of 25 and 50 kV and doses of $1x10^{14}$ ions/cm^2 and $5x10^{14}$ ions/cm^2. The higher dose implantations were found to partially amorphize the GaAs substrates while the lower dose implantations did not. 1 μm, 100 nm, and 50 nm thick InGaAs films were grown on lower dose Ar^+ pre-implanted

GaAs substrates. Growth on Ar^+ pre-implanted GaAs substrates was found to reduce InGaAs film roughness, increase film relaxation, and to increase or not significantly change the threading defect density of the films relative to similar films grown on unimplanted GaAs. These changes in film properties appear to occur because pre-implantation enhances the formation of threading defects in the InGaAs films, which allows them to relax more completely. By combining the film roughness and relaxation improvements provided by Ar^+ pre-implantation with a dislocation filtering structure, it may be possible to produce smooth, relaxed, and low threading defect density buffer layers on GaAs for lattice mismatched device layer growth. As an initial proof of concept, an InAlAs/InGaAs superlattice structure designed to filter dislocations was grown on 50 kV $1\text{x}10^{14}$ ions/cm^2 Ar^+ pre-implanted GaAs. This structure was able to filter out some but not all of the threading dislocations produced in the InGaAs layer at the bottom of the structure. It is possible that with further optimization a dislocation filtering structure grown on pre-implanted GaAs may be used to better remove threading defects from the system and so produce a high quality buffer layer for device growth.

Each of the four studies summarized above was conducted with different methods and applications in mind, but because each examined the response of III-V materials to ion irradiation some broader conclusions with regard to that common theme can be drawn. The FIB and broad beam implantation substrate modification portions of this work both at their simplest were focused on characterizing the effects of ion damage in the III-V semiconductors and understanding its influence on that material's surface properties. In the broad beam GaAs pre-implantation study, the ability of ion implantation damage to interact with the GaAs surface and so influence film growth was found to depend on implantation species, ion energy, and ion dose. Those parameters affected the location and types of ion damage created in the substrate material, and through those effects changed the characteristics of lattice mismatched films grown on the GaAs substrates. Similarly, in the FIB 3-D substrate patterning study, the affect of FIB irradiation on film growth was partially controlled by the nature of the damage inflicted on GaAs and InP substrates by FIB milling. The distribution of FIB milled regions created by a specific pattern and the degree of ion milling controlled the location and extent of FIB induced surface roughening and group III nanodot creation. These features in turn affected locally the characteristics of the lattice mismatched III-V film grown on or near them. These studies have shown that by controlling the nature and extent of the damage created in a III-V semiconductor material by ion irradiation, the properties of that material as substrate for epitaxial film growth may also be controlled.

The three FIB based studies that are part of this dissertation each highlight how the interplay of the ion beam responses of different materials may produce useful or unexpected results, and differences in the FIB sputtering behavior of different materials were exploited to produce several useful results. In the group III nanodot creation study, variation in each III-V material's capability to produce group III nanodots could be directly related to the differences in their sputtering rates and material properties. Differences in the sputtering rate of each individual III-V material and its group III nanodots established the final nanodot size distribution that could be created. InAs nanospike creation was also reliant on differences in the FIB response of the different materials present. The high preferential sputtering rate of InAs and the relatively slow sputtering rate of In droplets allowed the nanospikes to form, and without that interplay of their properties the self-masking mechanism of nanospike creation would not be active. Reliable control of nanospike templating also relied on differences between the FIB responses of two III-V materials. The inability of InP to form large In droplets or nanospikes under FIB irradiation meant that InAs/InP heterostructures could be used to control the movement of In droplets during FIB erosion and so control the location at which nanospikes formed. In the 3-D FIB substrate patterning study, the different FIB milling rates and nanodot forming capabilities of InP and GaAs affected the FIB parameters required to create different types of 3-D features and affected when and where group III nanodots would form on those patterns. Thus the GaAs and InP FIB responses controlled the types of patterning strategies that could be employed with each substrate material to control the influence of FIB damage and nanodot creation on the patterned regions. In all of the FIB based studies in this work, characterizing and understanding the different FIB responses of the III-V materials studied was fundamental to understanding experimental results in terms of basic physical processes and then interpreting those results with the applications which motivated each study in mind. In general the work presented in this dissertation shows that if ion irradiation is to be used in a controllable and repeatable fashion to create nano or device structures from III-V materials, it is absolutely necessary to understand the basic physical properties and processes which control their responses to ion beam irradiation.

Based on the complexity and variety of the ion beam induced effects observed in this study, it seems clear that there are still many avenues available for the continued examination of the ion beam response of the III-V materials. Future work specific to each of the four studies which compromise this dissertation and their intended applications were suggested at the end of each study's corresponding chapter. However, some broader general goals for future work in the III-V system may be suggested as well. Based on the number of different nanostructures created in the course of this work and the multiple different physical phenomena identified as responsible for their creation, it seems likely that other III-V nanostructures that might be created by ion irradiation remain as yet undiscovered. Experiments designed specifically to examine the interplay between the ion beam responses of different material combinations may lead to new nanostructure discovery. Examining the ion beam response and erosion of different III-V heterostructure combinations may result in the creation of unique nanostructures, and at a minimum may reveal ways to produce structures similar to nanospikes using systems other than InAs/InP. It may also be possible to erode more complex heterostructures, such as an InAs/InGaAs/InP film structure, to produce heterostructure nanospikes or other nanostructures with interesting electrical properties. Any further work exploring the material properties and mechanisms responsible for the ion beam creation of nanostructures, like the nanospikes produced in this work, may lead to new methods for exploiting those properties for novel nanostructure creation. Examination of the ion beam response of III-V alloy and heterostructure systems may also provide additional methods for more carefully controlling nanostructure creation as well. As an example, examination of the group III nanodot forming capabilities of the III-V alloys may demonstrate that composition variation may be used as another method for controlling nanostructure size distributions. Ion beam erosion of different III-V thin film heterostructures may also reveal other unique processing methods for controlling nanostructure features, similar to the effect of using an InAs/InP heterostructure on nanospike templating reported in this work. In general, further examination of the mechanisms which control ion beam induced nanostructure creation and the physical properties which control ion beam damage production in the III-V materials and their combinations will not only help to further understanding of those phenomena, but may also lead to the discovery of new structures and effects which may have useful applications. There is still much room both for further development of the ion beam applications discussed in this document and for discovery and development of other useful technological applications for ion beam irradiation and modification of materials in the III-V semiconductor system.